Czech Technical University in Prague
Faculty of Nuclear Sciences and Physical Engineering

Ph.D. Thesis

Heavy flavor physics in the STAR experiment

Prague, 2015 Ing. Olga Rusňáková

Bibliografický záznam

Autorka	Ing. Olga Rusňáková, České vysoké učení technické v Praze, Fakulta jaderná a fyzikálně inženýrská, Katedra fyziky
Název práce	Fyzika těžkých kvarků na experimentu STAR.
Studijní program	Aplikace přírodních věd
Studijní obor	Jaderné inženýrství
Školitel	Mgr. Jaroslav Bielčík Ph.D, České vysoké učení technické v Praze, Fakulta jaderná a fyzikálně inženýrská, Katedra fyziky
Akademický rok	2014/2015
Počet stran	151
Klíčová slova	ultrarelativistické srážky, těžké kvarky, nefotonické elektrony, jaderný modifikační faktor

Bibliographic Entry

Author	Ing. Olga Rusňáková, Czech Technical University in Prague, Faculty of Nuclear Sciences and Physical Engineering, Departement of physics
Title of Dissertation	Heavy flavor physics in the STAR experiment.
Degree Programme	Aplication of natural sciences
Field of Study	Nuclear engineering
Supervisor	Mgr. Jaroslav Bielčík Ph.D, Czech Technical University in Prague, Faculty of Nuclear Sciences and Physical Engineering, Departement of physics
Academic Year	2014/2015
Number of Pages	151
Keywords	ultra-relativistic collisions, heavy quarks, non-photonic electrons, nuclear modification factor

Acknowlegement

Foremost I would like to express my gratitude to my supervisor Jaro Bielčík for providing me immense support throughout my research. Without him I would have been forced to left the field of physics several years ago. I would like to thank to the STAR Collaboration for the opportunity to meet and work with so many great scientists and technicians who all live and breath for the STAR experiment. A tremendous acknowledgement belongs to Daniel Kikola, Wei Xie, Mustafa Mustafa for their priceless advices and critical view at my analysis. I also would like to thank to Michal Křelina and Barbara Trecziak for their careful reading of the manuscript and tons of corrections and many suggestions for the improvements. Last but not least, a big hug goes to my husband for his endless patience and continuous support.

Abstract

The properties of strongly interacting Quark-Gluon Plasma can be studied using heavy quarks, such as charm and bottom. Due to their large masses, heavy quarks are produced mainly during initial parton-parton interaction at RHIC, before the QGP phase, and their production rates can be calculable by pQCD. Thus they are good probes to study the QCD matter. They are expected to interact with the medium differently than the light quarks. Hot and cold nuclear matter effects, which affect the heavy quark production in heavy ion collisions, could be quantified with nuclear modification factor, where result from p+p collisions serves as a baseline. At RHIC, heavy quarks could be studied by measuring non-photonic electrons which are produced from semi-leptonic heavy flavor decays. The measurements of non-photonic electrons, produced by semileptonic decays of D and B mesons, provide information on heavy quarks production in the hot and dense nuclear matter created in relativistic heavy ion collisions.

The main part of this thesis is the analysis of non-photonic electrons in p+p collisons at $\sqrt{s} = 200$ GeV from the year 2009. This analysis was done in wide p_T range, from 0.5 GeV/c to 8 GeV/c and it extended current STAR results to the low p_T region. It means that presented p+p spectra are first STAR low-p_T NPE measurements. The foregoing analysis was done at p_T larger then 2.5 GeV/c. The final NPE spectrum was compared to the Fixed-Order plus Next-to-Leading-Log (FONLL) calculation. Results are in good agreement with FONLL calculation. There is also a good agreement between the two experiments at RHIC, STAR and PHENIX, and between both STAR data at high-p_T. The significant improvement with respect to the last results is evident.

Next analysis presented in this work is non-photonic electron analysis in d+Au collisions at $\sqrt{s_{NN}} = 200$ GeV from the year 2008. Analysis of d+Au or p+Au collisions are essential for study cold nuclear effect. Understanding of cold nuclear matter effect is necessary for understanding of physical message from heavy ion collisions measurements. During this analysis NPE spectrum was reconstructed for minimum bias and 20% of the most central collisions and was compared with FONLL calculation scaled by number of binary collisions. Finally, the nuclear modification factor R_AA was calculated for both MB and central results. Results are compared with the PHENIX results from d+Au collisions from the year 2008. Data are in a good agreement with the PHENIX results and with unity as well.

Contents

List of Figures

List of Tables

1 Introduction

At RHIC, heavy quarks can be studied via measurements of non-photonic electrons (NPE) which are produced in semi-leptonic heavy flavor decays. The measurements of NPE, produced by decays of D and B meson, provide information on heavy quarks production in the hot and dense nuclear matter created in relativistic heavy ion collisions. In this work I present the recent measurements in p+p and d+Au collisions at center of mass energy of $\sqrt{s_{NN}} = 200$ GeV at STAR.

I have been an active member of the STAR Collaboration since 2009, namely as a member of the embedding team in the years 2011-2012, as a detector operator, shift crew and offline QA assistant during several detector shifts and as a physicist working on analysis in heavy flavor physics working group (PWG) during my Masters and PhD studies.

Service work

During the years 2011-2012 I was a member of the STAR Collaboration embedding team as a QA embedding helper. Embedding team is responsible for simulation and reconstruction activities and for preparation of data sets used for efficiency and acceptance calculations for all STAR analysis. The embedding team is led by Embedding Coordinator, the rest of the team is formed by the Embedding Deputies and Embedding Helpers for each PWG.

The embedding QA helpers are members of each PWG who help to run the embedding and are responsible for QA tests which are done on samples provided upon the PWG request. The final embedding data sets are tested by QA embedding helpers as well. During my service work I made a QA of these 17 data sets: e^+/e^- run09 and run10, Upsilon 1S, 2S, and 3S run10, K^+/K^- run09 and run11, π^0 Dalitz decay run09 and run10, J/ψ run09 and run10, π^+/π^- run09 and run11, e^+/e^- $\sqrt{s_{NN}} = 39, 64$ GeV run10, Eta Dalitz decay run10, Gamma run10.

Data analysis

During the years 2011 and 2012 I reconstructed signal of non-photonic electrons (NPE) from d+Au collisions at $\sqrt{s_{NN}} = 200$ GeV. In this analysis I made all necessary steps for final results. I identified inclusive and photonic electron samples, calculated purity of the inclusive electron sample, using embedding I calculated

photonic electron reconstruction efficiency and electron PID reconstruction efficiency. Centrality in d+Au collisions is determined as charged particle multiplicity in the East FTPC detector which was calculated in three separate time periods due to the varying varying performance of the FTPC during the data taking. Finally I calculated the nuclear modification factor. Results, scaled by the number of binary collisions, were compared to FONLL calculation. Although the analysis was made carefully and precisely, due to small data sample, the final results poses large statistic uncertainties. For a stronger physical message it would be necessary to collect more d+Au or p+Au collisions and to combine them with this analysis. This is a plan for the STAR detector during the year 2015.

During the years 2013 and 2014 I worked on NPE analysis in p+p collisions at $\sqrt{s} = 200$ GeV in a wide range of p_T. I made all necessary steps for final results. The analysis was done in low-p_T and high-p_T part separately due to the fact that information from different sub-detectors was used in each momentum region. This analysis was done in a wide p_T range, from 0.5 GeV/c to 8 GeV/c. In contrary to previous STAR results the spectrum was extended to low p_T region. The foregoing analysis was done at p_T larger then 2.5 GeV/c. Therefore, these results are first low-p_T NPE measurement in the STAR Collaboration. My NPE p+p analysis was used as a baseline for nuclear modification factor calculation in a paper which is being prepared for submission to the Phys. Rev. C. I am one of the primary authors of this paper.

This thesis is organized as follows. In Chapter 2 is the introduction to heavy ion collisions, in Chapter 3 is discussed open heavy flavor measurement and theoretical predictions of its production. In Chapter 4 is discussed recent non-photonic electron results measured with STAR, PHENIX, and ALICE collaboration, in Chapter 5 is description of the STAR detector. In Chapters 6 and 7 the analysis results were discussed, and in Chapter 8 are listed and described systematic errors. Finally, in Chapter 9 the presented results as a part of STAR non-photonic electron measurement is discussed.

Published Papers With Author's Primary Contribution

- L. Adamczyk et al. (STAR Collaboration), Heavy Flavor Electron production and azimuthal anisotropy in Au+Au collisions at $\sqrt{s_{NN}} = 200$ GeV, in collaboration review, to be submitted to Phys.Rev.C (2014)

- Olga Rusňáková for STAR Collaboration, Measurements of non-photonic electrons with the STAR experiment, proceedings of the Hot Quarks 2014, accepted, arxiv 1412.2112 (2014).
- Olga Rusňáková for STAR Collaboration, The measurement of non-photonic electrons in Star, proceedings of the 2013 European Physical Society Conference on High Energy Physics, PoS(EPS-HEP 2013)177
- Olga Hájková (Rusňáková) for STAR Collaboration, The measurement of non-photonic electrons in STAR, Proceedings of 51st International Winter Meeting on Nuclear Physics, PoS(Bormio 2013)050
- Olga Hájková (Rusňáková) for STAR Collaboration, The measurement of non-photonic electrons in STAR, Proceedings of Hard Probes 2012, Nucl.Phys. A910-911 (2013) 387-390.
- Olga Hájková (Rusňáková) for STAR Collaboration, J/ψ measurement at STAR, Proceedings of Winter Workshop on Nuclear Dynamics 2012, J. Phys.: Conf. Ser. 389 012030
- Olga Hájková (Rusňáková) for STAR Collaboration, Quarkonia measurement at STAR, Proceedings of Conference of Czech and Slovak physicist, 2011
- Olga Hájková (Rusňáková) for STAR Collaboration, Charmonia at STAR, Proceedings of Students scientific conference, 2011

These papers are included in this thesis in the Appendix section.

2 Heavy ion collisions

2.1 QGP and its signatures

Quantum Chromodynamics (QCD) is the non-abelian gauge field theory that describes the strong interaction between quarks and gluons, constituents of hadrons. It is the SU(3) component of the SU(3)×SU(2)×U(1) of the Standard Model. Quarks have a quantum number called color and they are confined by the colored gluons in colorless hadrons, mesons and baryons. In QCD massive quarks interact via the exchanging massless gluons. There are three possible colors of quarks, and three possible anticolors of antiquarks. Gluons in QCD play same role as photons in QED, but in contrast to photon, gluons carry color and anticolor charge and therefore, they can interact with each other.

The QCD Lagrangian is given as

$$\mathcal{L} = \sum_{q,C} \bar{\psi}_{q,a}(i\gamma^\mu \partial_\mu \delta_{ab} - g_s \gamma^\mu t^C_{ab} A^C_\mu - m_q \delta_{ab})\psi_{q,b} - \frac{1}{4} F^A_{\mu\nu} F^{A\mu\nu}, \tag{1}$$

where ψ are quark-fields bispinors, q is a quark flavor, m_q is a quark mass, γ^μ are the Dirac γ matrices, and a is a color index which runs from 1 to 3. The A^C_μ are gluon fields with index C of the color combination running from 1 to 8. The field tensor $F^A_{\mu\nu}$ is defined as

$$F^A_{\mu\nu} = \partial_\mu A^A_\nu - \partial_\nu A^A_\mu - g_s f^{ABC} A^B_\mu A^C_\nu, \tag{2}$$

where the f_{ABC} are the structure constants. The interaction between two colored particles is characterized by the strong interaction running coupling constant α_s and by the quark-antiquark potential V_{strong}

$$\alpha_s(Q^2) = \frac{12\pi}{(33 - 2N_f)\ln(\frac{Q^2}{\Lambda_{QCD}})}, \tag{3}$$

$$V_{strong}(r) = \sigma r - \frac{4\alpha_s}{3r}, \tag{4}$$

where Q^2 is the four-momentum transfer, N_f is the number of quark flavors, Λ_{QCD} is the typical QCD scale ($\Lambda_{QCD} \sim 0.2$ GeV), r is the distance between quarks, and σ is the string constant. The strong coupling constant α_s is the only free parameter in the QCD Lagrangian. It is not observable itself but other experimental

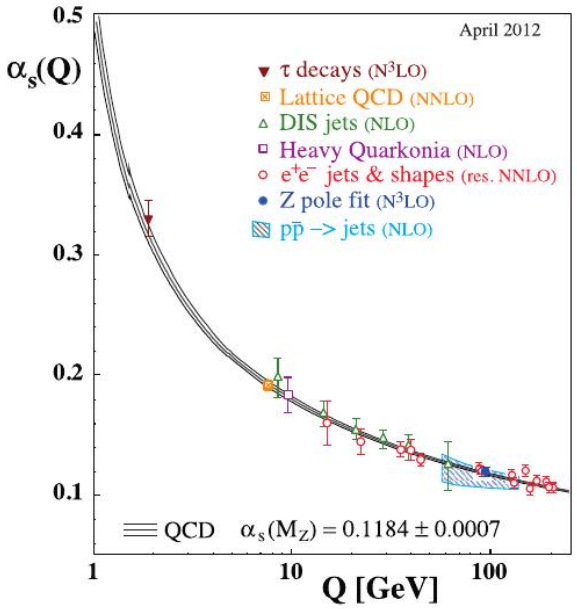

Figure 1: Summary of measurement of QCD running constant α_s as a function of the momentum transfer Q^2, determined from different processes. Taken from Ref. [1].

observables could be used to determine α_s. The summary of α_s measurements is in Fig. 1 [1].

At small distances the potential V_{strong} is dominated by Coulomb-like term $-\frac{4\alpha_s}{3r}$. The coupling constant α_s becomes smaller at shorter distances and/or large transverse four-momentum Q^2. Therefore at small distances and/or at large energies quarks behave like a free particles. This effect is known as the asymptotic freedom [2]. Another important property of the QCD is the color confinement. At the large distances the strong potential V_{strong} is dominated by linear term σr. With increasing distance between quarks the energy of color field is increasing. At some point it is energetically preferable to make new quark-antiquark pair, the original pair becomes two quark-antiquark pairs. Thus the free quarks cannot be observed in the nature.

When the system reaches the critical temperature, the color confinement is broken and matter passes through phase transition from the confined nuclear matter to the deconfined state. This new state of matter is called Quark Gluon Plasma (QGP). QGP is believed to exist in the early Universe, about 10^{-6} second, after

the Big Bang. Ultra-relativistic heavy-ion collisions provide a possibility to produce the QGP in the laboratory. Current calculations show that the transition happens around the critical temperature $T_c = 150 - 180$ MeV, which corresponds to an energy density of about $0.3 - 1.0$ GeV/fm^3[3]. A phase diagram of hadronic matter is shown in Fig. 2 as a function of temperature and the baryon density. The assumed phase transition line between hadron gas and QGP is denoted.

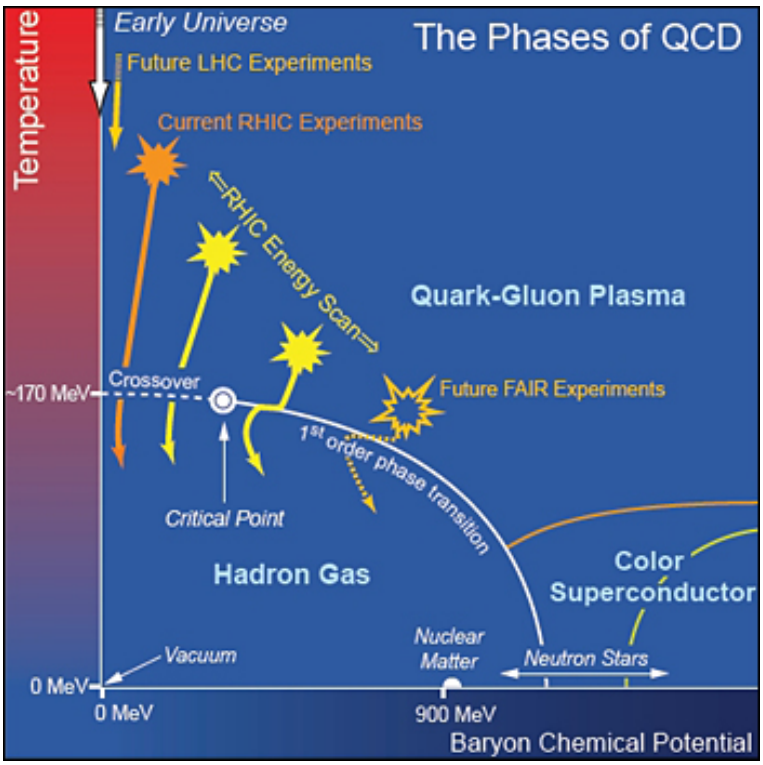

Figure 2: A phase diagram of QCD matter. Assumed phase transition lines are denoted. The circle represent the critical point. Taken from Ref. [5].

QGP can also exist at low temperature at very high baryon potential, therefore QGP may exist inside of neutron stars. It is also supposed that at low temperatures and extremely high density quarks and gluons are correlated into the Cooper pairs and form a new state of matter, the Color Superconductor [4].

Even if QGP is produced in a laboratory, its identification is difficult because of its very short lifetime. It is impossible to observe directly its thermodynamics properties. So, it is necessary to rely on indirect measurements of QGP formation. Certain signatures of the phase transition could allow us to establish whether

the matter is deconfined or not. Observable signatures in high energy heavy-ion collisions could be divided into three classes: hard, electromagnetic and soft probes. Single signatures of QGP are described in the next Chapter.

2.2 Space-time evolution of matter

The evolution of matter created in high-energy heavy-ion collisions can be illustrated by a space-time diagram (Fig. 3), with the longitudinal coordinate z and transversal coordinate t. It may be viewed as evolving through different stages that are expected to exist from the initial collisions to the final hadronic phase. It is assumed that the space-time evolution depends only on the proper time $\tau = \sqrt{t^2 - z^2}$:

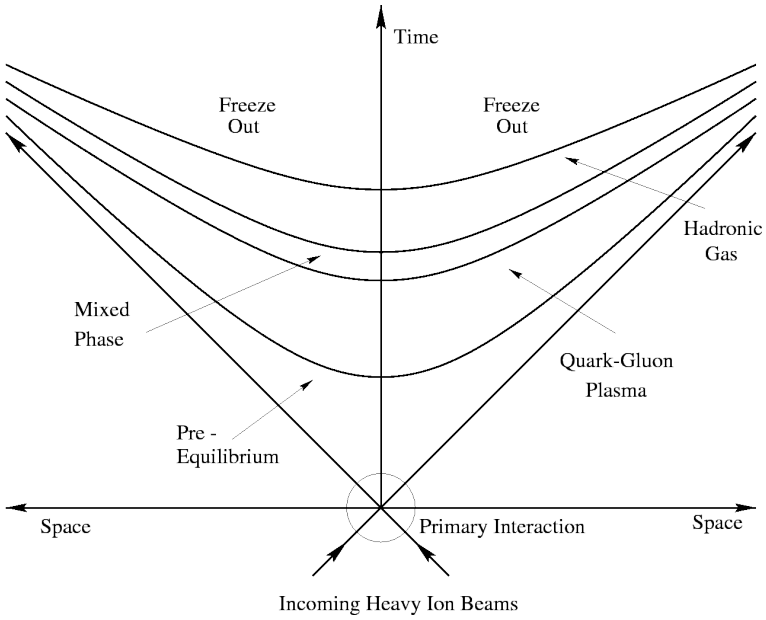

Figure 3: Time space evolution of matter created in a high energy heavy-ion collisions. Taken from Ref. [5]

At the proper time, $\tau = 0$, a huge amount of energy is deposited in a tiny volume. The expected energy density is high enough to form deconfined matter of quarks and gluons. The matter in this stage is not in the thermal equilibrium. Then the deconfined state of partons becomes in thermal equilibrium. This phase is called a QGP stage. The QGP expands and cools down according to the hydrodynamic laws. At $\tau = \tau_c$ the system has reached the critical temperature T_c,

and starts to hadronize. If the transition is of the first order, the matter passes through the mixed phase consisting of gluons, quarks and hadrons. The hadronization of the system is finishing, and hadrons are interacting with each other till the temperature drops to the thermal and chemical freeze-out temperature. At the freeze-out temperature hadrons finish interacting and leave the collision region.

2.3 Collision geometry

As shown in Fig. 4, nucleons in collision can be classified into two groups, spectators and participants. Due to the relativistic effects nuclei are Lorentz contracted. The nucleons in the overlap region participate in the collision, so they are called participants. Nucleons in the other nucleus region are called spectators. The main parameter of colliding nuclei that quantifies the size of the participant group is the impact parameter b, the distance between trajectories of centers of two colliding nuclei.

We can speak about central and peripheral collisions. Low b indicates a central collision, and high b a peripheral one. Since the impact parameter and the number of the participant nucleons, N_{part} , cannot be measured directly, the observed particle multiplicity is used as an indirect measure of centrality. The relation between particle multiplicity, the number of participants, and the number of binary collisions, N_{coll} , can be calculated from the Glauber model [6]. Finally, centrality classes are determined by dividing the event multiplicity distribution into required bins.

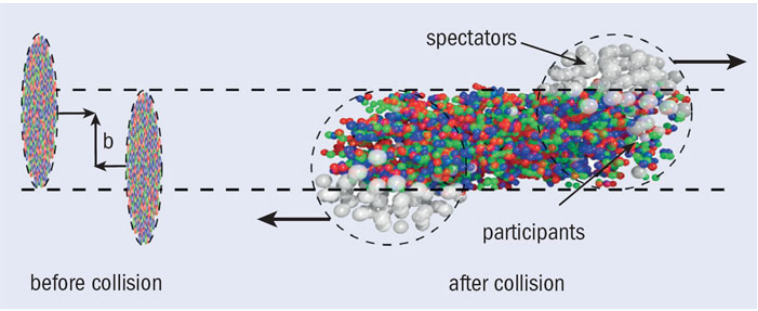

Figure 4: Spectators and participants of colliding nuclei. Parameter b denotes the impact parameter. Taken from Ref. [7].

2.4 Signatures of QGP formation

Ultra-relativistic heavy-ion collisions allow to study hot and dense nuclear matter. If the density is high enough QGP can be created. There is the strong experimental evidence that QGP is created in high energy heavy-ion collisions, such as Au+Au collisions at the center of mass energy of $\sqrt{s_{NN}}$=200 GeV at RHIC. The most important signatures of formation of QGP are strangeness enhancement, jet quenching, the quarkonia suppression, flow measurements. Some of QGP signatures are described bellow.

2.4.1 Jet quenching

One of the most important signal of creation of the QGP is the jet quenching. In ultra-relativistic heavy ion collisions, the leading jet particles lost part of their energy during the strong interaction with QGP. Due to this the measured jet spectra have reduced p_T [1]. The second observable related to the jet quenching is the azimuthal correlation of high-p_T hadrons in central Au+Au collisions. The absence of away-side ($\delta\phi \sim \pi$) peak is observed due to the fast partons energy loss in hot and dense medium. The correlations of high-p_T hadrons in p+p, d+Au, and Au+Au collisions in STAR are shown in Fig. 5.

In the top panel, there is the two-particle azimuthal distribution $\delta\phi$ in d+Au collisions for MB events (green points) and for 20% of the most central collisions (red points). Black points show p+p baseline. As trigger particles were accepted particles with transverse momentum $4 < p_T(trig) < 6$ GeV/c and for associated particles was required $2 < p_T < p_T(trig)$ GeV/c. The azimuthal distributions in d+Au collisions looks similar as in p+p collisions. The only difference between p+p and d+Au collisions it the growth of the pedestal. The bottom panel shows the azimuthal distributions after pedestal-subtraction for p+p, central d+Au and central Au+Au collisions (blue points). In Au+Au collisions the away-side peak disappeared. It indicates that Au+Au is produced medium which is not produced in d+Au collisions [8].

2.4.2 The suppression of heavy flavor meson production

One of the most important signature of the QGP formation is a suppression of heavy flavor mesons production. We can divide this phenomena into two parts,

[1] Transverse momentum p_T is the component of momentum transverse to the beamline.

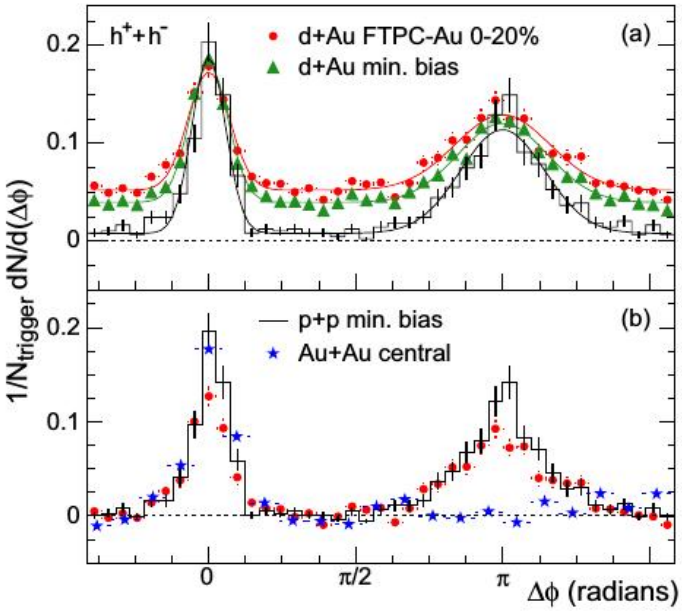

Figure 5: The correlations of high-p_T hadrons in p+p, d+Au, and Au+Au collisions. The trigger particle is in p_T range $4 < p_T(trig) < 6$ GeV/c, the associated particles are accepted in p_T range $2 < p_T < p_T(trig)$ GeV/c. Taken from Ref. [8].

quarkonia suppression (i.e. J/ψ, Υ) and open heavy flavor suppression. Suppression of J/ψ due to the Debye screening length has been considered as one of the most promising signatures of QGP formation. It was predicted by Matsui and Satz in 1986 [9]. Due to color screening of the surrounding nuclear matter, J/ψ is expected to disassociate in QGP. Measurements at RHIC and LHC confirmed this theoretical prediction. Suppression of J/ψ production measured at LHC is less than suppression measured at RHIC it is due to larger amount of J/ψ from recombination in collisions at higher collisional energy. Figure 6 shows measurement of the inclusive J/ψ R_{AA} in mid-rapidity as a function of number of participants, in other words as a function of centrality. Both results, ALICE and PHENIX, indicate strong suppression in PHENIX central and ALICE semi-central collisions [10]. To better understanding of this strong suppression the influence of cold nuclear matter effects (CNM) must be study in p+A collisions. CNM effects are discussed in Chapter 3.

Next way how to study heavy quark production is a study of the production of open heavy flavor. In this case, for the complex view, it is very eligible to study

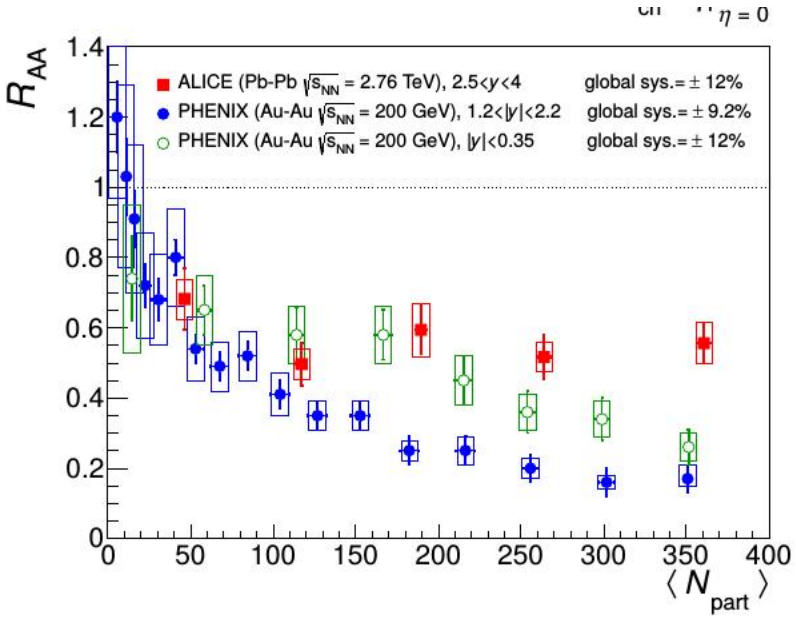

Figure 6: J/ψ nuclear modification factor R_{AA} measured in ALICE and PHENIX collaboration as a function of number of participants. Taken from Ref. [10].

heavy flavor suppression together with its elliptic flow v_2. The recent results from STAR, compared with number of theoretical models of the energy loss mechanism scenarios [11]-[19] are plotted in Fig. 7. The results show large suppression of non-photonic electrons (NPE) production in central Au+Au collisions. Non-photonic electrons come from semileptonic decay of D and B mesons. This suppression cannot be explained by the gluon radiation scenario only. Finite NPE elliptic flow v_2 is observed at low p_T which indicates a strong charm-medium interaction.

2.4.3 Elliptic flow

In semi-central and peripheral collisions, the colliding region has an almond shape in the transverse plane. It can be described by an ellipse. The impact parameter, the transverse distance between centers of two colliding nuclei, defines the reaction plane. Due to the spatial anisotropy, the pressure gradients are also anisotropic. The initial pressure gradient is larger along the minor axis of this ellipse. The anisotropy of pressure gradients induces the momentum anisotropy of hadrons in the final state. This final state anisotropy, named flow, can be measured. Flow provides information about the QCD matter in the early stages of the collisions

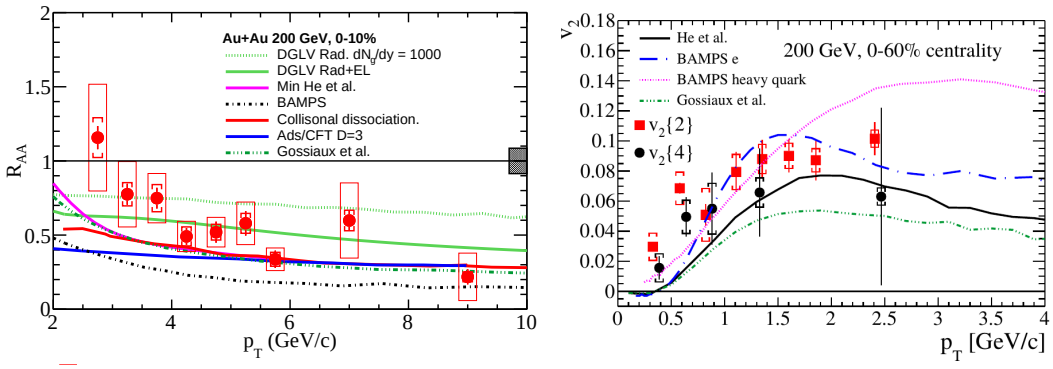

Figure 7: The non-photonic electron nuclear modification factor (left) and elliptic flow (right) in Au+Au collisions at $\sqrt{s_{NN}} = 200$ GeV measured with STAR. Both results are compared with number of theoretical predictions. In the left plot, the green dotted line represents energy loss via the gluon radiation only [11]; the green solid line is a gluon radiation together with the collisional losts [12]; the red line represents collisional dissociation model [14]; the black doted line shown BAMPS, that is the Boltzmann approach to multi-parton scattering; and the dotted-dashed lines on both figures shows model of Gossiaux [19].

and it is one of the signatures of the QGP formation. The flow can be studied by the Fourier expansion around reaction plane

$$E\frac{d^3N}{dp^3} = \frac{1}{2\pi}\frac{d^2N}{p_T dp_T dy}\left\{1 + \sum_{i=1}^{\infty} 2v_n \cos[n(\phi - \Phi_{RP})]\right\}, \tag{5}$$

$$v_n = \langle \cos[n(\phi - \Phi_{RP})]\rangle, \tag{6}$$

where Φ_{RP} is the reaction plane angle in the laboratory frame and ϕ is the azimuthal angle of particles in a given p_T bin. The coefficient v_2 is called an elliptic flow and quantify the difference between momentum distribution among the major and minor ellipse axis. It is assumed that hadronic elliptic flow comes from constituents quarks flow which carry elliptic flow before the hadronization. In a case of measurements of electrons from open heavy flavor decays the study of elliptic flow together with suppression is a great tool to study the QCD matter in initial state. The finite elliptic flow indicates that the system was in a deconfined stage before the hadronization.

3 Open Heavy Flavor

In this section, the motivation for studying of the open heavy flavor production in nucleon-nucleon and heavy ion collisions is presented. The perturbative QCD (pQCD) theoretical prediction for charm and bottom production is discussed and main energy loss models are introduced.

3.1 Open Heavy Flavor measurement

Due to their large masses, heavy quarks are produced mainly via the gluon fusion during the initial parton-parton interaction, and thus they are good probes to study of the QCD matter. The Feynman diagrams of the leading order heavy quark production in pQCD are shown in Fig. 8. The study of heavy flavor production in p+p collisions is a test of the validity of the pQCD. The pQCD theoretical model is described in Chapter 3.2. It is also used as a baseline to study the effects of nuclear matter on the production of heavy quarks in heavy-ion collisions. Nuclear matter effects can be divided into two catagories. Effects related to the formation of the hot and dense medium are called hot nuclear matter effects. Initial and final state effects that are due to a presence of ordinary ("cold") nuclear matter are refered to cold nuclear matter effects. Cold nuclear matter effects are discussed in detail in Chapter 3.3.

Hot nuclear matter effects, as energy loss or elliptic flow, affect heavy flavor p_T distribution but do not change the total heavy flavor yield. Due to the energy loss (cause by collisional or radiative processes) the heavy quark p_T distribution falls steeper then in p+p collisions, the transverse momentum of heavy quark is reduced. Figure 9 illustrated the collisional and radiative energy loss. The collisional energy loss is due to the scattering of the heavy quark with light quarks and radiative energy loss is due to gluon radiation [24].

When the momentum is sufficiently low, the quark takes the same velocity as surrounding medium and has a flow [25]. These hot nuclear matter effects, as well as cold nuclear matter effects, are quantified with nuclear modification factor (R_{AA}). R_{AA} is defined as a ratio of the particle production in nucleus-nucleus collisions to the production in proton-proton collisions, scaled by the average number of binary collisions N_{coll} for a given centrality. Number of binary collisions could be estimated from the Glauber calculation. R_{AA} can provide information about heavy quark energy loss. In case of no medium effects the nuclear modification

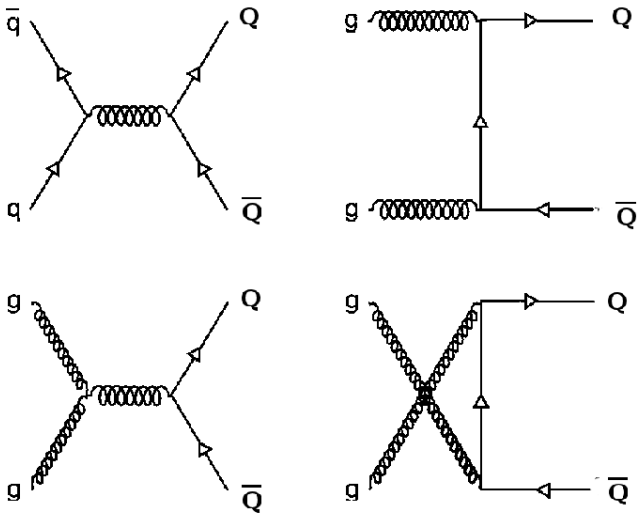

Figure 8: Feynman diagrams of the leading order heavy quark production in QCD.

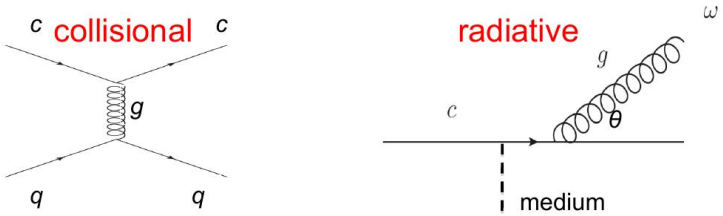

Figure 9: Schema of the radiative (right) and collisional (left) energy loss.

factor should be equal to one.

$$R_{AA} = \frac{d^2N_{AA}}{d^2N_{pp} \cdot \langle N_{coll} \rangle} \tag{7}$$

Although the RHIC is focused on study of hot nuclear matter effects, it is same important to study cold nuclear matter effects. The cold nuclear effects must be distinguished from the hot nuclear matter effects to see real strength of hot nuclear matter effects to the heavy flavor production. Therefore the study of heavy flavor production in d+Au collisions is required, where the presence of hot and dense medium is not expected. One of the cold nuclear effect that must be included in the case of open heavy flavor measurement is nPDF modification.

Open heavy flavor hadrons, D and B mesons, have short lifetimes ($c\tau_{D^0} =$

122.9 μm, $c\tau_{B^0}$ = 455 μm,). Therefore, they must be reconstructed from their decay products. The decay channel with the highest branching ratio is a hadronic decay channel. The problem of the reconstruction with the hadronic channel is very high hadronic background together with low production rates. At STAR the reconstruction of D^0 and D^* using hadronic decay channel was done, $D^0 \rightarrow K^{\pm}\pi^{\mp}$ and $D^{*\pm} \rightarrow D^0(\bar{D^0})\pi^{\pm}$. Figure 10 shows nuclear modification factor of D^0 mesons measured by STAR in Au+Au collisions at $\sqrt{s_{NN}}$ = 200 GeV [26]. Both effects, cold and hot nuclear matter effects, affect reconstructed spectrum. The Cronin effect could be observed in $p_T \sim 2$ GeV/c while hot nuclear matter effects dominated in high p_T region. On the other hand, the bump can be also explain within the coalescence scenerio and it is still under the study. After the Heavy Flavor Tracker installation, the STAR will be able to reconstruct secondary vertices, the place of D and B mesons decay, of heavy mesons and then reject most of hadronic background.

The other way to study open heavy flavor production is by non-photonic electrons (NPE) measurement, products of semi-leptonic heavy flavor decays. Semileptonic decay channels have a large branching ratio (electron semileptonic decay for B mesons 10.86%, and for D mesons 9.6%). The advantage of this measurement is relatively easy reconstruction of electrons. The main disadvantage is problem with distinguish between electrons from B mesons and D mesons. This problem is solved by Heavy Flavor Tracker (HTF) upgrade to STAR detector in the year 2014 as was mentioned above.

3.2 pQCD predictions for Charm and Bottom production at RHIC

Charm or bottom quarks production cross-section can be calculated within pQCD. In this section, the pQCD prediction for the open charm and bottom production and prediction of NPE production at RHIC in p+p collisions at $\sqrt{s} = 200$ GeV are discussed. These predictions provide a benchmark with which the data could be compared. The theoretical predictions are given with their uncertainties, in order to better compare to data.

Theoretical calculations of NPE production cross-section consist of three main components: p_T and η distributions of the heavy quark Q in p+p collisions at $\sqrt{s} = 200$ GeV (heavy quark production cross-section calculated within pQCD),

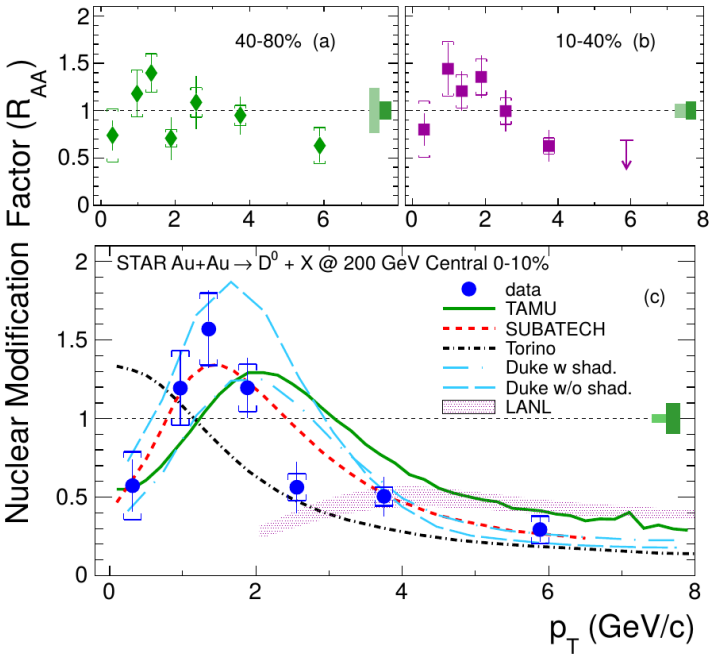

Figure 10: D^0 nuclear modification factor for peripheral collisions (top left), semi-central collisions (top right), and central collisions (bottom). The central collisions result is compared with theoretical calculations, TAMU (green solid curve), SUBATECH (red dashed curve), TORINO (black dot-dashed curve), Duke (blue curves), and LANL groups (filled band). Taken from Ref. [26].

fragmentation of heavy quark into heavy mesons H_Q (described by fenomenological inputs), and the decay of H_Q into electrons. The NPE cross-section could be schematically written as:

$$E\frac{d^3\sigma(e)}{dp^3} = E_Q\frac{d^3\sigma(Q)}{dp_Q^3} \otimes D(Q \to H_Q) \otimes f(H_Q \to e). \tag{8}$$

The cross-section $E_Q d^3\sigma(Q)/dp_Q^3$ is calculated in the Fixed-Order plus Next-to-Leading-Log (FONLL) algorithm [27]. In addition to including the fixed-order NLO results the FONLL also calculate with a large perturbative terms proportional to $\alpha_s^n log^k(p_T/m)$ [28] [29]. The perturbative parameters are m and α_s, where m is the heavy quark mass and α_s is the strong coupling constant. As a reference value of the quark mass were used $m_c = 1.5$ GeV/c^2 and $m_b = 4.75$ GeV/c^2, and quark mass was varied over ranges $1.3 < m_c < 1.7$ GeV/c^2 and $4.5 < m_b < 5.0$ GeV/c^2

for charm and bottom quark respectively [30]. From this mass variation the uncertainties were obtained. The QCD scale Λ was set to 0.226 GeV. The perturbative calculations also depends on the unphysical factorization μ_F and renormalization μ_R scales. The cross-section of their variation was used to estimate the perturbative uncertainties. During discussed calculation were used $\mu_{F,R} = \mu_0 = \sqrt{p_T^2 + m^2}$ as a central value and they were varied independently within the region defined by $\mu_{R,F} = \xi_{R,F}\mu_0$, $0.5 \leq \xi_{R,F} \leq 2$. The envelope containing the resulting curves defines the uncertainties. To the final uncertainty calculation come uncorrelated errors from the quark mass and from the scale [27].

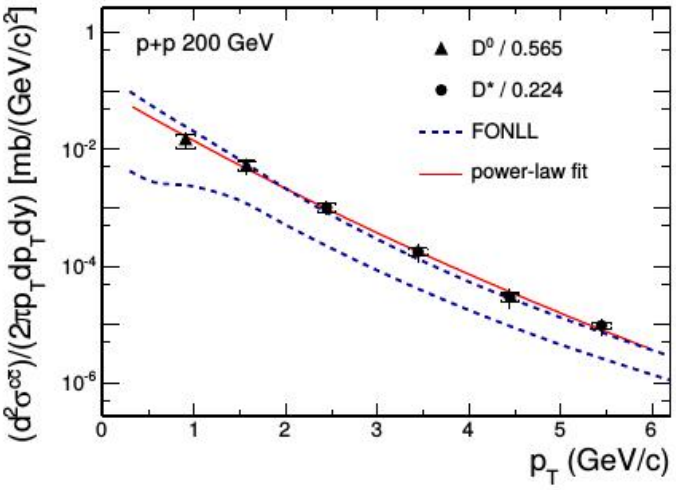

Figure 11: The theoretical FONLL prediction of the D meson production cross-section (dashed line) as a function of p_T, compared to D meson cross-section measured in p+p collision at $\sqrt{s} = 200$ GeV. Taken from Ref. [31].

These inputs resulting to a FONLL predict the total $c\bar{c}$ and $b\bar{b}$ cross-section in p+p collisions at $\sqrt{s} = 200$ GeV ($\sigma_{c\bar{c}}^{FONLL} = 256^{+400}_{-146}$ μb, $\sigma_{b\bar{b}}^{FONLL} = 1.87^{+0.99}_{-0.67}$ μb).

The fragmentation functions, D($c \to D$) and D($b \to B$) were extracted from e^+e^- data in the context of a FONLL calculation [32]-[34]. For the decay spectra normalization the branching rations were used, $BR(B \to e) = 10.86 \pm 0.35\%$, $BR(D \to e) = 10.3 \pm 1.2\%$, $BR(B \to D \to e) = 9.6 \pm 1.2\%$.

Figure 11 shows FONLL prediction of the D meson production cross-section as a function of p_T, where the FONLL prediction is displayed as the uncertainty bands. The uncertainty bands are wider at low p_T due to the large value of α_s

at low scales. Due to this fact, the analysis of the open heavy flavor in low p_T is essential. Data points are from the D meson analysis in p+p collisions at $\sqrt{s}$=200 GeV measured with STAR experiment [31] and they are consistent with upper FONLL boundary. Due to the hard fragmentation function, the D mesons and charm quarks theoretical bands are different for $p_T > 9$ GeV/c as is visible in Fig. 12.

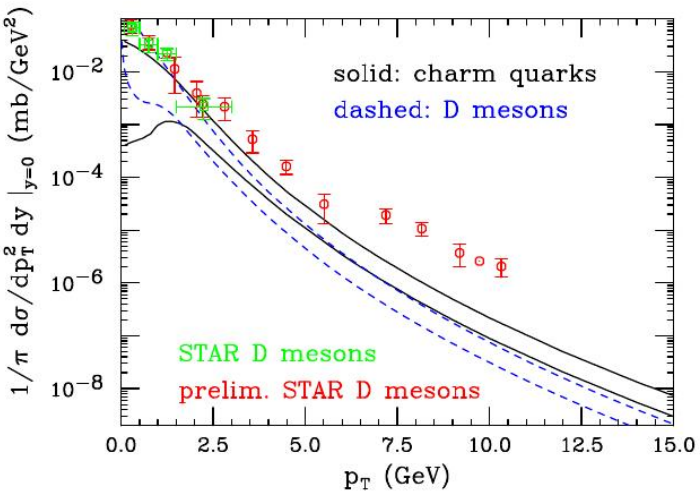

Figure 12: The theoretical prediction for the charm quark (solid lines) and D meson (dashed lines) p_T distributions in p+p collisions at $\sqrt{s} = 200$ GeV, using BR$(c \to D) = 1$. The data are from STAR d+Au collisions at $\sqrt{s_{NN}} = 200$ GeV, scaled by the number of binary collisions. Taken from Ref. [27].

The FONLL theoretical predictions for bottom quarks and B mesons at $\sqrt{s} =$ 200 GeV are figured in Fig. 13. Because of the harder fragmentation functions the bands for the b quarks and B mesons have an overlap up to $p_T \simeq 20$ GeV/c.

In Fig. 14, the FONLL calculations of NPE distribution for $D \to e$ (dashed lines), $B \to e$ (dotted lines), and $B \to D \to e$ (dot-dashed lines) are shown. Lines border the uncertainties. Due to the low branching ratio, the latest one could be negligible. The NPE spectrum from B mesons crossing over the NPE spectrum from D mesons at $p_T \simeq 4$ GeV/c [27].

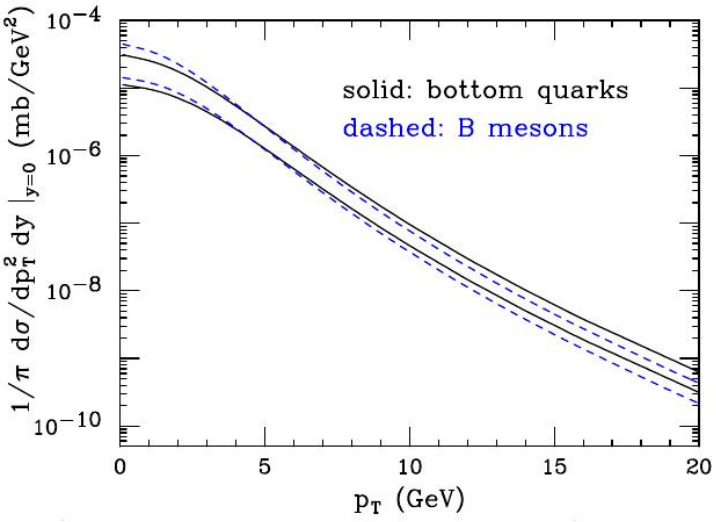

Figure 13: The theoretical prediction for the bottom quarks (solid lines) and B mesons (dashed lines) p_T distributions in p+p collisions at $\sqrt{s} = 200$ GeV, using BR($b \to B$) = 1. Taken from Ref. [27].

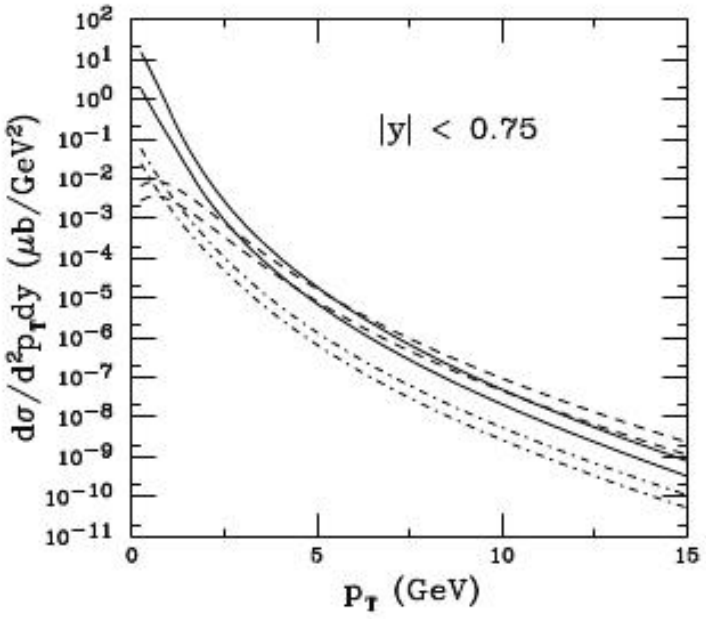

Figure 14: The theoretical FONLL value of the NPE from D mesons (solid lines), B mesons (dashed lines), and $B \to D \to e$ (dotted-dashed). Lines denote upper and lower uncertainty limits of the FONLL calculation. Taken from Ref. [35].

In Fig. 15 the theoretical calculation is compared to the recent experimental results of NPE in p+p collisions at $\sqrt{s} = 200$ GeV measured by STAR (blue [36] and black points, this thesis) and PHENIX (green points) [37] collaborations. The blue line presents central FONLL calculations and black dashed lines show FONLL uncertainties. Experimental results are in a good agreement with FONLL within its uncertainties and at low-p_T region are consistent with FONLL upper limit.

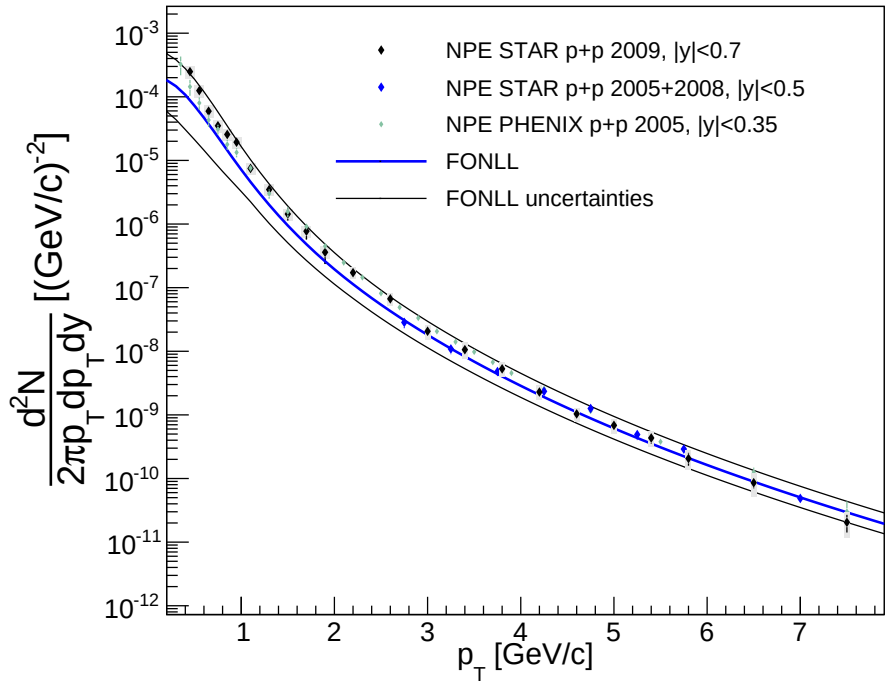

Figure 15: The theoretical pQCD FONLL prediction for the NPE p_T spectrum from all sources together [35]. The FONLL calculation is compared with the experimental STAR results from the years 2008+2005 data (blue points) [36] and from the year 2009 (black points, this thesis) and PHENIX (green points) [37].

Before Heavy Flavor Tracker (HFT) installation, there was impossible, in STAR experiment, to distinguish NPE from D and B mesons directly. However, due to the different charm and bottom quark mass and consequently different heavy flavour meson decay kinematics, NPE from these two sources could be separated via the charged hadron-NPE azimuthal correlations study [38]. Relative B meson contribution to NPE could be obtained by comparing of NPE-hadron correlations from data with PYTHIA calculation (Fig. 16). Data results were fitted with PYTHIA for the charm (red) and bottom (blue) part and with combined shape (black). In Fig. 17, the relative B contribution as a function of p_T at $\sqrt{s}$=200 GeV is shown. The B decay contribution increases with p_T, and is comparable with the contribution from the D meson decay at p_T higher than 5 GeV/c at $\sqrt{s}$=200 GeV. Results are compared with FONLL calculation and there is a good agreement [38].

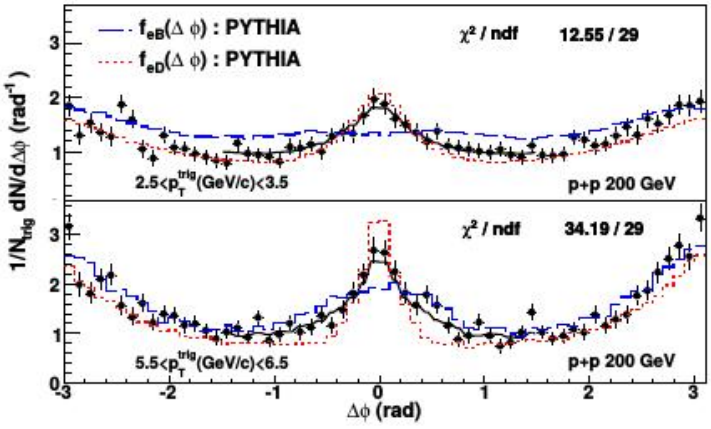

Figure 16: Non-photonic-hadron azimuthal correlations from data in p+p collisions at $\sqrt{s}$=200 GeV (black) compared with PYTHIA simulations of electron (from B/D mesons decays)-hadron correlations (blue dashed and red dotted lines respectively). The black lines are combined fits to the data. Taken from Ref. [38].

3.3 Cold nuclear matter effects

The cold nuclear matter effects (CNM effects) can be studied in hadron-nucleus interactions, where no hot and dense matter is presented. At RHIC energy, the most important and discussed CNM effects are gluon shadowing and Cronin effect. These effects are included into the initial-state effects based on the fact, that

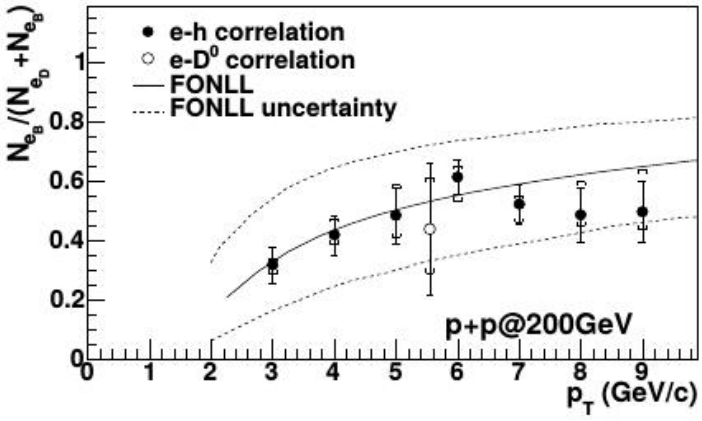

Figure 17: The relative bottom contribution to NPE electrons in p+p collisions at $\sqrt{s}$=200 GeV compared with the FONLL prediction. Taken from Ref. [38].

parton density in a free proton is different from that in a nucleus. Therefore nuclear parton distribution function (nPDF) is different from the basic superposition of its constituents parton distribution functions (PDF). PDF characterizes inner structure of proton. This phenomena have been discovered in DIS (deep inelastic scattering) of leptons on a nucleus and have been used to constrain free PDF [39]. nPDF was discovered in p+A collisions and in l+A collisions, where l is a lepton. This is plan to be study on eRHIC experiment which is a future Electron-Ion Collider (EIC) in BNL based on the RHIC facility. It is plan to replace RHIC during the twenties [40].

Since heavy quarks are produced mainly via gluon fusion during the initial parton-parton interaction the gluon shadowing has a significant impact to the heavy flavor production. The Cronin effect is also significant in open heavy flavor measurements and it is caused by a multi-particle scattering at initial stage and causes enhancement at intermediate p_T. Figure 18 shows the schematic plot of the nuclear modification factor $R_i^A(x)$ as a function of Bjorken x_Bj, where known modifications of nPDF are shown: gluon shadowing, Cronin effect, EMC effect, and Fermi motion, from the lowest to the highest value of x_Bj respectively. The nuclear modification factor $R_i^A(x)$ is defined as

$$R_i^A(x,Q^2) = \frac{f_i^A(x,Q^2)}{Af_i^N(x,Q^2)}, \tag{9}$$

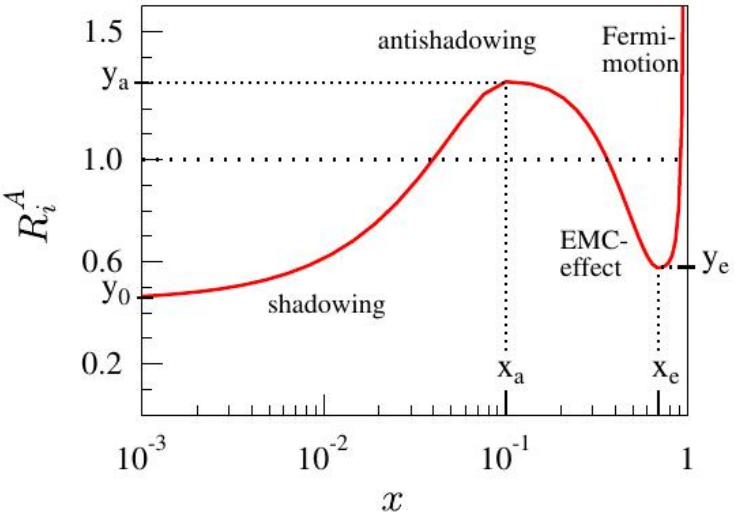

Figure 18: The schema of EPS09 parametrization of nPDF modification as a function of Bjorken x_Bj. Taken from Ref. [41].

where A is the nucleus mass number, and f_i^A is a nPDF, and f_i^N is a PDF for quark, antiquark, and gluon [42].

The EPS09 model [41] [42] extends previous leading order (LO) models of the nuclear PDF to the next-to-leading-order (NLO). In contrast to the previous models inclusive pions were take into account also with Drell-Yan (DY) production and data from DIS. This additional part of model calculation improves the determination the the gluon density. The DY and DIS data are sensitive to the discrimination between valence and see quarks. The comparison between EPS09 model and measured inclusive pions from d+Au collisions at RHIC is plotted in Fig. 19. Nuclear modification factor from the STAR (green circles) and the PHENIX (red squares) experiment and are good described by EPS09 model within errors. Large systematic uncertainties of model comes mainly from small and large x_Bj or gluon [42].

Figure 20 shows cold nuclear matter effects in proton-lead collisions at LHC. Nuclear modification factors for valence quarks, sea quarks and gluons are plotted separately (R_V, R_S, R_G). The recent model [42] is compared with previous published models as well.

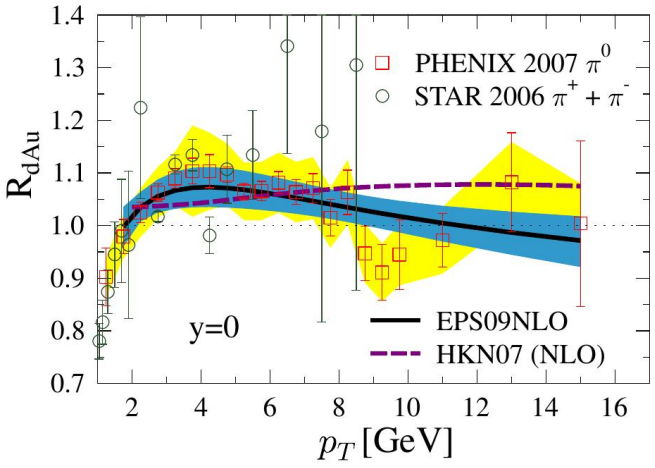

Figure 19: Nuclear modification factor of inclusive π compared with EPS09 model. Taken from Ref. [42].

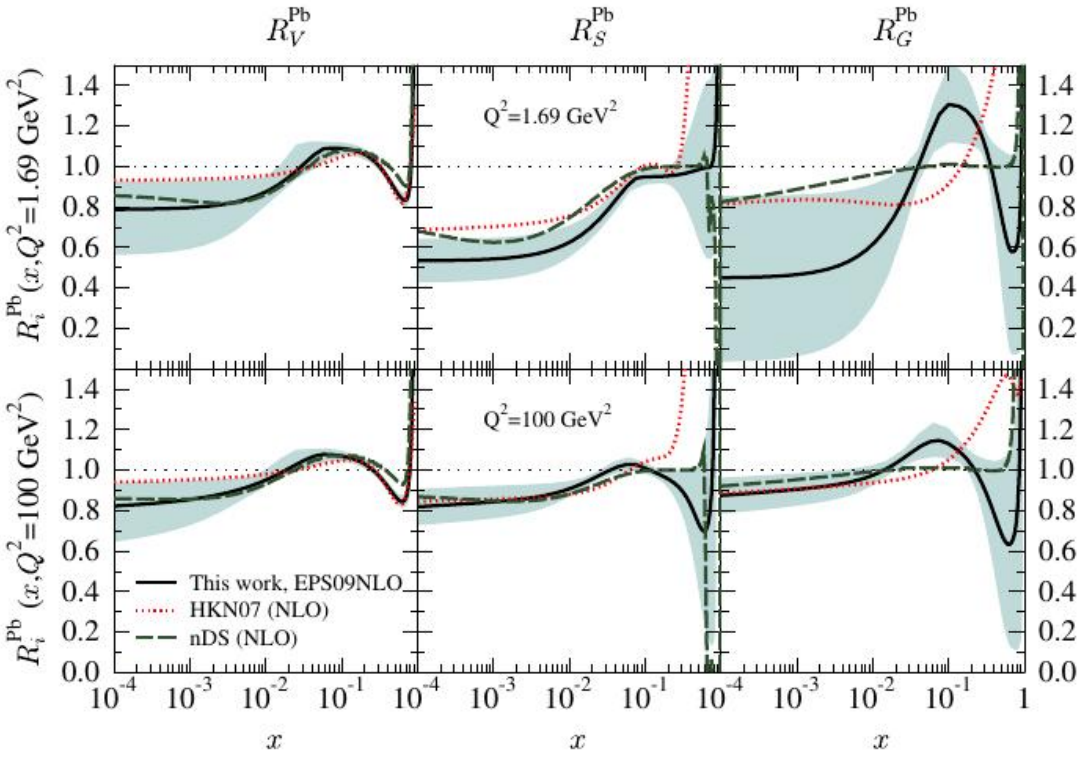

Figure 20: Model of cold nuclear matter effect for valence quarks, see quarks and gluons at LHC. Taken from Ref. [42].

4 Non-photonic electron results at RHIC and LHC

In this Chapter the recent results of non-photonic electron (NPE) measurement from the STAR, ALICE, and PHENIX experiments are presented. At first, NPE production results from RHIC will be discussed, included NPE yield, nuclear modification factor (R_{AA}), and elliptic flow (v_2) at wide range of collision energies. At the end of this chapter recent ALICE results will be discussed to show the consistency between both accelerators.

4.1 Non-photonic electron production at STAR experiment

In this section recent STAR NPE results will be discussed. First STAR NPE results were published in the year 2007 and then corrected in the year 2011 [43]. The NPE spectrum in p+p, d+Au, and Au+Au collisions at $\sqrt{s_{NN}}$=200 GeV measured in the year 2003 and the year 2004 were reconstructed and nuclear modification factor was calculated.

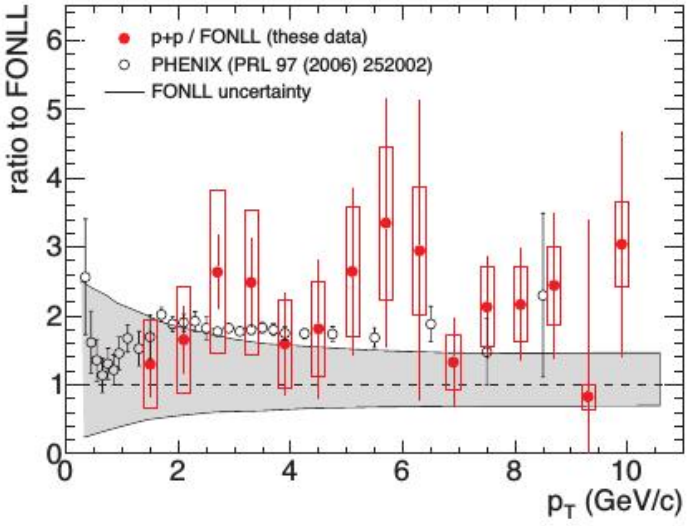

Figure 21: NPE data to FONLL ratio in p+p collisions. The shaded band denotes FONLL uncertainties. Taken from Ref. [43].

Results have large statistics and systematic errors and for better understand of heavy quark production it was necessary to make another, more precise, analysis.

In Fig. 21 is presented p+p data to FONLL ratio and in Fig. 22 is shown the nuclear modification factor R_{AA} for d+Au and Au+Au collisions at $\sqrt{s_{NN}}$=200 GeV.

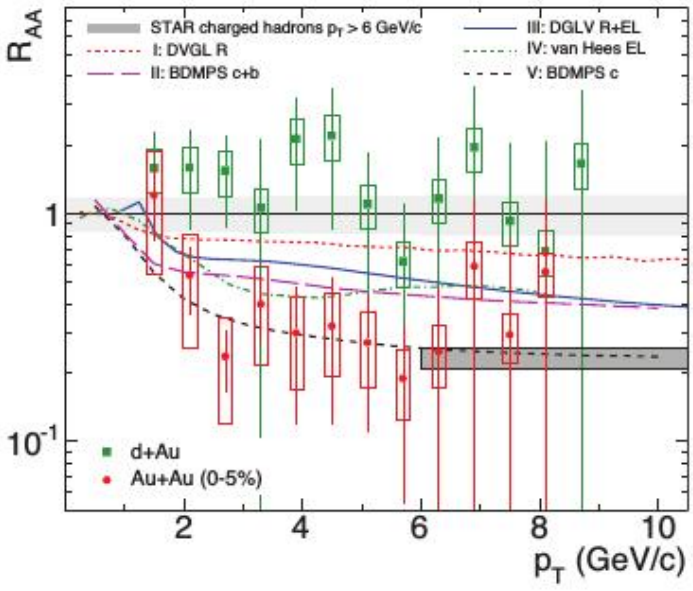

Figure 22: Non-photonic electron R_{AA} in d+Au and Au+Au collisions at $\sqrt{s_{NN}}$=200 GeV measured in STAR during the year 2003 and the year 2004. Taken from Ref. [43].

In Fig. 23 there is the NPE invariant yield in Au+Au collisions at $\sqrt{s_{NN}}$=200 GeV at midrapidity as a function of p_T. Blue points represent the minimum bias data, and red points denote NPE yield for different centrality bins. The NPE invariant yields were compared with FONLL calculations scaled by the average number of binary collisions in five centrality bins (red points). In central and semicentral Au+Au collisions we observed a significant suppression of NPE production compared to the FONLL calculation [30].

Figure 24 shows NPE R_{AA} for the 0-10% most central collisions compared to several theoretical models of heavy quark energy loss [11] - [18]. Gluon radiation scenario alone [11] (dashed green line) fails to explain the large NPE suppression at high p_T even though it describing the suppression of light hadron correctly. When the collisional energy loss is added model calculations describe the data better. The collisional dissociation model [14] (red line) and the AdS/CFT calculation

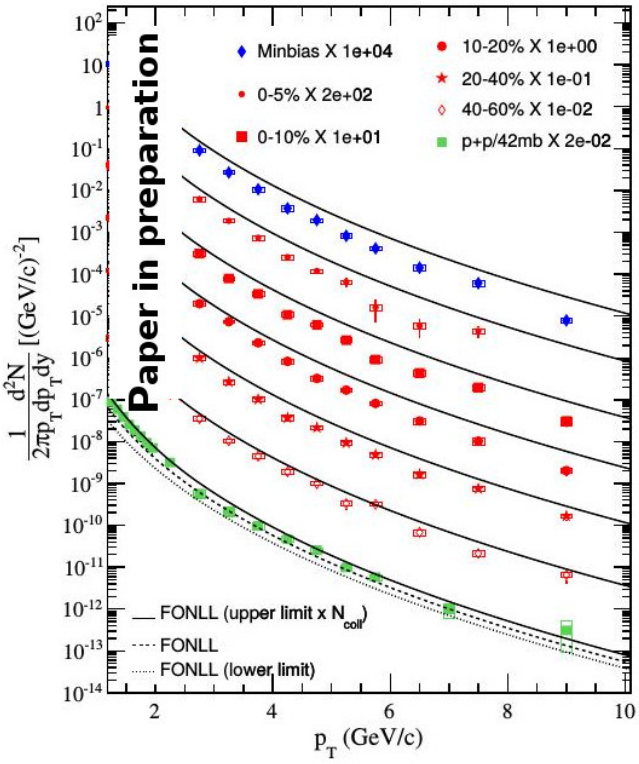

Figure 23: NPE invariant yield in Au+Au collisions at $\sqrt{s_{NN}}$=200 GeV at midrapidity in STAR. Blue points denote minimum bias results while red points show NPE yield in different centrality bins. Green points represent NPE yield p+p collisions (this thesis). Solid black lines represent central FONLL calculation scaled by number of binary collisions [30].

[15] (blue line) also describe the data well. The baseline for nuclear modification factor calculation is produced from new p+p results from 2009 data (analysis presented in this thesis), R_{AA} was extended to low p_T region.

Figure 25 shows a measurements of NPE v_2 in Au+Au collisions at $\sqrt{s_{NN}}$=200 GeV. These results are obtained using 2-particle ($v_2\{2\}$) and 4-particle ($v_2\{4\}$) correlations [20]. These results are compared with theoretical models [21]-[19]. We observe finite v_2 at low p_T and at high p_T we observe increasing of v_2 which can arise from non-flow effects such as jet-like correlations.

TMatrix model, dissociation model, and Gossiaux model describe R_{AA} results in the high-p_T well, but miss the mid-p_T region or/and low-p_T region. To resolve

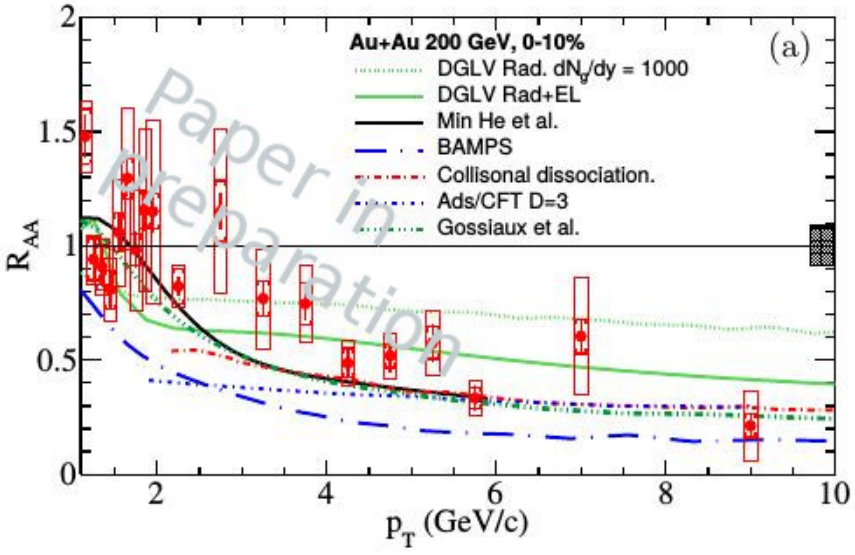

Figure 24: Non-photonic electron results from Au+Au collisions at $\sqrt{s}$=200 GeV from the year 2010. Results are compared with theoretical models [11]-[18].

between these models it is necessary to study NPE R_{AA} with v_2 together. It is a challenging task to describe both results, R_{AA} and v_2 via one theoretical model.

Figure 26 shows NPE v_2 measured in data from Au+Au collisions at collision energies $\sqrt{s_{NN}}$=39, 62.4, and 200 GeV [44] (black, blue, and red points respectively). Finite v_2 at low p_T is observed at $\sqrt{s_{NN}}$= 200 GeV while at lower energy no v_2 is observed.

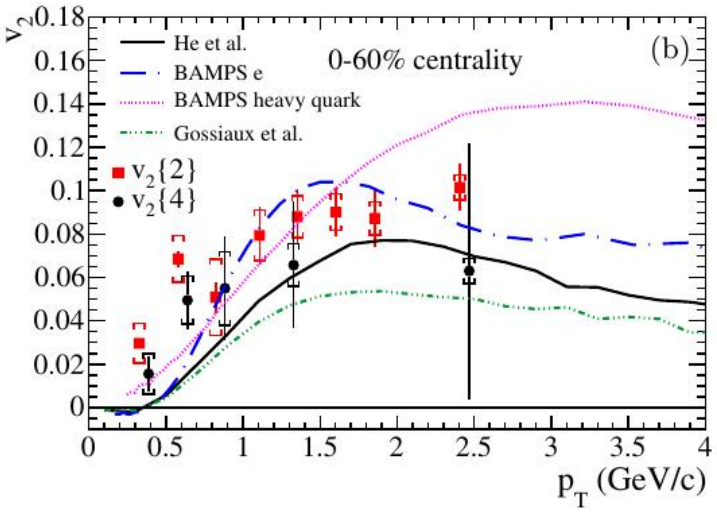

Figure 25: Non-photonic electron elliptic flow compared with several theoretical models [19] - [21].

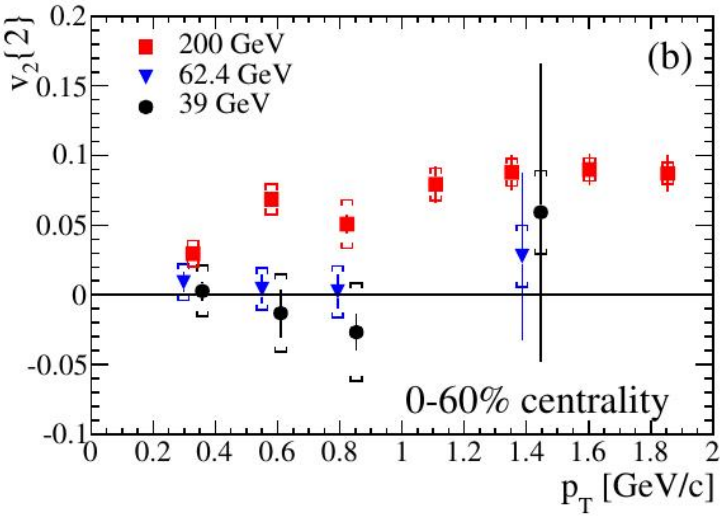

Figure 26: Non-photonic electron elliptic flow in Au+Au collisions at $\sqrt{s_{NN}}$=39, 62.4, and 200 GeV compared with several theoretical models. Taken from Ref. [44].

4.2 Non-photonic electron production at PHENIX experiment

NPE results from PHENIX experiment include analysis in various colliding systems: d+Au, Cu+Cu, and Au+Au at the same energy $\sqrt{s_{NN}} = 200$ GeV [45], and Au+Au R_{AA} and v_2 at $\sqrt{s_{NN}} = 62$ GeV [46]. Figure 27 shows R_{AA} from Cu+Cu collisions at midrapidity. These results are very important because the Cu+Cu collision system size is between Au+Au and d+Au collision system sizes and provide a connection between these two previous results. Therefore it is possible to study cold and hot nuclear matter effects to NPE production. Figure 27 shows the R_{AA} for minimum bias events (centrality 0-94%), and for 5 different centrality bins (0-10%, 0-20%, 20-40%, 40-60%, and 60-94% of the most central collisions). Central results have a connection to Au+Au collisions, $< N_{coll} \approx 182 >$) and peripheral collisions provide a connection to d+Au collisions, $< N_{coll} \approx 5.1 >$). The suppression was observed as a dominant effect in central collisions, whereas the enhancement was observed in peripheral collisions.

Figure 28 shows NPE R_{dA} in d+Au collisions at $\sqrt{s_{NN}} = 200$ GeV at midrapidity. The d+Au collision system is great to study cold nuclear matter effects because hot and dense medium effects are neglected due to the low multiplicity of this colliding system. Top panel of Fig. 28 presents NPE R_{AA} for 20% of the most central collisions ($< N_{coll} > \approx 15.1$), and the bottom panel shows NPE R_{AA} for peripheral collisions ($< N_{coll} > \approx 3.2$) [47]. In central R_{dAu} the enhancement is observed as a cold nuclear matter effect. It is supposed that this enhancement should be present in the initial state of A+A collisions and it is summed with the suppression caused by hot and dense matter.

Figure 29 shows comparison between R_{AA} and R_{dAu} for NPE and neutral pions [47]. At low- and mid-p_T strong CNM effects are observed for NPE in d+Au collisions, while neutral pion has no CNM effects. In this region the suppression of NPE is smaller then for π^0. However, in the range, where CNM effects are comparable for NPE and π^0 (above ≈ 5 GeV/c) their suppression have a same level. This could suggest that the difference in CNM effects caused by mass-dependent Cronin enhancement is seen in suppression in Au+Au collisions. This results support above discussed unexpected STAR results that unapproved mass-dependent partonic energy loss in the hot and dense medium. To sum extend it could also explain the unexpected similar suppresion of NPE and light hadrons observed in STAR.

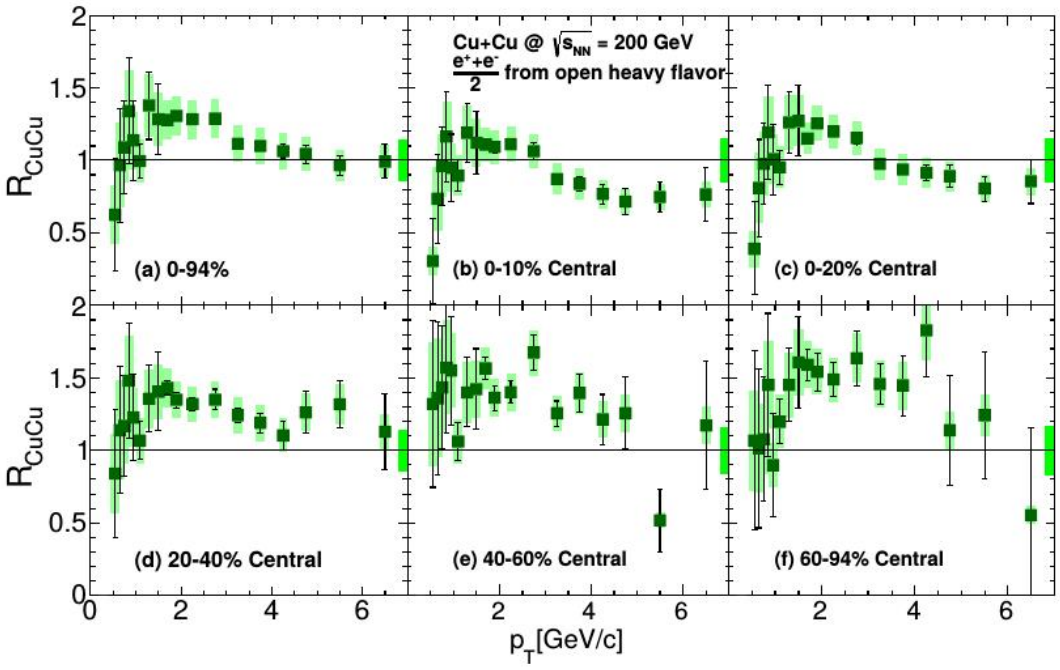

Figure 27: Non-photonic electron R_{AA} in Cu+Cu collisions at $\sqrt{s_{NN}} = 200$ GeV at PHENIX for minimum bias and 5 different centrality bins. Taken from Ref. [45].

Single NPE results from Cu+Cu, d+Au and Au+Au collisions were compared together. Figure 30 compares R_{AA} in Cu+Cu (green squares) and Au+Au (red circles) collisions in similar sized system (similar number of participants) as a function of p_T, 0-10% and 0-20% of the most central collisions in Cu+Cu could be compared with semicentral results in Au+Au collisions (20-40% and 40-60% respectively). Figure 31 shows comparison between Cu+Cu and d+Au (blue triangles) R_{AA} in the similar sized system. Central (semicentral) d+Au NPE R_{dA} is comparable with semi-central (peripheral) Cu+Cu NPE R_{AA}. All results are consistent with each other and distributions have same shapes.

In order to look at a trend of the entire collision system, Fig. 32 shows R_{AA} as a function of $< N_{coll} >$. In d+Au and peripheral Cu+Cu collisions enhancement effects are dominant while at central Cu+Cu collisions and Au+Au collisions the suppression is observed. The enhancement seen in central d+Au collisions at mid and backward rapidity regions is larger than the expectation from initial state effects, and a model calculation inspired by recent results of hydrodynamic

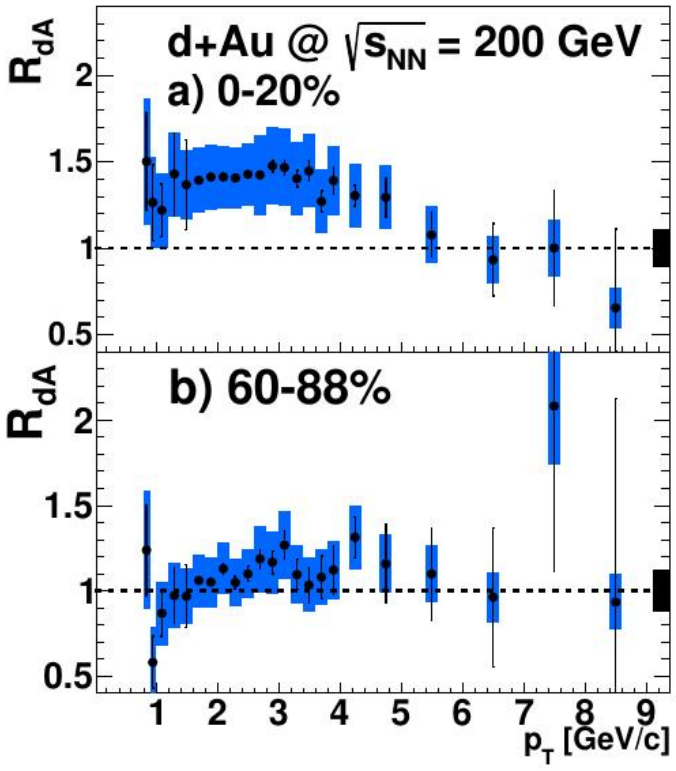

Figure 28: Non-photonic electron R_{dA} in d+Au collisions at $\sqrt{s_{NN}}$ = 200 GeV at PHENIX. Central collisions are shown in the top panel, and peripheral in the bottom panel. Taken from Ref. [45].

behavior in d+Au collisions raises the possibility of final state interaction [45].

As is discussed in previous section the strong suppression of NPE production was observed. Together with finite v_2 it is signal of QGP formation. The study of these two observables as a function of collision energy is a key tool to study the transition from hadronic matter to the QGP. In this section NPE results at $\sqrt{s_{NN}}$ = 62 GeV is discussed. Figure 33 shows NPE yield in p+p collisions at $\sqrt{s_{NN}}$ = 62 GeV from 3 independent analysis that agree with each other [46]. The black line is a power-law fit to the data points used as a p+p baseline for nuclear modification factor calculation. Yield in Au+Au collisions was divided into 3 centrality bins (0-20%, 20-40%, and 40-60%), Fig.34 shows invariant yields for minimum bias data and in all centrality bins compared with FONLL calculation. Right panel shows NPE invariant yield in p+p collisions. The solid red line denotes

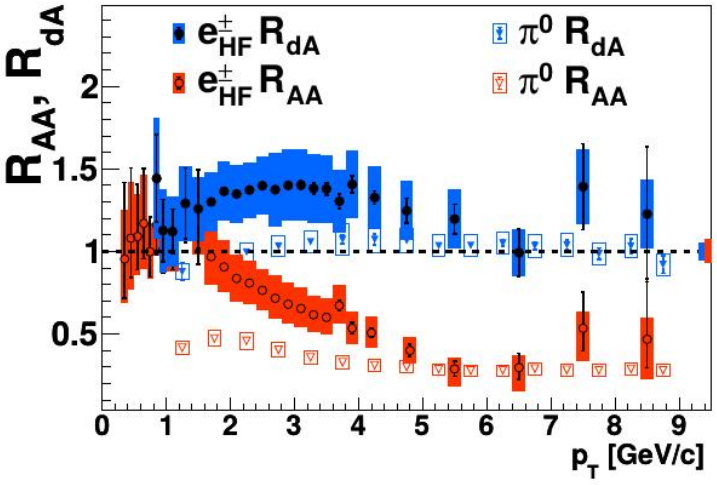

Figure 29: Non-photonic electron R_{AA} in d+Au collisions (blue) and Au+Au collisions (red) at $\sqrt{s_{NN}}$ = 200 GeV at PHENIX compared with light hadron measurement (same color triangles). Taken from Ref. [47].

FONLL central calculation and red dashed lines FONLL uncertainties. While p+p results are consistent with upper FONLL limit, Au+Au yields are systematically higher than upper FONLL limit.

In Fig. 35 NPE R_{AA} for different centrality bins and minimum bias data at $p_T < 5$ GeV/c region are shown [46]. The enhancement is observed in all centrality bins, it is possible that the initial state Cronin effect becomes dominant compared to energy loss in medium at lower beam energy. Figure 36 shows the comparison between measured R_{AA} in central collisions and theoretical model of heavy-flavor energy loss [48]. This theoretical model which includes energy-loss of heavy quarks in the QGP as well as a dissociation of D and B mesons underpredict the measured data [46].

Figure 37 shows the azimuthal anisotropy v_2 in Au+Au collisions at $\sqrt{s_{NN}}$ = 64 GeV measured by PHENIX [46]. The elliptic flow v_2 is the second Fourier coefficient of the NPE azimuthal distribution with respect to the reaction plane. Observed v_2 is compared with several theoretical predictions. While at low p_T data is consistent with models at high p_T no model describe data well.

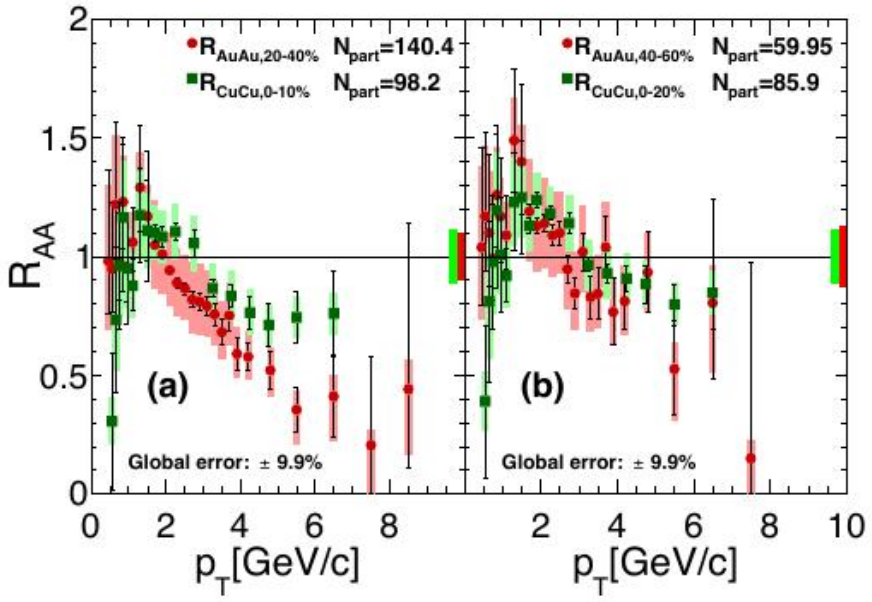

Figure 30: Comparison of NPE R_{AA} in similar sized system in Au+Au and Cu+Cu collisions. Taken from Ref. [45].

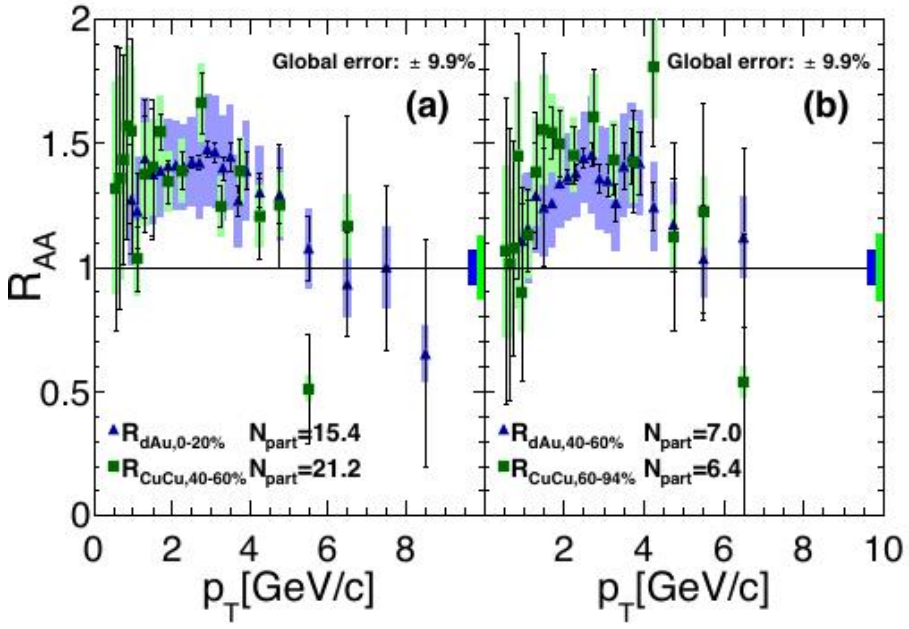

Figure 31: Comparison of NPE R_{AA} in similar sized system in Cu+Cu and d+Au collisions. Taken from Ref. [45].

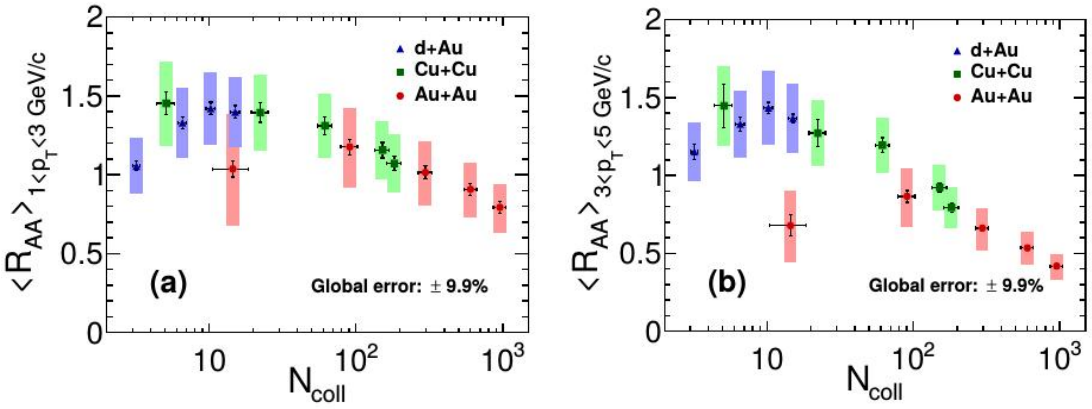

Figure 32: NPE R_{AA} as a function of number of binary collisions for 3 different colliding systems (Au+Au, Cu+Cu, d+Au). Taken from Ref. [45].

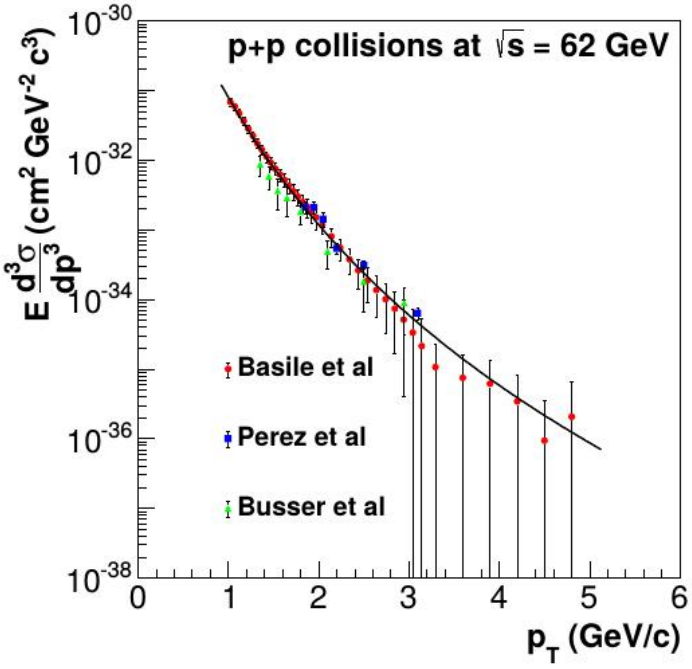

Figure 33: The NPE invariant yield in p+p collisions at $\sqrt{s_{NN}} = 62$ GeV measured with PHENIX. Red, blue, and green points present independent analysis. The solid black line is a power-law fit to the data used as a p+p baseline. Taken from Ref. [46].

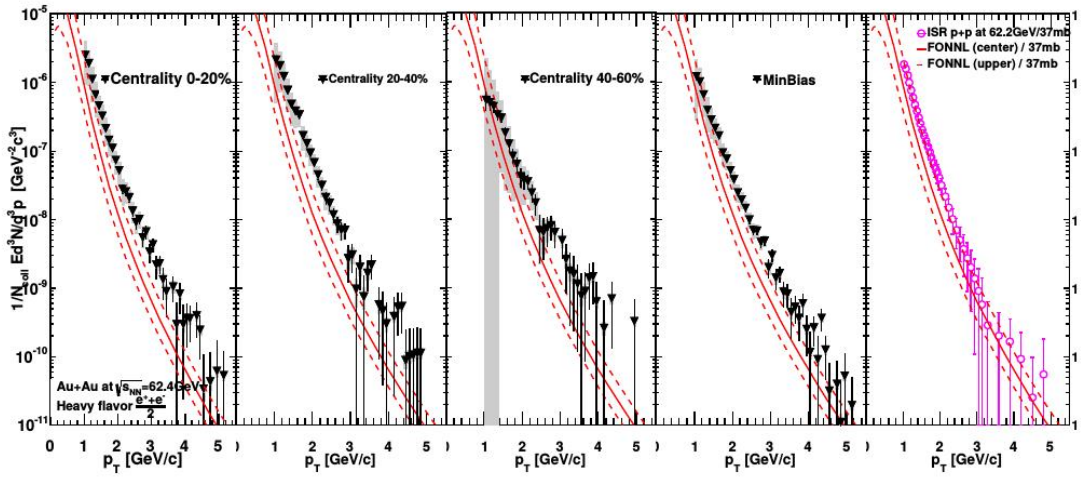

Figure 34: The NPE invariant yield in p+p (right panel) and Au+Au collisions at $\sqrt{s_{NN}} = 62$ GeV measured with PHENIX. Results are divided into 3 centrality bins (0-20%, 20-40%, 40-60%). The solid red line denotes FONLL calculation and dashed lines show FONLL uncertainties. Taken from Ref. [46].

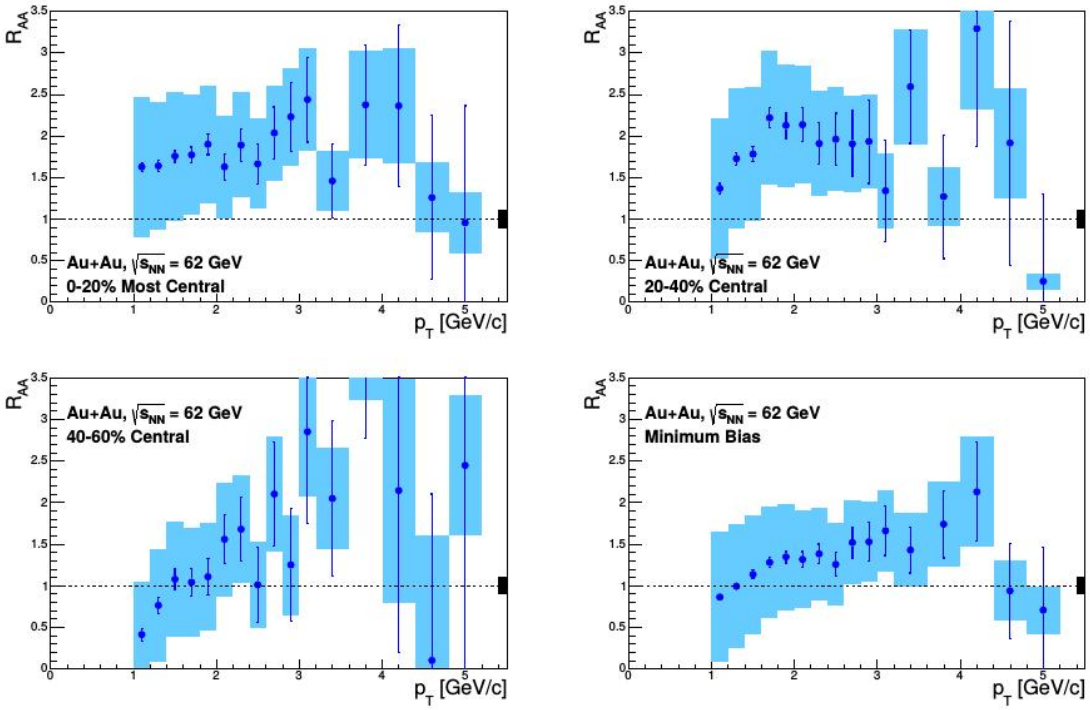

Figure 35: The NPE R_{AA} at $\sqrt{s_{NN}} = 64$ GeV in PHENIX for different centrality bins. Taken from Ref. [46].

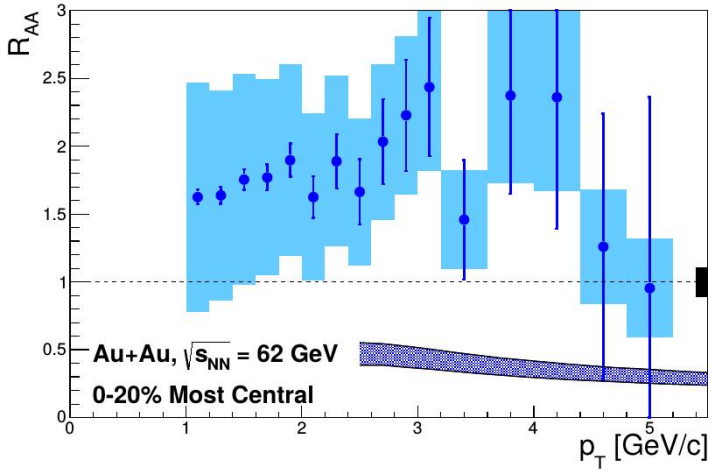

Figure 36: The NPE R_{AA} at $\sqrt{s_{NN}} = 64$ GeV in PHENIX for different centrality bins. Taken from Ref. [46].

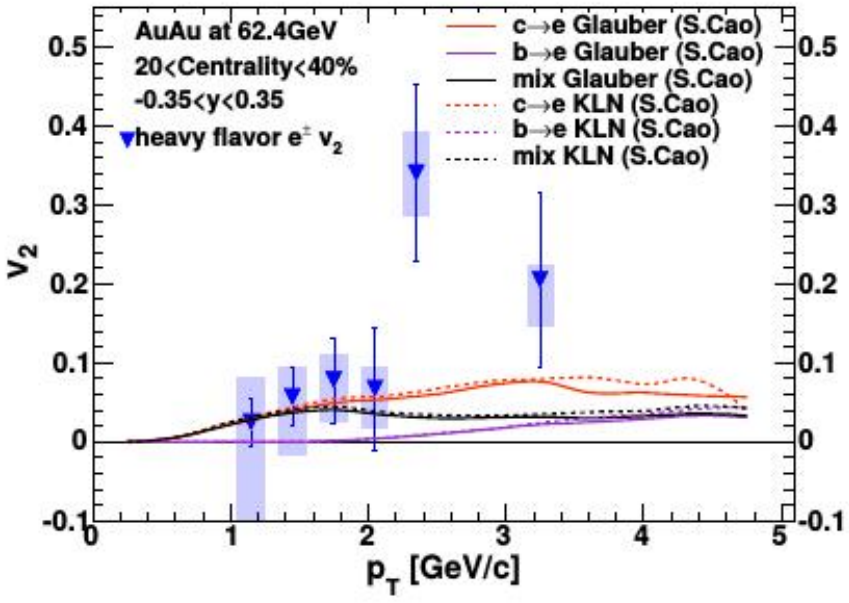

Figure 37: NPE v_2 in Au+Au collisions at $\sqrt{s_{NN}} = 64$ GeV in PHENIX compared to several models. Taken from Ref. [46].

4.3 Non-photonic electron production at ALICE experiment

Figure 38 shows NPE p+p results at $\sqrt{s} = 2.74$ TeV at midrapidity [49]. Data were recorded as a minimum-bias data (MB) and Electromagnetic Calorimeter (EMCal) triggered (ET) data. For the MB sample analysis the information from TPC were used ($2 < p_T < 7$ GeV/c). Low p_T electrons ($0.5 < p_T < 5$ GeV/c) were analyzed with information from TPC and TOF together. The ET data were analyzed using combine information from TPC and EMCal ($2 < p_T < 12$ GeV/c). Results from these independent analysis are consistent in overlapping p_T regions. The presented p_T cross-section (Fig. 38 top) is a combine result from these different analysis and was obtained from invariant yield normalizing to the MB cross section (55.4 ± 1.0mb). Finally, results were compared to theoretical pQCD FONLL calculation [50] [51], GM-VFNS [52]-[54], and k_T-factorization [55] (Fig. 38 from the second panel to the bottom, respectively). Results are consistent with theoretical prediction within statistical and systematic errors.

Figure 39 (left panel) shows the nuclear modification factor (R_{AA}) of electrons and muons from heavy flavor meson semileptonic decays in Pb+Pb collisions at $\sqrt{s} = 2.74$ TeV [56]. As well as in previous discussed p+p NPE analysis electrons were identified using information from TPC, TOF, and EMCal at midrapidity ($-0.6 < \eta < 0.6$), while for muon analysis was used information from Forward Muon Spectrometer at forward rapidity ($-4 < \eta < -2.5$). As a baseline were used results from p+p analysis at $\sqrt{s} = 2.74$ TeV and $\sqrt{s} = 7$ TeV. Strong suppression is observed for both electron and muons from heavy flavour meson decays.

The fraction of NPE from B meson decays was extracted from the fit to the impact parameter distribution where shapes of different sources of electrons were obtained from simulation. The R_{AA} for bottom NPE is plotted in Fig. 39 (right panel), the suppression was observed for $p_T > 3$ GeV/c.

Figure 40 (left panel) shows the NPE R_{pA} in p+Pb collisions at $\sqrt{s_{NN}} = 5.04$ TeV [57]. Electron at low-p_T region were identified using TPC together with TOF (red circles), and at high-p_T using TPC with EMCal (blue circles). The right panel shows B meson-to-electrons decays R_{pA} (red) compared to all NPE R_{pA} (black circles).

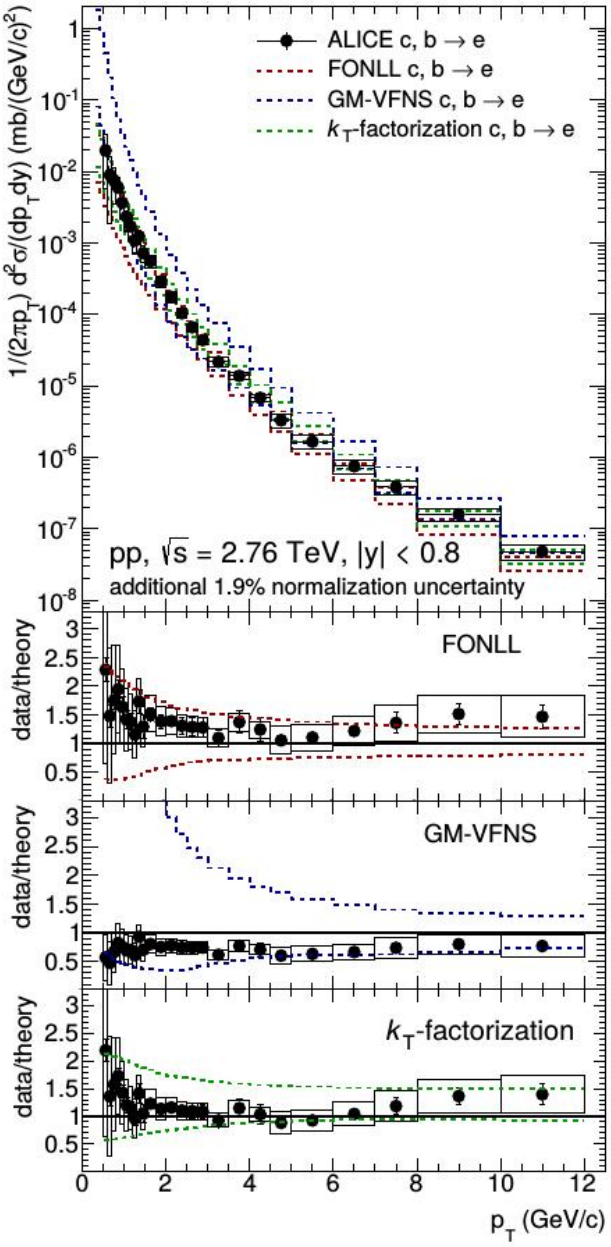

Figure 38: The NPE differential cross-section as a function of p_T (p+p collisions at $\sqrt{s}$ = 2.74 TeV, ALICE) [49] is shown in the top panel compared to pQCD FONLL calculation (red line) [50] [51], GM-VFNS [52]-[54] (blue line), and k_T-factorization [55] (green line). Bottom panels show rations between data and theoretical predictions FONLL, GM-VFNS, and k_T-factorization from the top to bottom respectively. Taken from Ref. [49].

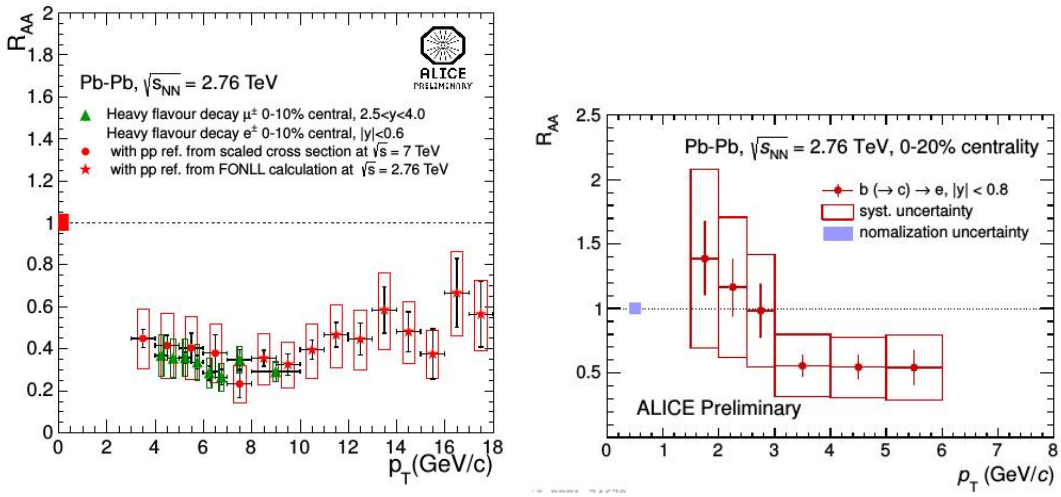

Figure 39: The nuclear modification factor for the 10% of the most central Pb+Pb collisions at $\sqrt{s} = 2.74$ at ALICE. Top panel shows R_{AA} for both electrons (midrapidity) and muons (forward rapidity) from semileptonic decays of heavy flavor mesons. Bottom panel shows R_{AA} for bottom NPE. Taken from Ref. [56].

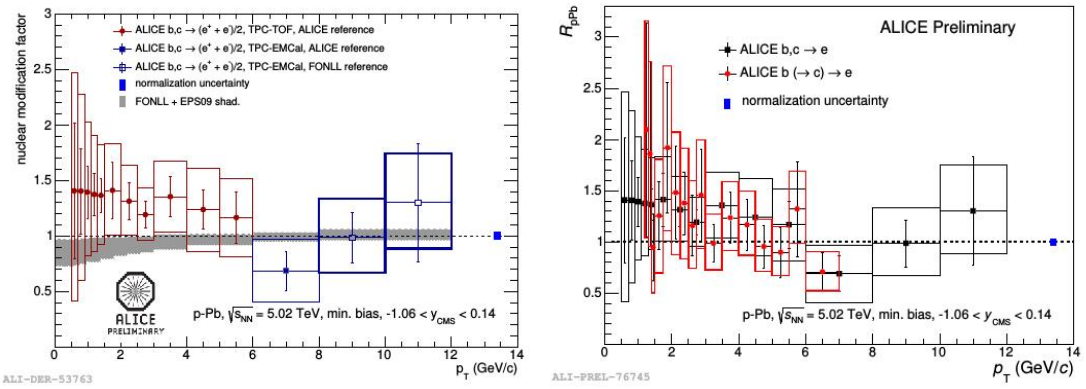

Figure 40: NPE R_{pA} in p+Pb collisions at $\sqrt{s_{NN}} = 5.04$ TeV (top panel), and comparison between all NPE R_{pA} to the only B meson electron decays R_{pA}. Taken from Ref. [57].

5 RHIC and the STAR detector

The Relativistic Heavy Ion Collider (RHIC) is located at the Brookhaven National Laboratory in Upton, New York. The RHIC started its operation in 2000. Research at the RHIC is focuses on the study of Quark Gluon Plasma, the primordial state of matter that existed in the early universe. Key features of the nuclear environment at the RHIC are a large number of produced particles and a production of high momentum particles from hard parton-parton scattering. The goal is to obtain a fundamental understanding of the microscopic structure of these hadronic interactions at high energy densities [58]. In this Chapter, the RHIC system and the STAR experiment is described in detail.

Figure 41: A schematic view of the RHIC complex. Taken from Ref. [60].

5.1 The Relativistic Heavy Ion Collider

The RHIC is an intersection storage ring (ISR) particle accelerator composed of two independent rings. It is designed to collide light nuclei as polarized protons and heavy nuclei such as Cu, Au and U. The RHIC has a circumference of about 3.8 km with six intersection points, where particles collide. Originally, there were four experiments at intersection points: STAR, PHENIX, BRAHMS and PHOBOS. BRAHMS and PHOBOS completed their program already. The whole RHIC complex is illustrated in Fig. 41, there are also figured accelerators used to accelerate particles up to RHIC injection energy.

Before reaching the RHIC storage ring, each particle passes through several stages. Heavy ions started their acceleration in the Tandem Van de Graaf, where ions are accelerated to an energy of about 1 MeV per nucleon. Then ions are stripped of electrons and passed through the Tandem-to-Booster line, the Booster synchrotron. After having passed through the Booster line, ions have an energy of about 95 MeV per nucleon. The next station on the way to the RHIC is the Alternating Gradient Synchrotron (AGS) that was used for fixed target experiments in the past, and where ions are accelerated to an energy of 8.86 GeV per nucleon. Finally, ions are sent through the AGS-To-RHIC (ATR) transfer line. At the end of this process, ion bunches are sent by switching magnets to one of two beam lines. Then the bunches are colliding in one of four interaction point.

Since its commission in the year 2000, RHIC has successfully collided number of systems at different energies: $p+p$, $Au+Au$, $Cu+Cu$, $Cu+Au$, $p+Au$, $d+Au$, $U+U$. The top energy for heavy ions is 200 GeV per one nucleon-nucleon pair, and 500 GeV for proton-proton collisions. Very important and specific for RHIC accelerator is the fact that RHIC is able to collide ions with wide range of energies. It is so called Beam Energy Scan (BES), in phase I of BES were collected data of $Au+Au$ collisions at 7.7, 11.5, 19, 27, and 39 GeV. Together with earlier data at 62, 130, and 200 GeV they cover interval which is believed to contain the Critical Point, the end of first order phase transition between hadron gas and QGP [61] [62]. The schematic QCD phase diagram was shown in Chapter 2 in Fig. 2.

For mid-to-late 2020s is planed to build and electron-ion collider, the new research tool on the existing RHIC facility. This new collider, eRHIC, will allow to answer to fundamental questions related to QCD as: How are the sea quarks and gluons distributed in the space and momentum inside the nucleon? Where does the saturation of gluon densities set is? How does the nuclear environment

affect the distribution of quarks and gluons and their interaction in nuclei [40]? Upgraded STAR and sPHENIX detectors are planed to operating at eRHIC.

5.2 The STAR

The Solenoidal Tracker at the RHIC (STAR) is a massive detector that was designed especially for a study of the hadron production and the search for signatures of the quark gluon plasma formation and its properties and for studies of other physical effects, which occur under extreme conditions in a relativistic heavy-ion collisions.

Compared with other experiments at the RHIC, it is unique in its full azimuthal coverage that makes possible a study of azimuthal particle correlations. Due to this and a good coverage of pseudo-rapidity $|\eta| < 1.8$, the STAR detector is able to measure a wide variety of physical phenomena [58].

Most constituents of the STAR experiment are inside a large solenoidal magnet with an approximately uniform magnetic field (B=0.5 T maximally) parallel to the beam pipe. The main tracking detector is the Time Projection Chamber (TPC) that is discussed in detail in Chapter 5.3. The TPC can record only charged particles, although the decay vertices from neutral hadrons can be reconstructed from tracks of charged decay products left in the TPC. The TPC is a strong tool for particle identification, similarly to the Time of Flight detector (TOF, Chapter 5.4) based on the Multi-gap Resistive Plate Chamber (MRPC) technology [63]. Another important part of the STAR detector is the Barrel Electromagnetic Calorimeter (BEMC) that will be discussed in more detail further (Chapter 5.5). The general STAR detector schema is shown in Fig. 42. The Heavy flavor tracker (HFT, Chapter 5.7) is a new STAR subdetector implemented in the year 2014. The HFT detector allows more accurate measurement of heavy flavor mesons and baryons and allows to distinguish between electrons from D and B meson decays. Second upgrade, very important for heavy flavor measurements, is Muon Telescope Detector (MTD). It provides unique measurement of electron-muon correlations and distinguish between different Υ states [59].

5.3 The Time Projection Chamber

The Time Projection Chamber (TPC) is a central element of the STAR detector, located in the solenoidal magnet that surrounds the interaction vertex. The schema

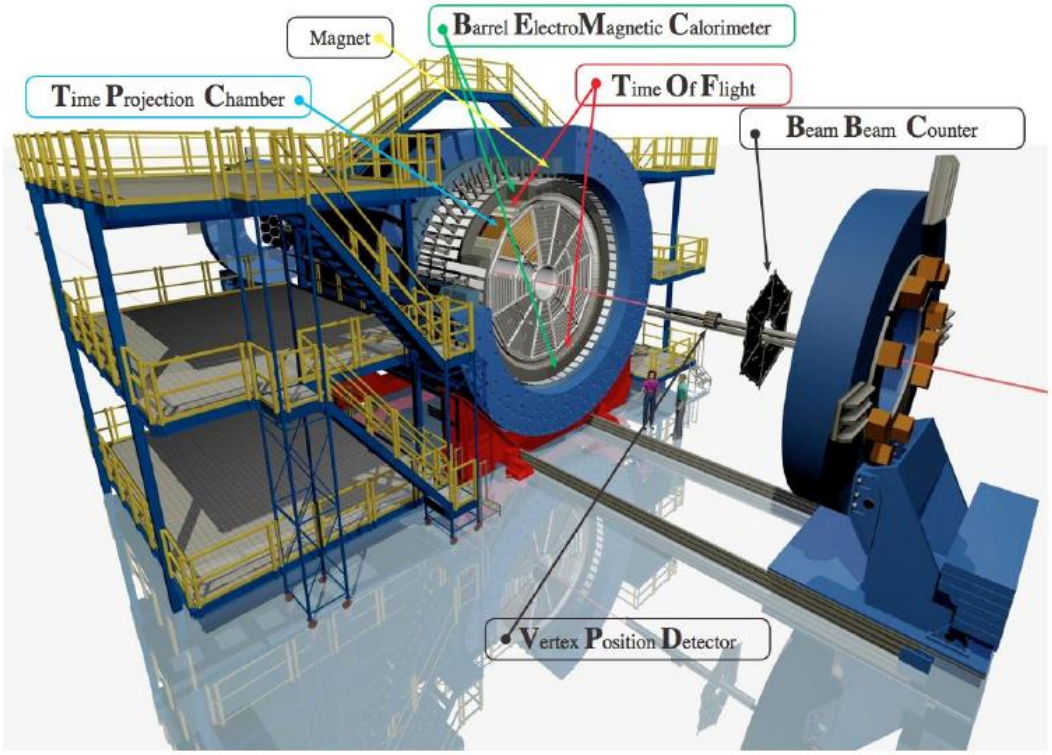

Figure 42: The experimental setup of the STAR detector.

of the TPC is shown in Fig. 43. Since the TPC, with TOF together, plays key role in an analysis presented in this thesis, we describe it in detail. The TPC has 4.2 m along the beam axis, and 4 m in a diameter, and it is a main tracking device of the STAR detector that registers tracks of particles, measures their momentum, and identifies particles via the ionization loss energy (dE/dx). Its acceptance covers ± 1.8 units of pseudo-rapidity through the full azimuthal angle. Charged particles with momenta greater than 100 MeV/c are recorded. More than 3000 tracks per event are routinely reconstructed [64].

The TPC is an empty volume filled with an argon-methane gas mixture (10% of methane, 90% of argon) regulated at 2 mbar above the atmospheric pressure. This gas was chosen with respect to its minimum attenuation of drifting secondary electrons. Its primary attribute is fast drift velocity that peaks at a low electric field (Fig. 44). It is important, because operating on the peak of the velocity curve provides stable drift velocity, and makes it insensitive to small pressure and temperature fluctuations. Low voltage provides the field cage design simplier.

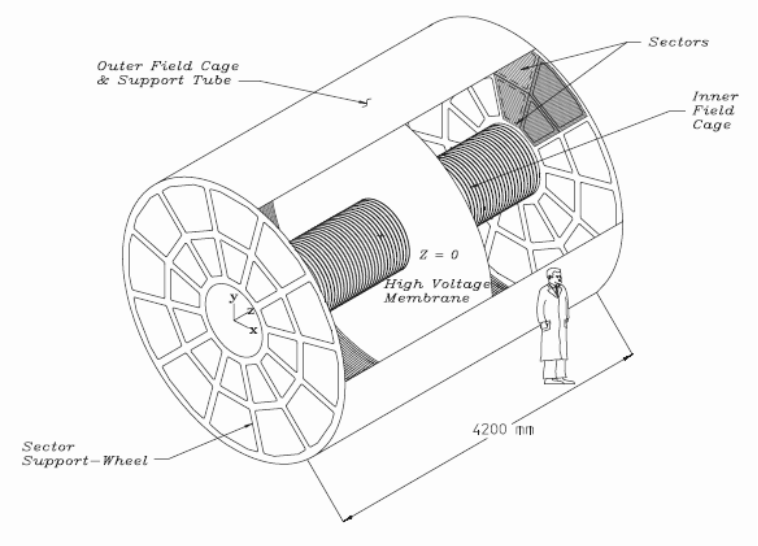

Figure 43: STAR TPC schema. Taken from Ref. [64].

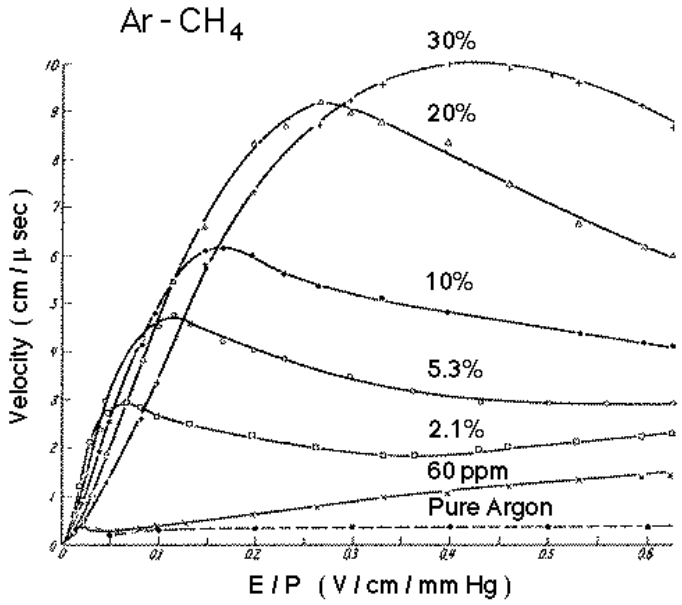

Figure 44: Electron drift velocity as a function of reduced electric field for different gas mixtures. Taken from Ref. [64].

Nearly perfect electric field is provided by an inner and an outer field cage and

by a high voltage central membrane. These properties allow secondary electrons drift to the anode plane without any distortion in recorded tracks. Both cages also serve the purpose of determining the active gas volume, and were designed in such a way as to prevent TPC gas from contamination by outside air. The mechanical design was optimized to reduce mass, minimize track distortions from multiple Coulomb scattering, and to reduce secondary particle production background [64].

In the middle of the TPC there is the central membrane located as shown in Fig. 43. This thin conductive membrane is under high voltage, and defines a uniform electric field required to drift electrons. The membrane is operated at 28 kV.

Pad planes are organized into sectors and are held at the ground potential. The space between the central membrane and the anode planes is divided by a series of gradient rings. Each ring is separated from the next one by a 2 Ω resistor, which provides a uniform gradient between the central membrane and the grounded endcaps. The readout endcap modules are split into 12 sectors around the beam pipe. Each sector is divided into an outer and an inner sub-sector in the readout plane. In the inner sub-sector the density of tracks is higher, and therefore, pads are smaller than in the outer sub-sector. One of these sectors is figured in Fig. 45, where the inner sub-sector is on the right and the outer one on the left.

The x and y coordinates of the track are reconstructed from the pad signal. The z position is determined from the drift time of a cluster of secondary electrons from the point of origin to the endcaps and from the average drift velocity. The most important features of the STAR TPC are listed in Tab. 1.

Vertex resolution

If the vertex resolution is good enough, the primary vertex can be distinguished from the secondary vertices. As mentioned further, the primary vertex can be used to improve the transverse momentum resolution. The primary vertex can be found by extrapolating all tracks reconstructed in the TPC to the origin. Than the total average is considered the primary vertex position. The total average is calculated by comparing positions of vertices that are reconstructed using each endcap of the TPC separately. The resolution decreases with the square root of the number of tracks used in calculation. A resolution of 350 μm is achieved when there are more than 1000 tracks used in calculation. The primary vertex resolution as a function of the particle multiplicity is shown in Fig. 46.

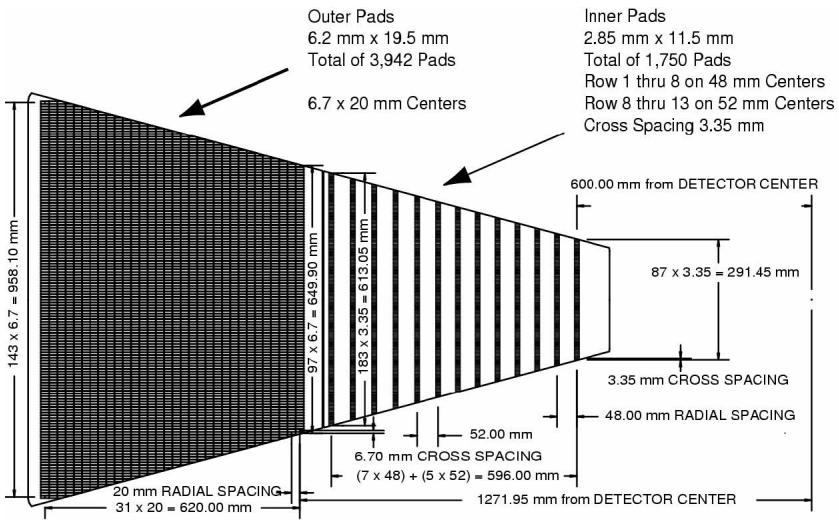

Figure 45: One sector of the readout endcap module. The inner sub-sector is on the right with small pads arranged in widely spaced rows. The outer sub-sector is on the left and is densely packed with larger pads. Taken from Ref. [64].

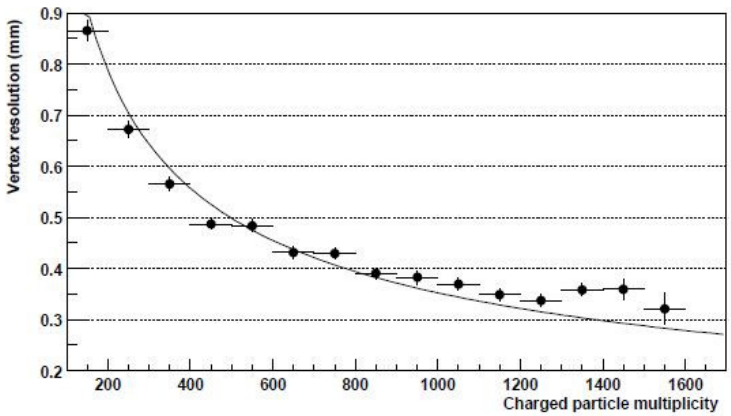

Figure 46: Primary vertex resolution in the transverse plane in $Au + Au$ collisions at $\sqrt{s_{NN}} = 130$ GeV. Taken from Ref. [64].

Momentum resolution

Charged particle transverse momentum is solved by fitting a curve (in x and y coordinates) along the particle track. The total momentum is calculated from this

Length	420 cm
Outer diameter	400 cm
Inner diameter	100 cm
Cathode potential	28 kV
Drift gas	P10 (10% methane + 90% argon)
Pressure	2 mbar above atmospheric pressure
Number of anode sectors	24 (12 per each end)
Number of pads	136608
Signal to bg ratio	20:1
Drift Velocity	5.45 cm/μs
Transverse Diffusion	230 μm/pcm 140 V/cm
Longitudinal Diffusion	360 μm/pcm 140 V/cm

Table 1: The most important features of the STAR TPC [64].

radius and the angle that the track makes with respect to the Z axis. For all primary particles, this can be done with respect to the primary vertex; for secondary particles, the transverse momentum fitting must be done without this reference. That means that the transverse momentum resolution is lower for secondary particles than for primary particles.

The transverse momentum resolution of primary particles tracks fit through the primary vertex is shown in Fig. 47. For transverse momentum above 1 GeV/c, it is more difficult to resolve the curvature of the track. This means that the momentum relative error increases for high p_T. At low momenta, the resolution is affected by the energy loss in the TPC. Due to their smaller energy these low momentum particles lose a significant proportion of their energy in the TPC, do not travel through the whole volume in the TPC, and therefore their tracks are shorter. The momentum measurement error increases as a consequence. Finally, the energy loss in the TPC is dependent not only on the particle momentum, but also on the mass of the particle, so that there are differences in the resolution for different particles at low momenta, as figured in Fig. 47 for antiprotons and pions. The best relative momentum resolution for pions is 2% at $p_T = 0.5$ GeV/c and it is increasing with p_T up to 10%.

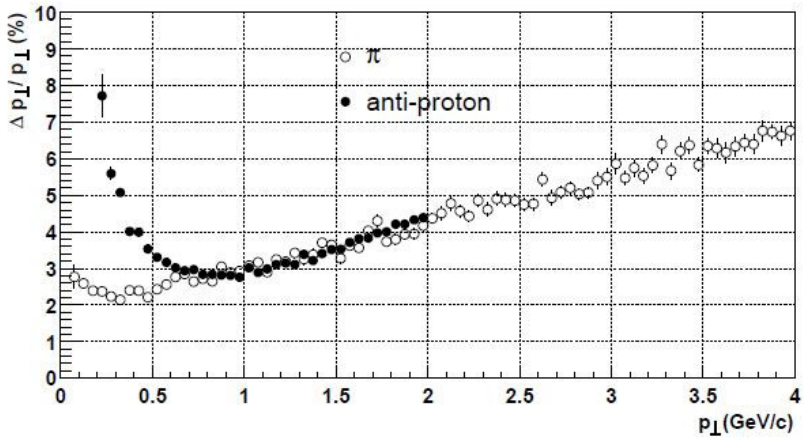

Figure 47: The transverse momentum resolution of the STAR TPC for π^-, and antiprotons in $Au + Au$ collisions at $\sqrt{s_{NN}} = 130$ GeV. Taken from Ref. [64].

Particle identification through ionization energy loss

A charged particle that traverses the TPC volume ionizes gas atoms along its path and leaves clusters of electrons. These clusters of electrons drift to the anode plane where their positions and time of arrival are recorded. Trajectories of primary ionizing particles are reconstructed from these released secondary electrons. The ionization energy loss (dE/dx) is calculated from the energy loss measured on up to 45 pad rows, and it is a powerful device used to identify particles. The energy loss per unit length is described by the Bethe-Bloch formula [65]

$$-\frac{dE}{dx} = \frac{1}{4\pi\epsilon_0}\frac{z^2e^4}{m_ec^2}\frac{1}{\beta^2}\left[\ln\frac{2m_ec^2\beta^2}{I(1-\beta^2)} - \beta^2\right], \tag{10}$$

where m_e is the electron mass, z is the charge of the particle, ϵ is the free space permitivity, I is the mean excitation potential, and n is the particle density in the target. The ionization energy loss dE/dx as a function of particle momentum is shown in Fig. 48, where the dE/dx resolution is depicted by color bands.

Ionization fluctuations and finite track lengths limit the dE/dx particle identification. Based on the less mass-dependent energy loss for high momentum particles, the relative dE/dx resolution was established at 7% [64]. This resolution is achieved by requiring at least 20 of 45 hits in the TPC used for the track recon-

struction. Only tracks satisfying this condition are accepted. Next to the number of hits recorded in the TPC, the dE/dx resolution depends on event multiplicity, beam luminosity, magnetic field settings, track length, and drift distance. The resolution improves with more hits in the TPC, stronger magnetic field, longer tracks, shorter drift distance, lower beam luminosity, and for lower multiplicity. Another uncertainties of the dE/dx measurement depend on the gas gain that itself depends on the pressure in the TPC, which varies with time. The gas gain is monitored by a wire chamber. The read out electronics also introduce inaccuracy in the dE/dx signal. Other uncertainties are generated due to different responses of readout boards, and there are also small variations between single pads.

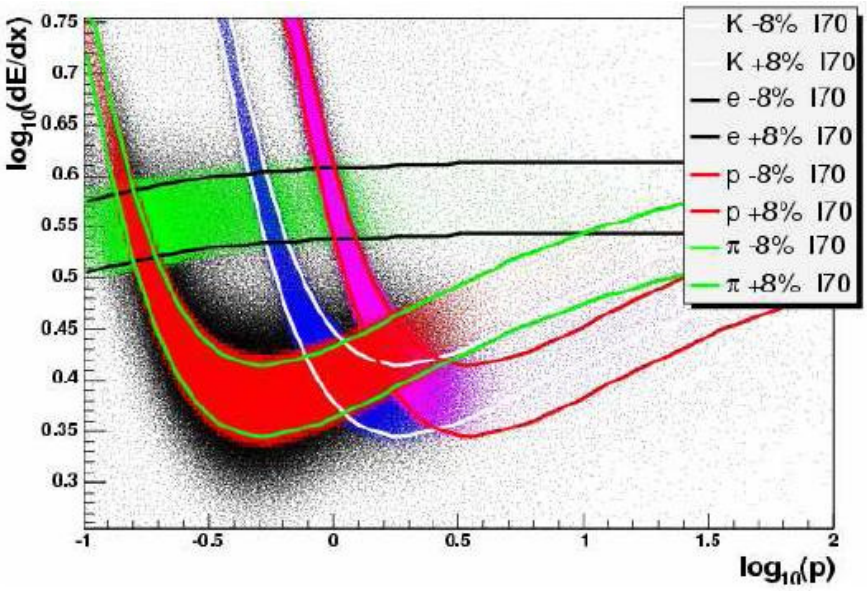

Figure 48: The dE/dx distribution as a function of momentum for electrons, pions, protons and Kaons. The dE/dx resolution is denoted by color bands. Taken from Ref. [68].

5.4 Time of Flight detector

The STAR TOF system consists of two detectors, the vertex position detector (VPD) as an events start detector and the multi-gap resistive chamber (MRPC) as a charged particle stop detector. The MRPC technology was developed by the CERN ALICE group [70]. It has the necessary timing resolution. The MRPC is

made of resistive glass plates with the uniform gas interspace as is shown in Fig. 49 and covers 2π in azimuth, and $|\eta| < 0.9$ in psedorapidity. In each gas gap is the strong electric field therefore charged particles going through the gas generate avalanges.

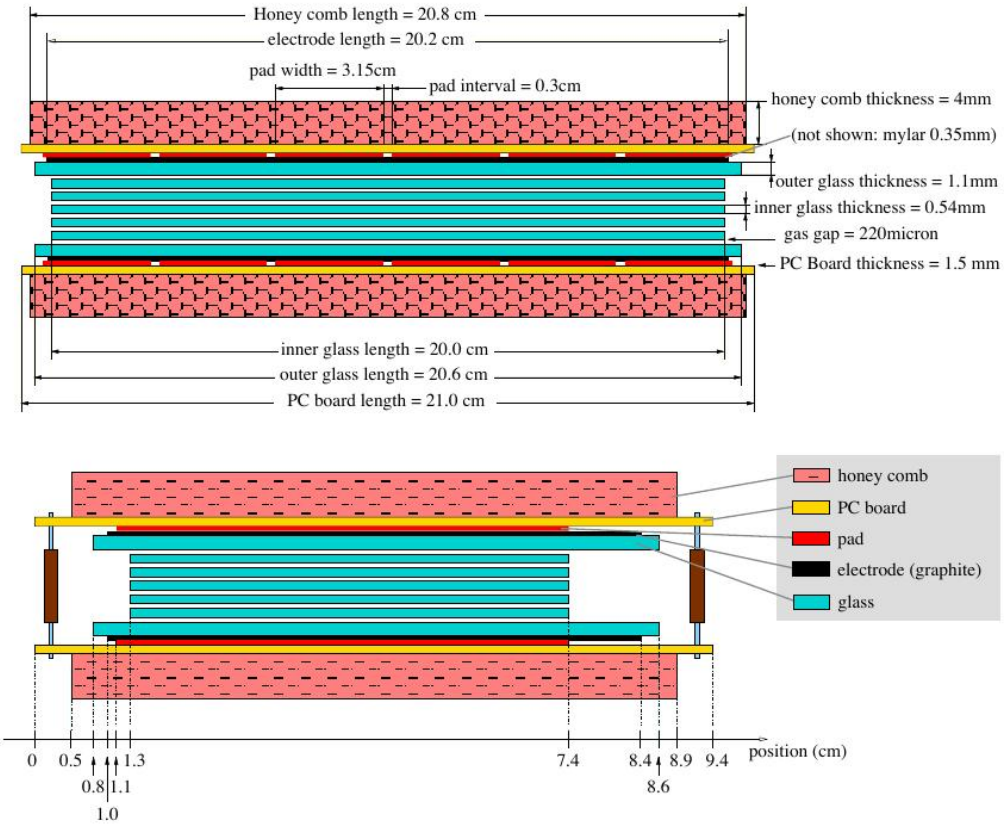

Figure 49: The long (short) views of the structure of an multi-gap resistive chamber. Taken from Ref. [69].

Time intervals Δt between signal in the VPD detector and in the MRPC are are associated with track in the TPC by tracks extrapolation to the MRPC. From TPC information the momentum p and the path length L are calculated. Then it is able to calculate the velocity β as

$$\frac{1}{\beta} = \frac{c\Delta t}{L}. \tag{11}$$

Particle momentum from TPC together with this velocity allow to calculate par-

ticle mass

$$M = p\sqrt{(1/\beta)^2 - 1}. \tag{12}$$

The STAR TOF system has a time interval resolution of 100 ps. The PID capability is plotted in Fig. 50, In regions without overlapping the particles can be identified. Solid lines correspond to the pseudorapidity around 0, thus in the center of the TPC, and dashed lines correspond to the pseudorapidity around 1, which are particles with longer path length. It is clear from Fig. 50 that TOF is a great tool for particle identification at low p_T region. The system provides

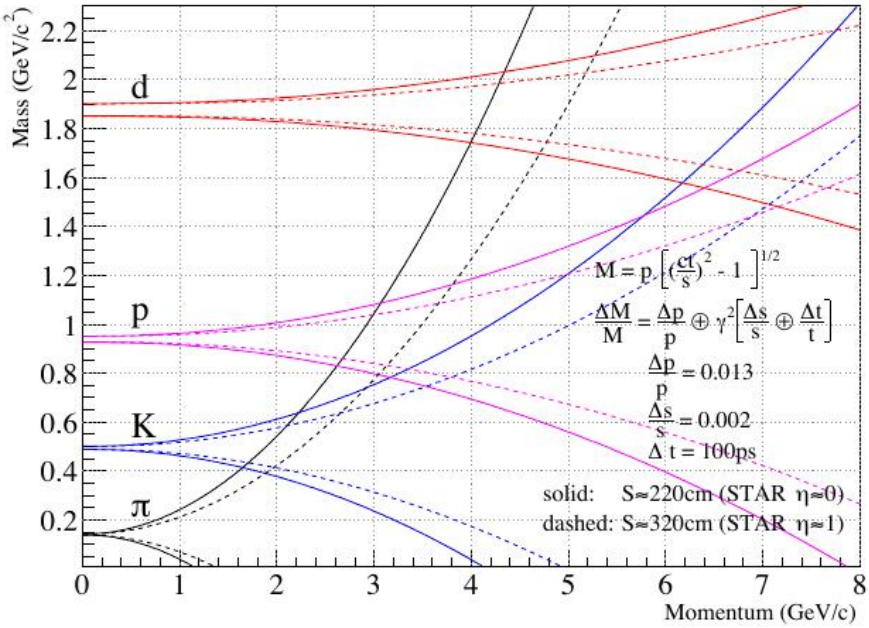

Figure 50: The momentum dependance of the particle mass resolution for the STAR TOF system. In regions where lines are non-overlapping the particle can be identified. Taken from Ref. [69].

to distinguish between electrons(pions), kaons, and protons up to p 1.5 GeV/c as is shown in Fig. 51. It is impossible to distinguish between electrons and pions based on TOF information only.

The STAR particle identification capability could be enhanced by using the Time of Flight (TOF) information and the data from TPC together. It is a very useful improvement if electrons are identified by using dE/dx information from

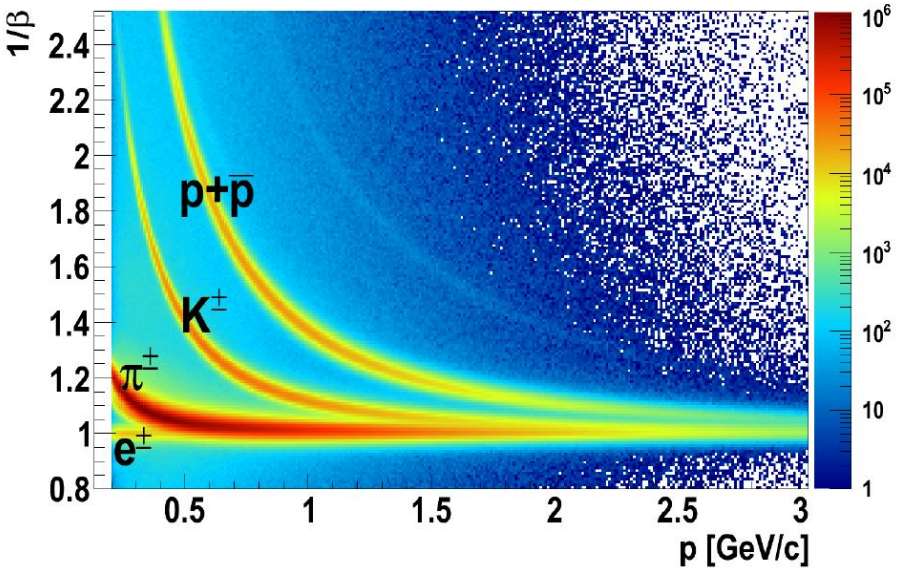

Figure 51: Value $1/\beta$ as a function of the momentum for electrons, pions, Kaons and protons from TOF at 200 GeV in $Au + Au$ collisions. The visible separation between electrons and kaons is reached for $p_T < 1.5$ GeV/c. Taken from Ref. [68].

the TPC and velocity information from the TOF. It makes electron sample purer and more efficient.

While TPC is a strong tool for identification particles with higher p_T, the TOF detector is a powerful component for distinguishing low p_T particles. It can be seen from Fig. 48 and Fig. 51 that neither TPC nor TOF alone are able to distinguish charged hadrons in the intermediate p_T range. However, the combination of both pieces of information provides good PID capability. With the combination of dE/dx information from the TPC and β from the TOF, electrons can be identified above $p_T > 0.15$ GeV/c, while the high p_T reach is limited by the statistics in analysis. The dE/dx distribution in the TPC after TOF cuts application is figured in Fig. 66.

5.5 The Barrel Electromagnetic Calorimeter

The Barrel Electromagnetic Calorimeter (BEMC) is located inside the STAR solenoid and covers $|\eta|$ <1 and 2π in azimuth, thus matching the acceptance for full TPC tracking. The inner surface of the BEMC has a radius of about 220 cm,

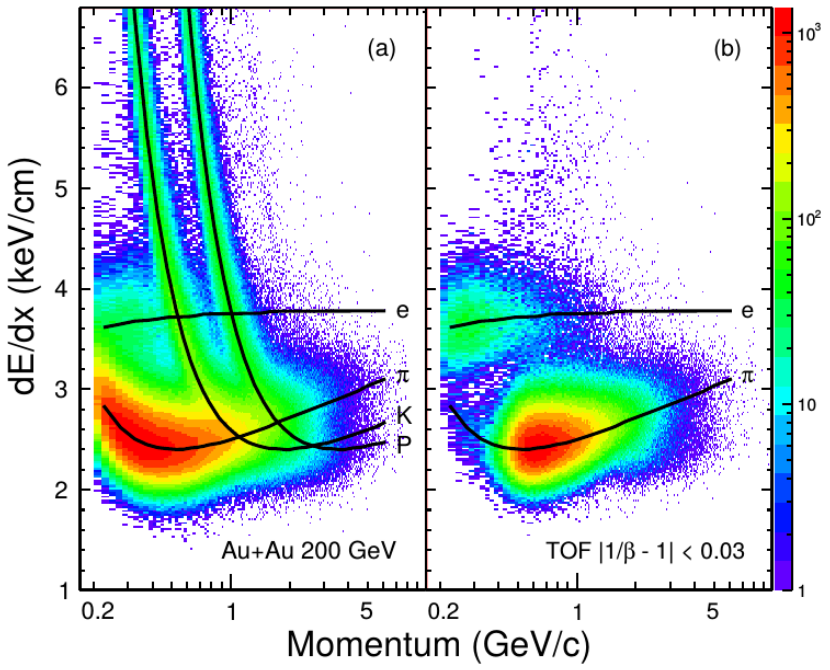

Figure 52: Energy loss dE/dx distribution without TOF cut apply (left), and after TOF cut use (right). Combined TPC and TOF information allows to distinguished electrons from hadrons at low p_T region.

and the outer radius is about 250 cm. The BEMC consists of 120 calorimeter modules, each of them segmented into 40 towers 20 in $\Delta\eta$ and 2 in $\Delta\phi$. Each module is about 26 cm wide and 293 cm long, and covers one unit in pseudorapidity and $2\pi/60$ in azimuthal direction. Thus the STAR BEMC is consists of 4800 towers oriented to the direction of the interaction point. Figure 54 shows side view of a BEMC single module [71].

In each module there are 21 active plastic, 19 layers are 5 mm thick and 2, associated with the Preshower detector, are 6 mm thick. Active layers alternate with absorber layers made from lead. Two layers of Shower Maximum Detector (SMD), placed at the position of 5 radiation lengths from the beam line, provide a precise spatial reconstruction (display in Fig. 54 and Fig. 53). The SMD is consisted of two layers of gas wire pad chambers orthogonal in transverse direction, it allows to obtain η and ϕ image of shower. Generally, the BEMC provides the precise energy resolution while the SMD provides high spatial resolution. This is

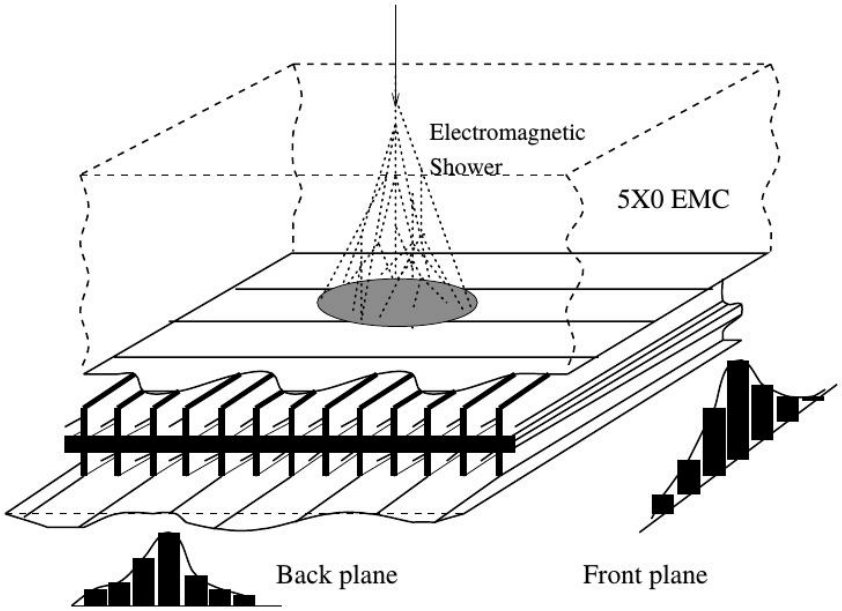

Figure 53: An illustration of an electromagnetic shower in the SMD. Taken from Ref. [71].

necessary for electron identification, information from SMD were used in analysis present in this thesis.

Electron identification with the Barrel Electromagnetic Calorimeter

Since BEMC has a depth of 20 radiation lengths electrons are expected to deposit full of their energy in a tower. In contrast to electrons hadrons deposit only part their total energy. Electrons at STAR are ultra relativistic and their energy is approximately equal to its momentum. Therefore the ratio p/E can be use for the electron identification, for electrons is about 1 while for hadrons is significantly higher.

High energy electrons trigger

High Tower (HT) triggers are based on BEMC information and are dedicated for high p_T electrons. They require the energy deposited in at least one tower of BEMC is higher then given threshold. HT triggers are defined on the top of Minimum

Bias (MB) trigger conditions. The MB trigger is based on signal coincidence in two VPD detectors as is discussed in next Chapter. For high-p_T region high-energy electron triggers are used. In presented p+p analysis 2 HT triggers (HT0, HT2), in d+Au analysis 4 HT triggers (HT0, HT1, HT2, HT4). Each of these triggers is operating at different energy thresholds and prescales, which are specified in Chapter 6 and Chapter 7.

5.6 Vertex Position Detector

The Vertex Position Detector (VPD) is a position detector fully integrated into STAR trigger system. It provides input to the MB trigger. The VPD consist of two detector assemblies, one on the east and one on the west of STAR. These two assemblies are consist of 19 detectors composed of a Pb converter followed by a fast, plastic scintillator which is read out by a photomultiplier tube. A schematic view and photograph of a VPD assembly is shown in Fig. 55 and a side view of the detector is shown in Fig. 56.

Two VPD detectors provide the start time for time-of-flight measurement in TOF detector. The information from the detector is used both in the STAR Level-0 trigger and offline to measure the location of the primary collision vertex along the beam pipe (Vz).

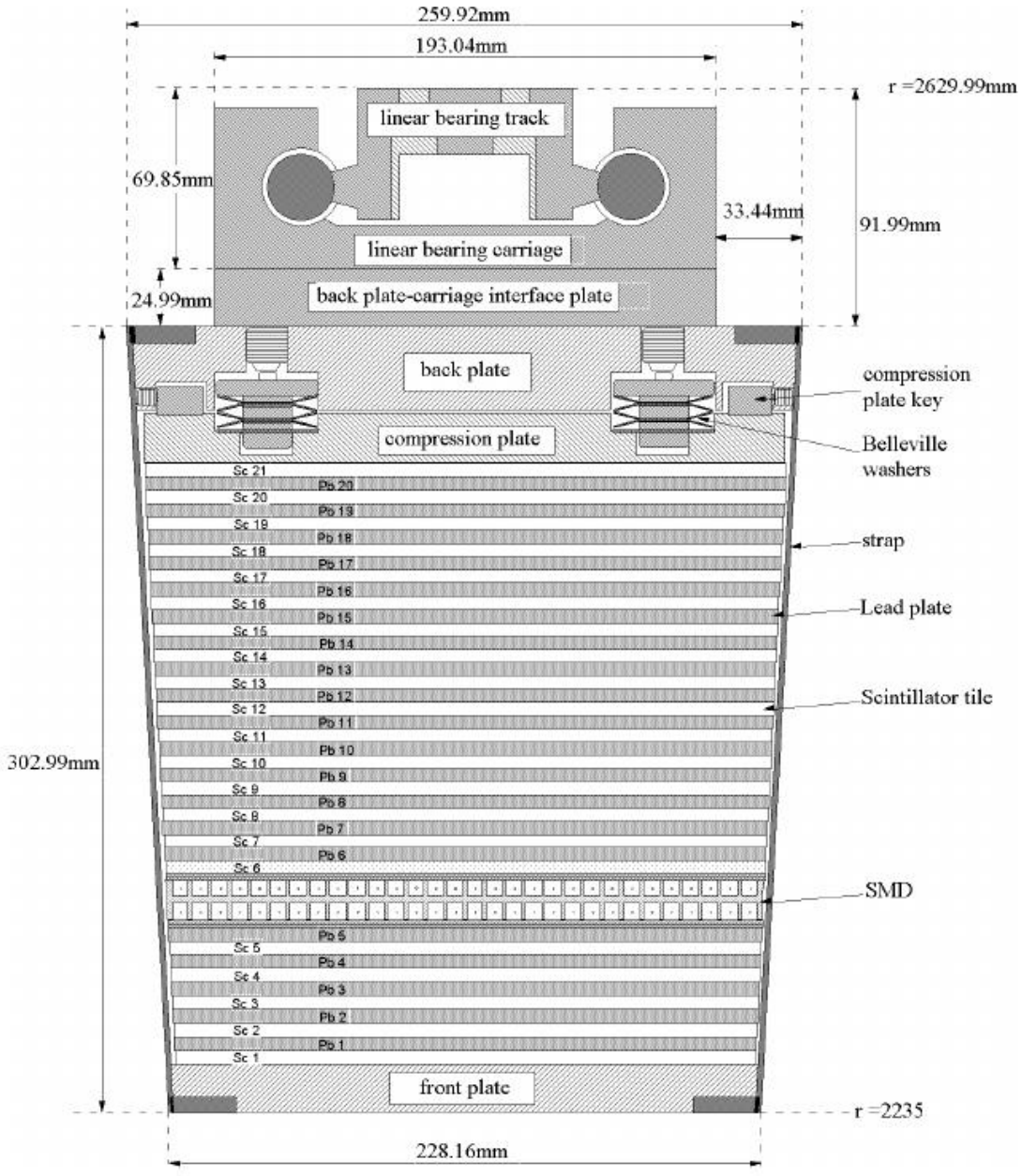

Figure 54: Side view of a BEMC module. Taken from Ref. [71].

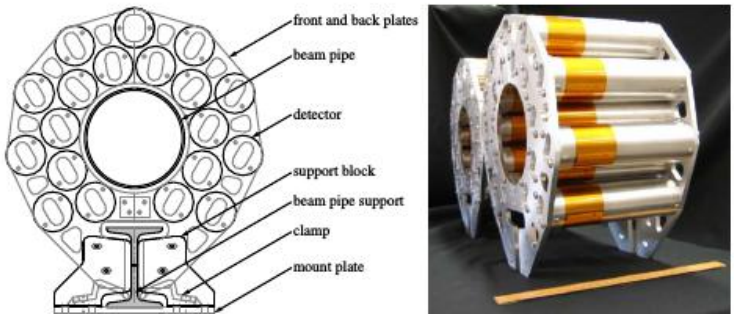

Figure 55: A schematic side of a VPD assembly (left) and a photograph of both VPD assemblies. Taken from Ref. [72].

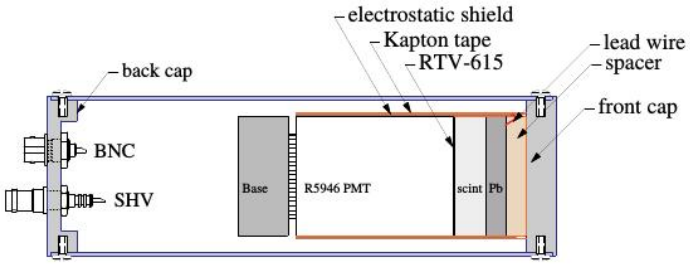

Figure 56: A schematic side view of VPD detector. Taken from Ref. [72].

5.7 The Heavy Flavor Tracker

The new STAR detector, Heavy Flavor Tracker (HFT), started its operation in 2014. HFT has a 2π coverage and it is placed inside of the TPC. HFT consists of 4 layers of silicon detector grouped into thrree subsystems, 2 inner pixel layers (PXL) at 2.5 and 8 cm from the beam pipe, the Intermediate Silicon Tracker (IST) at 14 cm, and the Silicon Strip Detector (SSD) at 22 cm. A schematic view of HFT layers is shown in Fig. 57.

While the pointing resolution in the TPC is ∼1 mm, the HFT pointing resolution is from the inner to the outer system ∼ 40 μm first layer of PXL, ∼ 125 μ m second layer of PXL, ∼ 400 μ m IST, ∼ 400 μ m SSD.

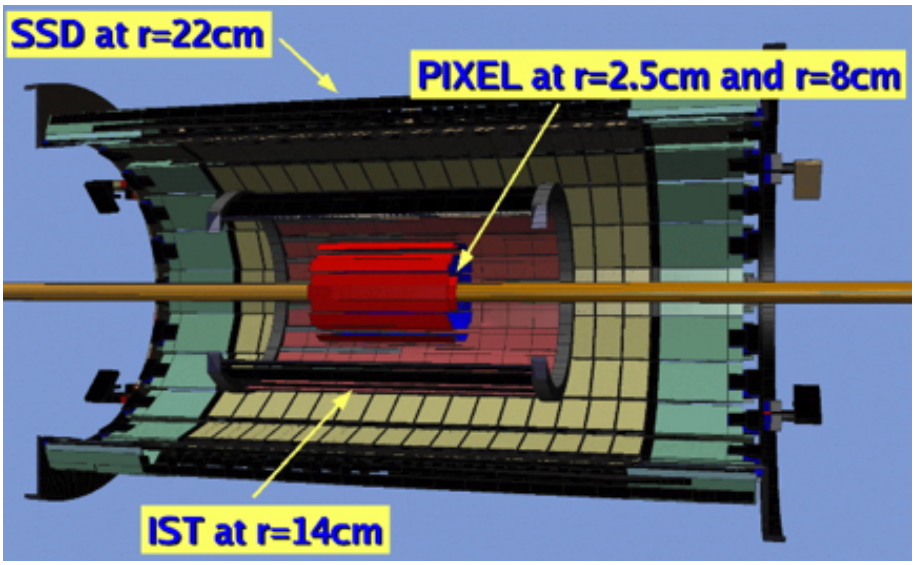

Figure 57: A schematic view of the HFT. Taken from Ref. [73].

The HFT detector extends the STAR particle identification capability to the short lived particles, such as particles containing heavy quark. The HFT is able to topologically reconstruct charm mesons and baryons. This is made by the reconstruction of the secondary vertices with a high precision ($\sim 30\mu$). The heavy flavor measurements are important for study of QGP properties. Suppression of heavy flavor mesons was observed in central Au+Au collisions. This suppression is similar as for light quarks. It is very surprising, since it is expected less suppression for the heavy quarks due to the dead cone effect. New results from HFT could shed light on this unexpected result. In NPE measurement will be possible to distinguish

between electrons from D and B mesons. Expected spectrum for electrons from these two sources is shown in Fig. 58.

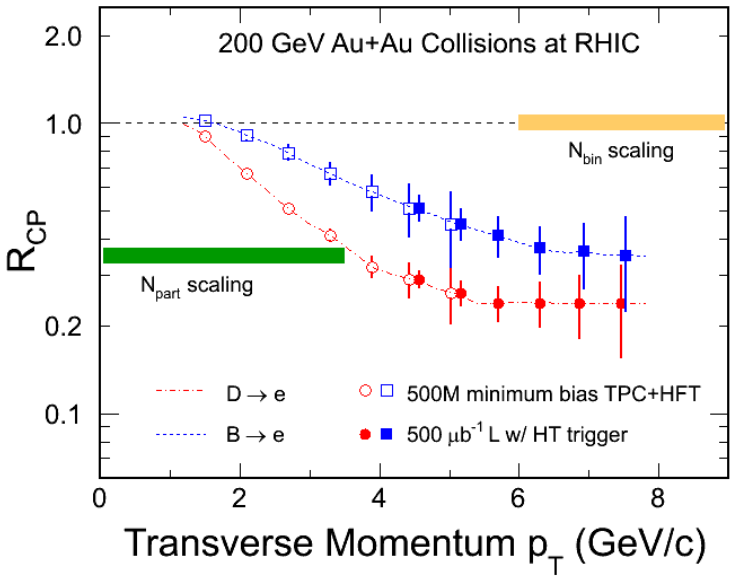

Figure 58: A study of R_{CP} of non-photonic electrons from D (blue) a B (red) mesons simulations separately with errors expected at data record with HFT. Open symbols come from 500M Au+Au simulated minimum-bias events, and filled symbols come from HT trigger simulated data with 500 μb^{-}1 sampled luminosity. Taken from Ref. [73].

After instalation of the HFT STAR has the best pointing resolution from collising experiment. The preliminary DCA pointing resolution is shown in Fig. 59. It appears to be as expected and meets the design goals [74].

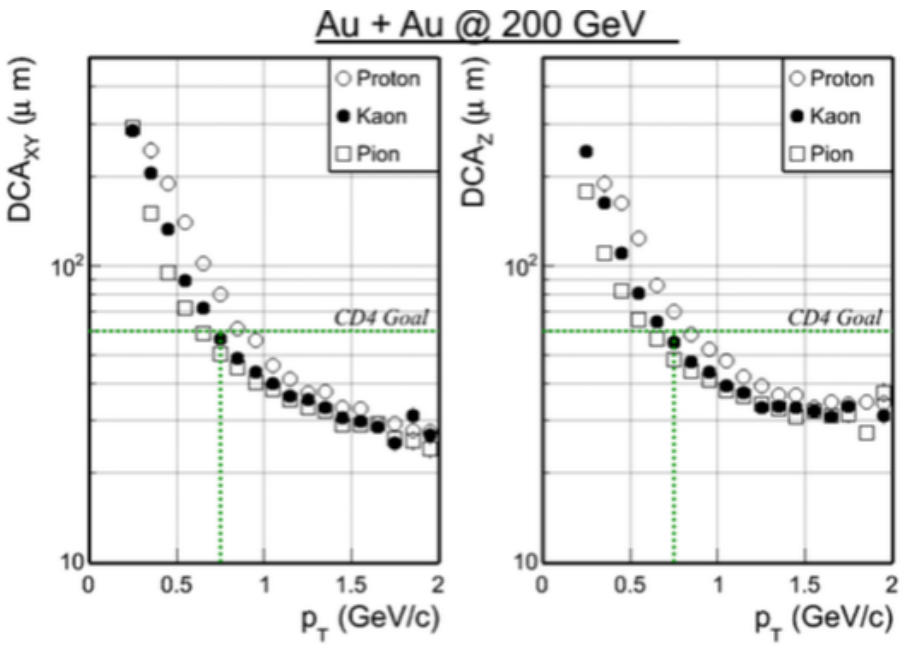

Figure 59: HFT position resolution in z-direction and ϕ-direction [74].

6 Non-photonic electrons in p+p collisions at $\sqrt{s}$=200 GeV

This chapter describes the analysis of non-photonic electrons (NPE) in p+p collisions at $\sqrt{s}$=200 GeV taken during the year 2009 with STAR experiment at RHIC in BNL. STAR Libraries and STAR MuDst production of p+p 2009 were used. The MuDst files were reduced to ROOT Trees containing fundamental information necessary for our analysis. In following paragraphs the analysis methods, partial results and final results are presented.

6.1 Data

In this analysis data recorded in p+p collisions at $\sqrt{s}$=200 GeV are used. Data from VPD minimum-bias (VPDMB) trigger were used for low-p_T region (0.4-2 GeV/c). The minimum bias trigger is based on signal coincidence in two VPD detectors. For high-p_T region (2-10 GeV/c), two high-energy electron triggers were used. They are high tower triggers (HT0, HT2) operating at different energy thresholds and prescales. These HT triggers require coincidence in VPD detectors as minimum bias trigger and accepted events with energy deposited in at least one BEMC tower above a given threshold. Transverse energy thresholds are 2.6 GeV for HT0, and 4.3 GeV for HT2. Events that satisfied both VPDMB trigger and HT triggers conditions are combined together, double-counted signal was removed. Combined spectrum is defined as

$$\text{BHT0}*\text{VPDMB}*!\text{BHT2}(11 < \text{ADC} <= 18)+\text{BHT2}*\text{VPDMB}(\text{ADC} > 18), \quad (13)$$

where BHT0 and BHT2 denote the high tower triggers thresholds, VPDMB minimum bias trigger conditions, and ADC is an electron adc value obtained from trigger simulator. In low-p_T region 300M VPD events were analyzed, at high-p_T region 36M HT0 events and 3.2M HT2 events were used. Each of these triggers has an independent prescale factor. It is used to regulate the amount of data read by detector during collision. The HT triggers has low prescale factor due to the fact that these events are less common and we would like study spectrum to high-p_T (1.5 for HT0 and 1 for HT2), while common MB events has high prescale factor ($\sim$ 268).

6.2 BEMC hot towers

Figure 60 shows the BEMC towers firing frequency. The frequency of hot towers is significantly higher than the frequency of normal ones. All towers with more than 12000 fires were rejected. In total, 217 hot towers were rejected.

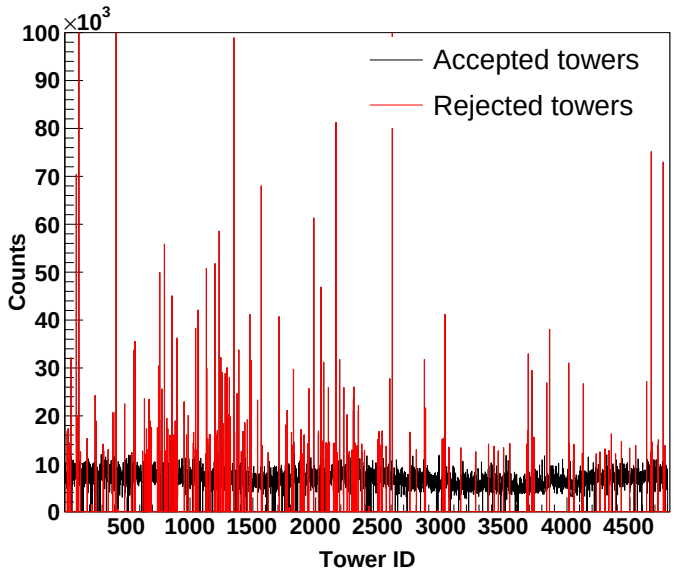

Figure 60: Firing frequency for single towers. Red towers were rejected as hot towers, red lines denote hot towers.

List of ID of rejected towers: 2, 23, 30, 31, 35, 48, 50, 51, 95, 96, 103, 114, 128, 181, 245, 251, 308, 312, 348, 349, 385, 405, 409, 412, 479, 536, 555, 561, 562, 622, 637, 650, 653, 665, 671, 674, 681, 682, 691, 740, 749, 750, 758, 759, 760, 775, 796, 801, 814, 815, 816, 822, 840, 857, 860, 873, 880, 882, 897, 899, 953, 954, 972, 986, 1026, 1028, 1042, 1044, 1046, 1056, 1063, 1128, 1130, 1131, 1132, 1140, 1153, 1154, 1160, 1197, 1198, 1204, 1217, 1219, 1232, 1238, 1244, 1256, 1257, 1263, 1280, 1282, 1294, 1304, 1313, 1318, 1348, 1354, 1375, 1378, 1387, 1408, 1422, 1427, 1435, 1456, 1475, 1486, 1487, 1537, 1567, 1574, 1575, 1622, 1709, 1762, 1773, 1807, 1819, 1823, 1825, 1882, 1892, 1904, 1906, 1909, 1938, 1945, 1984, 2021, 2022, 2043, 2051, 2063, 2083, 2097, 2101, 2109, 2141, 2145, 2162, 2164, 2171, 2190, 2222, 2223, 2250, 2267, 2288, 2299, 2300, 2303, 2313, 2322, 2327, 2339, 2340, 2366, 2368, 2388, 2493, 2504, 2521, 2529, 2561, 2589, 2610, 2749, 2750, 2801, 2865, 2874, 3007, 3020, 3028, 3061, 3154, 3273, 3375, 3420, 3453, 3495, 3544, 3679, 3690, 3692, 3718, 3720, 3726,

3738, 3838, 3861, 4013, 4017, 4019, 4053, 4057, 4122, 4130, 4233, 4262, 4302, 4333, 4353, 4386, 4433, 4498, 4546, 4633, 4667, 4671, 4678, 4722, 4727, 4766, 4778.

6.3 Trigger efficiency

For analysis of NPE at high-p_T region, events satisfying HT triggers conditions were used. The p_T spectrum obtained by HT trigger combination is plotted in Fig. 61. One can see that HT triggers are not efficient at p_T region from 2 to 4 GeV/c. Therefore the electron spectrum was corrected for trigger efficiency. This efficiency was calculated from comparison of inclusive electron spectrum based on VPDMB trigger (Figure 61, blue points) with the same spectrum obtained from both HT triggers. Final trigger efficiency is plotted in Fig. 62. Trigger efficiency was compared with HT trigger efficiency used for p+p analysis from the year 2008 and from simulation, all results are in agreement [36].

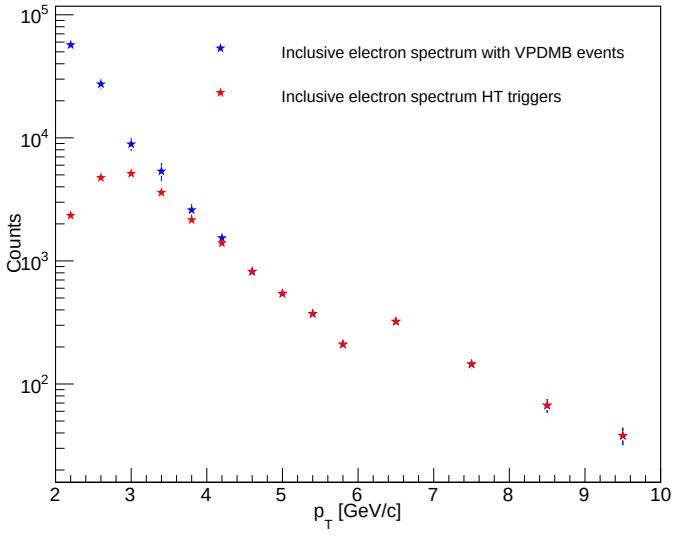

Figure 61: Inclusive electron spectrum from VPDMB trigger (blue), and from HT triggers (red).

6.4 Analysis principle

Non-photonic electrons, i.e. electrons originating from semileptonic decays of B and D mesons, could be reconstructed as

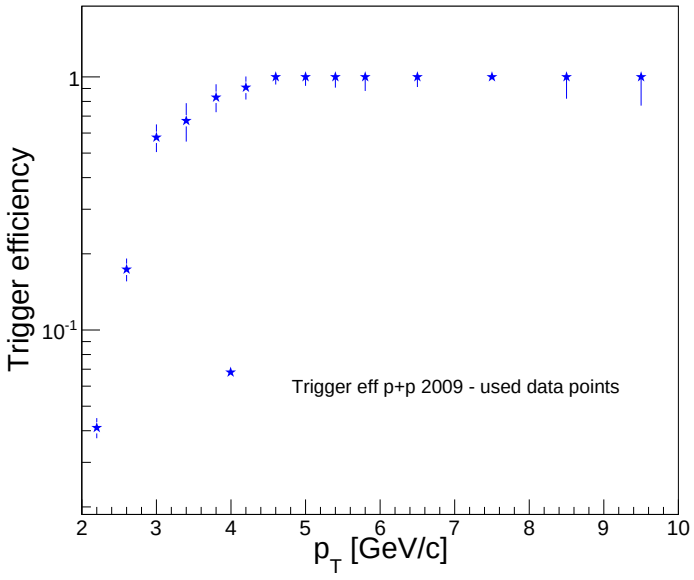

Figure 62: Final trigger efficiency.

$$\text{NPE} = \text{Inclusive} * \text{Purity} - \frac{\text{PHE}}{\epsilon_{\text{PHErec}}}, \tag{14}$$

where *Inclusive* stands for all reconstructed electron candidates, *Purity* is a quantification of the hadron contamination of the electron sample, PHE denotes photonic electrons as a main background of the analysis, ϵ_{PHErec} is the photonic electron reconstruction efficiency, and NPE denotes raw non-photonic electrons spectrum. The spectrum needs to be subsequently corrected for tracking and electron identification efficiency. At first, electron candidates must be identified. Electron identification was done using information from TPC and TOF for low-p_T, and from TPC with BEMC for high-p_T region. Purity of inclusive electron sample was calculated from constraint multi-Gaussian fit to the spectrum of the particle ionization loss in TPC (further n$\sigma_{electron}$ spectrum). Inclusive electron spectrum consists of both non-photonic electrons and photonic electron background. The main background consists of gamma conversion electrons and Dalitz decay of π^0 and η mesons was reconstructed statistically using small invariant mass cut (M_{ee} <0.24 GeV/c^2) into electron-positron spectrum.

Due to detector acceptance and tracking efficiency the spectrum must be corrected by factor ϵ_{PHErec}. Correction factor was calculated using simulated photons

embedded into real events. After these steps raw NPE spectrum was obtained, according to Eq. 14. Finally NPE spectrum was corrected for single electron identification efficiency and tracking efficiency. As a last step, secondary background was subtracted. The main part of the secondary background comes from J/ψ decay to electron-positron pairs. Analysis scheme is illustrated in Fig. 63.

6.5 Event and track selection

Events that satisfied primary vertex location cut |zvtx| < 30cm from the detector mid-point were used. In high-p_T part of this analysis HT trigger information is required as well, only events with high energy (above the given threshold) deposited in at least one BEMC tower are accepted. Additional criterium for high-p_T events requires more than 1 fired strip in phi plane and pseudorapidity direction in Shower Maximum Detector, BSMD($|\phi| > 1$) and BSMD($|\eta| > 1$). As was discusses in previous Chapter the SMD provides high spatial resolution and it is necessary for electron identification. For low-p_T only events with TOF information were accepted. Another criterium was psedorapidity cut which accepted only tracks with $|\eta| < 0.7$.

The main criterium for the track quality selection is the number of hits reconstructed in the TPC readout system. If only few hits are associated with a track, they may give an arbitrary result. Only tracks with more then 20 points in TPC and tracks that have at least 52% of the maximum TPC points were accepted. The requirement for 52% of maximum possible number of hit points in TPC removes split tracks. Since NPE come from the primary vertex, the cut for the distance of the closest approach (DCA) was applied as gDCA< 1.5 cm. It removes a portion of photonic electrons. For further reduction of the contribution from conversion electrons, radial distance between the beam pipe and the first point of the track in TPC was required, to fulfill $R_{TPC} < 73$ cm.

During the Run 2009 only 72% of TOF was installed. Figure 64 shows the TOF efficiency as a function of pseudorapidity and ϕ.

Due to thee ϕ and η dependence on efficiency, additional cuts were applied in regions with the lowest efficiency. In the pseudorapidity region $-0.7 < \eta < 0.2$ tracks with $-123^\circ < \phi < -63^\circ$ were rejected. The missing region was corrected via simulation.

Finally, cut to number of fit points in dE/dx was applied (ndE/dx >10). It is number of points from TPC used for dE/dx calculation, this cut improves the

dE/dx resolution. All track cuts are listed in Tab 2.

0 <flag< 1000
nHitPoints> 20
nHitPoints/nMaxPoints> 0.51
ndE/dx>10
gDCA< 1.5 cm
$\eta < 0.7$
ndE/dx>10
$\text{TPC}^{\text{1stpoint}}$ <73 cm

Table 2: Track quality cuts used in p+p NPE analysis.

6.6 Inclusive electron identification

For electron identification the information from TPC, TOF, and BEMC were used. At low-p_T region combined information from TOF and TPC was used, and at high-p_T region tracks coming from TPC and BEMC were employed.

Electrons throughout the full p_T-range were identified by the mass-dependent ionization energy loss dE/dx that is measured in the TPC detector. Electrons with $-1 < n\sigma_{electron} < 3$ were accepted. The $n\sigma_{electron}$ variable is define as

$$n\sigma_e = ln\left(\frac{dE/dx_{\text{measured}}}{dE/dx_{\text{BetheBloch}}}\right)/\sigma, \tag{15}$$

where dE/dx_{measured} is a measured ionization loss, $dE/dx_{\text{BetheBloch}}$ is a theoretical ionization loss of the electron obtained from Bichsel function, and σ is the error associated with dE/dx measurement. For the STAR TPC detector $\sigma = 0.075$ [76]. The dE/dx distribution as a function of p_T is plotted in Fig. 66 (left).

As shown in Figure 66 (left), the separation of charged hadrons (pions, kaons, protons) and electrons using only information from the TPC is very complicated at low p_T region. Kaon and proton distributions intersect the electron distribution at $p_T \sim 0.5$ GeV/c and $p_T \sim 1$ GeV/c, respectively. Great improvement of elecron identification capability is acquired when the data from TPC and TOF are combined together. Figure 65 shows velocity distibution of electrons, pions, kaons, and protons measured by TOF detector. Improvement after combining information from TPC and TOF is illustrated in Fig. 66, where at the left plot is

$p_T < 2$GeV/c	$p_T > 2$GeV/c
-1< $n\sigma_{electron}$ < 3	-1< $n\sigma_{electron}$ < 3
-	0<p/E<2 cm
-	|bsmdedz| <3 cm
-	|bsmdedphi| <0.06 cm
-	|bsmdpdz| <15 cm
-	|bsmdpdphi| <0.02 cm
-	|btowdz| <10 cm
-	|btowdphi| <0.05 cm
$\|1/(1 - /beta)\| < 0.03$	-

Table 3: List of electron identification cuts.

dE/dx distribution without any additional TOF cut and at the right plot is dE/dx distribution after the TOF cut application. Therefore at low-p_T region the TOF cut $|1/(1-\beta)| < 0.03$ was applied.

For high-p_T electrons identification, information from Barrel Electromagnetic Calorimeter was used to reduce hadron contamination in the inclusive electron sample. In the BEMC, particles deposit specific amount of their kinetic energy depending on the particle species. Electrons deposit almost all their energy via electro-magnetic showers. Therefore, considering the ultra-relativistic state of electrons, the momentum-to-energy ratio must be approximately equal to one. The tracks with momentum-to-energy ratio from 0 to 2 were accepted. Additional BEMC cuts are the following: BSMD and BTOW cluster cuts: bsmdpdz, bsmdpdphi, bsmdedz, bsmdephi, btowdz, and btowdhi, where dz and $dphi$ denote pseudorapidity and azimuthal directions. Values of these cuts were established from photonic electrons unlike-sign (electron-positron pair) minus like-sign (electron-electron or positron-positron pair) distributions for different p_T bins. Figures 67 - 70 show clusters distribution for each p_T bin, solid line denotes used cut. All electron identification cuts are listed in Tab 3.

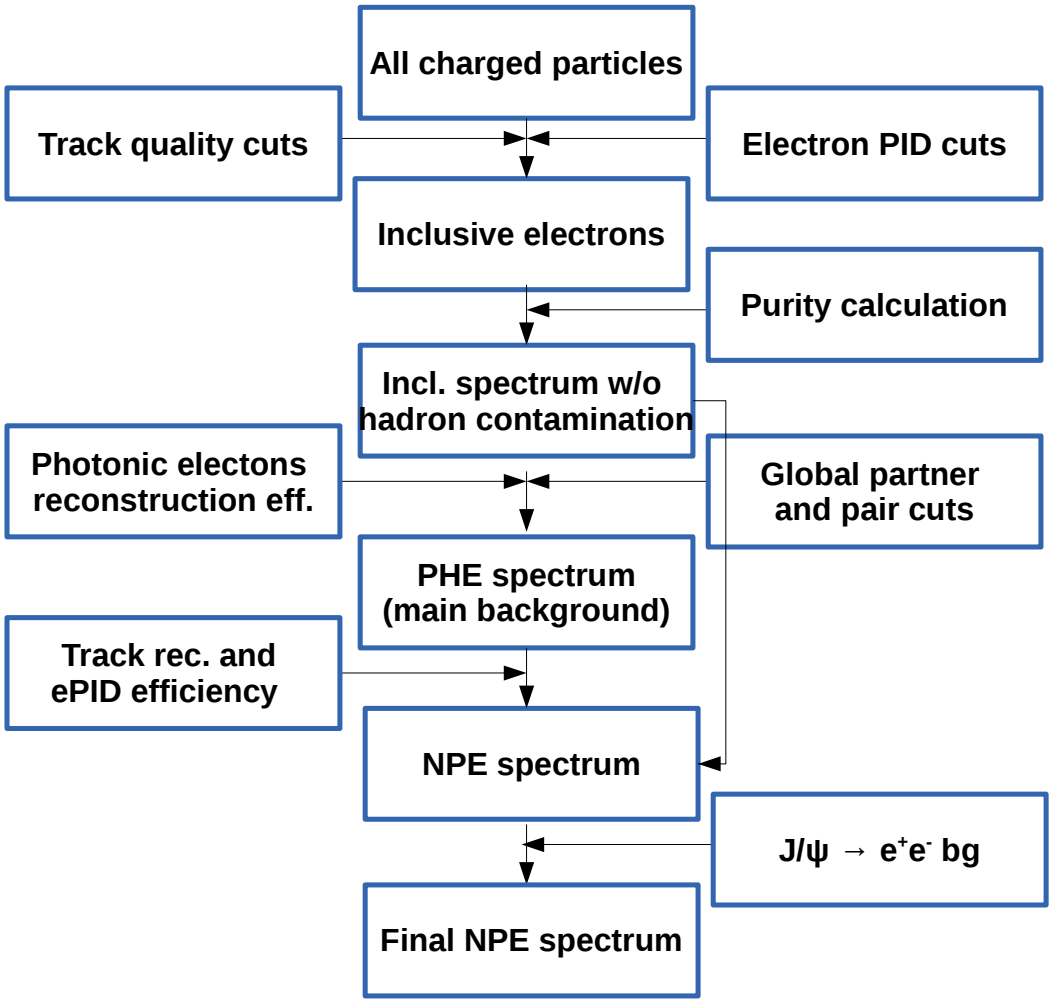

Figure 63: Scheme of the analysis principle.

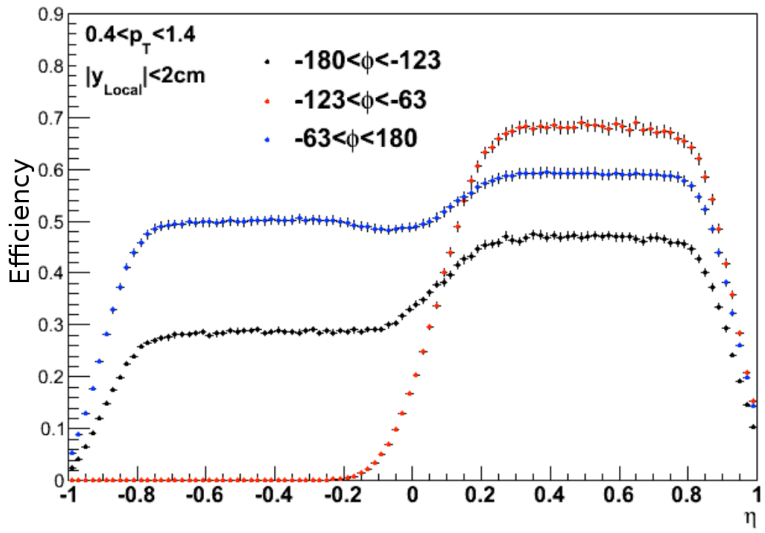

Figure 64: Particle reconstruction efficiency of the TOF detector as a function of η and ϕ range.

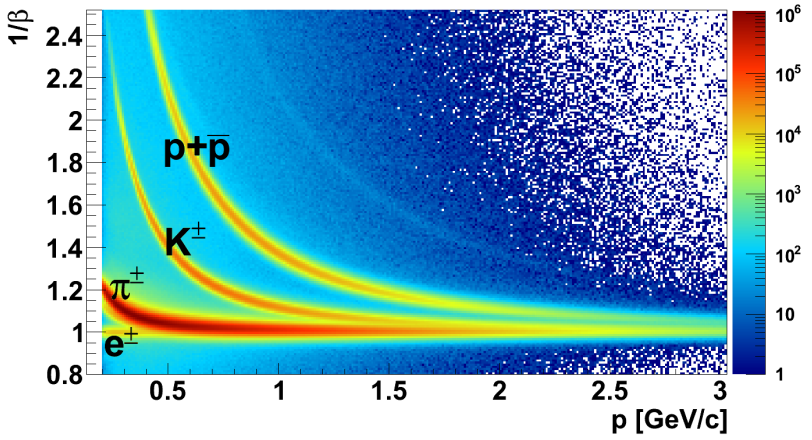

Figure 65: $1/\beta$ of electrons, pions, kaons, and protons measured by TOF. Using TOF information it is possible to distinguished electrons from kaons and protons.

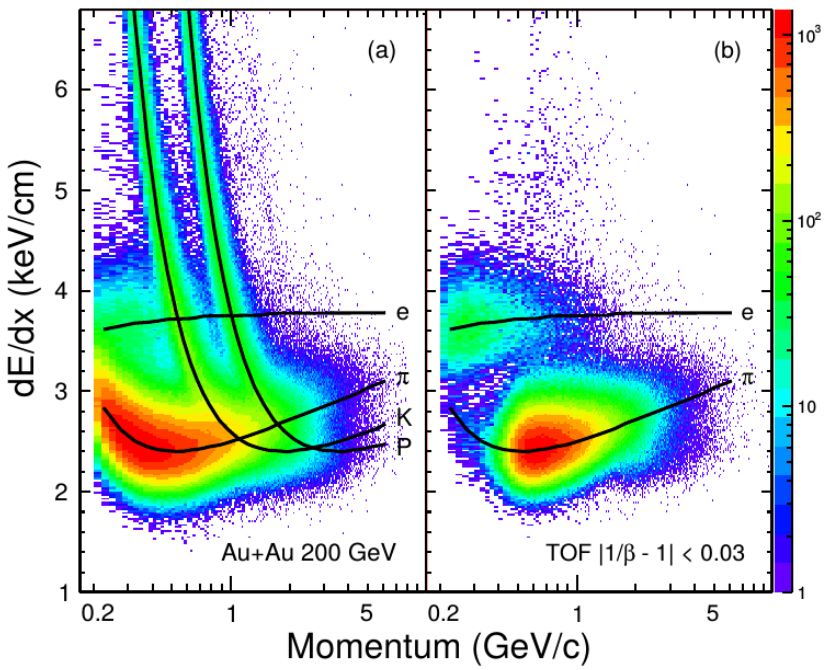

Figure 66: Energy loss distribution without TOF cut apply (left), and after TOF cut use (right). Combined TPC and TOF information allows to distinguished electrons from hadrons at low p_T region.

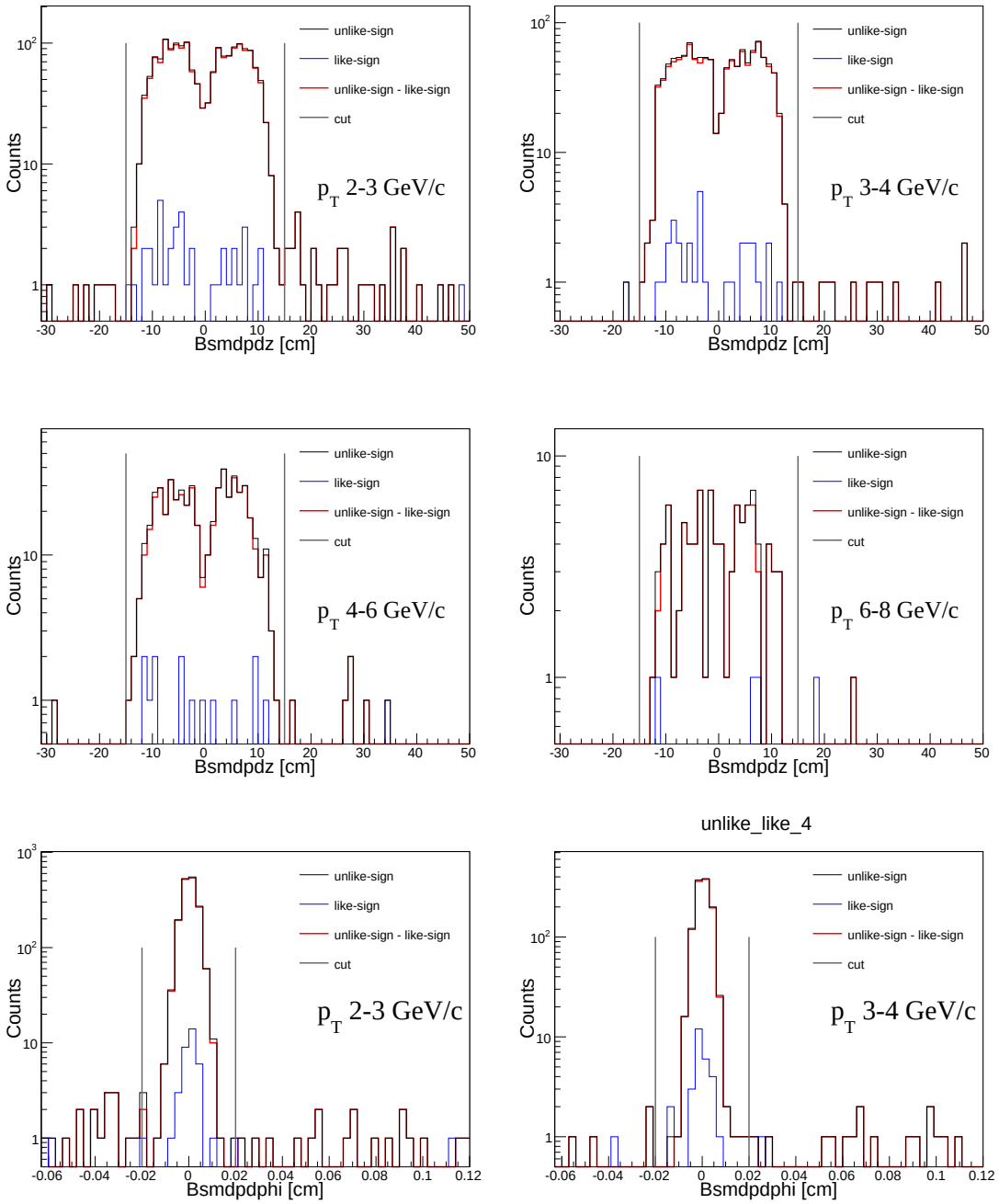

Figure 67: Photonic electrons BEMC bsmdpdz and bsmdpdphi distributions for different p_T bins. Black line denotes unlike-sign distribution, blue line denotes like-sign distribution and red line unlike-sign minus like-sing.

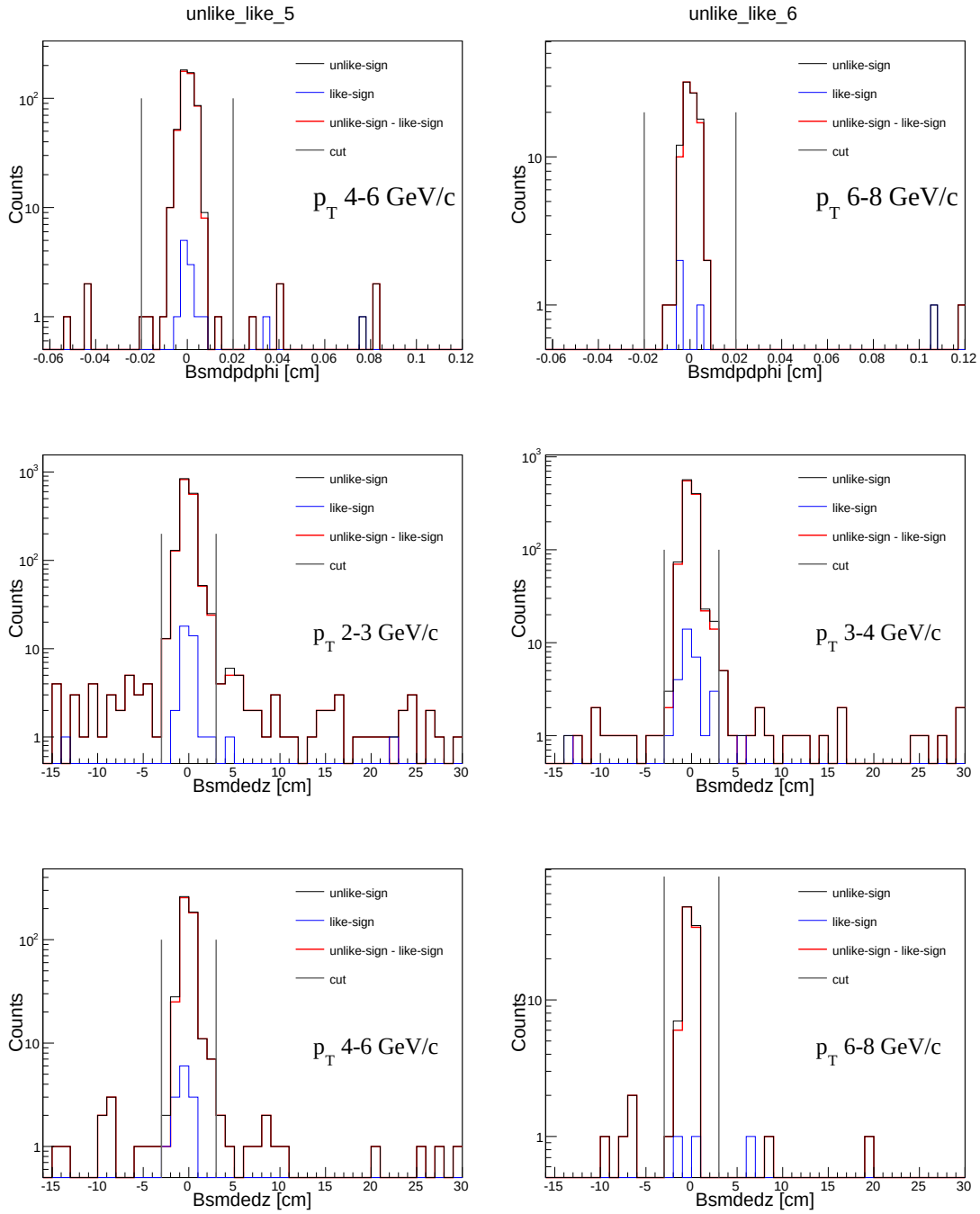

Figure 68: Photonic electrons BEMC bsmdpdphi and bsmdedz distributions for different p_T bins. Black line denotes unlike-sign distribution, blue line denotes like-sign distribution and red line unlike-sign minus like-sing.

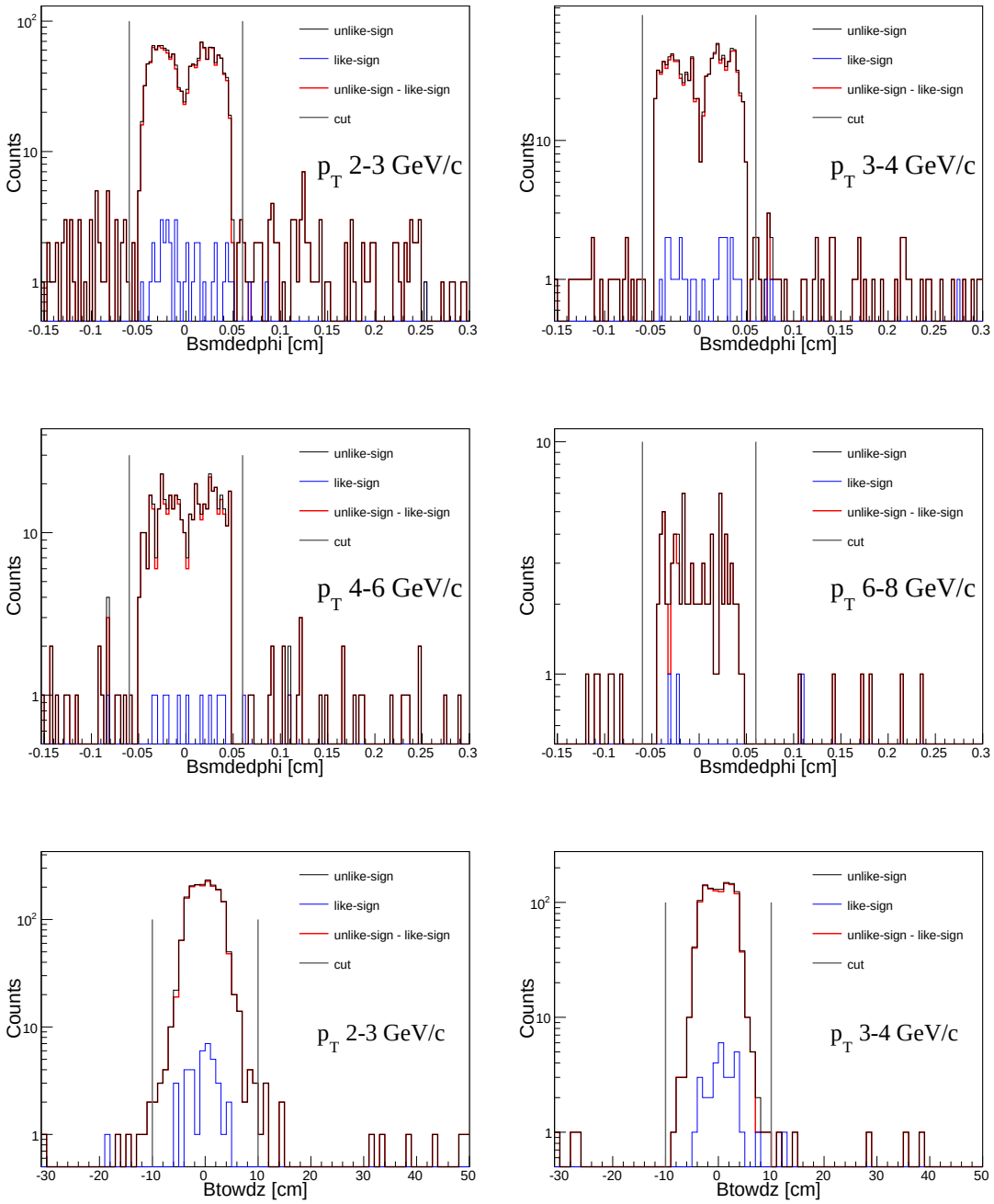

Figure 69: Photonic electrons BEMC bsmdedphi and btowdz distributions for different p_T bins. Black line denotes unlike-sign distribution, blue line denotes like-sign distribution and red line unlike-sign minus like-sing.

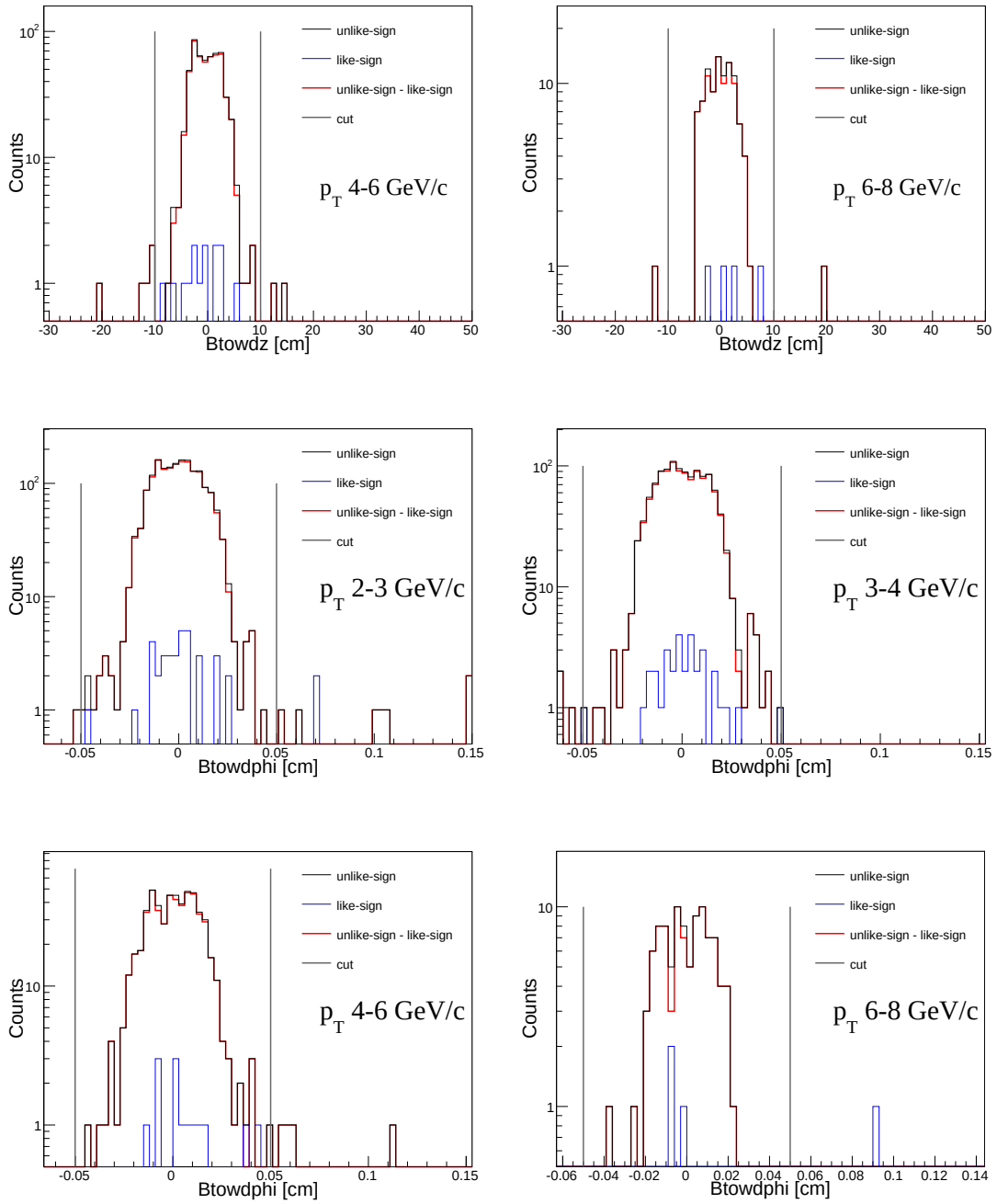

Figure 70: Photonic electrons BEMC btowdz and btowdphi distributions for different p_T bins. Black line denotes unlike-sign distribution, blue line denotes like-sign distribution and red line unlike-sign minus like-sing.

6.7 Photonic electron background reconstruction

The dominant background in non-photonic electron analysis comes from photonic electrons. Photonic electrons come mainly from the 2-body γ conversion $\gamma \rightarrow e^+ + e^-$ and 3-body Dalitz decay of $\pi^0 \rightarrow \gamma + e^+ + e^-$ and $\eta \rightarrow \gamma + e^+ + e^-$. They can be reconstructed statistically as a low-mass peak in the unlike-sign minus like-sign di-electron invariant mass spectrum as is shown in Fig. 71. In the STAR detector all tracks are calculated with the assumption that they originate in a primary vertex. Therefore the primary vertex is a part of the track. Taking into consideration the fact that conversion electrons mostly takes place in detector materials, the primary track momentum of photonic electrons should be biased. Due to this the global track, which is not including the primary vertex as a part of trajectory, was used for photonic electron reconstruction.

For each primary electron candidate satisfying track quality cuts and electron identification cuts listed in Tab. 2 and Tab. 3 was searched for opposite charged global partner which satisfied requested partner cuts. Cuts for partner are p_T >0.3 GeV/c, and $3 < dE/dx < 5$ keV/cm and track quality cuts. Global partner cuts are based only on TPC information, there are no BEMC and TOF cuts for partner tracks. For photonic electron identification the additional pair cuts were applied: di-electron invariant $M_{ee} > 0.24$ GeV/c^2 and pairDCA<1cm, where pairDCA means distance of the closest approach between helices of the electron and positron candidates.

6.8 Photonic electron reconstruction efficiency

Due to the finite TPC acceptance, some of the photonic electrons cannot be reconstructed. Therefore the photonic electron reconstruction efficiency must be calculated. The efficiency was obtained using full GEANT simulation of gamma-to-electrons decay embedded into real events. Such enriched events are analyzed the same way as real data, the cuts used for primary and global partner are the same as in proper analysis. Simulated gamma particles have flat p_T distribution and therefore the p_T distribution must be weighted. As function for this p_T weighting was used fit to the direct photon production measured by PHENIX [78]. In Fig. 72 the invariant cross-section of direct photons in p+p collisions at $\sqrt{s}$=200 GeV is shown. The curves on the p+p data represents pQCD calculation (solid line) and a modified power-low fits [78].

The PHE reconstruction efficiency is defined as a ratio of found embedded photonic electrons over all embedded photonic electrons in which at least one electron of the pair was detected in TPC. The PHE reconstruction efficiency as a function of p_T is shown in Fig. 73. Systematic uncentainty of PHE reconstruction efficiency was estimated as 5% and will be discuss in detail in Chapter 8.

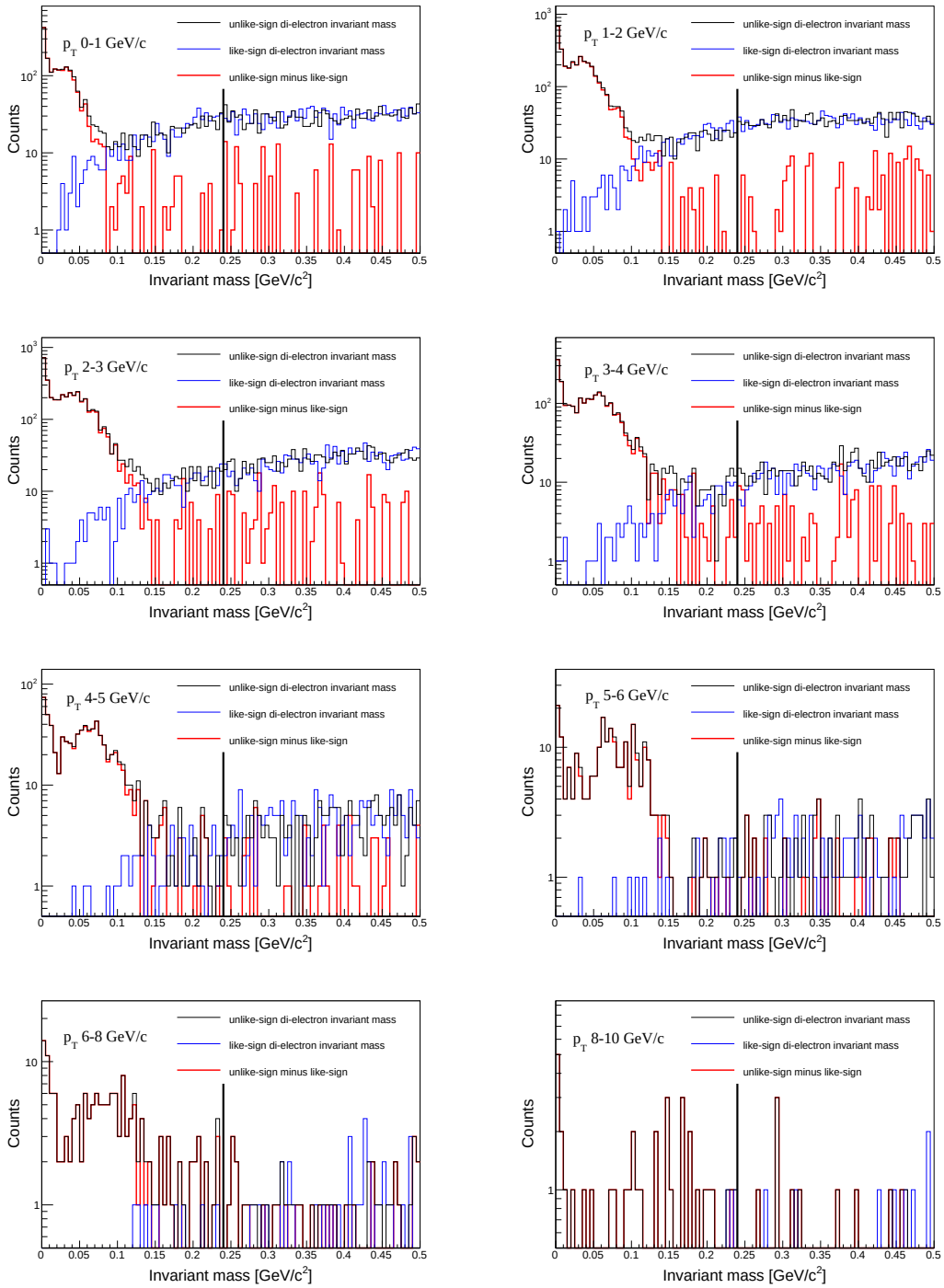

Figure 71: Dielectron invariant mass for different primary electron p_T bins. Black line is the unlike-sign distribution, blue line is the like-sign distribution and red line is the unlike-sign minus like-sign. Black straight line referents used cut.

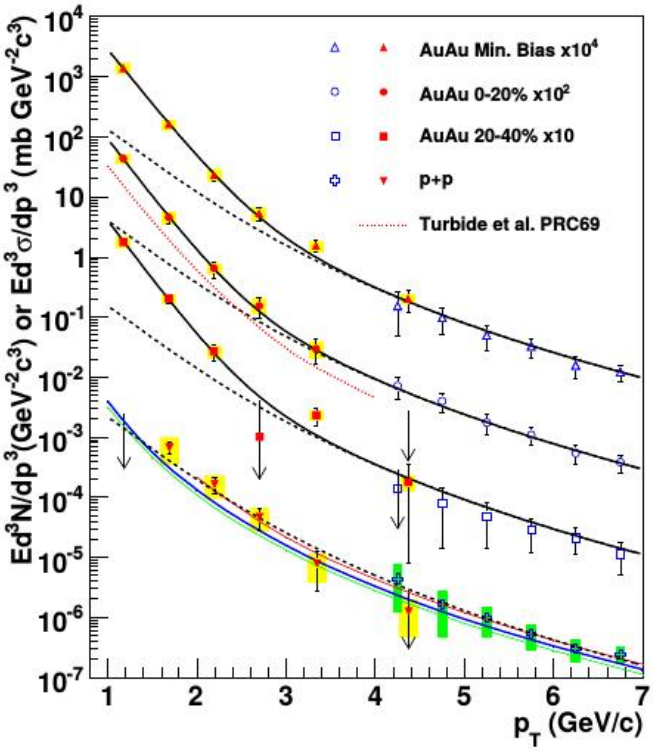

Figure 72: The invariant cross-section of direct photons in p+p collisions at $\sqrt{s}$=200 GeV. The solid line represents pQCD calculation and a dashed lines modified power-low fits [78].

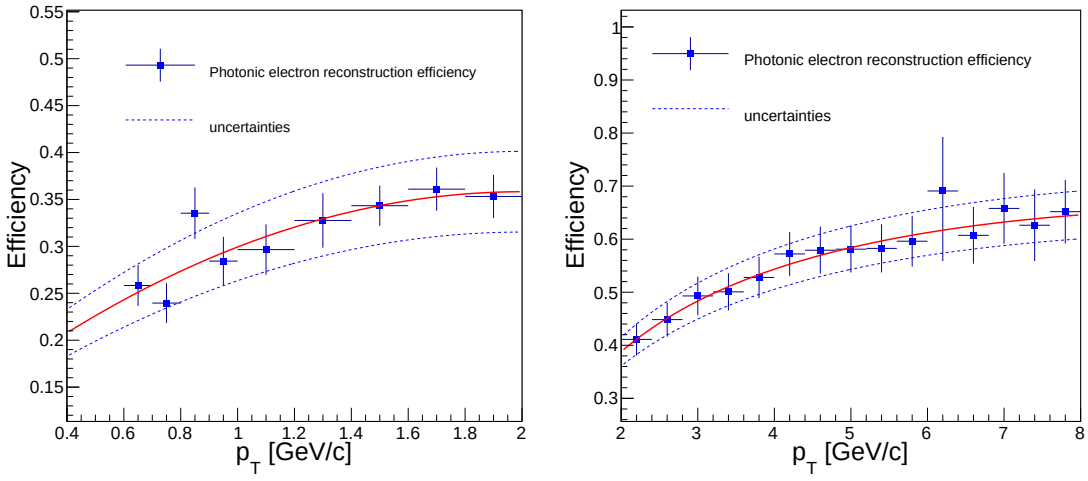

Figure 73: Photonic electron reconstruction efficiency for low-p_T (left) and high-p_T electrons. Blue dashed lines show systematic uncertainties.

6.9 Purity of inclusive electron sample

After the application of all electron identification cuts there were still non-negligible hadron contamination of the electron candidates sample. Therefore, it was necessary to calculate purity of the sample. Purity is changing with p_T and therefore it must be calculated for each p_T-bin separately. Purity of inclusive electron sample was estimated from constraint multi-Gaussian fit to the n$\sigma_{electron}$ distributions. Single Gaussians in the fit represent different particle species and they are summed together to the final multi-Gaussian fit. Constraints for electrons mean and width were estimated from single Gaussian fit to the nσ_electron distribution of the primary electron from the photonic electron pair. The electron mean was estimated as mean of the Gaussian fit and its one standard deviation was taken as electron distribution width. The photonic electron n$\sigma_{electron}$ distribution was obtained statistically as di-electron unlike-sign minus like-sign distribution. It is obtained in the same way as the invariant mass spectrum (see Chapter 6.7). Photonic electrons n$\sigma_{electron}$ distributions are plotted in Fig. 74 - 76. Electron mean and width as a function of p_T are plotted in Fig. 77, the uncertainties of the distributions were estimated by varying constrains in Gaussian fits.

Hadron constraints to multi-Gaussian fit were estimated using theoretical Bischel function allowing varying in parameter. In Fig. 97 - Fig. 81 there are multi-Gaussian fit for different p_T bins, where red line denotes electrons, blue line pions, magenta line protons, and turquoise line kaons. For each p_T bin purity was calculated as a ratio of integral bellow electron fit in the area defined by n$\sigma_{electron}$ cut ($-1 <$n$\sigma_{electron} < 3$) over the interval bellow total multi-Gaussian fit in the same range.

Systematic errors were obtained by variation of the electron fit parameters by one standard deviation and are discussed in detail in Chapter 8. Final purity plots for low-p_T and high-p_T electron sample separately are shown in Fig. 82. The huge difference between low-p_T plot and high-p_T plot at $p_T = 2$ GeV/c comes from the different set of cuts used for low-p_T and high-p_T region.

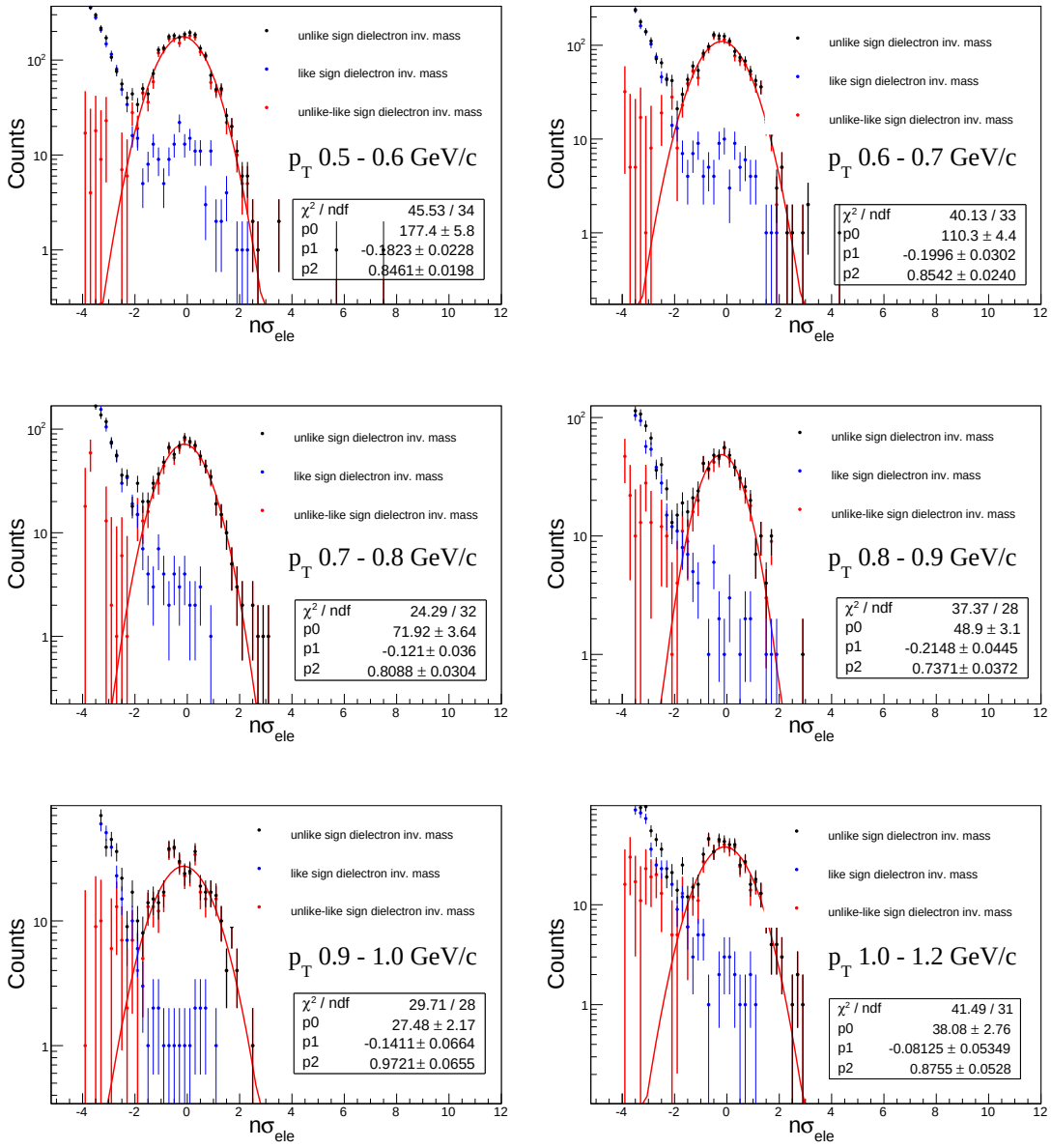

Figure 74: The Gaussian fit to the photonic n$\sigma_{electron}$ distribution for diferent p_T bins.

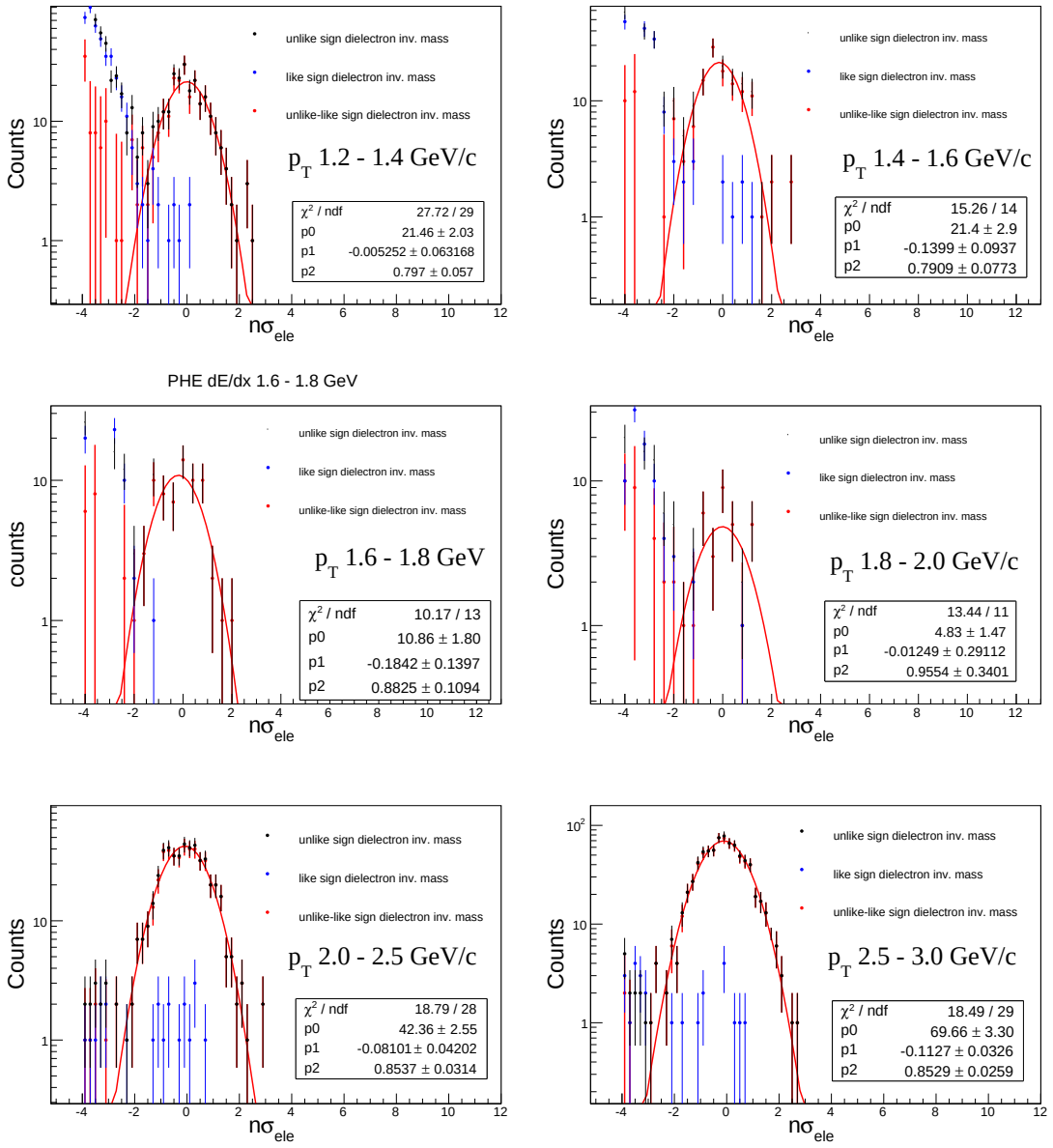

Figure 75: The Gaussian fit to the photonic n$\sigma_{electron}$ distribution for diferent p_T bins.

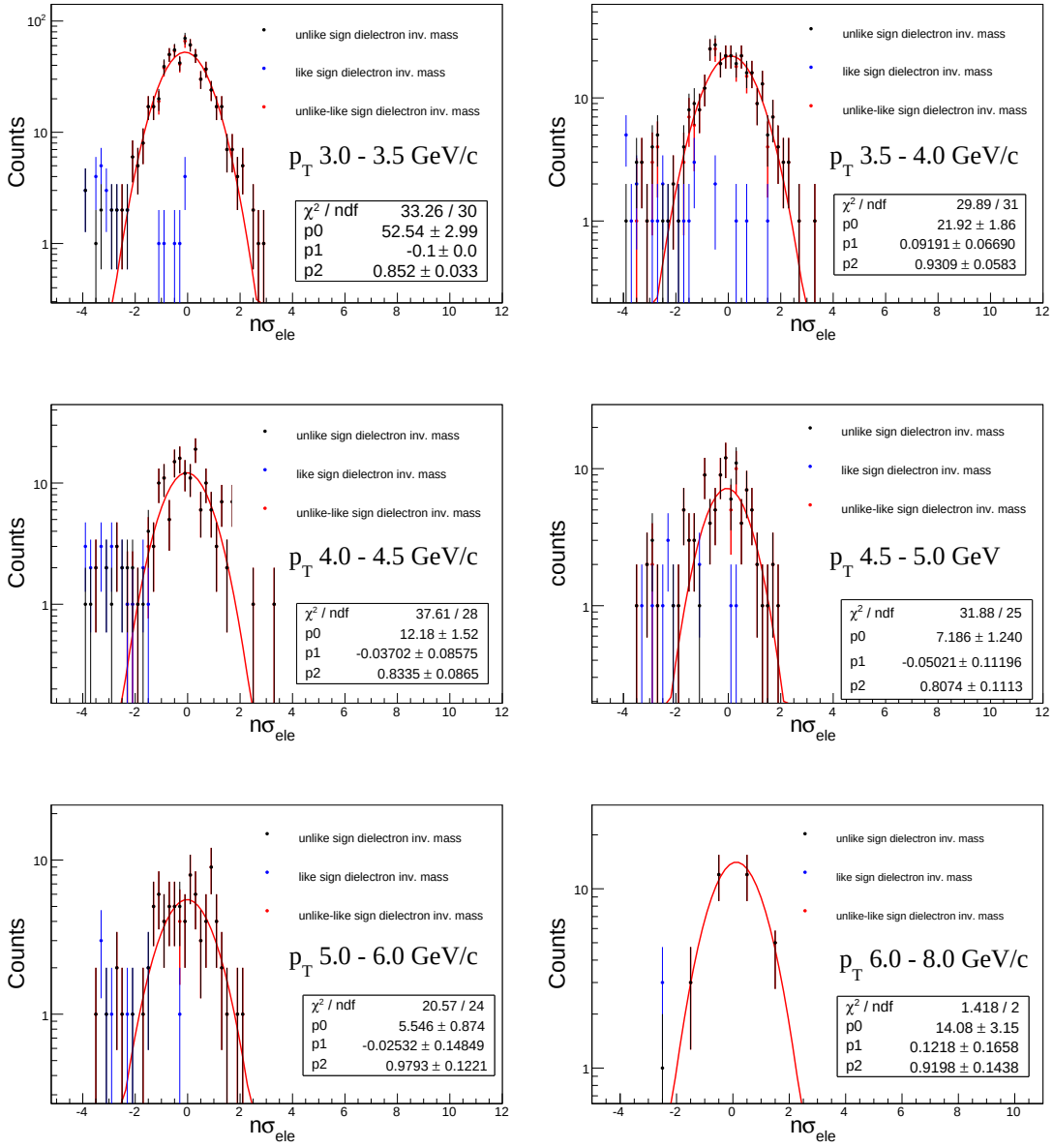

Figure 76: The Gaussian fit to the photonic n$\sigma_{electron}$ distribution for diferent p_T bins.

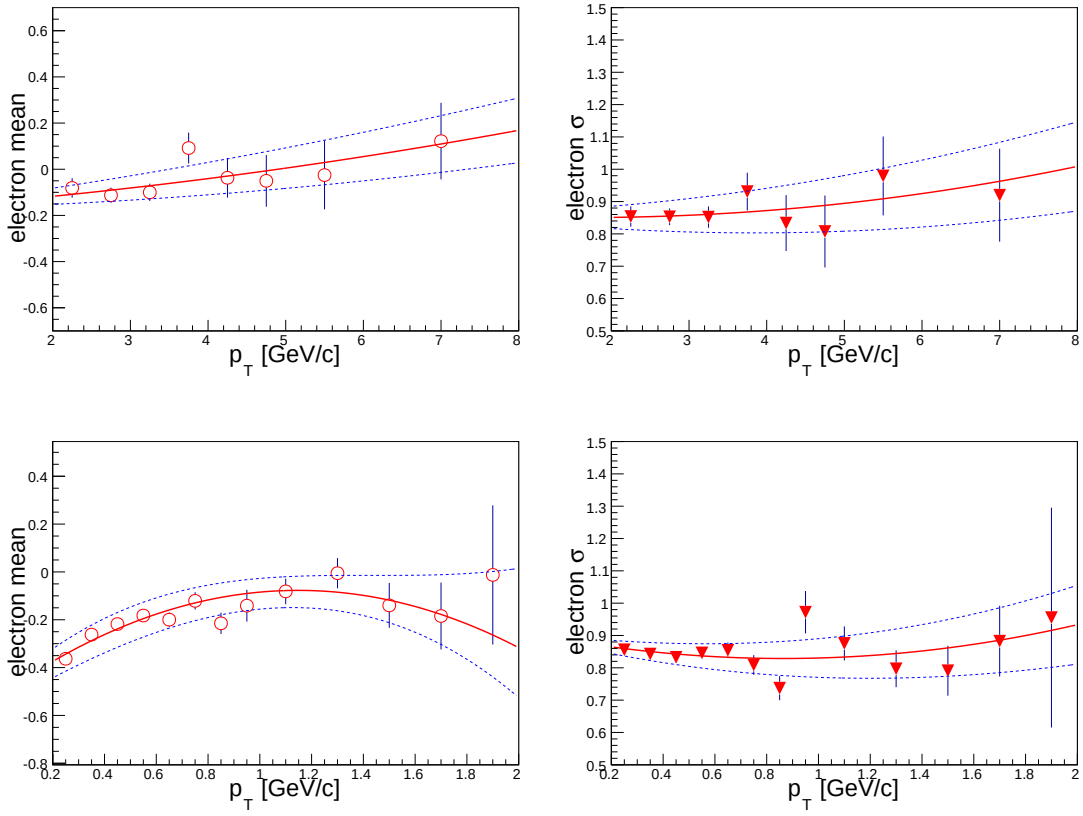

Figure 77: The electron mean (left) and width (right) as a function of p_T.

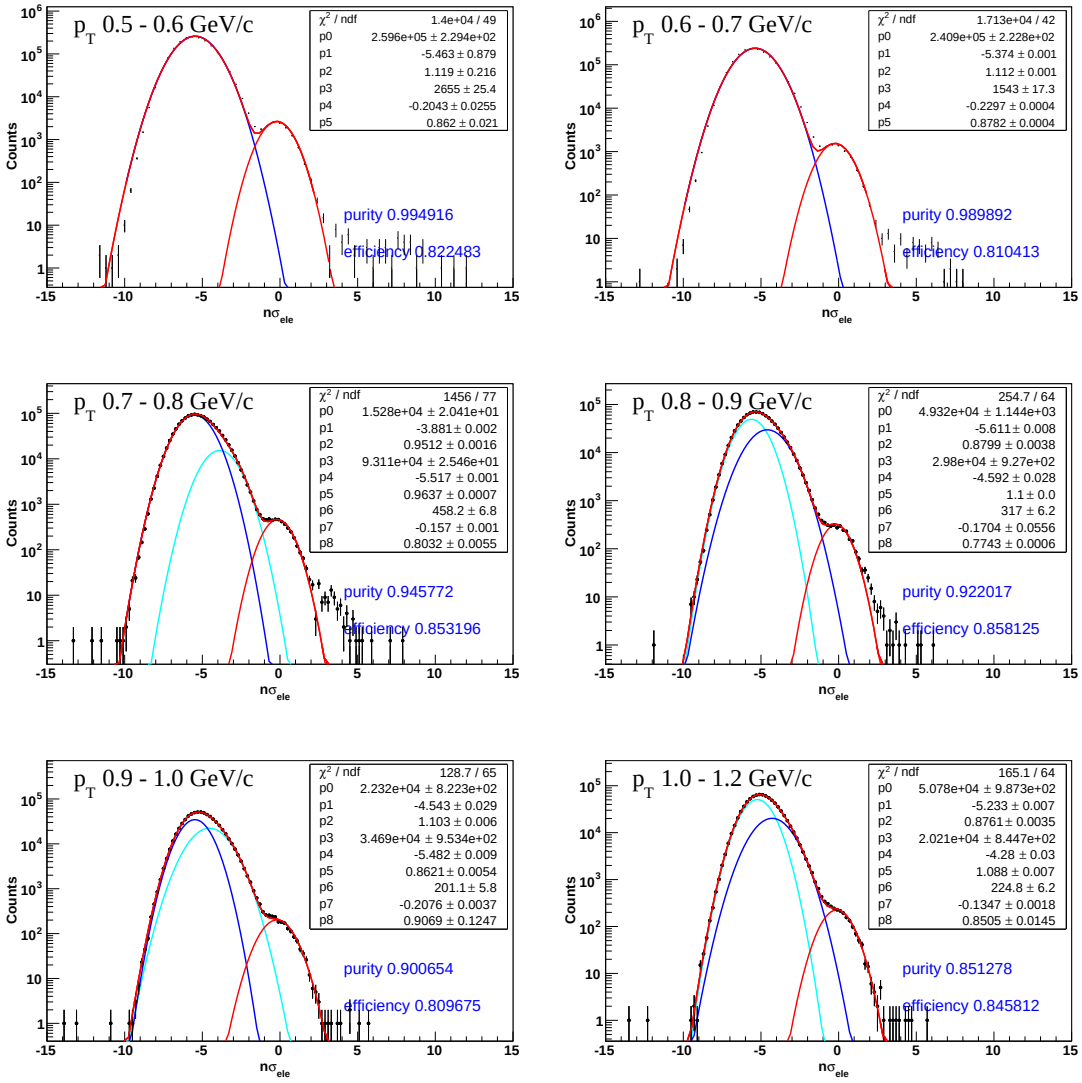

Figure 78: Multi-Gaussian fits to the n$\sigma_{electron}$ distribution of all charged particles which pass all track quality cuts and electron identification cuts except n$\sigma_{electron}$ one. Red, blue, magenta and turquoise lines denote electrons, pions, protons with kaons, and kaons respectively.

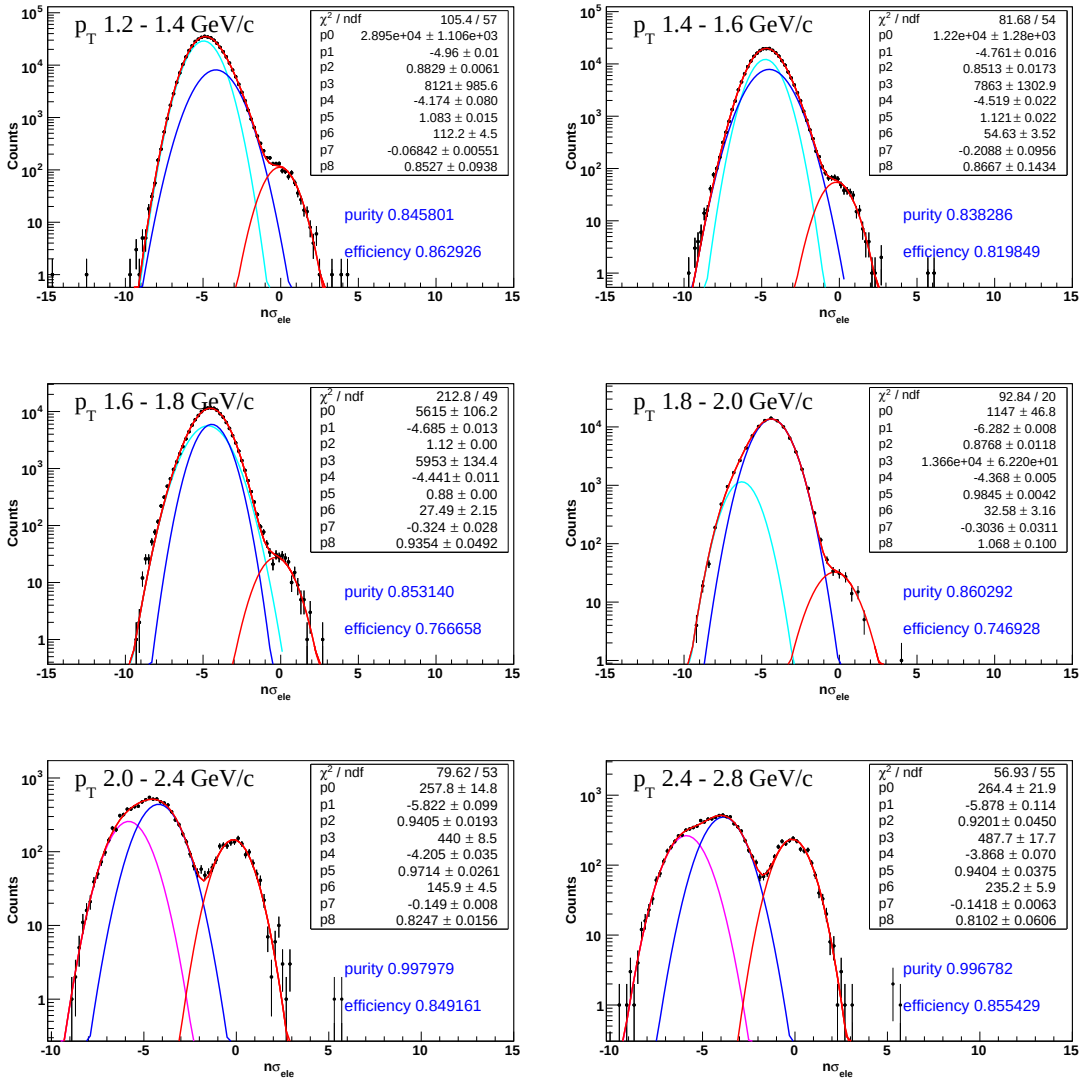

Figure 79: Multi-Gaussian fits to the n$\sigma_{electron}$ distribution of all charged particles which pass all track quality cuts and electron identification cuts except n$\sigma_{electron}$ one. Red, blue, magenta and turquoise lines denote electrons, pions, protons with kaons, and kaons respectively.

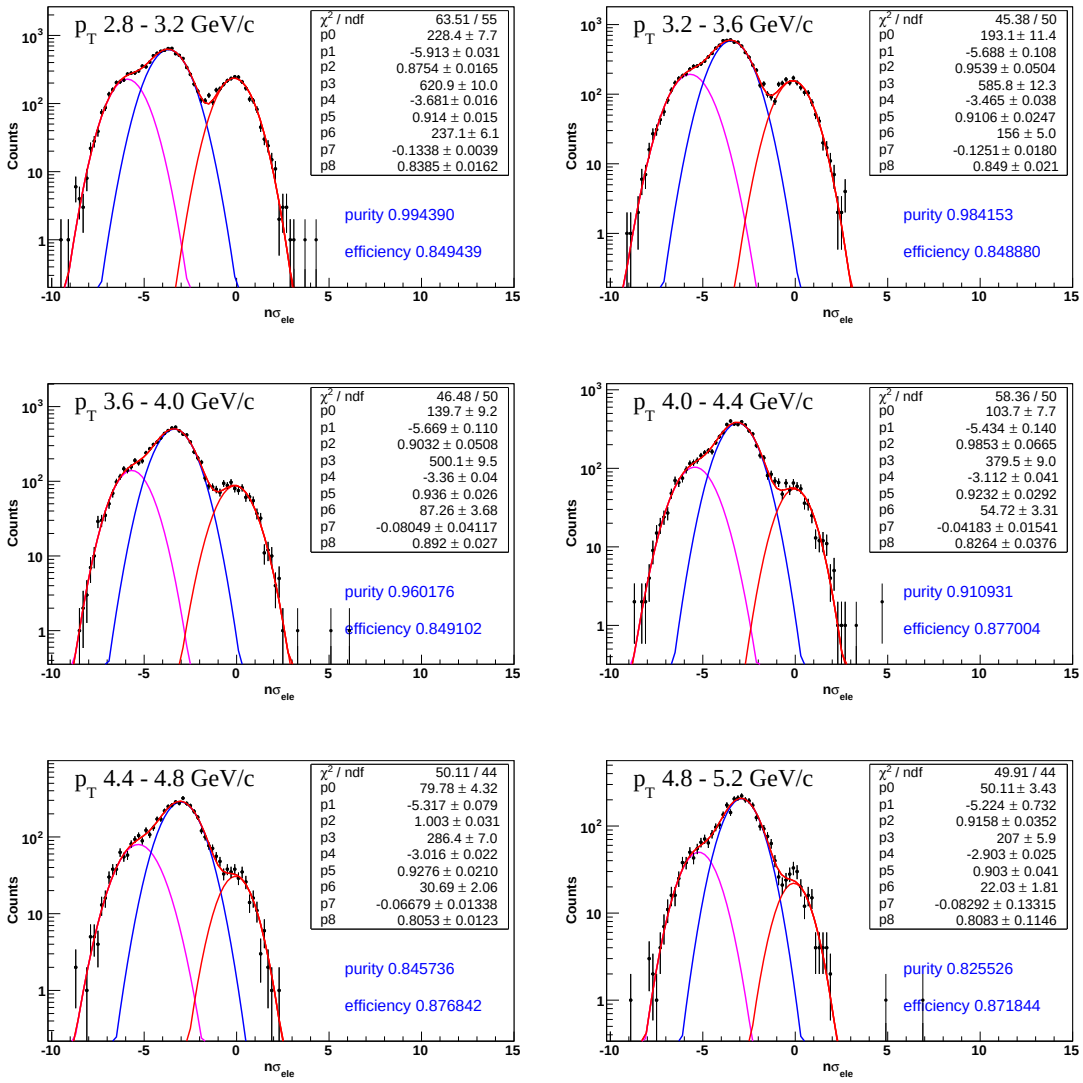

Figure 80: Multi-Gaussian fits to the n$\sigma_{electron}$ distribution of all charged particles which pass all track quality cuts and electron identification cuts except n$\sigma_{electron}$ one. Red, blue, magenta and turquoise lines denote electrons, pions, protons with kaons, and kaons respectively.

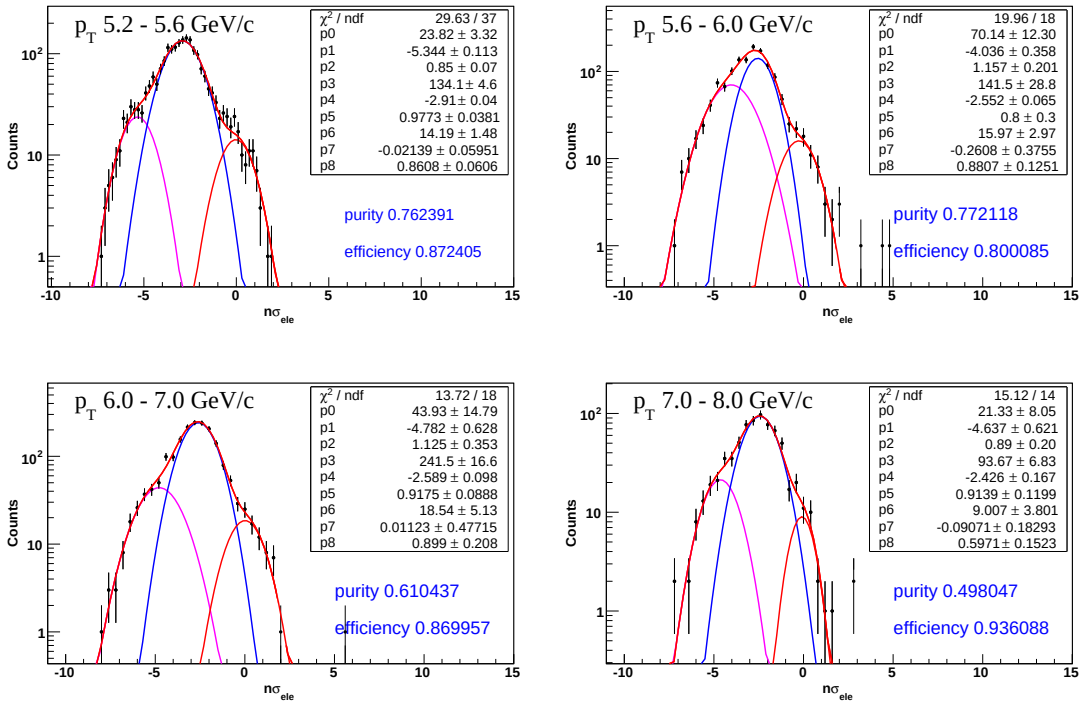

Figure 81: Multi-Gaussian fits to the n$\sigma_{electron}$ distribution of all charged particles which pass all track quality cuts and electron identification cuts except n$\sigma_{electron}$ one. Red, blue, magenta and turquoise lines denote electrons, pions, protons with kaons, and kaons respectively.

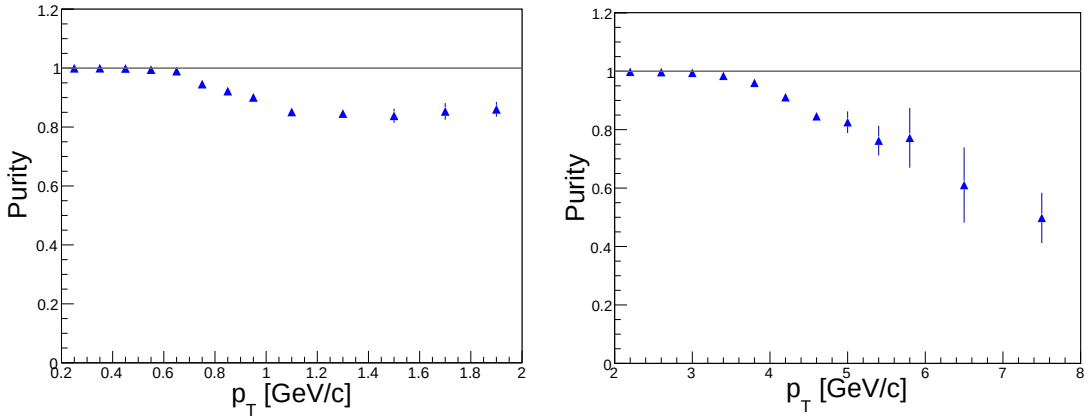

Figure 82: Final purity for low-p_T (left) and high-p_T (right) region. The difference between purities comes from different set of electron selection criteria.

6.10 Signal to background ratio

After calculation of hadron contamination in inclusive electron sample and reconstruction of photonic electron background it is possible to calculate the signal to background ratio. Figure 83 shows the S/B ratio as a function of p_T (red points), where signal stands for non-photonic electrons and background means photonic electrons. As the amount of photonic electrons decreases with p_T faster than the yield of non-photonic electrons the S/B ratio increases with p_T. The ratio needs to be further connected by subtraction of J/ψ contribution to the non-photonic electron yield. The S/B ratio is compared with same quantity measured in the previous STAR NPE measurement (blue points) [36]. Both measurements agree with each other in the corresponding p_T region.

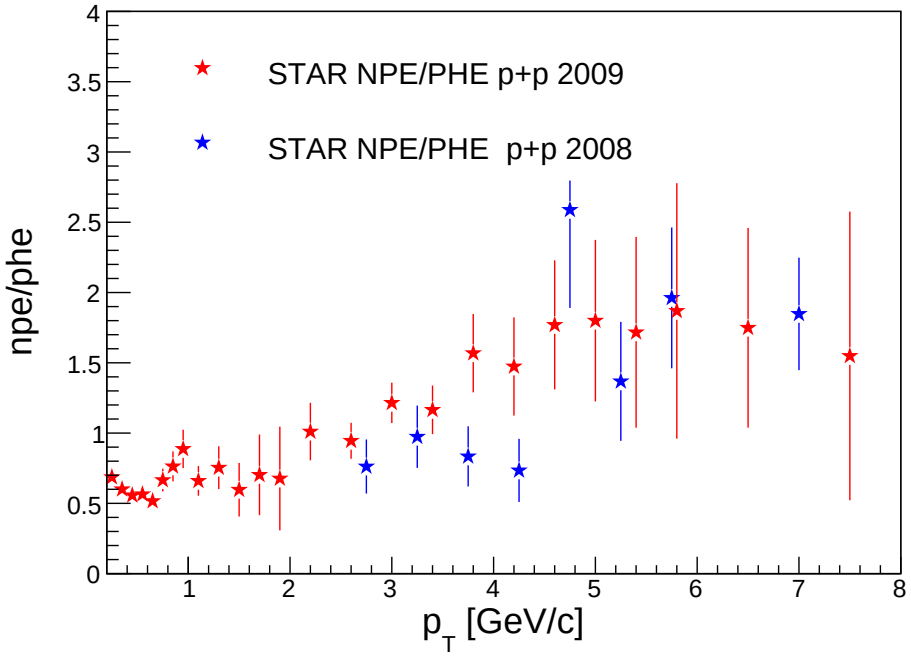

Figure 83: Non-photonic electrons yield over photonic electrons background ratio measured in p+p collisions at $\sqrt{s}$=200 GeV during the year 2009 (red), and during the year 2008 (blue).

6.11 Track reconstruction and electron identification efficiency

Next step of the NPE analysis was calculation of the track reconstruction efficiency and the electron identification efficiency. These were obtained partially using simulated electrons embeded into real events and partially from real data. In the simulation part full GEANT simulation of electrons and positrons embedded into real events was used. Such enriched events are analyzed the same way as real data. At first all distributions from simulated electrons (e.g. p/E distribution, number of fit points in TPC, BMSD cluster distributions) were checked. Examples of QA plots are shown in Fig. 84, where red line denotes real-data distribution and blue line denotes distribution from simulated electrons and positrons.

Simulation results were used for the tracking efficiency calculation and for estimation of BEMC PID cuts efficiency. TOF reconstruction efficiency was calculated from pp2pp data and was used track-by-track during inclusive electron reconstruction. Electron PID efficiency together with tracking efficiency from embedding is plotted in Fig. 85.

Efficiency of the n$\sigma_{electron}$ cut was quantified from the real data using the n$\sigma_{electron}$ distributions which were discussed in Chapter 6.9. Efficiency is taken as a ratio of the integral of electron Gaussian at the range of the n$\sigma_{electron}$ cut over the integral over the whole electron Gaussian (electron Gaussian is displayed as red line). The n$\sigma_{electron}$ cut efficiency as a function of p_T is shown in Fig. 86.

Finally after corrections for tracking and ePID the secondary background coming from decays of J/ψ was subtracted. The subtraction was based on Thomas Ullrich study [79]. The combined J/ψ data collected in p+p collissions at $\sqrt{s} = 200$ GeV from STAR [80] and PHENIX [81] were used. Data points were fit with the 5 parameter xzb-fun function [79] (Fig. 87). Tsallis fit with 3 parameters was use as well but it does not fit combined spectra well.

$$E\frac{d^3\sigma}{dp^3} = \frac{A}{(\exp^{-ap_T - bp_T^2 + \frac{p_T}{p_0}})^n}. \tag{16}$$

The upper and lower error bounds of the fit parametrization were used to evaluate the uncertainties as is shown in Fig. 109. The J/ψ contribution to the NPE spectrum ranging from 11.4 to 15.8 %.

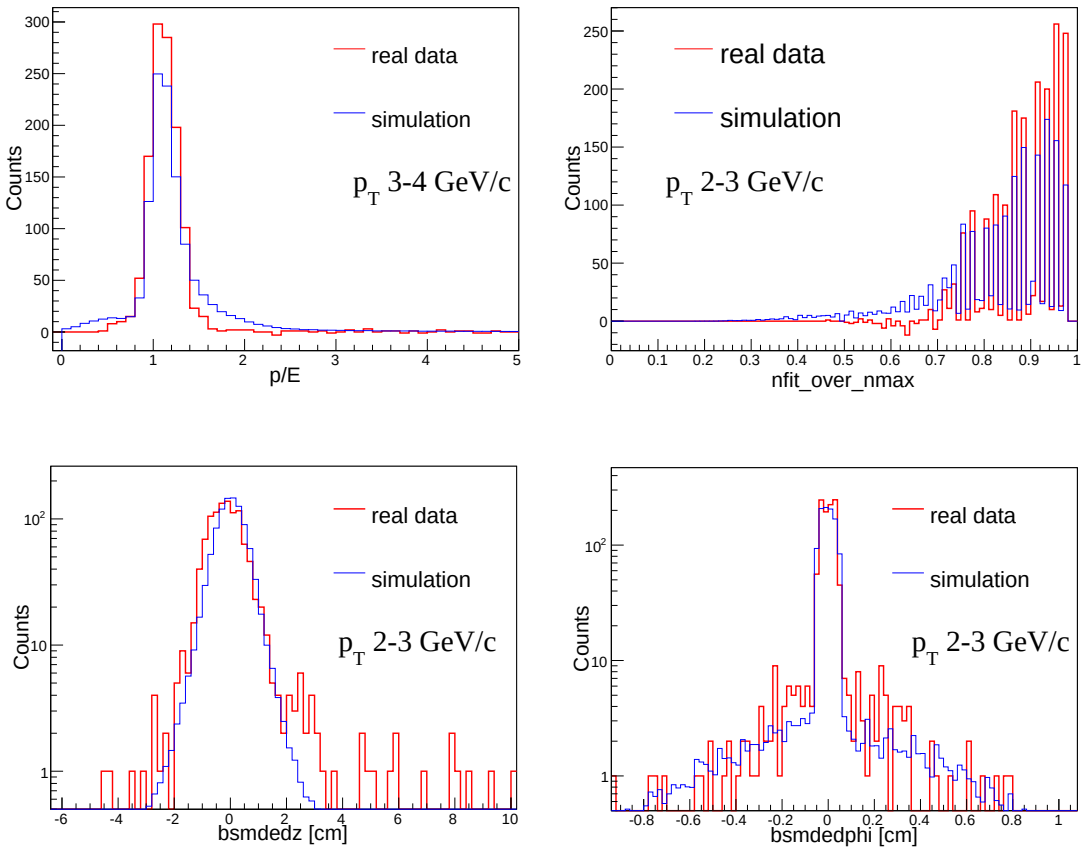

Figure 84: Examples of comparison between simulated and real events. Simulated events were used for efficiency calculation.

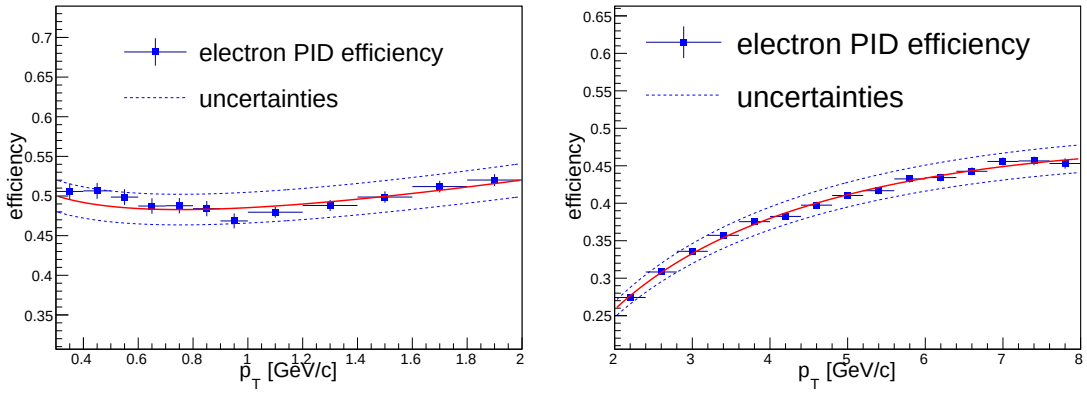

Figure 85: Tracking and electron reconstruction efficiency calculated from embedded data for low-p_T (left) and high-p_T electrons. Blue dashed lines show systematic uncertainty.

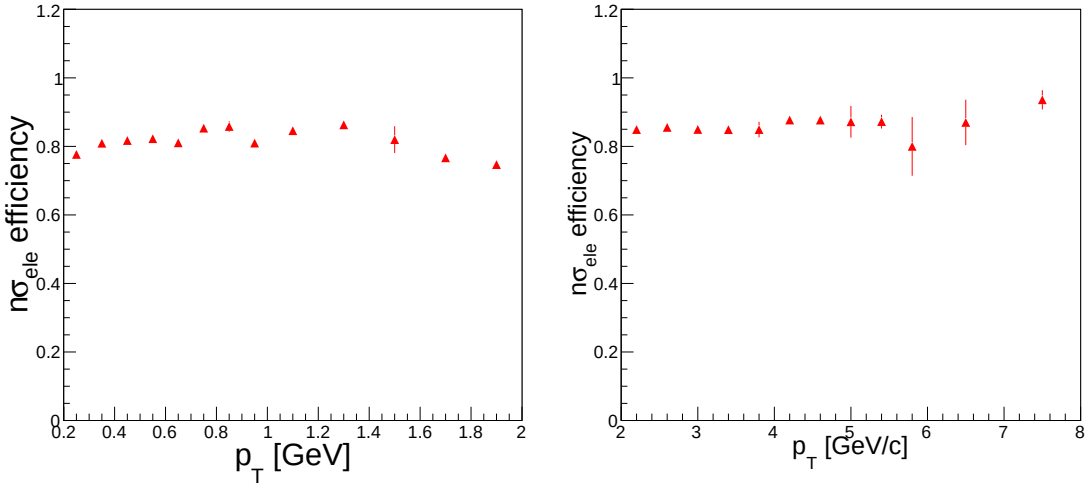

Figure 86: Efficiency of n$\sigma_{electron}$ cut calculated from real data for low-p_T (left) and high-p_T electrons.

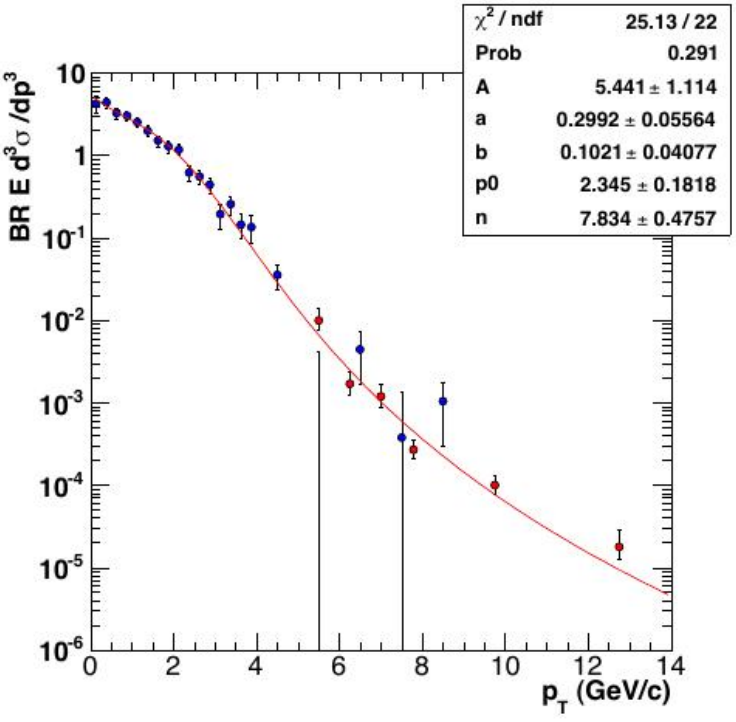

Figure 87: Xzb-fun function fit to the combined J/ψ spectrum. Data were collected in p+p collisions at $\sqrt{s} = 200$ GeV at STAR and PHENIX. Taken from Ref. [79].

6.12 Non-photonic electron yield in p+p collisions at $\sqrt{s}$=200 GeV

In this chapter, NPE yield obtained from non-photonic electron analysis in p+p collisions at $\sqrt{s}$=200 GeV using data taken during the year 2009 at the STAR experiment are presented. The invariant yield of non-photonic electrons was calculated as

$$\frac{B}{2\pi p_T}\frac{d^2N}{dp_T dy} = \frac{1}{2\pi p_T}\frac{1}{\Delta p_T}\frac{1}{\Delta y}\frac{N_{npe}}{N_{events}}\frac{1}{\epsilon_{total}}, \tag{17}$$

where N_{npe} is the raw yield of NPE, N_{events} is the number of events in used V_z cut, and ϵ_{total} is the product of TPC tracking efficiency, electron PID efficiency, and trigger efficiency (for $p_T > 2$ GeV/c), Δp_T is the p_T coverage, Δy pseudorapidity coverage. The TOF tracking efficiency (for $p_T < 2$ GeV/c) were applied track-by-track during electron spectra reconstruction. Figure 101 presents NPE yield as a function of p_T, where black marks show results obtained in presented analysis and blue points show former analysis results [36]. In comparison with the results from the year 2008 (pseudorapidity range $|\eta| < 0.5$), the p_T range was extended to the low p_T region. Green points represent data from PHENIX experiment (pseudorapidity range $|\eta| < 0.35$) [37]. Both results, PHENIX and the results hereby presented are consistent at full p_T range. Results are also compared with pQCD FONLL (Fixed Order plus Next-to-Leading Logarithms [30]) calculation, in plot is this theoretical prediction presented by blue solid line and its upper and lower uncertainties by black lines. Presented results are in good agreement with FONLL and lie between its central value and the upper limit.

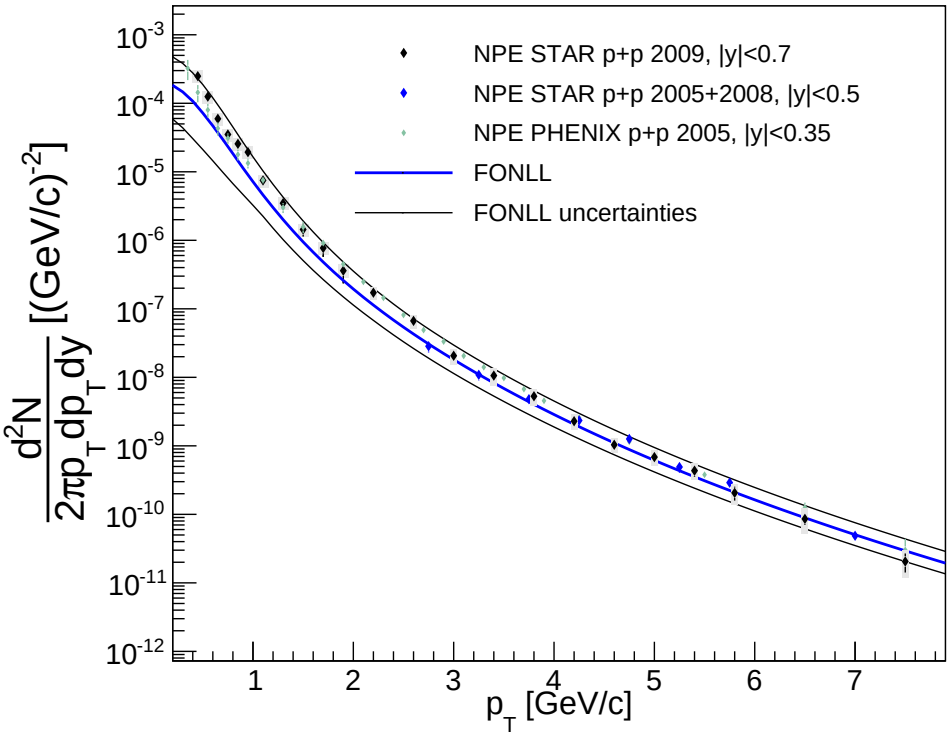

Figure 88: Non-photonic electrons yield measured in p+p collisions at $\sqrt{s}$=200 GeV using data taken during the years 2008 (blue) and 2009 (black, this thesis) compared with FONLL calculations [30] [36] [37].

7 Non-photonic electrons in d+Au colisions at $\sqrt{s_{NN}}$=200 GeV

In this chapter a non-photonic electron analysis in d+Au colisions at $\sqrt{s_{MM}}$=200 GeV is presented. Since the analysis' principle is same as in the case of p+p collisions, only the parts specific for the d+Au analysis are discussed.

7.1 Data

In this analysis data recorded in d+Au collisions at $\sqrt{s_{NN}}$=200 GeV during the year 2008 are used. Data were analyzed in high-p_T region (2-10 GeV/c) using four high tower triggers (HT0, HT1, HT2, HT4) with different energy thresholds and prescales. The transverse energy thresholds for these HT triggers are 2.64 GeV for HT0, 3.6 GeV for HT1, 4.3 GeV for HT2 and 8.4 GeV for HT4. Events which satisfied the HT trigger conditions are combined together, double counting was removed. The spectra for each HT trigger and the combined spectrum are defined as follows

$\mathrm{N_{HT0}} = (\mathrm{HT0}\ \&\&\ !=(\mathrm{HT1}|\mathrm{HT2}|\mathrm{HT4})\ \&\&\ (11 < \mathrm{ADC} \leq 15)) \cdot \mathrm{ps10}$,
$\mathrm{N_{HT1}} = (\mathrm{HT1}\ \&\&\ !=(\mathrm{HT2}|\mathrm{HT4})\ \&\&\ (15 < \mathrm{ADC} \leq 18)) \cdot \mathrm{ps11}$,
$\mathrm{N_{HT2}} = (\mathrm{HT2}\ \&\&\ !=(\mathrm{HT4})\ \&\&\ (18 < \mathrm{ADC} \leq 35)) \cdot \mathrm{ps12}$,
$\mathrm{N_{HT4}} = (\mathrm{HT4}\ \&\&\ (35 < \mathrm{ADC})) \cdot \mathrm{ps14}$,
$\mathrm{N_{combo}} = \mathrm{N_{HT0}} + \mathrm{N_{HT1}} + \mathrm{N_{HT2}} + \mathrm{N_{HT4}}$,

where *ps* denotes prescale factor. 3.3 M HT0 events, 3.4 M HT1 events, 5.2 M HT2 events, and 0.6 M HT4 events were used in the analysis. These numbers are before prescaling.

7.2 Trigger efficiency

For the non-photonic electron analysis at high-p$_T$ region events that satisfied HT triggers conditions were used. Same as in the p+p case, HT triggers are inefficient at p_T region from 2 to 4 GeV/c. Due to this, inclusive electron spectrum was corrected for trigger efficiency. This efficiency was calculated by comparing the inclusive electron spectrum based on VPDMB trigger with the same spectrum obtained from 4 HT triggers. The trigger efficiency based on the d+Au data was already calculated during the p+p analysis from the year 2008 [36] and the results are presented in Fig. 89.

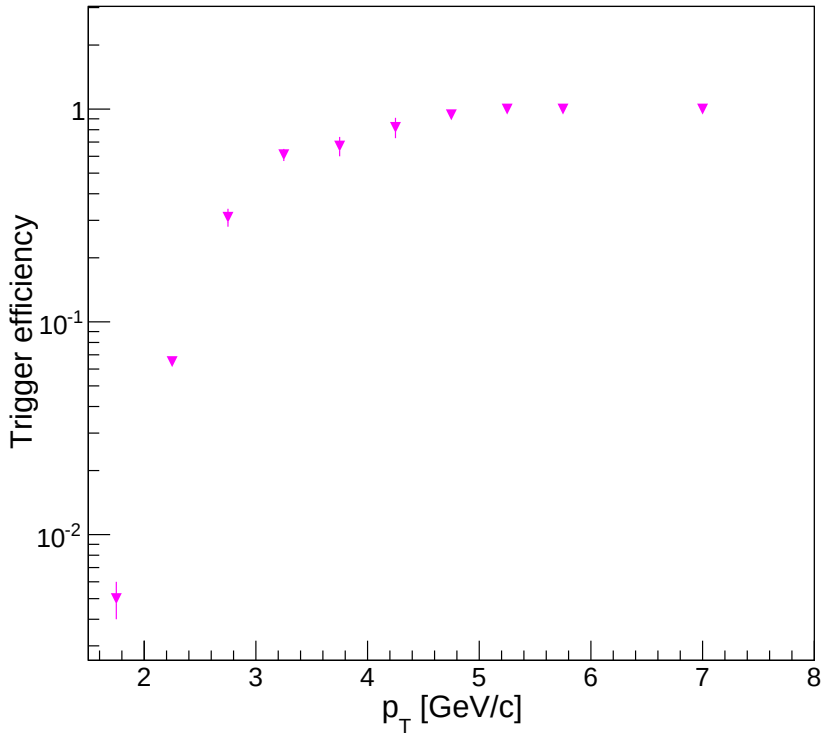

Figure 89: High Tower trigger efficiency in d+Au collisions in the year 2008.

7.3 Centrality determination

Centrality in d+Au collisions is determined as charged particle multiplicity in the East Forward TPC detector. Due to the varying performance of the FTPC during the data taking, data were divided into three sets by the time periods (Run Period 1: Run 8340015 - 9008109, Run Period 2: Run 9009007 - 9020089, Run Period 3: Run > 9021001). Figure 90 shows average East FTPC multiplicity as a function of the day number [82].

The z-vertex position dependence of the east FTPC multiplicity for each run period was studied and it is plotted in Fig. 91. Distributions were compared with Glauber calculation and a high deficit in peripheral collisions was observed. Reweighting based on the distributions of the FTPC multiplicity in the data and Glauber calculation was done, for peripheral and semi-peripheral collisions (refMult< 10 for Period 1 and Period 2 and refMult<8 for Period 3). Runs with

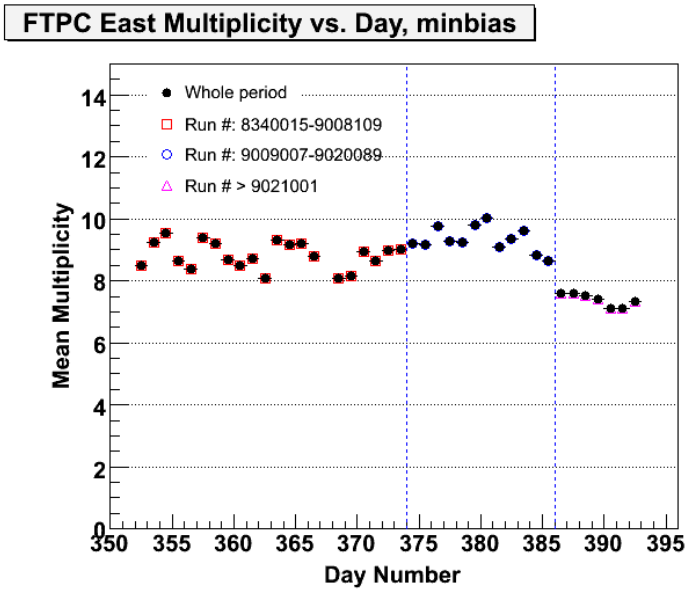

Figure 90: Average charged particle multiplicity in the East FTPC in d+Au collisons in the year 2008 as a function of the day number [82].

no information from the FTPC were removed. Figure 92 (left) shows charge particle multiplicity in FTPC during the Period 3 compared with the Galuber calculation, in the right panel the reweighting factors as a function of multiplicity are plotted. The reweighing factors were studied in 2 cm wide slices in z-vertex. The dependence on the z-vertex position is found to be small.

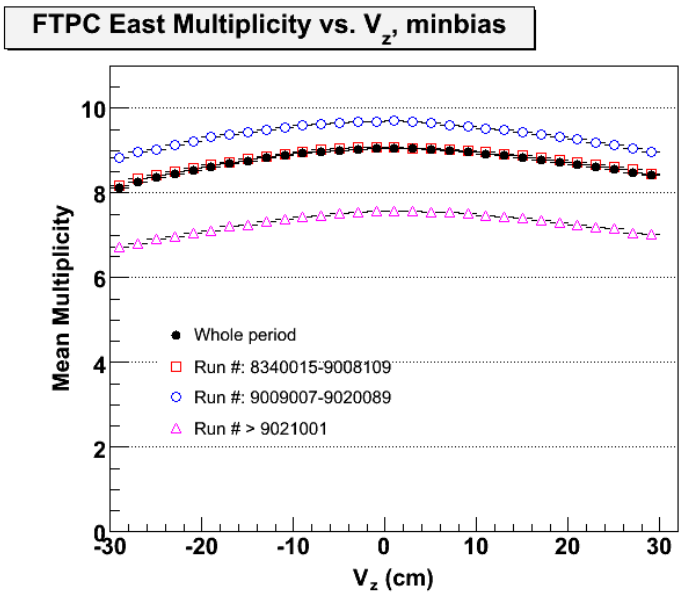

Figure 91: Average charged particle multiplicity in the East FTPC in d+Au collisons in the year 2008 as a function of the z-vertex position [82].

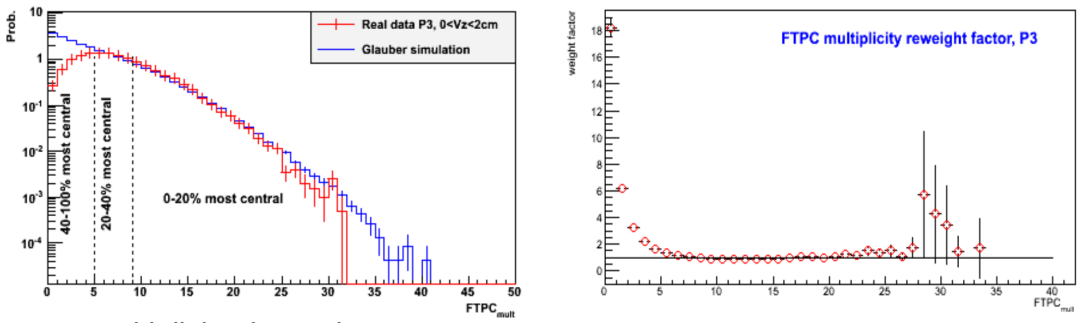

Figure 92: Left plot shows the charged particle multiplicity measured in FTPC in run Period 3 and with z-vertex cut $0 < zvtx < 2$ cm (red line) compared with Glauber calculation (blue line). The reweighting factors as a function of multiplicity are plotted on the right.

7.4 Track quality and particle identification cuts used in d+Au analysis

During the d+Au analysis similar cuts were applied for events, tracks and electron identification. Events that satisfied primary vertex location cut |zvtx| < 30cm were used. Events with more then 1 fired strip of the BSMD detector in ϕ-plane and pseudorapidity location, BSMD($|\phi| > 1$) and BSMD($|\eta| > 1$) were accepted. All track cuts are listed in Tab 4.

0 <flag< 1000
nHitPoints> 20
nHitPoints/nMaxPoints> 0.51
gDCA< 1.5 cm
eta< 0.7
ndE/dx>10
$TPC^{1stpoint}$ <90 cm

Table 4: Track quality cuts used in d+Au analysis.

Information from the Time projection chamber (TPC) and Barrel electromagnetic calorimeter (BEMC) was used together for electron identification. Electrons were identified in the same way as described in Chapter 6.6. All electron identification cuts are listed in Tab 5.

1<nsigma electron< 3
0<p/E<2 cm
|bsmdedz| <3 cm
|bsmdedphi| <0.06 cm
|bsmdpdz| <20 cm
|bsmdpdphi| <0.02 cm
|btowdz| <10 cm
|btowdphi| <0.06 cm

Table 5: Electron identification cuts used in d+Au collisons.

7.5 Photonic electron background and PHE reconstruction efficiency

Photonic electrons were reconstructed in a same way as in p+p collisions. Cuts for partner, excepting the tracking quality cuts, are $p_T > 0.3$ GeV/c, dE/dx from 3 to 5 keV/cm, di-electron invariant mass> 0.24 GeV/c^2 and pairDCA$<$1cm, where pairDCA means distance of the closest approach between electrons helixes.

Due to the TPC acceptance, some of photonic electrons cannot be reconstructed. The photonic electron reconstruction efficiency must be calculated. This efficiency was obtained using single gamma embedding. Since the d+Au embedding is not available the p+p embedding from year 2008 was used to calculate photonic reconstruction efficiency. Final PHE reconstruction efficiency is plotted in Fig. 93. Since the difference between p+p and d+Au efficiency was supposed, the study of difference between p+p and Au+Au embedding was made and estimated difference between p+p and d+Au embedding were add in systematic. The cuts used for primary and global partner are same as in proper analysis.

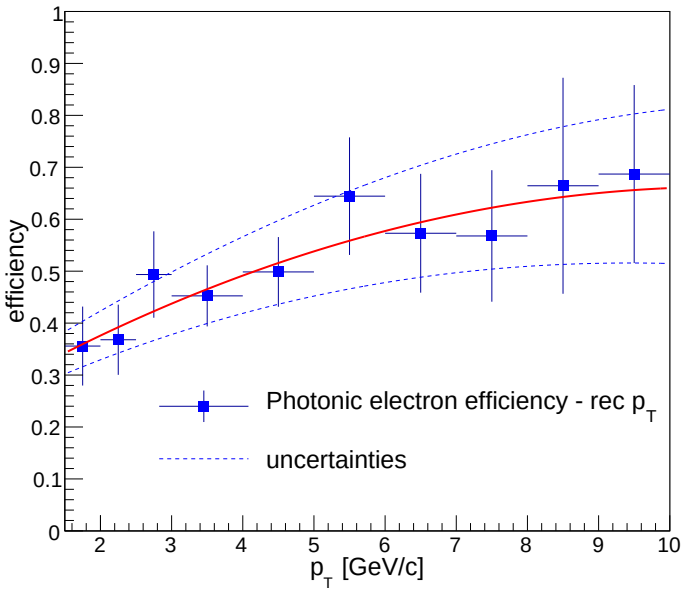

Figure 93: Photonic electrons reconstruction efficiency in d+Au collisions. Blue dashed lines show systematic uncertainty.

7.6 Purity of inclusive electron sample

The purity of the inclusive electron sample was calculated same way as descibed in p+p analysis. All figures used during the purity calculation in the d+Au NPE analysis are listed in this Chapter, Fig. 95 - Fig. 98. Final purity of the inclusive electron sample in d+Au collisions is plotted in Fig. 98 and it is decreasing with increasing p_T.

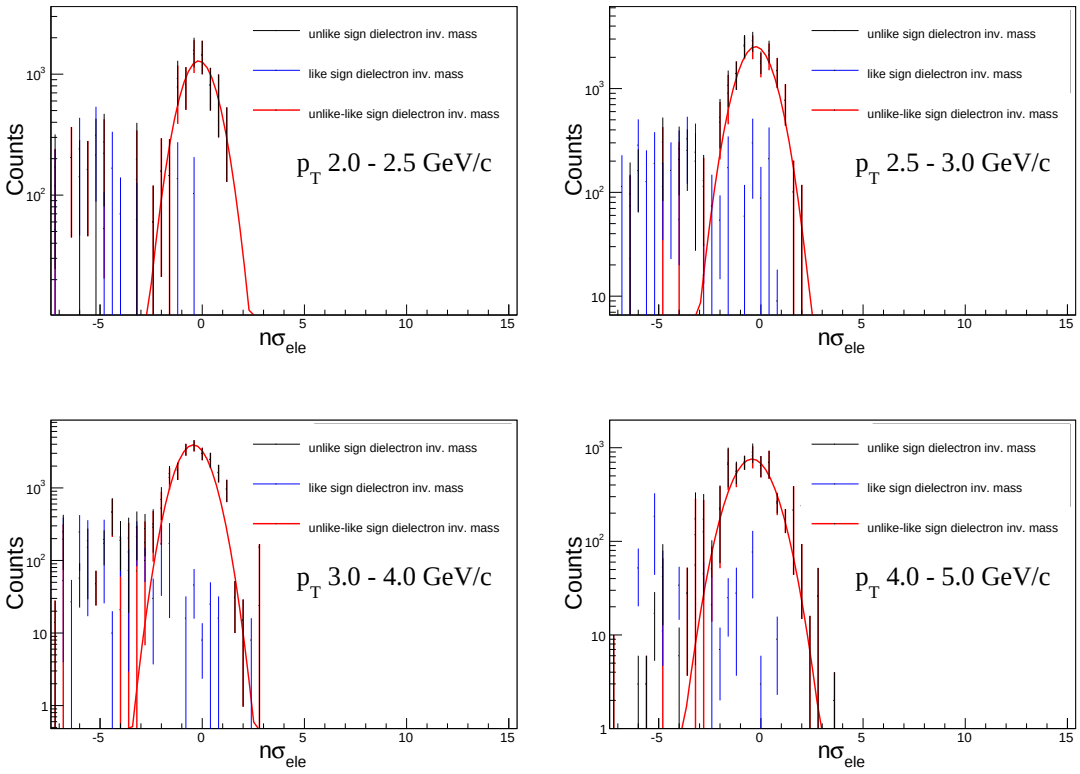

Figure 94: A Gaussian fit to the photonic nsigma_electron distribution for different p_T bins in d+Au collisions.

Final purity of the inclusive electron sample in d+Au collisions is shown in Fig. 98. The efficiency of n$\sigma_{electron}$ cut was calculated from same distributions as purity and final plot is in Fig. 99.

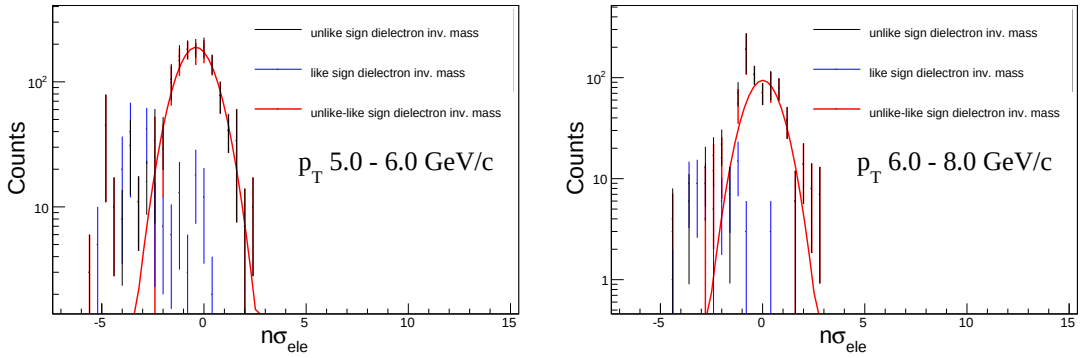

Figure 95: A Gaussian fit to the photonic nsigma_electron distribution for different p_T bins in d+Au collisions.

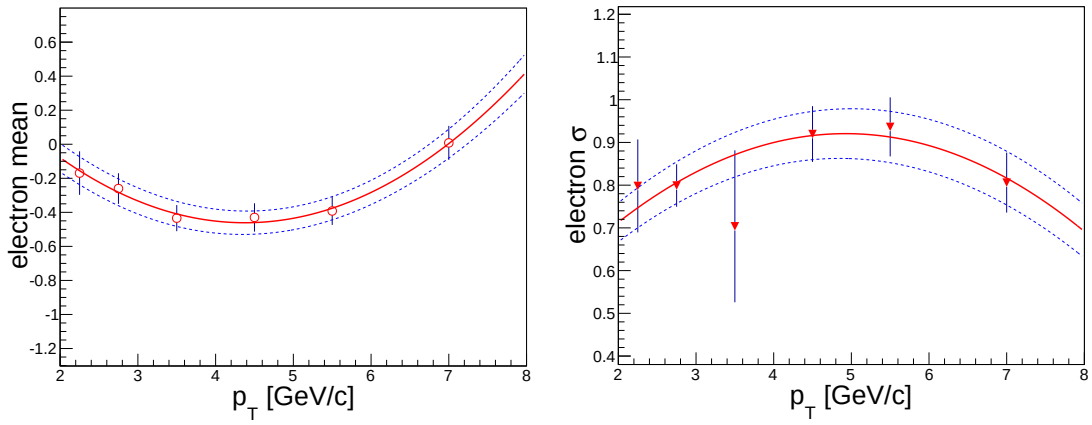

Figure 96: The electron mean (left) and width (right) as a function of p_T.

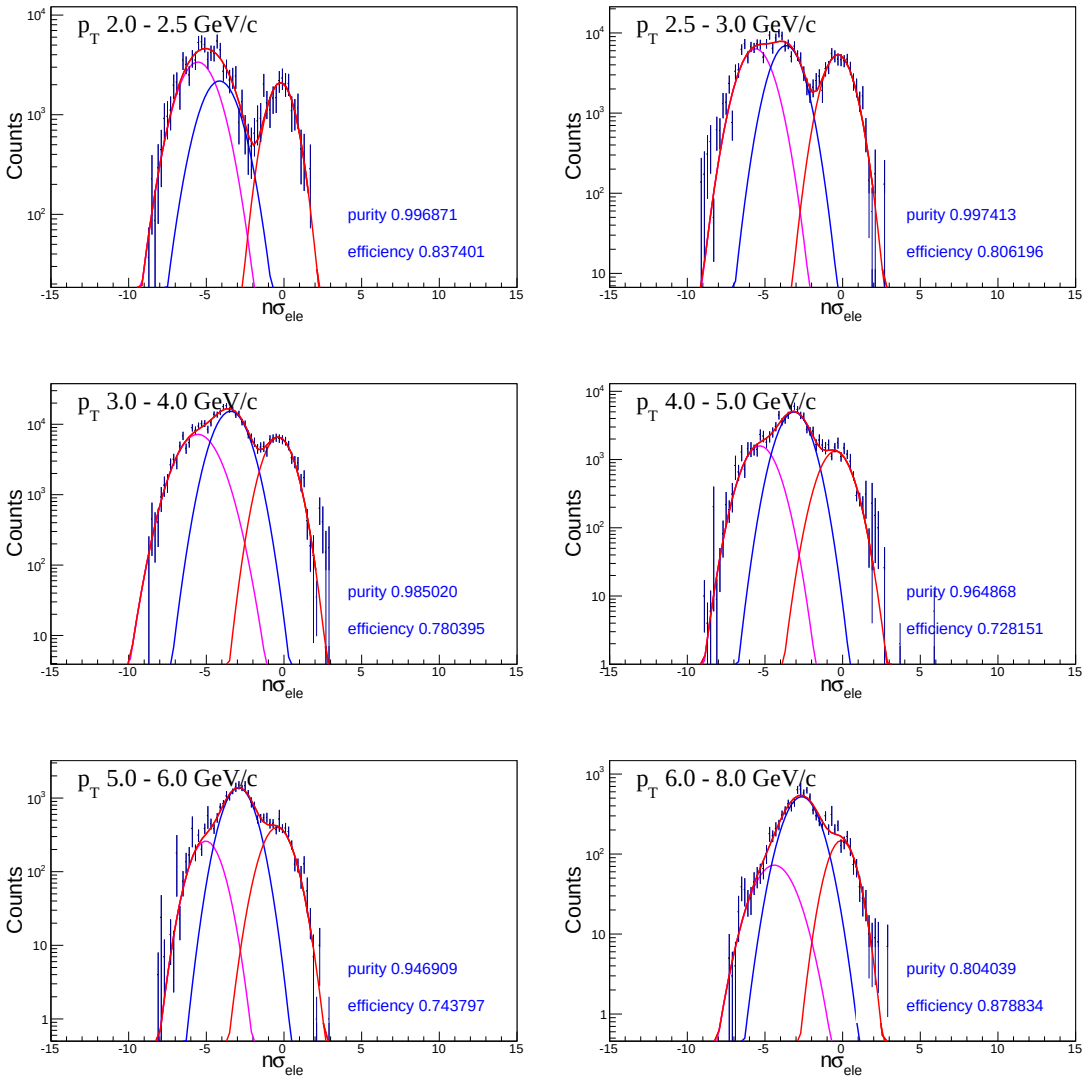

Figure 97: Multi-Gaussian fits to the nσ_electron distribution of all charged particles which pass all track quality cuts and elecron identification cuts except the nsigma_electron one. Red, blue, magenta and turquoise lines denote electrons, pions, protons with kaons, and kaons respectively.

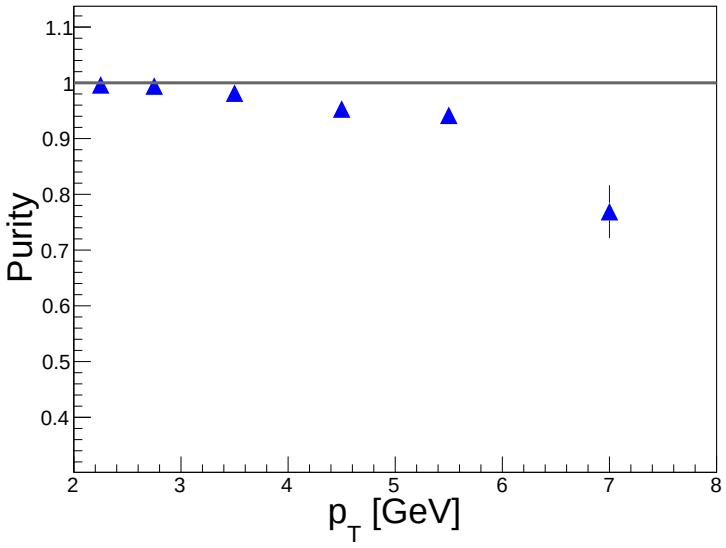

Figure 98: Final purity calculated from the the multi-Gaussian fits to the n$\sigma_{electron}$ distributions.

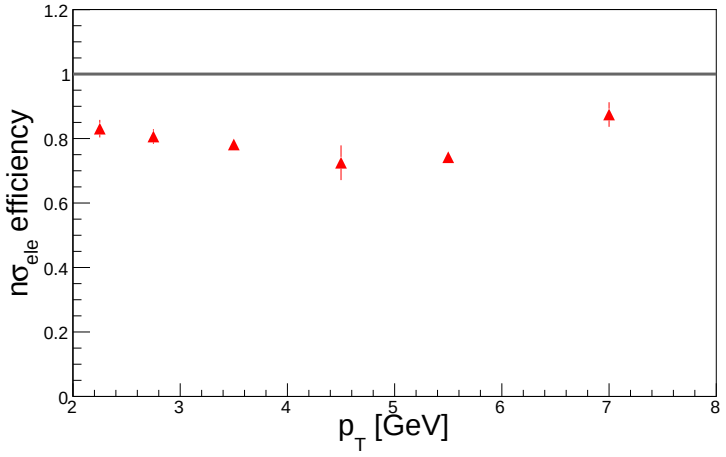

Figure 99: The efficiency of n$\sigma_{electron}$ cut in d+Au analysis calculated from distributions in different p_T bins.

7.7 Track reconstruction and electron identification efficiency

Track reconstruction and electron identification efficiency were obtained using simulated electrons embedded into real events as was described in previous chapter. Embedding from p+p 2008 was used. These events were then analyzed same way as the real data. The final electron efficiency is plotted in Fig. 100. Finally the J/ψ contribution to the NPE spectrum was subtracted [79].

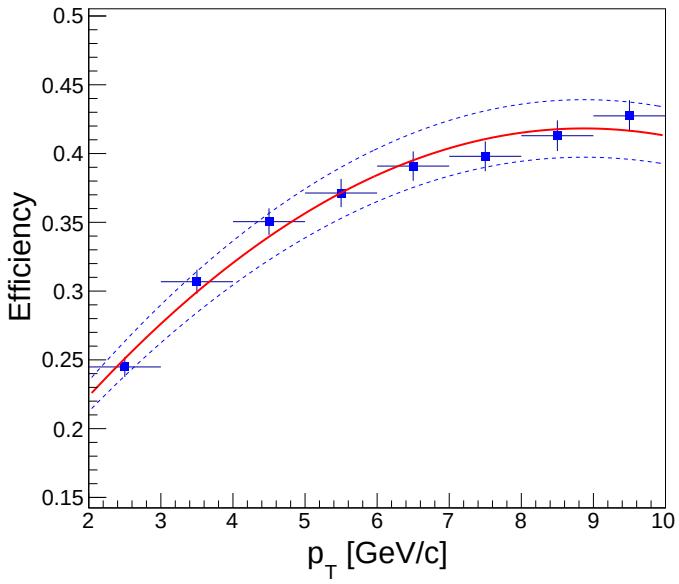

Figure 100: Electron reconstruction efficiency in d+Au analysis calculated from p+p embedding with its uncertainties.

7.8 Results

In this subchapter, results obtained in the non-photonic electron analysis in d+Au collisions at $\sqrt{s_{NN}}$=200 GeV using data taken during the year 2008 at the STAR experiment are presented. The invariant yield of non-photonic electrons was calculated as

$$\frac{B}{2\pi p_T}\frac{d^2N}{dp_T dy} = \frac{1}{2\pi p_T}\frac{1}{\Delta p_T}\frac{1}{\Delta y}\frac{N_{npe}}{N_{events}}\frac{1}{\epsilon_{tot}}, \tag{18}$$

where N_{npe} is the raw yield of NPE, N_{events} is the number of events in used V_z cut, and ϵ_{tot} is the product of TPC tracking efficiency, electron PID efficiency, and trigger efficiency (for $p_T > 2$ GeV/c), Δp_T is the p_T coverage, Δy pseudorapidity coverage. Figure 101 presents NPE yield as a function of p_T, where red marks show results obtained in presented d+Au analysis, green marks show PHENIX NPE yield measured in data from the year 2008, blue points show STAR p+p results [36] and black points PHENIX p+p baseline [37]. Results are also compared with pQCD FONLL (Fixed Order plus Next-to-Leading Logarithms [30]) calculation scaled by number of binary collisions ($\langle N_{coll}\rangle = 7.6$ for the MB data, $\langle N_{coll}\rangle = 14.6$ for the central collisions).

Figure 103 shows the ratio of NPE yield to FONLL calculation scaled by the number of binary collisions [30], $\langle N_{coll}\rangle$ for MB data is estimated from Glaber calculation as 7.6. MB data means that the result is obtained combining all centrality classes together. Figure 104 shows the results obtained using 20% of the most central collisions, number of binary collisions for this centrality class was estimated as 14.6. Results are compared to the d+Au results from the year 2008 from the PHENIX collaboration .

In Figure 105 and Figure 106 the NPE nuclear modification factor is presented for MB collisions and 20% of the most central collisions, respectively. Nuclear modification factor as was discussed in Chapter 3 is defined as

$$R_{dA} = \frac{d^2N_{dA}}{d^2N_{pp}\cdot\langle N_{coll}\rangle}. \tag{19}$$

Results are compared with the PHENIX results from d+Au collisions from the year 2008. Due to the low statistics a strong physical output cannot be drawn from this result. Data are in a good agreement with the PHENIX results and with unity as well. For a better understanding of the cold nuclear matter effects a larger data set would be needed.

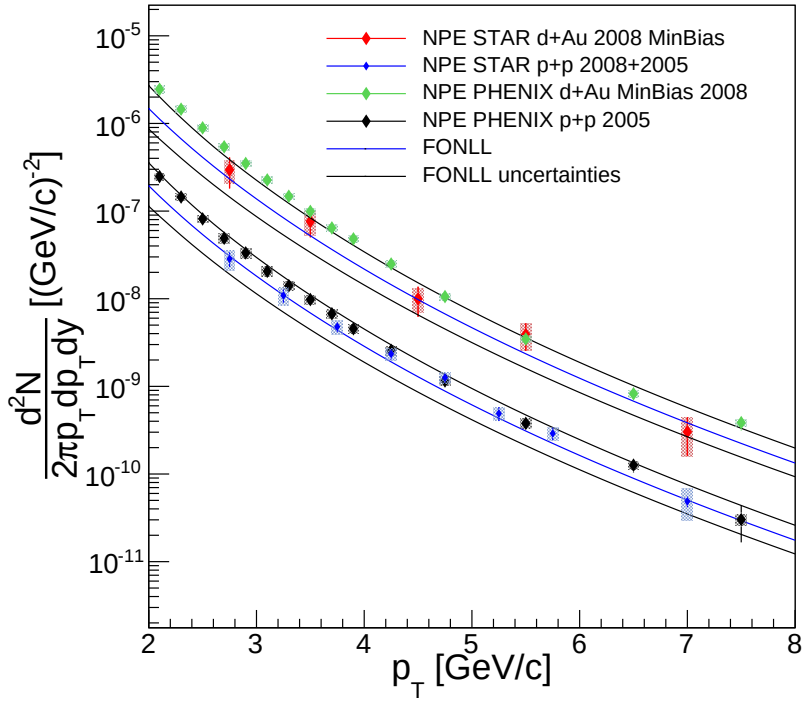

Figure 101: Non-photonic electrons yield for all centrality together measured in d+Au collisions at $\sqrt{s_{NN}}$=200 GeV using data taken during the year 2008 (red, this thesis) compared with PHENIX d+Au results from the same year (green). Blue marks denote p+p baseline measured with STAR in the year 2008 [36] and black points denote PHENIX p+p baseline [37]. Theoretical FONLL calculations is presented by blue lines, where the upper line is scaled by number of binary collisions ($\langle N_{coll} \rangle = 7.6$) [30].

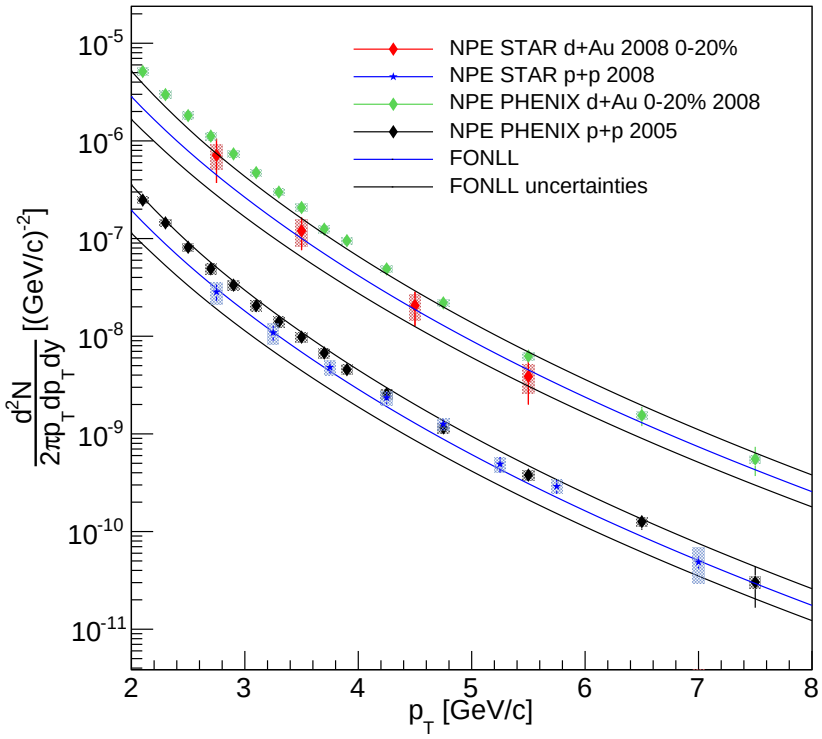

Figure 102: Non-photonic electrons yield for 20% of the most central collisions measured in d+Au collisions at $\sqrt{s_{NN}}$=200 GeV using data taken during the year 2008 (red, this thesis) compared with PHENIX d+Au results from the same year (green). Blue marks denote p+p baseline measured with STAR in the year 2008 [36] and black points denote PHENIX p+p baseline [37]. Theoretical FONLL calculations is presented by blue lines, where the upper line is scaled by number of binary collisions ($\langle N_{coll} \rangle = 14.6$) [30].

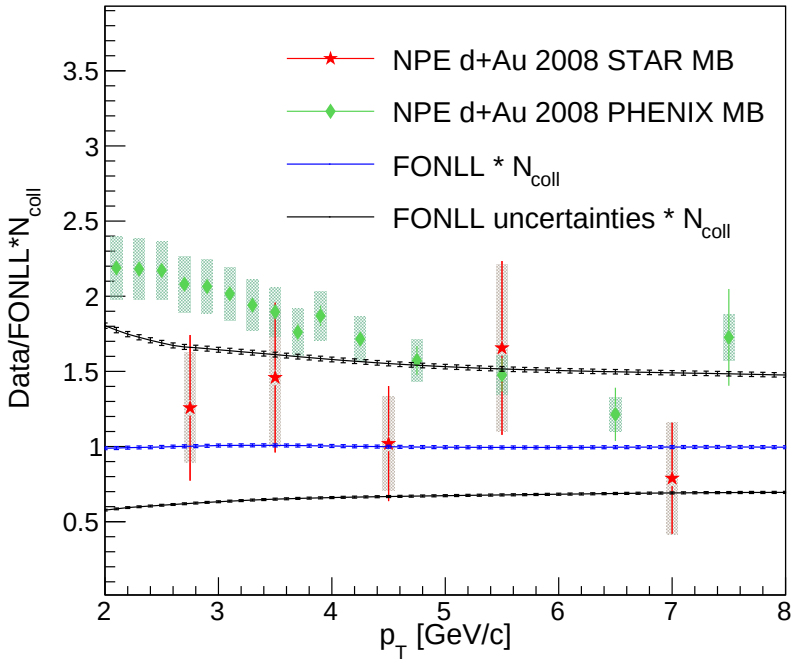

Figure 103: Non-photonic electron data over FONLL ratio in d+Au collisions at $\sqrt{s_{NN}}$=200 GeV using the data taken during the years 2008 in STAR (red, this thesis) and PHENIX (green) [30]. All centrality classes are combined together.

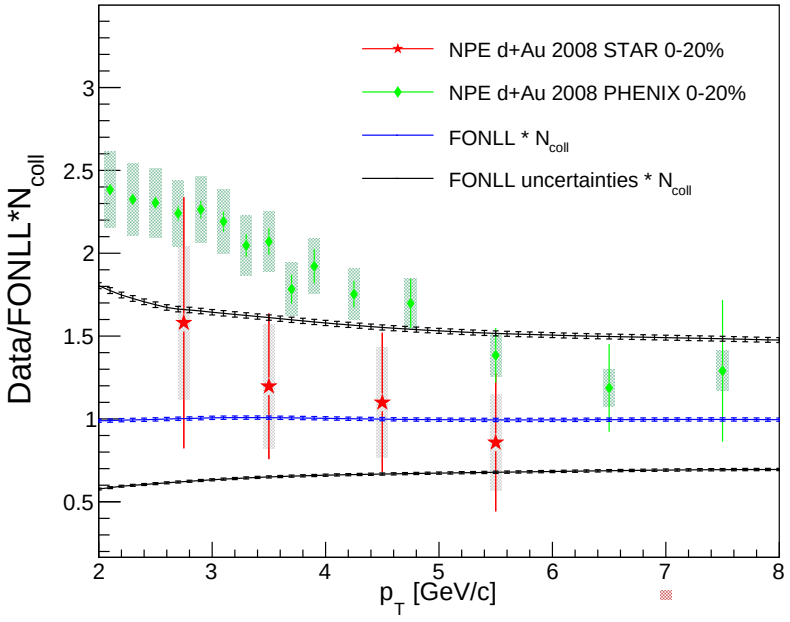

Figure 104: Non-photonic electron data over FONLL ratio in d+Au collisions at $\sqrt{s_{NN}}$=200 GeV using the data taken during the years 2008 in STAR (red, this thesis) and PHENIX (green) [30]. Presented results were obtained using only data from 20% of the most central collisions.

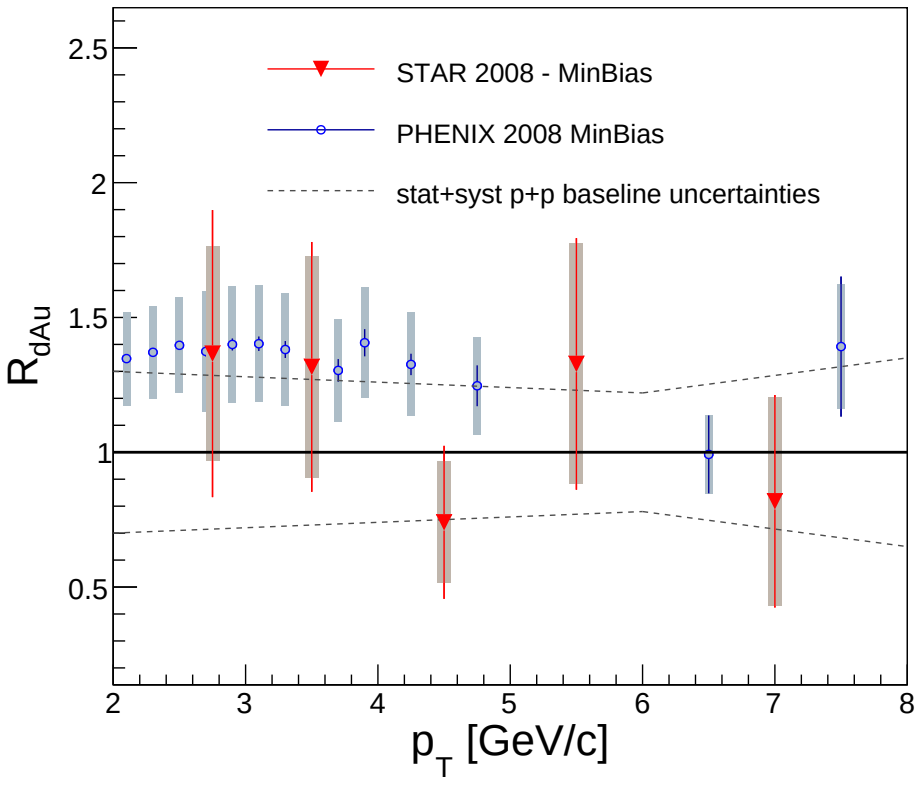

Figure 105: NPE nuclear modification factor $R_A A$ in d+Au collisions for MB collisions. Red points denote STAR results from the year 2008 (this thesis) and blue points denote results from PHENIX the same year analysis

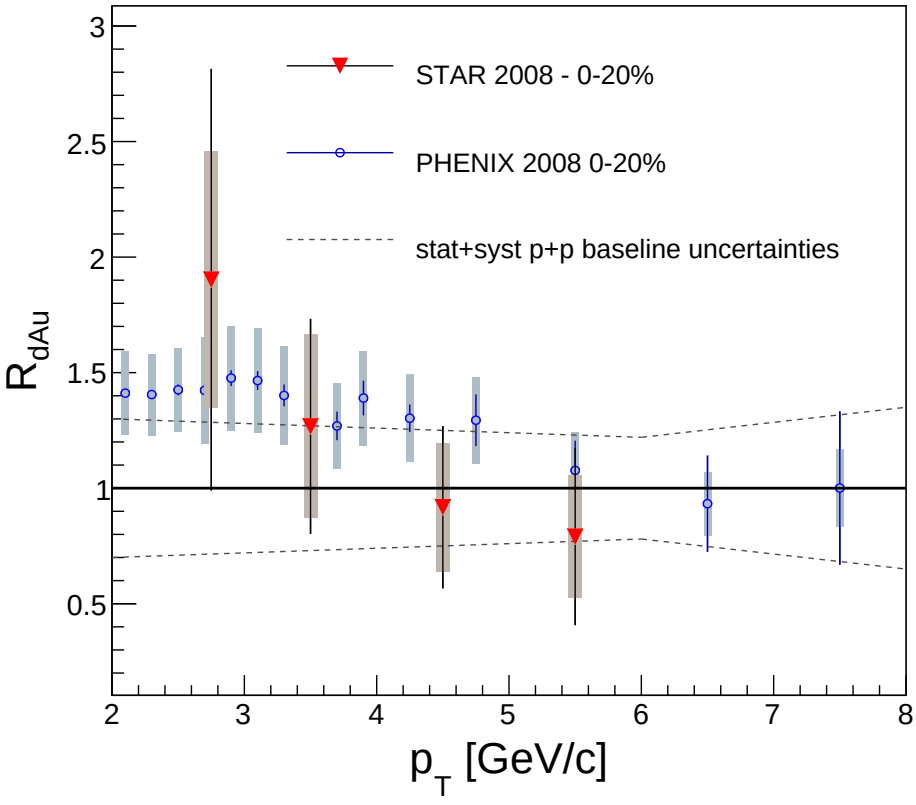

Figure 106: NPE nuclear modification factor in d+Au for 20% of the most central collisons.

8 Systematic errors

In this chapter the main sources of the systematic errors at both p+p and d+Au are discussed. These are for both presented analysis mainly the electron PID efficiency uncertainty, PHE reconstruction efficiency uncertainty, purity estimation error, trigger efficiency uncertainty, error of the bin shift correction and J/ψ contribution error.

8.1 The purity estimation uncertainty

An error of the purity calculation is associated with the Gaussian fit to the n$\sigma_{electron}$ distribution. As mentioned above, the inclusive electron sample purity is calculated by performing a multiple Gaussian fit to the n$\sigma_{electron}$ distribution in each p_T bin. Parameters of the pion and proton+kaon Gaussians were determined with respect to the Bethe-Bloch functions for pion and proton. Parameters for the electron were estimated from Gaussian fit to the photonic electron $\sigma_{electron}$ distribution. It is assumed that this PHE sample is a pure electron sample.

The purity estimation uncertainty was determined by shifting the electron Gaussian parameters by one standard deviation of the fit result for each p_T bin. The example of the parameter shift is shown in Fig. 107.

Purity calculation uncertainty is increasing with p_T up to 20% in p+p and up to 30% in d+Au analysis.

8.2 Trigger efficiency calculation uncertainty

In both analysis HT trigger data were used in the high-p_T region. This triggers have finite efficiency and its inefficiency in the p_T region 2-4 GeV/c comes from the thresholds as discussed in the analysis chapters. The systematic errors of trigger efficiency calculation comes from statistics errors of the trigger efficiency estimation and it decreases with p_T from 12% in p_T bin 2-2.4 GeV/c to negligible value at $p_T > 5.5$ GeV/c.

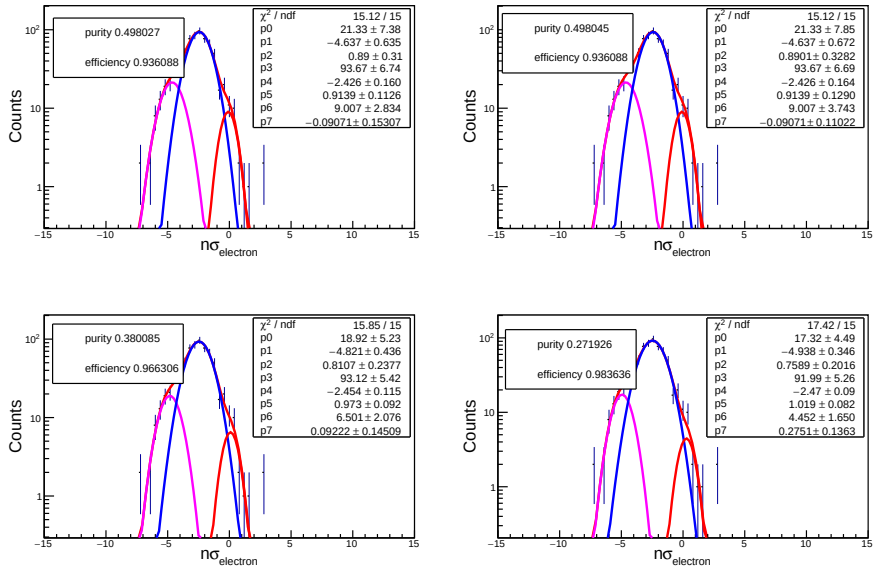

Figure 107: Example of the estimation of purity calculation uncertainty.

8.3 Electron identification and PHE reconstruction efficiency uncertainties

Electron PID uncertainty has two different sources, an error associated with the embedding and an error coming from the efficiency of $n\sigma_{electron}$ cut calculated from data. Uncertainty in the embedding comes from the difference between variables (nHitPoints, nHitPoints/nMaxPoints, gDCA, $TPC^{1stpoint}$, BEMC cluster cuts, etc.) distributions in the embedding and data. This difference was shown and discussed in Chapter 6.11 and was estimated as 4% in all p_T regions.

The $n\sigma_{electron}$ cut efficiency was calculated in a same way as purity uncertainty (Fig. 107) and it is increasing with p_T ut to 8% for the case of p+p collisions and up to 15% in d+Au collisions.

Photonic reconstruction efficiency uncertainty was calculated by comparing the embedding and real data distributions as discussed above and it is 7% at low-p_T region and 11% at high-p_T region in both analysis. Electron PID efficiency uncertainty calculated from embedding as well was estimated as 4% fro both analysis. As was discussed in previous chapter, the d+Au embedding is not available thus the p+p embedding from year 2008 was used in d+Au analysis.

The difference between the p+p and peripheral Au+Au embedding was studied

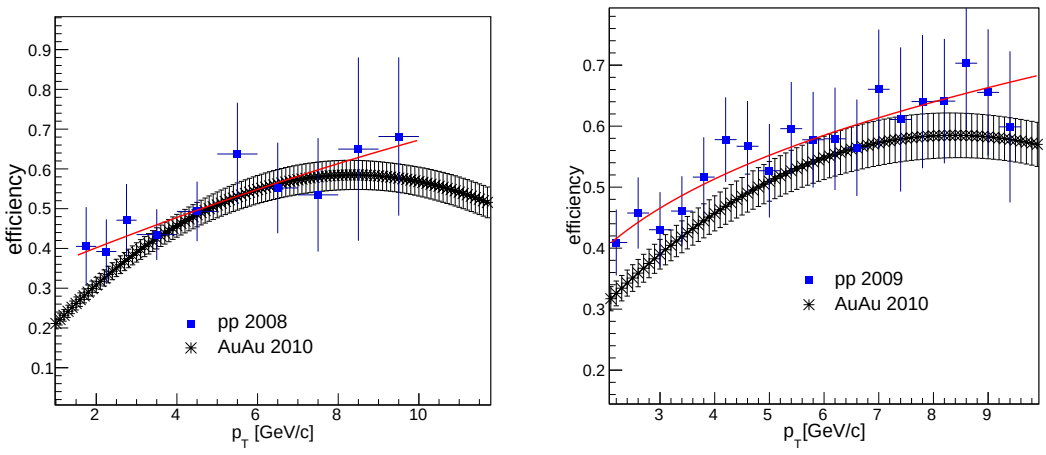

Figure 108: Difference between p+p and Au+Au embedding. Blue points denote photonic electron reconstruction efficiency calculated from embedding in p+p collisions and black points in peripheral Au+Au collisions. Left plot shows embedding from the year 2008 and right plot shows embedding from the year 2009.

to estimated uncertainties that come from the use of p+p embedding in d+Au analysis and it is shown in Fig. 108. As a result the difference between the p+p and d+Au embedding was estimated as 8%.

8.4 J/ψ contribution uncertainty

The subtraction of J/ψ secondary background was based on Thomas Ullrich's study [79]. Data points were fit with the xzb-fun function [79] and the upper and lower error bounds of the fit parameterization were used to evaluate the uncertainties. Fit to the data and the uncertainties were shown in Fig. 109.

The total systematic uncertainty increases with p_T from 21% to 41% in p+p collisions and from 28% up to 50% in d+Au collisions. In Table 6 is a list of contribution to the systematic uncertainty.

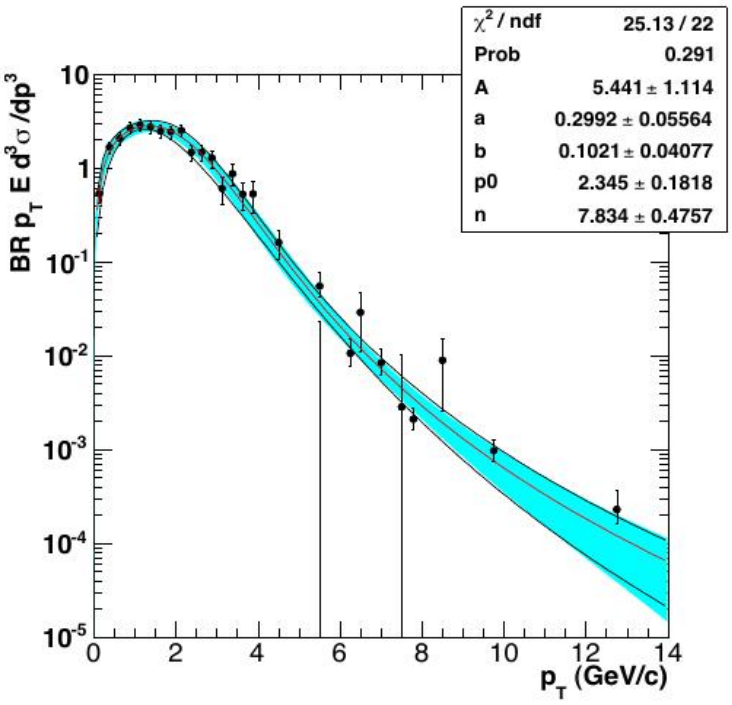

Figure 109: Crossection of J/ψ contribution to the NPE with lower and upper limits. Taken from Ref. [79].

Type of uncertainty	p+p analysis	d+Au analysis
Purity estimation	up to 20%	up to 30%
Trigger eff.	up to 12%	up to 12%
ePID eff.	4%	4%
PHE rec. eff.	7%, 11%	11%
J/ψ contribution	10%-37%	17%-37%
Bin shift corr.	up to 8%	up to 11%
n$\sigma_{electron}$ eff.	up to 8%	up to 15%
Diff. between embedding and data	4%	4%
Use of p+p embedding	-	8%

Table 6: List of contributions to the systematic error.

9 Results

In this Chapter the NPE p+p results in context of the STAR NPE measurement will be discussed. Presented p+p NPE analysis was used as a baseline for the nuclear modification factor (R_{AA}) calculation in Au+Au collisions at $\sqrt{s_{NN}}$ = 200 GeV. For a better comparison of the FONLL calculation with the results (as discussed in previous Chapter), the ratio of data and FONLL is plotted in Fig. 110. New results are compared with the last published p+p results at $\sqrt{s}$=200 GeV from the year 2008 [36] and with results from the PHENIX experiment [37]. Black points denote present analysis, green points denote PHENIX results, and blue points represent the STAR p+p results from the year 2008. Overall there is a good agreement between the two experiments at RHIC and between both STAR data and a significant improvement with respect to the last results is evident.

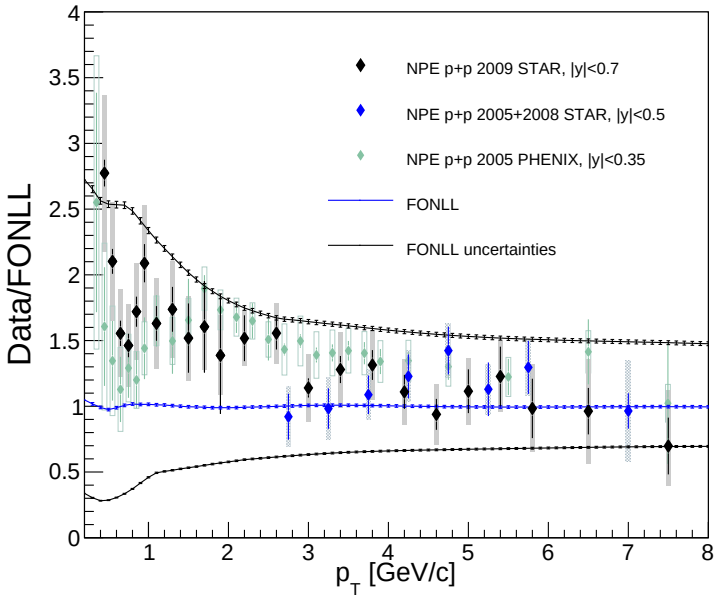

Figure 110: Ratio of data over FONLL calculation [30], STAR results from p+p collisions at $\sqrt{s}$=200 GeV from the year 2009 (black, this thesis) compared with STAR data from the year 2008 (blue) [36] and PHENIX p+p results [37].

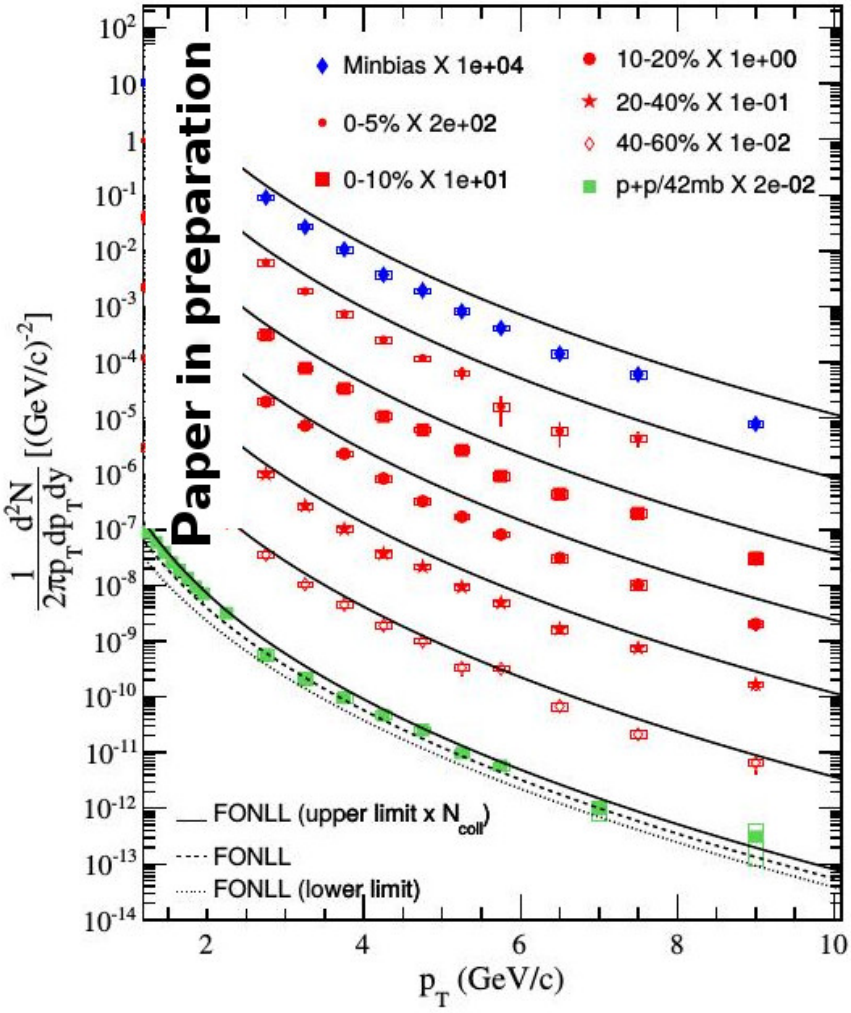

Figure 111: NPE invariant yield in p+p and Au+Au collisions at $\sqrt{s_{NN}}$=200 GeV at midrapidity in STAR. Blue points denote minimum bias results and red points show NPE yield in Au+Au collisions in different centrality bins. Solid black lines represent central FONLL calculation scaled by number of binary collisions [30]. Green points represent p+p baseline (this thesis), the baseline built by combining data from the years 2005, 2008 [36], and 2009.

Figure 111 shows the NPE invariant yield as a function of p_T in p+p and Au+Au collisions at $\sqrt{s_{NN}} = 200$ GeV measured with STAR. The p+p spectrum at $p_T > 2.5$ GeV/c was obtained by combining p+p data from the year 2009 (analysis presented in this thesis) with published results from the year 2005 and 2008 [36]. At low-p_T region only data from the year 2009 were used (this thesis data). Au+Au data set is from the year 2010 and NPE spectrum is divided into different centrality bins. The data are compared with pQCD FONLL calculation [30] scaled by number of average binary collisions in given centrality bin. Calculation of the number of binary collisions is based on Glauber model.

Finally the nuclear modification factor (R_{AA}) was calculated. As was mentioned in Chapter 3 R_{AA} is defined as a ratio of the particle production in nucleus-nucleus collisions to the production in proton-proton collisions, scaled by the average number of binary collisions N_{coll} for a given centrality and R_{AA} can provide information about heavy quark energy loss. $R_{AA} = \frac{d^2N_{AA}}{d^2N_{pp}\cdot\langle N_{coll}\rangle}$. The NPE R_{AA} as a function of p_T for different centralities was calculated. Strong NPE suppression at high-p_T is observed in central and semicentral collisions. The level of suppression is similar as that of light hadrons.

Figure 112 shows NPE R_{AA} for 10% most central collisions compared to several theoretical models of the energy loss mechanisms. The gluon radiation only model (DGLV, dashed green line [11]) fails to explain large suppression at high-p_T region. This model was successful at describing the suppression of light hadrons. A modified DGLV+EL model including collisional energy loss predicts larger suppression and describe data better (solid green line). Dot-dashed red line denotes a collisional dissociation model [14]. The energy loss is due to the hadronization of th heavy quarks to heavy mesons, which then dissociate into heavy quarks. Another model Ads/CFT [15] also describes our data at high-p_T well. In the BAMPS transport model (Boltzman approach to the multi-particle scattering [16]), heavy quarks loss their energy in elastic collisions with the rest of the hot medium. The TMatrix interaction model by He et al. [17] is a non-perturbative approach to the heavy quarks energy loss. The QCD inspired model with pQCD description of the heavy quark quenching and additional non-perturbative corrections is the Gossiaux et al. model [18].

TMatrix model, dissociation model, and Gossiaux model describe results in the high-p_T well, but miss the mid-p_T region or/and low-p_T region. To resolve between these models it is necessary to study NPE R_AA with v_2 together. As was

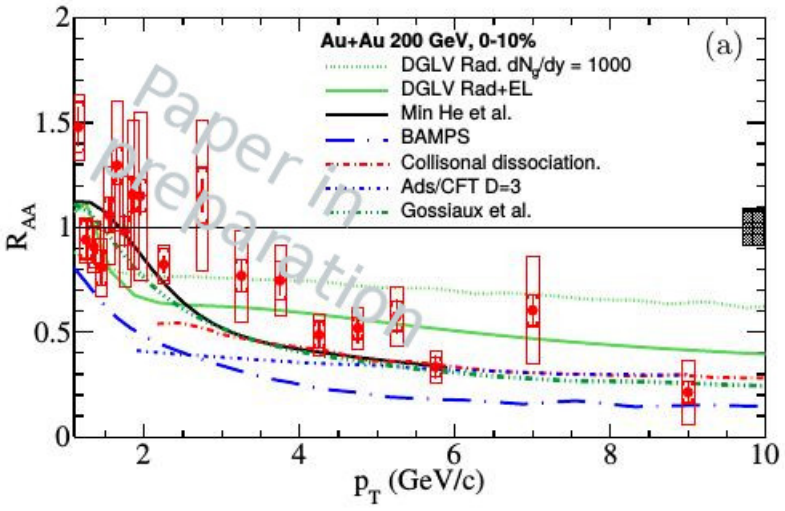

Figure 112: Non-photonic electron results from Au+Au collisions at $\sqrt{s}$=200 GeV from the year 2010. Results are compared with theoretical models [11]-[18].

discussed in Chapter 5 at STAR we observe finite v_2 at low p_T. It is a challenging task to describe both results, $R_A A$ and v_2 via one theoretical model.

Conclusion

Non-photonic electrons productions in p+p and d+Au collisions at $\sqrt{s}$=200 GeV recorded during data taking in the years 2009 and 2008, respectively, were analyzed and presented in this thesis in detail.

In p+p collisions NPE analysis was done in wide p_T region, while NPE analysis in p+p collisions in low-p_T region was performed in STAR for the first time. The non-photonic electron invariant yield in p+p collisions was calculated and compared with Fixed-Order plus Next-to-Leading-Log (FONLL) pQCD calculation. Results are in good agreement with FONLL calculation, data points lay between central value of FONLL and its upper limit. Compared to the last published data the NPE spectum was extended to low-p_T region, and in consequence NPE nuclear modification factor in Au+Au collisions was calculated first time in low-p_T region too. Strong suppression of NPE production at high-p_T is observed in central and semicentral collisions. The level of suppression is similar as that of light hadrons. The R_{AA} results were compared to the number of theoretical models. TMatrix model, dissociation model, and Gossiaux model describe results in the high-p_T well, but miss the mid-p_T region or/and low-p_T region. To resolve between these models it is necessary to study NPE R_AA with v_2 together. It is a challenging task to describe both results, R_AA and v_2 via one theoretical model. Presented results are finalized and they are part of a new STAR Collaboration paper.

Non-photonic electron analysis in d+Au collisions at $\sqrt{s_{NN}}$ = 200 GeV from the year 2008 was presented. During this analysis NPE spectrum was reconstructed for minimum bias and 20% of the most central collisions and was compared with FONLL calculation scaled by number of binary collisions. Finally, the nuclear modification factor R_{AA} was calculated for both MB and central results. Results are compared with the PHENIX results from d+Au collisions from the year 2008. Data are in a good agreement with the PHENIX results and with unity as well. For a better understanding of the cold nuclear matter effects a larger data set would be needed.

References

[1] J. Beringer et al. (Particle Data Group), Phys. Rev. D 86, 010001 (2012).

[2] David J. Gross and Frank Wilczek, Phys. Rev. Lett. 30, 1343 (1973).

[3] Gines Martinez, arXiv:1304.1452 (2011).

[4] Yasuo Miake Kohsuke Yagi, Tetsuo Hatsuda, Quark-Gluon Plasma: From Big Bang to Little Bang, Cambridge University Press (2006).

[5] http://www.bnl.gov/newsroom/news.php?a=21870 [online 1/31/2014].

[6] R. J. Glauber, Lectures on Theoretical Physics, Interscience, New York, Vol. I. (1959).

[7] ALICE collaboration, Phys. Rev. Lett. 107 032301 (2011).

[8] J. Adams et al., (STAR Collaboration), Phys.Rev.Lett. 91 072304 (2003).

[9] T.Matsui, H.Satz, J/ψ Suppresion by Quark Gluon Plasma, Physics Letters B, vol.178, no.4 (1986).

[10] ALICE Collaboration, Phys. Rev. Lett. 109 072301 (2012).

[11] M. Djordjevic, M. Gyulassy, R. Vogt, and S. Wicks, Phys. Lett. B 632, 81 (2006).

[12] A. Buzzatti, M. Gyulassi, arXiv:1207.6020 (2008).

[13] H. Van Hees, M. Mannarelli, V. Greco, and R. Rapp, Phys. Rev. Lett. 100, 192301 (2008).

[14] R. Sharma, I. Vitev, B. Zhang, Phys. Rev. C 80, 054902 (2009).

[15] W. A. Horowitz, J.Phys. G35 044025 (2008).

[16] J. Uphoff, O. Fochler, Z. Xu, and C. Greiner, Phys. Lett. B717, 430 (2012).

[17] M. He, R. J. Fries, and R. Rapp, Phys. Rev. C78, 014904 (2008).

[18] P. Gossiaux, J. Aichelin, T. Gousset, and V. Guiho, J.Phys. G37, 094019 (2010).

[19] Gossiaux, J. Aichelin, T. Gousset, and V. Guiho, J.Phys. G37 094019 (2010).

[20] L.Adamczyk et al. (STAR Collaboration), arXiv:1405.6348 (2014).

[21] J. Uphoff, O. Fochler, Z. Xu, C. Greiner, Phys.Rev. C84 024908 (2011).

[22] J. Uphoff, O. Fochler, Z. Xu, C. Greiner, Phys.Lett. B717 430–435 (2012).

[23] M. He, R. J. Fries, and R. Rapp, Phys.Rev. C86 014903 (2012).

[24] J. Aichelin 1, P.B. Gossiaux, T. Gousset, J. Phys.: Conf. Ser. 455 012046 (2013).

[25] A. D. Frawley, T. Ullrich, and R. Vogt, Phys. Rept. 462, 125 (2008).

[26] L. Adamczyk et al. (STAR Collaboration), arXiv:1404.6185 (2014).

[27] M. Cacciari, M. Greco, P. Nason, JHEP 9805:007 (1998).

[28] P. Nason, S. Dawson and R. K. Ellis, Nucl. Phys. B 303, 607 (1988).

[29] W. Beenakker, W. L. van Neerven, R. Meng, G. A. Schuler and J. Smith, Nucl. Phys. B 351, 507 (1991).

[30] M. Cacciari, P. Nason and R. Vogt, Phys. Rev. Lett. 95, 122001 (2005).

[31] L. Adamczyk et al., Phys. Rev. D 86, 072013 (2012).

[32] M. Cacciari and P. Nason, Phys. Rev. Lett. 89, 122003 (2002).

[33] M. Cacciari, S. Frixione, M. L. Mangano, P. Nason and G. Ridolfi, JHEP 0407, 033 (2004).

[34] M. Cacciari and P. Nason, JHEP 0309, 006 (2003).

[35] A. D. Frawley, T. Ullrich, and R. Vogt, Phys. Rept. 462, 125-175 (2008).

[36] H. Agakishiev et al. (STAR Collaboration), Phys. Rev. D83, 052006,(2011).

[37] A.Adare et al. (PHENIX Collaboration), , Phys. Rev. C84, 044905 (2011).

[38] M. M. Aggarwal et al. (STAR Collaboration), Phys. Rev. Lett. 105, 202301 (2010).

[39] N. Armesto, Nuclear shadowing, J. Phys. G32 R367-R394 (2006).

[40] A. Accardi, J. L. Albacete, M. Anselmino et al., JLAB-PHY-12-1652 (2014).

[41] K. J. Eskola, H. Paukkunen, and C. A. Salgado, JHEP 04, 065 (2009).

[42] I. Helenius, K. J. Eskola, H. Honkanen, and C. A. Salgado, JHEP 1207, 073 (2012).

[43] B. I. Abelev et al. [STAR Collaboration], Phys.Rev.Lett. 98, 192301 (2007); Erratum-ibid. 106, 159902 (2011).

[44] Adamczyk et al. (STAR Collaboration), arXiv:1405.6348 (2014).

[45] A. Adare et al. (PHENIX collaboration), Phys. Rev. C 90, 034903 (2014).

[46] A. Adare et al. (PHENIX collaboration), arXiv:1405.3301 (2014).

[47] A. Adare et al. (PHENIX collaboration), Phys. Rev. Lett. 109, 242301 (2012).

[48] R. Sharma, I. Vitev, and B.-W. Zhang, Phys. Rev. C 80 054902 (2009).

[49] B. Abelev et al. (ALICE Collaboration), arXiv:1405.4117 (2014).

[50] M.Cacciari, M. Greco, and P. Nason, JHEP, 9805:007 (1998).

[51] M.Cacciari, S. Frixione, and P. Nason, JHEP, 0103:006 (2001).

[52] B.A. Kniehl, G. Kramer, I. Schienbein, and H. Spiesberger. Eur.Phys.J., C72:2082, (2012).

[53] P. Bolzoni and G. Kramer. Nuclear Physics B, 872(2):253 – 264, (2013).

[54] P. Bolzoni and G. Kramer. Nuclear Physics B, 876(1):334 – 337, (2013).

[55] [40]R. Maciuła and A. Szczurek. Phys.Rev., D87:094022, (2013).

[56] Andrea Festanti (ALICE Collaboration), arXiv:1407.6541 (2014).

[57] Shuang Li (ALICE Collaboration), arXiv:1408.1915 (2014).

[58] J.Wolf et al. (STAR Collaboration), STAR detector overview (2003).

[59] L.Ruan et al., J. Phys. G Nucl. Part. Phys. 36, 095001 (2009).

[60] M. Harisson et al., RHIC project overview, Nucl. Instr. and Meth. A 499 235 (2003).

[61] Grazyna Odyniec (STAR Collaboration), Journal of Phys, Conference Series 455, 010237 (2013).

[62] http://www.rhichome.bnl.gov/RHIC/Runs/ [online 1/31/2014].

[63] P. Fachini, Zhangbu Xu et al. (STAR TOF Collaboration), STAR TOF Proposal (2004).

[64] M. Anderson et al. (STAR Collaboration), Nucl. Instrum. Meth. A499 (2003).

[65] Hans Bichsel (STAR Collaboration), Particle identification at STAR-TPC with ionization measurements (2003).

[66] K.H. Ackermann et al. (STAR Collaboration), Nucl. Instrum. Meth. A499 (2003).

[67] M. Sharma, A study of fluctuations in ultra-relativistic heavy ion collisions, PhD thesis, Panjab University, (2008.)

[68] Ming Shao, Olga Barannikova et al. (STAR Collaboration), Nucl. Instrum. Meth. A558 (2006).

[69] The STAR TOF Collaboration, Proposal for a large area time of flight system for STAR, (2004).

[70] M.C.S. Williams, Nucl. Phys. A 698, 464 (2002).

[71] M.Beddo et al. (STAR Collaboration), The STAR Barrel Electromagnetic Calorimeter (2002).

[72] W. J. Llope et al., The STAR Vertex Position Detector, arXiv:1403.6855 (2014).

[73] The STAR Heavy Flavor Tracker, Technical Design Report, (2011).

[74] Giacomo Contin, ICHEP 2014, Valencia, (2014).

[75] J. Adams et al. (STAR Collaboration), Phys. Rev. Lett. 105, 202301 (2010).

[76] Ming Shao, PhD thesis, MExtensive particle identification with TPC and TOF at the STAR experiment, University of Science and Technology of China, (2006).

[77] Barbara Trzeciak, private communication.

[78] A. Adare et al. (PHENIX Collaboration), Phys. Rev. Lett. 104, 132301 (2010).

[79] www.star.bnl.gov/protected/heavy/ullrich/jpsiee.pdf [online 1/31/2014].

[80] H. Agakishiev et al. (STAR Collaboration), PRC80, 41902 (2009).

[81] A. Adare et al. (PHENIX collaboration), Phys. Rev. Lett. 98, 232002 (2007).

[82] www.star.bnl.gov/protected/lfspectra/cjena [online 1/31/2014].

List of Publications

Presentations

- 2014 - Hot Quarks 2014, Spain, Non-Photonic Electron Measurement With STAR Experiment
- 2013 - High Energy Physics in the LHC Era, Valparaiso, Chile, STAR results of non-photonic electrons measurement in p+p and Au+Au collisions.
- 2013 - European Physical Society Conference on High Energy Physics, Stockholm, Sweden, The measurement of non-photonic electrons at STAR.
- 2013 - 51st International Winter Meeting on Nuclear Physics, Bormio, Italy, The measurement of non-photonic electrons at STAR.
- 2012 - Hard Probes, Cagliari, Italy, The measurement of non-photonic electrons in STAR.
- 2012 - Winter Workshop on Nuclear Dynamics, Dorado del Mar, Puerto Rico, J/ψ measurement at STAR.
- 2011 - Czech and Slovak physicist conference, Žilina, Slovakia, Quarkonia measurement at STAR.
- 2011 - Students scientific conference, Ostrava, Czech Republic, Charmonia at STAR.

Posters

- 2014 - Quark Matter, Darmstad, Germany, Measurements Of Non-Photonic Electron Production And Correlation With STAR Experiment.

Publications

- L. Adamczyk et al. (STAR Collaboration), Heavy Flavor Electron production and azimuthal anisotropy in Au+Au collisions at $\sqrt{s_N N} = 200$ GeV, in collaboration review, to be submitted to Phys.Rev.C (2014)

- Olga Rusňáková for STAR Collaboration, Measurements of non-photonic electrons with the STAR experiment, proceedings of the Hot Quarks 2014, accepted, arxiv 1412.2112 (2014).

- Olga Rusňáková for STAR Collaboration, The measurement of non-photonic electrons in Star, proceedings of the 2013 European Physical Society Conference on High Energy Physics, PoS(EPS-HEP 2013)177

- Olga Hájková (Rusňáková) for STAR Collaboration, The measurement of non-photonic electrons in STAR, Proceedings of 51st International Winter Meeting on Nuclear Physics, PoS(Bormio 2013)050

- Olga Hájková (Rusňáková) for STAR Collaboration, The measurement of non-photonic electrons in STAR, Proceedings of Hard Probes 2012, Nucl.Phys. A910-911 (2013) 387-390.

- Olga Hájková (Rusňáková) for STAR Collaboration, J/ψ measurement at STAR, Proceedings of Winter Workshop on Nuclear Dynamics 2012, J. Phys.: Conf. Ser. 389 012030

- Olga Hájková (Rusňáková) for STAR Collaboration, Quarkonia measurement at STAR, Proceedings of Czech and Slovak physicist conference, 2011

- Olga Hájková (Rusňáková) for STAR Collaboration, Charmonia at STAR, Proceedings of Students scientific conference, 2011

Collaboration articles

- L. Adamczyk et al. (STAR Collaboration), Dielectron Azimuthal Anisotropy at mid-rapidity in Au+Au collisions at $\sqrt{s_N N} = 200$ GeV, arXiv:1402.1791

- L. Adamczyk et al. (STAR Collaboration), Beam-Energy Dependence of Directed Flow of Protons, Antiprotons and Pions in Au+Au Collisions, arXiv:1401.3043

- L. Adamczyk et al. (STAR Collaboration), Beam energy dependence of moments of the net-charge multiplicity distributions in Au+Au collisions at RHIC, arXiv:1402.1558

- L. Adamczyk et al. (STAR Collaboration), Dielectron Mass Spectra from Au+Au Collisions at $\sqrt{s_N N}$ = 200 GeV, arXiv:1312.7397
- L. Adamczyk et al. (STAR Collaboration), Suppression of Upsilon Production in d+Au and Au+Au Collisions at $\sqrt{s_N N}$ = 200 GeV, arXiv:1312.3675
- L. Adamczyk et al. (STAR Collaboration), J/ψ polarization in p+p collisions at $\sqrt{s}$ = 200 GeV in STAR, arXiv:1311.1621
- L. Adamczyk et al. (STAR Collaboration), J/ψ production at low pT in Au+Au and Cu+Cu collisions at $\sqrt{s_N N}$ =200 GeV at STAR, arXiv:1310.3563
- L. Adamczyk et al. (STAR Collaboration), Energy Dependence of Moments of Net-proton Multiplicity Distributions at RHIC, Phys.Rev.Lett. 112 (2014) 032302
- L. Adamczyk et al. (STAR Collaboration), Neutral pion cross section and spin asymmetries at intermediate pseudorapidity in polarized proton collisions at sqrts = 200 GeV, Phys.Rev. D89 (2014) 012001
- L. Adamczyk et al. (STAR Collaboration), Measurement of Charge Multiplicity Asymmetry Correlations in High Energy Nucleus-Nucleus Collisions at 200 GeV, arXiv:1303.0901
- L. Adamczyk et al. (STAR Collaboration), Jet-Hadron Correlations in $\sqrt{s}$ =200 GeV Au+Au and p+p Collisions, arXiv:1302.6184
- L. Adamczyk et al. (STAR Collaboration), Fluctuations of charge separation perpendicular to the event plane and local parity violation in sNN$\sqrt{}$=200 GeV Au+Au collisions at RHIC, arXiv:1302.3802
- L. Adamczyk et al. (STAR Collaboration), Freeze-out Dynamics via Charged Kaon Femtoscopy in $\sqrt{s_N N}$ =200 GeV Central Au+Au Collisions, Phys.Rev. C88 (2013) 034906
- L. Adamczyk et al. (STAR Collaboration), System Size Dependence of Transverse Momentum Correlations at RHIC, Phys.Rev. C87 (2013) 064902
- L. Adamczyk et al. (STAR Collaboration), Elliptic flow of identified hadrons in Au+Au collisions at $\sqrt{s_N N}$ =7.7-62.4 GeV, Phys.Rev. C88 (2013) 1, 014902

- L. Adamczyk et al. (STAR Collaboration), Observation of an energy-dependent difference in elliptic flow between particles and anti-particles in relativistic heavy ion collisions, Phys.Rev.Lett. 110 (2013) 142301

- L. Adamczyk et al. (STAR Collaboration), Third Harmonic Flow of Charged Particles in Au+Au Collisions at $\sqrt{s_N N}$ =200 GeV, Phys.Rev. C88 (2013) 014904

- L. Adamczyk et al. (STAR Collaboration), Measurement of J/ψ Azimuthal Anisotropy in Au+Au Collisions at $\sqrt{s_N N}$ =200 GeV, Phys.Rev.Lett. 111 (2013) 052301

- L. Adamczyk et al. (STAR Collaboration), Experimental studies of di-jets in Au + Au collisions using angular correlations with respect to back-to-back leading hadrons, Phys.Rev. C87 (2013) 4, 044903

- L. Adamczyk et al. (STAR Collaboration), J/ψ production at high transverse momenta in p+p and Au+Au collisions at $\sqrt{s_{NN}}$ =200 GeV., arXiv:1208.2736

- L. Adamczyk et al. (STAR Collaboration), Inclusive charged hadron elliptic flow in Au + Au collisions at $\sqrt{s_{NN}}$ = 7.7 - 39 GeV., arXiv:1206.5528

- L. Adamczyk et al. (STAR Collaboration), Single Spin Asymmetry AN in Polarized Proton-Proton Elastic Scattering at $\sqrt{s}$ =200 GeV., arXiv:1206.1928

- L. Adamczyk et al. (STAR Collaboration), Transverse Single-Spin Asymmetry and Cross-Section for π_0 and η Mesons at Large Feynman-x in Polarized p+p Collisions at 200 GeV, Phys.Rev. D86 (2012) 051101

- L. Adamczyk et al. (STAR Collaboration), Longitudinal and transverse spin asymmetries for inclusive jet production at mid-rapidity in polarized p+p collisions at $\sqrt{s}$ =200 GeV., Phys.Rev. D86 (2012) 032006

- L. Adamczyk et al. (STAR Collaboration), Measurements of D0 and D$*$ Production in p+p Collisions at $\sqrt{s}$ =200 GeV., arXiv:1204.4244

- L. Adamczyk et al. (STAR Collaboration), Di-electron spectrum at mid-rapidity in p+p collisions at $\sqrt{s}$ =200 GeV., Phys.Rev. C86 (2012) 024906

- L. Adamczyk et al. (STAR Collaboration), Directed Flow of Identified Particles in Au + Au Collisions at $\sqrt{s_{NN}}$ = GeV at RHIC., Phys.Rev.Lett. 108 (2012) 202301

- L. Adamczyk et al. (STAR Collaboration), Measurement of the W $\rightarrow$ and Z/$\gamma\star$ $\rightarrow$e+e$-$ Production Cross Sections at Mid-rapidity in Proton-Proton Collisions at $\sqrt{s}$ =500 GeV., Phys.Rev. D85 (2012) 092010

- G. Agakishiev et al. (STAR Collaboration), Energy and system-size dependence of two- and four-particle v2 measurements in heavy-ion collisions at RHIC and their implications on flow fluctuations and nonflow., Phys.Rev. C86 (2012) 014904

- G. Agakishievk et al. (STAR Collaboration), System size and energy dependence of near-side di-hadron correlations., Phys.Rev. C85 (2012) 014903

- G. Agakishiev et al. (STAR Collaboration), Identified hadron compositions in p+p and Au+Au collisions at high transverse momenta at $\sqrt{s_{NN}}$ =200 GeV., Phys.Rev.Lett. 108 (2012) 072302

- G. Agakishiev et al. (STAR Collaboration), Directed and elliptic flow of charged particles in Cu+Cu collisions at $\sqrt{s_{NN}}$ =22.4 GeV., Phys.Rev. C85 (2012) 014901

- G. Agakishiev et al. (STAR Collaboration), Anomalous centrality evolution of two-particle angular correlations from Au-Au collisions at $\sqrt{s_{NN}}$ =62 and 200 GeV., arXiv:1109.4380

- G. Agakishiev et al. (STAR Collaboration), ρ0 Photoproduction in AuAu Collisions at $\sqrt{s_{NN}}$ =62.4 GeV with STAR., Phys.Rev. C85 (2012) 014910

- G. Agakishiev et al. (STAR Collaboration), Strangeness Enhancement in Cu+Cu and Au+Au Collisions at $\sqrt{s_{NN}}$ =200 GeV., Phys.Rev.Lett. 108 (2012) 072301

- G. Agakishiev et al. (STAR Collaboration), Evolution of the differential transverse momentum correlation function with centrality in Au+Au collisions at $\sqrt{s_{NN}}$ =200 GeV., Phys.Lett. B704 (2011) 467-473

- G. Agakishiev et al. (STAR Collaboration), Observation of the antimatter helium-4 nucleus., Nature 473 (2011) 353, Erratum-ibid. 475 (2011) 412
- G. Agakishiev et al. (STAR Collaboration), High pT non-photonic electron production in p+p collisions at$\sqrt{s}$ =200 GeV., Phys.Rev. D83 (2011) 052006
- G. Agakishiev et al. (STAR Collaboration), Studies of di-jet survival and surface emission bias in Au+Au collisions via angular correlations with respect to back-to-back leading hadrons., Phys.Rev. C83 (2011) 061901
- G. Agakishiev et al. (STAR Collaboration), Measurements of Dihadron Correlations Relative to the Event Plane in Au+Au Collisions at $\sqrt{s_{NN}}$ =200 GeV., arXiv:1010.0690
- M.M. Aggarwal et al. (STAR Collaboration), Strange and Multi-strange Particle Production in Au+Au Collisions at $\sqrt{s_{NN}}$ =62.4 GeV., Phys.Rev. C83 (2011) 024901

Published Papers

Following pages contain full texts of published papers.

J/ measurements in STAR Experiment at RHIC

2012 J. Phys.: Conf. Ser. 389 012030

(http://iopscience.iop.org/1742-6596/389/1/012030)

Journal of Physics: Conference Series **389** (2012) 012030 doi:10.1088/1742-6596/389/1/012030

J/ψ measurements in STAR Experiment at RHIC

Olga Hájková for the STAR Collaboration

Czech Technical University in Prague, Faculty of Nuclear Sciences and Physical Engineering, Behov 7, 11519, Prague 1, Czech Republic

E-mail: olga.hajkova@fjfi.cvut.cz

Abstract. During the last decade STAR experiment has studied the hot and dense nuclear matter produced in heavy ion collisions at RHIC. The study of quarkonia, such as J/ψ meson, production provides the information about properties of this nuclear matter. It is predicted that due to the Debye screening the quarkonia production is suppressed when Quark Gluon Plasma (QGP) is presented. In order to understand the properties of hot and dense nuclear matter, it is necessary to study the production of quarkonia in hadron-hadron, hadron-ion, and ion-ion collisions separately to distinguish cold nuclear matter effect, such as gluon shadowing, from the suppression due to the formation of QGP. Moreover, the J/ψ hadron azimuthal correlations allow to extract the fraction of J/ψ that originates from B-mesons. This proceedings presents recent J/ψ measurements at mid-rapidity in p+p, and Au+Au collisions at $\sqrt{s_{NN}} = 200$ GeV at STAR, the fraction of J/ψ originates from B-mesons, and J/ψ eliptic flow v_2 as a function of transverse momentum in Au+Au collisions in $\sqrt{s_{NN}} = 200$ GeV at STAR.

1. Introduction

The strongly interacting matter at sufficiently high density or temperature undergoes a phase transition from the hadronic matter to a new state, so-called quark gluon plasma (QGP), when quarks are no longer confined into color neutral bound states. One of the probes, proposed by Matsui and Satz [1], for searching for QGP and for investigating its properties is a study of the quarkonia production. It is predicted that due to the color screening the quarkonia production is suppressed when QGP is presented at sufficiently high temperature. Before resolving whether QGP was formed or not, it is necessary to study the production of J/ψ in hadron-hadron, hadron-ion and ion-ion collisions separately to distinguish cold nuclear matter effects from the suppression due to the formation of QGP. Other effect which play the important role in J/ψ production is recombination from charm quarks [2] [3]. It is expected that in the high-p_T region the J/ψ production is less influenced by the cold nuclear matter effects and charm quark recombination effect. Therefore study of J/ψ production in high-p_T region provides a cleaner probe to search for evidence of color-screening effect [4] [5] [6]. STAR previous measurement in high-p_T region in Cu+Cu colisions shows no suppression, but the measurement of larger system such as Au+Au is necessary to interpret these results.

In this proceedings the measurements of low-p_T and high-p_T J/ψ spectra in p+p and in Au+Au collisons at $\sqrt{s}$=200 GeV in the years 2009 and 2010 in STAR are presented. We also present the measurement of J/ψ elliptic flow v_2 in semi-central collisions in Au+Au collisions.

2. Analysis

Data reported in this proceedings were collected in p+p collisions at $\sqrt{s}$=200 GeV in the year 2009 and in Au+Au collisions at $\sqrt{s_{NN}}$=200 GeV in the year 2010 with Minimum Bias Trigger for low p_T J/ψ, and with High Tower Trigger for high p_T J/ψ. Main detectors used in presented measurements are the Time Projection Chamber (TPC), which is the main charged particle tracking device in the STAR detector used for particle identification and momentum determination, the Barrel Electromagnetic Calorimeter (BEMC), which is used for deposited energy measurement, Barrel Shower Maximum Detector (BSMD) and also as a trigger detector, and the Time Of Flight (TOF). TOF was completely installed and full functional in year 2010 Au+Au run. During the year 2009 p+p run, 72% of TOF trays was installed. TPC and TOF together are great tool for distinguish electrons and hadrons from low to high p_T region. J/ψ were reconstructed through its dilepton decay channel, J/$\psi \rightarrow e^+ + e^-$ with branching ratio 5.9%.

3. J/ψ spectra in p+p and Au+Au collisions

Figure 1 (left) shows the J/ψ invariant mass distribution in p+p collisions at $\sqrt{s}$=200 GeV in the year 2009. Background was reconstructed via like-sign method, unlike-sign signal (solid circles) and background (gray band). We reconstructed 376 J/ψ in high p_T region ($4 < p_T < 12$ GeV/c), with very suitable signal over background ratio $S/B = 22$. As high S/B ratio is very useful for J/ψ-hadron correlation study. Figure 1 (right) shows the fully corrected J/ψ p_T spectra in p+p collisions at $\sqrt{s}$=200 GeV in the year 2009. STAR and PHENIX results are consistent with each other. The solid magenta line shows the calculation from Color Evaporation Model (CEM) [8].

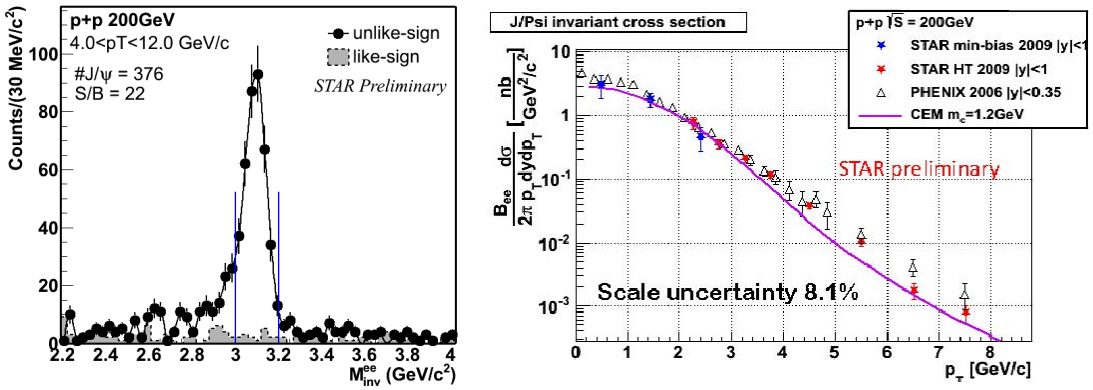

Figure 1. Left: High p_T J/ψ invariant mass distribution in p+p collisions at 200 GeV in the year 2009 reconstructed via dilepton decay channel. Right: Fully correlated J/ψ p_T spectra in p+p collisions in the year 2009. Low p_T spectra reconstructed from Minimum Bias Trigger events (blue stars) and high p_T spectra reconstructed from High Tower Trigger events (red stars). Magenta solid line shows the calculation from Color Evaporation Model (CEM) [7] [8].

Figure 2 (left) shows the high p_T J/ψ invariant mass distribution in Au+Au collisions at $\sqrt{s_{NN}}$=200 GeV in the year 2010. Figure 2 (right) shows fully corrected J/ψ p_T spectra in Au+Au collisions at $\sqrt{s_N N}$=200 GeV with different centralities. STAR and PHENIX results are consistent with each other in their overlapping p_T region, we extend our results p_T region up to 10 GeV/c [3]. The solid and dash-dotted lines present Tsallis Blast-Wave model (TBW) fit to the STAR data points and TBW theoretical predictions which assuming the same radial flow and freeze-out conditions for J/ψ as for light hadrons. Measured spectra do not follow the TBW model predictions from light hadrons in low p_T region [9]. This could indicate significant contribution to the J/ψ spectra from charm quark recombination at low p_T or small J/ψ radial flow.

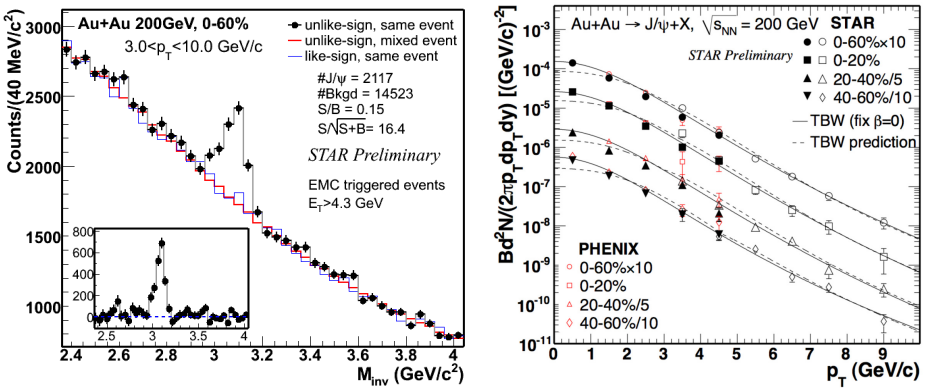

Figure 2. Left: High p_T J/ψ invariant mass distribution in Au+Au collisions at $\sqrt{s}$=200 GeV in the year 2010. Right: Fully correlated J/ψ p_T spectra in Au+Au collisions for different centralities. Solid and dash-dotted lines represent TBW fit to the STAR data points and TBW theoretical predictions respectively [3] [9].

4. J/ψ nuclear modification factor R_{AA}

Figure 3 (left) shows the J/ψ nuclear modification factor R_{AA} in Au+Au collisions at $\sqrt{s_{NN}}$ = 200 GeV as a function of the number of participants for low-p_T and high-p_T J/ψ separately. The result in Cu+Cu collisions at $\sqrt{s_{NN}}$ = 200 GeV for high-p_T is also plotted [10]. Both results for high-p_T J/ψ are consistent with each other, and they show no suppresion in semi-central collisions. In central collisions high-p_T J/ψ is significantly suppresed. The low-p_T J/ψ measurements show suppresion in both, central and semi-central collisions. Low p_T PHENIX results are also plotted and are consistent with low-p_T STAR results [3]. Figure 3 (right) shows the J/ψ nuclear modification factor R_{AA} in Au+Au collisions at $\sqrt{s_{NN}}$ = 200 GeV as a function of p_T for 0-20% central and semicentral (40-60%) collisions separately. The solid and dashed lines represent theoretical calculation include both primordial production or regeneration from charm quarks [11] [12].

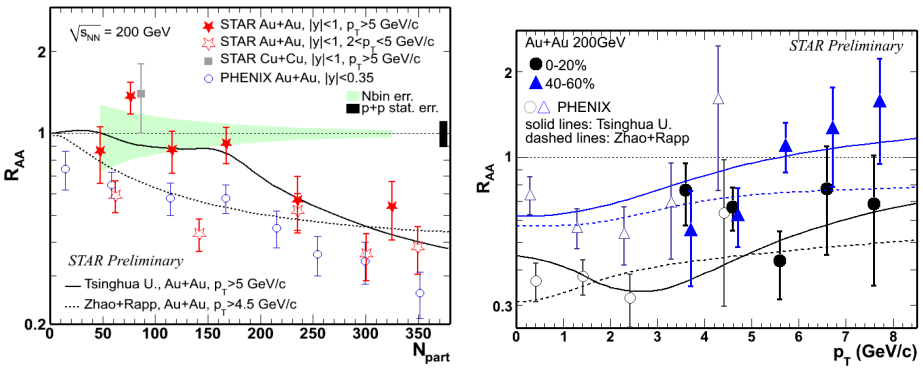

Figure 3. Left: J/ψ nuclear modification factor (R_{AA}) in Au+Au collisions at $\sqrt{s_{NN}}$ = 200 GeV as a function of multiplicity for low p_T (openstars) and high p_T (fullstars). The gray square presents the result in Cu+Cu collisions at $\sqrt{s_{NN}}$ = 200 GeV. The solid and the dashed lines represent theoretical calculations [10] [11] [12]. Right: J/ψ nuclear modification factor (R_{AA}) as a function of p_T in central (0-20%, black circles) and semi-central (40-60%, blue triangles) collisions. The solid and the dashed lines represent theoretical calculations [11] [12].

5. J/ψ elliptic flow v_2

Figure 4 shows J/ψ v_2 as a function of p_T for semi-central Au+Au collisions at $\sqrt{s_{NN}} = 200$ GeV. The data points are plotted as black points, lines are represent different theoretical models. J/ψ v_2 is consistent with zero at high-p_T and disfavors the scenario that coalescence from thermalized charm quarks dominate J/ψ production at $p_T > 2$ GeV/c [13] - [18].

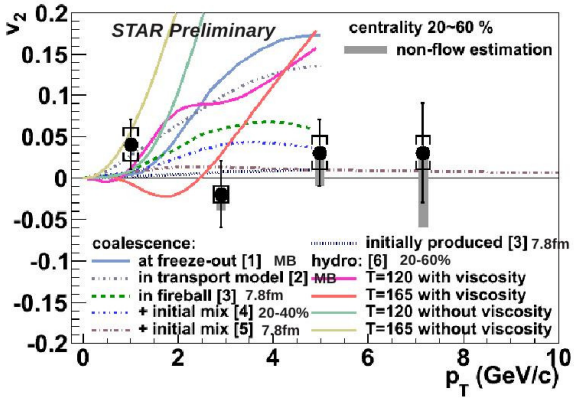

Figure 4. J/ψ v_2 as a function of p_T for semi-central Au+Au collisions (20-60%), lines represent theoretical models [13] - [18]

6. Summary and Outlook

In this proceedings, results of J/ψ measurements in p+p collisions at $\sqrt{s}$=200 GeV and in Au+Au collisions at $\sqrt{s_{NN}}$=200 GeV from STAR are presented. The measurement of nuclear modification factor indicates that suppression in high-p_T region is smaller than in low-p_T region. The preliminary results of J/ψ v_2 show that elliptic flow v_2 is consistent with zero at high-p_T and disfavors the scenario that coalescence from thermalized charm quarks dominate J/ψ production at $p_T > 2$ GeV/c.

This work was supported by grant INGO LA09013 of the Ministry of Education, Youth and Sports of the Czech Republic, and by the Grant Agency of the Czech Technical University in Prague, grant No. SGS10/292/OHK4/3T/14 .

[1] T. Matsui, H. Satz, Phys. Lett. B 178 (1986) 416.
[2] M. C. Abreu et al., Phys. Lett. B 499 (2001) 8596.
[3] A. Adare et al., Phys. Rev. Lett. 98 (2007) 232301.
[4] Y.-p. Liu, Z. Qu, N. Xu, P.-f. Zhuang, Phys. Lett. B 678 (2009) 7276.
[5] X. Zhao, R. Rapp, Phys. Rev. C 82 (2010) 064905.
[6] H. Liu, K. Rajagopal, U.A.Wiedemann, Phys. Rev. Lett. 98 (2007) 182301.
[7] A. Adare et al., Phys. Rev. D 82,(2010) 012001.
[8] M. Bedjidian, et al., hep-ph/0311048.
[9] Z.Tang et al., arXiv:1101.1912, JPG 37, 08194 (2010).
[10] B. I. Abelev et al., Phys. Rev. C 80 (2009) 41902.
[11] Y.-p. Liu, Z. Qu, N. Xu, P.-f. Zhuang, Phys. Lett. B 678 (2009) 7276.
[12] X. Zhao, R. Rapp, Phys. Rev. C 82 (2010) 064905.
[13] V. Greco, C.M. Ko, R. Rapp, Phys. Lett. B 595 (2004) 202.
[14] L. Ravagli, R. Rapp, Phys. Lett. B 655, (2007) 126.
[15] L. Yan, P. Zhuang, N. Xu, Phys. Rev. Lett. 97, (2006) 232301.
[16] X. Zhao, R. Rapp, 24th WWND (2008).
[17] Y. Liu, N. Xu, P. Zhuang, Nucl. Phy. A 834, (2010) 317.
[18] U. Heinz, C. Shen, private communication.

PROCEEDINGS OF SCIENCE

The measurement of non-photonic electrons in STAR

Olga Hájková for the STAR Collaboration*
Czech Technical University in Prague, Faculty of Nuclear Sciences and Physical Engineering, Břehová 7, 11519, Prague 1, Czech Republic
E-mail: olga.hajkova@fjfi.cvut.cz

The measurements of non-photonic electrons, produced by semileptonic decays of D and B mesons, provide information on heavy quarks production as well as hot and dense nuclear matter created in relativistic in heavy ion collisions. In this proceedings we present the recent measurements of non-photonic production in p+p collisions at $\sqrt{s} = 200$ GeV and its suppression in Au+Au at $\sqrt{s_{NN}} = 200$ GeV, and azimuthal anisotropy at $\sqrt{s_{NN}} = 200$ GeV.

International Winter Meeting on Nuclear Physics,
21-25 January 2013
Bormio, Italy

*Speaker.

PoS(Bormio 2013)050

1. Introduction

Due to their large masses, heavy quarks are produced mainly during initial parton-parton interaction at RHIC, and they are good probes to study QCD matter. Study of heavy flavor production in p+p collisions is a test of the validity of the perturbative QCD. It is also used as a baseline to study the effects of hot and dense nuclear matter on the production of heavy quarks in heavy ion collisions [1]. These hot nuclear matter effects, as well as cold nuclear matter effects, are quantified with nuclear modification factor (R_{AA}). R_{AA} is defined as a ratio of the particle production in nucleus-nucleus collisions to the production in proton-proton collisions, scaled by the average number of binary collisions for a given centrality. R_{AA} can provide information about heavy quark energy loss

At RHIC, heavy quarks could be studied by non-photonic electrons (NPE) measurement, products of semi-leptonic heavy flavor decays or by study of D mesons production [2] [3]. For better understanding of the heavy quark interaction with the medium, it is important to have separate measurements on charm and bottom production. This could be done in p+p collisions via non-photonic electrons and charged hadrons azimuthal correlations, taking into account the fact that near side correlations have different shape for electrons from D and B decays [4]. Measurement of NPE azimuthal anisotropy, especially elliptic flow (v_2), is necessary to distinguish between different energy loss scenarios and can be a good proxy to reveal heavy flavor collectivity, which can improve our understanding of the medium thermalization. In this proceedings we present the recent measurements of NPE production in p+p collisions at $\sqrt{s} = 200$ GeV and its suppression in Au+Au $\sqrt{s} = 200$ GeV, and azimuthal anisotropy at $\sqrt{s_{NN}} = 200$ GeV.

2. Analysis

Data reported in this proceedings were collected in p+p collisions at $\sqrt{s} = 200$, and 500 GeV in the years 2005, 2008, and 2009 with High Tower Triggers (high-pT electron triggers), and in Au+Au collisions at $\sqrt{s_{NN}} = 200$ GeV in the year 2010 with Minimum Bias Trigger and High Tower Triggers, where Minimum Bias Triggered data were used for $p_T < 2$ GeV/c results while High Tower Triggered data were used for $p_T > 2$ GeV results.

Main detectors used in presented measurements are the Time Projection Chamber (TPC), the main charged particle tracking device in the STAR detector used for particle identification and momentum determination, the Barrel Electromagnetic Calorimeter (BEMC), used for deposited energy measurement, and also as a trigger detector, and the Barrel Shower Maximum Detector (BSMD). Hadron contamination at low p_T was minimized using information from Time Of Flight (ToF) detector. At low-pT, Electron candidates were identified via specific ionization energy loss from the TPC combined with ToF information. Electrons at high-pT are selected using the ratio of track momentum to the energy deposited in the BEMC, the BSMD shower profile, and the distance between TPC track projected position at BEMC and reconstructed BEMC cluster position. The obtained inclusive electron sample includes non-photonic electrons, photonic electrons background, and hadron contamination. Non-photonic electrons yield is calculated as: $N_{NPE} = N_{Inclusive} * \varepsilon_{purity} - N_{PHE}/\varepsilon_{photonic}$, where N_{NPE} is non-photonic electrons yield, $N_{Inclusive}$ represents all electron candidates yield, ε_{purity} is a purity of inclusive electron sample, N_{PHE} is

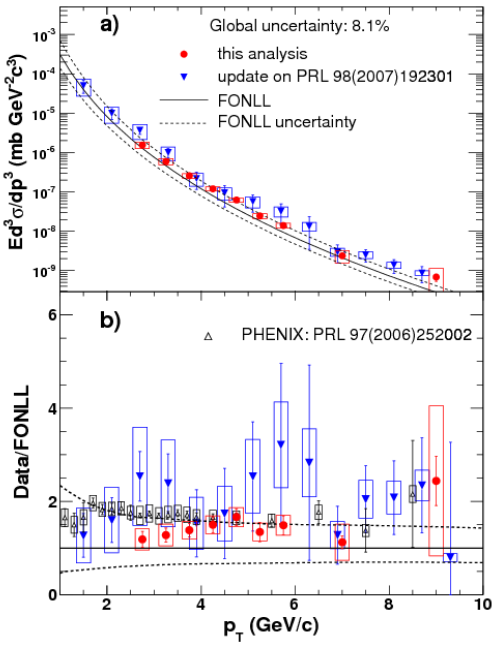

Figure 1: Top: Invariant cross section of non-photonic electrons after combining results from the years 2005 and 2008 (red circles). Taken from [5]. Bottom: The combined data results over FONLL ratio [5] [7].

yield of reconstructed photonic electron background, which mainly comes from photon conversion in the detector material and from Dalitz decay of π^0 and η mesons, and $\varepsilon_{photonic}$ is photonic electron reconstruction efficiency. This efficiency is determined by embedding simulated gammas and pi^0 into real data. The photonic electron reconstruction efficiency is found to be 0.3 - 0.7 and increases with p_T [5].

3. Non-photonic electrons in p+p collisions

Non-photonic electrons spectra were measured in the years 2005 and 2008. In the year 2005 the STAR detector setup included the silicon vertex detector in front of the TPC that led to much more gamma conversion background, and consequently to significantly lower NPE/PHE ratio, where PHE is photonic electron background. Despite of the large difference in photonic background, results from the years 2005 and 2008 agree with each other. After combining both results, the invariant cross section of non-photonic electron production in p+p collisions was obtained and compared with the FONLL calculation [7] - see Figure 1 (up). In Figure 1 (down) the data over FONLL ratio are shown. Data from PHENIX and corrected results from the year 2003 are shown there as well. All these results agree with each other [5] [6].

Non-photonic electrons originate dominantly from semi-leptonic decays of D and B mesons. Due to the different charm and bottom quark mass and consequently different decay kinematics, NPE from these two sources could be separated via charged hadron-NPE azimuthal correlations study. Relative B meson contribution to NPE could be obtained by comparing NPE-hadron correlations from data with PYTHIA calculation (Figure 2 left). Data results were fitted with PYTHIA templates for the charm and bottom part and with combined shape. In Figure 2 (right) the relative

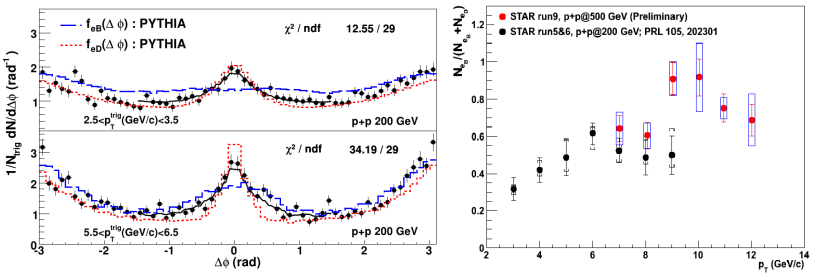

Figure 2: Left: Non-photonic-hadron azimuthal correlations from data in p+p collisions at $\sqrt{s}$=200 GeV (black) compared with PYTHIA simulations of electron(from B/D mesons decays)-hadron correlations (blue dashed and red dotted lines respectively). The black lines are combined fits to the data. Taken from [8]. Right: The relative bottom contribution to NPE electrons in p+p collisions at $\sqrt{s}$=200 GeV (black points), and at $\sqrt{s}$=500 GeV (red points)[8].

B contribution as a function of p_T at $\sqrt{s}$=200 GeV and $\sqrt{s}$=500 GeV is shown. The B decay contribution increases with p_T, and is comparable with the contribution from the D meson decay at p_T higher than 5 GeV/c at $\sqrt{s}$=200 GeV. The ratio of the B contribution to NPE is about 60% for p+p collisions at 500GeV at high p_T. The B contribution is systematically higher at 500 GeV than at 200 GeV in the overlap p_T region.

Using the information of the relative contribution of the bottom to NPE spectra, it is possible to compare the charm as well as the bottom NPE spectra to FONLL calculations. The measured spectra and calculations are consistent [5].

4. Non-photonic electrons in Au+Au collisions

The recent results of non-photonic electron measurements in Au+Au collisions at $\sqrt{s_{NN}}$=200 GeV from the year 2010 are shown in Figures 3 and 4. Figure 3 shows NPE invariant yield in five centrality bins compared with scaled FONLL calculation. The p_T range of results was extended up to 10 GeV/c [10]. The nuclear modification factor (R_{AA}) for 0-10% most central collisions is plotted in Figure 4. For R_{AA} calculation we used p+p results which have been discussed above. Results are compared to a number of theoretical models of energy loss mechanisms [11]-[15]. It is seen that gluon radiation scenario alone (dashed green line) fails to explain large NPE suppression which was observed at high p_T.

Measurements of NPE v_2 in Au+Au collisions at $\sqrt{s_{NN}}$=200 GeV is shown in Figure 5. These results are obtained using 2- ($v_2\{2\}$) and 4- ($v_2\{4\}$) particles correlations and event plane method ($v_2\{EP\}$). All these results are consistent with each other for $p_T < 3$ GeV/c. Finite v_2 at low p_T indicates strong charm-medium interaction. At high p_T we observe increase of v_2 which can arise from jet-like correlations or from path length dependence of heavy quark energy loss.

5. Summary and Outlook

In this proceedings, results of non-photonic electrons measurements in p+p collisions at $\sqrt{s}$=200 GeV and $\sqrt{s_{NN}}$=500 GeV and results of the NPE analysis in Au+Au collisions at $\sqrt{s_{NN}}$=200 GeV from STAR are presented. The preliminary results show large suppression of NPE production

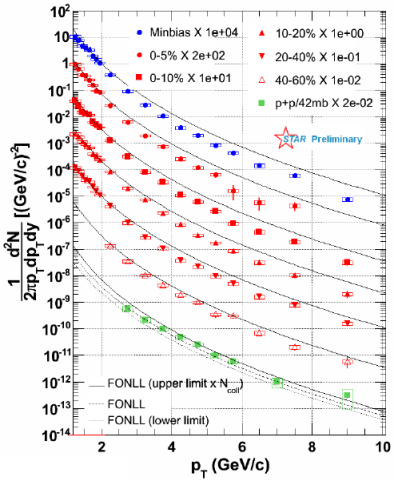

Figure 3: Non-photonic electrons p_T spectra in Au+Au collisions at $\sqrt{s_{NN}}$=200 GeV. Spectrum was divided into 5 centrality bins which are plotted separately. Solid lines represent FONLL calculations scaled by number of binary collisions [10].

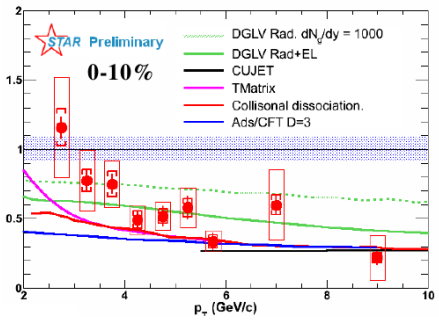

Figure 4: Nuclear modification factor for 0-10% most central collisions compared to theoretical models [11]-[15].

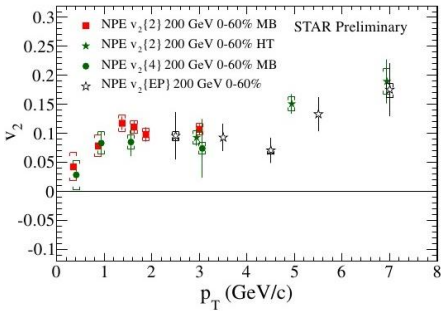

Figure 5: NPE azimuthal anisotropy in Au+Au collisions at $\sqrt{s_{NN}}$=200 GeV [10].

in central Au+Au collisions. This suppression cannnot be explained by gluon radiation scenario alone. Large NPE v_2 was observed at low p_T which indicates a strong charm-medium interaction.

This work was supported by Grant Agency of the Czech Technical University in Prague, grant No. SGS13/215/OHK4/3T/14 and by Grant Agency of the Czech Republic, grant No.13-20841S.

References

[1] A. D. Frawley, T. Ullrich, and R. Vogt, Phys. Rept. 462, 125 (2008).

[2] David Tlusty [STAR Collaboration], arXiv:1211.5995 (2012).

[3] L. Adamczyk et al. [STAR Collaboration], arXiv: 1204.4244 (2011).

[4] J. Adams et al. [STAR Collaboration], Phys. Rev. Lett. 105, 202301 (2010).

[5] H. Agakishiev et al. [STAR Collaboration], Phys. Rev. D83, 052006,(2011).

[6] B. I. Abelev et al. [STAR Collaboration], Phys.Rev.Lett. 98, 192301 (2007); Erratum-ibid. 106, 159902 (2011).

[7] M. Cacciari, P. Nason and R. Vogt, Phys. Rev. Lett. 95, 122001 (2005).

[8] M. M. Aggarwal et al. [STAR Collaboration], Phys. Rev. Lett. 105, 202301 (2010).

[9] J. Adams et al. [STAR Collaboration], Phys. Rev. C 72, 014904 (2005).

[10] M. Mustafa [STAR Collaboration], arXiv:1210.5199, (2012)

[11] M. Djordjevic, M. Gyulassy, R. Vogt, and S. Wicks, Phys. Lett. B 632, 81 (2006).

[12] A. Buzzatti, M. Gyulassi, arXiv:1207.6020.

[13] H. Van Hees, M. Mannarelli, V. Greco, and R. Rapp, Phys. Rev. Lett. 100, 192301 (2008).

[14] R. Sharma, I. Vitev, B. Zhang, Phys. Rev. C 80, 054902 (2009).

[15] W. A. Horowitz, Ph.D thesis, Columbia University, arXiv:1011.4316 (2008).

PROCEEDINGS OF SCIENCE

The measurement of non-photonic electrons in STAR

Olga Rusňáková for the STAR Collaboration*
Czech Technical University in Prague, Faculty of Nuclear Sciences and Physical Engineering, Břehová 7, 11519, Prague 1, Czech Republic
E-mail: olga.hajkova@fjfi.cvut.cz

The measurements of non-photonic electrons, produced by semileptonic decays of D and B mesons, provide information on heavy quarks production in the hot and dense nuclear matter created in relativistic heavy ion collisions. In this proceedings we present the recent measurements of centrality dependence of non-photonic electron p_T distributions, its nuclear modification factor and elliptic flow v_2 in Au+Au collisions at $\sqrt{s_{NN}} = 200$ GeV.

The European Physical Society Conference on High Energy Physics -EPS-HEP2013
18-24 July 2013
Stockholm, Sweden

*Speaker.

PoS(EPS-HEP 2013)177

1. Introduction

The properties of strongly interacting Quark-Gluon Plasma can be studied using heavy quarks, such as charm and bottom. Due to their large masses, heavy quarks are produced mainly during initial parton-parton interaction at RHIC, before the QGP phase, and their production rates can be calculable by pQCD. Thus they are good probes to study the QCD matter [1]. They are expected to interact with the medium differently than the light quarks. Hot and cold nuclear matter effects, which affect the heavy quark production in heavy ion collisions, could be quantified with nuclear modification factor (R_{AA}, R_{dA}) where result from p + p collisions serves as a baseline. At RHIC, heavy quarks could be studied by measuring non-photonic electrons (NPE) which are produced from semi-leptonic heavy flavor decays [2] or by study of D mesons production [3]. Measurements of NPE nuclear modification factor, together with the NPE elliptic flow, are necessary to distinguish between different energy loss scenarios. Elliptic flow measurement can be a good proxy to reveal heavy flavor collectivity, which can improve our understanding of the medium thermalization.

2. Analysis

Data reported in this proceedings were collected in Au+Au collisions at $\sqrt{s_{NN}} = 200$ GeV in the year 2010 with Minimum Bias Trigger and High Tower Triggers, where minimum bias triggered data are used for $p_T < 2$ GeV/c results while High Tower triggered data are used for $p_T > 2$ GeV/c results.

Main detectors used in presented measurements are the Time Projection Chamber (TPC), the main charged particle tracking device in the STAR detector used for particle identification and momentum determination, the Barrel Electromagnetic Calorimeter (BEMC), used for deposited energy measurement and for online trigger, and the Barrel Shower Maximum Detector (BSMD). Hadron contamination at low p_T is minimized using information from Time Of Flight (TOF) detector. At low-p_T, electron candidates are identified via specific ionization energy loss from the TPC combined with ToF information. Electrons at high-p_T are selected using the ratio of track momentum and the energy deposited in the BEMC, the BSMD shower profile, and the distance between TPC track projected position at BEMC and reconstructed BEMC cluster position. The obtained inclusive electron sample includes non-photonic electrons, photonic electrons background, and hadron contamination. Non-photonic electrons yield is calculated as: $N_{NPE} = N_{Inclusive} * \varepsilon_{purity} - N_{PHE}/\varepsilon_{photonic}$, where N_{NPE} is non-photonic electrons yield, $N_{Inclusive}$ represents all electron candidates yield, ε_{purity} is a purity of inclusive electron sample, N_{PHE} is yield of reconstructed photonic electron background, which mainly originates from photon conversion in the detector material and from Dalitz decay of π^0 and η mesons, and $\varepsilon_{photonic}$ is photonic electron reconstruction efficiency. This efficiency is determined by embedding simulated gammas and π^0 into real data. Finally, NPE yield is corrected by reconstruction and electron identification efficiency.

3. Results

The recent results of non-photonic electron measurements in Au+Au collisions at $\sqrt{s_{NN}}$=200 GeV from the year 2010 are shown in Fig. 1 and 2. Figure 1 shows NPE invariant yield in five

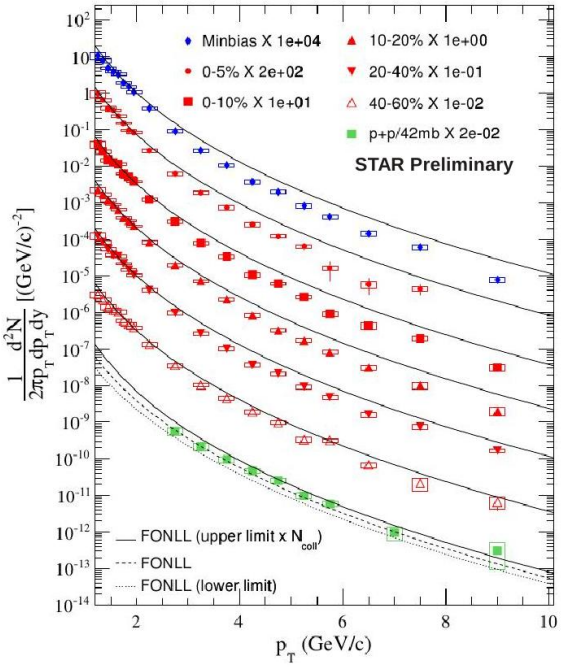

Figure 1: Non-photonic electrons p_T spectra in Au+Au collisions at $\sqrt{s_{NN}}$=200 GeV. Spectrum is divided into 5 centrality bins which are plotted separately. Solid lines represent FONLL calculations scaled by number of binary collisions [4]. Green color represents result from p+p collisions at $\sqrt{s_{NN}}$=200 GeV.

centrality bins compared with Fixed Order plus Next-to-Leading Logarithms (FONLL) calculation scaled by number of binary collisions which correspond to the given centrality bin. In central and semicentral collisions we observed the suppresion of NPE compared to the FONLL calculation [4]. The invariant yield of combined non-photonic electron production in p+p collisions from the year 2005 and year 2008 is shown as well and this result could be very good described by FONLL calculation [2].

The nuclear modification factor (R_{AA}) for 0-10% most central collisions is plot in Fig. 2. Results are compared to a several theoretical models of energy loss mechanism [5]-[9]. It is seen that gluon radiation scenario alone [5] (dashed green line) fails to explain large NPE suppression which is observed at high p_T. When the collisional energy is added to the the gluon radiative scenario (green line), the model describes data better. The collisional dissociation model [8] (red line) and the AdS/CFT calculation [9] (blue line) describe data also well. The baseline for nuclear modification factor calculation is produced from a combination of non-photonic electrons spectra measured in the years 2005 and 2008 [2].

Measurements of NPE v_2 in Au+Au collisions at $\sqrt{s_{NN}}$=200 GeV is shown in Fig. 3. These results are obtained using 2-particle ($v_2$2) and 4-particle ($v_2$4) correlations. These results are compared with theoretical models [10] [11]. Finite v_2 at low p_T indicates strong charm-medium interaction. At high p_T we observe increase of v_2 which can arise from non-flow effects such as jet-like correlations or from path length dependence of heavy quark energy loss.

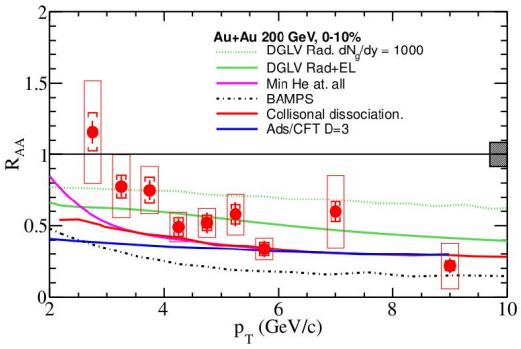

Figure 2: Nuclear modification factor for 0-10% most central collisions in Au+Au at $\sqrt{s_{NN}}$=200 GeV. The results are compared to theoretical models [5]-[9].

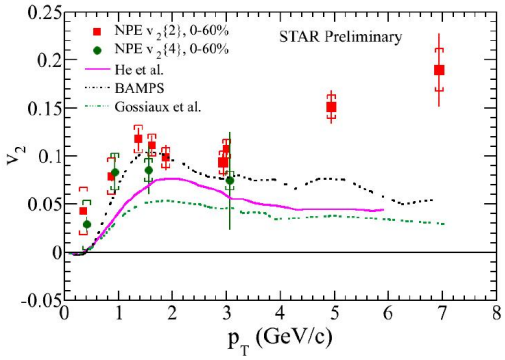

Figure 3: NPE elliptic flow v_2 in Au+Au collisions at $\sqrt{s_{NN}}$=200 GeV.

4. Summary

In this proceedings, results of non-photonic electrons measurements in Au+Au collisions at $\sqrt{s_{NN}}$=200 GeV from STAR are presented. The preliminary results show large suppression of NPE production in central Au+Au collisions. This suppression cannnot be explained by gluon radiation scenario alone. Large NPE v_2 is observed at low p_T which indicates a strong charm-medium interaction.

This work was supported by Grant Agency of the Czech Technical University in Prague, grant No. SGS13/215/OHK4/3T/14 and by Grant Agency of the Czech Republic, grant No.13-20841S.

References

[1] A. D. Frawley, T. Ullrich, and R. Vogt, Phys. Rept. 462, 125 (2008).

[2] H. Agakishiev et al. [STAR Collaboration], Phys. Rev. D83, 052006,(2011).

[3] L. Adamczyk et al. [STAR Collaboration], arXiv: 1204.4244 (2011).

[4] M. Cacciari, P. Nason and R. Vogt, Phys. Rev. Lett. 95, 122001 (2005).

[5] M. Djordjevic, M. Gyulassy, R. Vogt, and S. Wicks, Phys. Lett. B 632, 81 (2006).

[6] A. Buzzatti, M. Gyulassi, arXiv:1207.6020.

[7] H. Van Hees, M. Mannarelli, V. Greco, and R. Rapp, Phys. Rev. Lett. 100, 192301 (2008).

[8] R. Sharma, I. Vitev, B. Zhang, Phys. Rev. C 80, 054902 (2009).

[9] W. A. Horowitz, J.Phys. G35 044025 (2008).

[10] M. He, R. J. Fries, and R. Rapp, Phys.Rev. C86 014903 (2012).

[11] Gossiaux, J. Aichelin, T. Gousset, and V. Guiho, J.Phys. G37 094019 (2010).

Available online at www.sciencedirect.com

SciVerse ScienceDirect

Nuclear Physics A 910–911 (2013) 387–390

NUCLEAR PHYSICS A

www.elsevier.com/locate/nuclphysa

The measurement of non-photonic electrons in STAR

Olga Hájková for the STAR Collaboration

Czech Technical University in Prague, Faculty of Nuclear Sciences and Physical Engineering, Břehová 7, 11519, Prague 1, Czech Republic

Abstract

The measurements of non-photonic electrons (NPE), mainly produced by semileptonic decays of D and B mesons, provide information on heavy quarks production as well as properties of nuclear matter produced in heavy ion collisons. In order to interpret the NPE measurements it is important to determine the relative charm and bottom contribution to the NPE spectrum. In this proceedings we present the measurements of NPE spectra and NPE-hadron azimuthal correlations in p+p collisions at $\sqrt{s}$=200 GeV and at $\sqrt{s}$=500 GeV. NPE-hadron correlations allow extraction of the B decay contribution to the NPE. The B decay contribution is comparable to the contribution from the D meson decay at $\sqrt{s}$=200 GeV at p_T higher than 5 GeV/c, and is about 60% at $\sqrt{s}$=500 GeV at p_T higher than 5 GeV/c. STAR measured NPE spectrum in p+p collisions as well as relative constribution of bottom decays to the spectrum is consistent with FONLL pQCD calculations. The preliminary results of NPE spectra and NPE-hadron correlations in Au+Au collisions at $\sqrt{s}$=200 GeV is shown.

Keywords: non-photonic electrons, STAR, electron-hadron correlation

1. Introduction

Due to their large masses, heavy quarks are produced mainly during initial parton-parton interaction at RHIC, and they are good probes to study QCD matter. Study of heavy flavor production in p+p collisions is a test of the validity of the perturbative QCD. It is also used as a baseline to study effects of hot and dense nuclear matter from the production of heavy quarks in heavy ion collisions [1].

The nuclear modification factor of non-photonic electrons at $p_T > 6$ GeV/c measured in central Au+Au collisions at $\sqrt{s_{NN}}$=200 GeV is comparable to that of light hadrons [2]. Theoretical predictions suggest smaller energy loss of heavy quarks compared with light quarks due to the dead cone effect [3] [4] [5], if the dominant energy loss process is gluon radiation. In order to address this B and D contribution to the total NPE yield must be quantified. This could be done via non-photonic electrons - charged hadrons azimuthal correlations, taking into account the fact that electrons from D and B decays have different near side correlation shape [6].

2. Analysis

Data reported in this proceedings were collected in p+p collisions at $\sqrt{s}$=200 GeV and at $\sqrt{s}$=500 GeV in the years 2005, 2008, and 2009 with High Tower Trigger, and in Au+Au collisions at $\sqrt{s}$=200 GeV in the year 2010 with Minimum Bias Trigger. Main detectors used in presented measurements are the Time Projection Chamber

Email address: olga.hajkova@fjfi.cvut.cz (Olga Hájková for the STAR Collaboration)

http://dx.doi.org/10.1016/j.nuclphysa.2012.12.038

(TPC), the main charged particle tracking device in the STAR detector used for particle identification and momentum determination, the Barrel Electromagnetic Calorimeter (BEMC), used for deposited energy measurement, and also as a trigger detector, and the Barrel Shower Maximum Detector (BSMD). Electron candidates were identified via specific ionization energy loss from the TPC, the ratio of track momentum to the energy deposited in the BEMC, the BSMD shower profile, and the distance between TPC track projected position at BEMC and reconstructed BEMC cluster position. The obtained inclusive electron sample includes non-photonic electrons, photonic electrons background, and hadron contamination. Non-photonic electrons yield is calculated as:

$$N_{NPE} = N_{Inclusive} * \epsilon_{purity} - N_{PHE}/\epsilon_{photonic},$$

where N_{NPE} is non-photonic electrons yield, $N_{Inclusive}$ is all identified electrons yield, ϵ_{purity} is the purity of inclusive electron sample, N_{PHE} is yield of reconstructed photonic electron background, mainly comes from photon conversion in the detector material and from Dalitz decay of π^0 and η mesons, and $\epsilon_{photonic}$ is photonic electron reconstruction efficiency. This efficiency was determined from embedding simulated gammas and pions into real data. The photonic electron reconstruction efficiency was found to be 0.3 - 0.7 as an increasing function of p_T [7].

3. Non-photonic electrons in p+p collisions

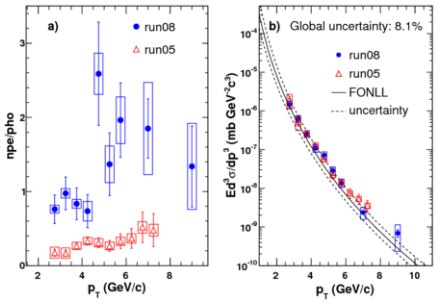

Figure 1: Left: The non-photonic to photonic electrons ratio in p+p collisions at $\sqrt{s}$=200 GeV in the year 2005 (red triangles), and in the year 2008 (blue circles). Right: Non-photonic electron invariant cross section from the years 2005 and 2008 (red triangles and blue circles respectively). The solid line is the FONLL calculation and dashed lines are FONLL uncertainties. [7] [8].

Figure 1 shows a comparison between results in p+p collisions at $\sqrt{s}$=200 GeV in the years 2005 and 2008. In the year 2005 the STAR detector setup included the silicon vertex detector in front of the TPC that led to much more gamma conversion background, and consequently to low NPE/PHE ratio, where PHE is photonic electron background. Due to the less material run, the NPE/PHE ratio is much larger in the year 2008 than in the year 2005 - see Figure 1 (left). Despite of the large difference in photonic background, results from the years 2005 and 2008 agree with each other - see Figure 1 (right). After combining both results, the invariant cross section of non-photonic electron production in p+p collisions was obtained and compared with the FONLL calculation - see Figure 2 (up). In Figure 2 (down) the data over FONLL ratio are shown. Data from PHENIX and corrected results from the year 2003 are shown there as well. All these results agree with each other [7] [2].

NPE originate dominantly from the bottom and charm meson decays. NPE from these two sources could be separated via charged hadron-NPE azimuthal correlations study. The relative B meson contribution to NPE could be obtained by comparing NPE-hadron correlations from data with PYTHIA calculation (Figure 3 left at $\sqrt{s}$=200 GeV, and central at $\sqrt{s}$=500 GeV), fitting the data with PYTHIA shapes for the charm and bottom part. In Figure 3 (right) the relative B contribution as a function of p_T at $\sqrt{s}$=200 GeV and $\sqrt{s}$=500 GeV is shown. The B decay contribution increases with p_T, and is comparable to the contribution from the D meson decay at p_T higher than 5 GeV/c at $\sqrt{s}$=200 GeV. The ratio of the B contribution to NPE is about 60% for p+p collisions at 500GeV at high p_T. The B contribution is systematically higher at 500 GeV than at 200 GeV in the overlap p_T region.

Using the information of the relative contribution of the bottom to NPE spectra, it is possible to compare the charm as well as the bottom NPE spectra to FONLL calculations. Spectra and calculations are consistent [7].

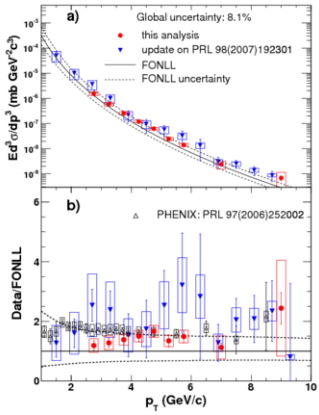

Figure 2: Top: Invariant cross section of non-photonic electrons after combining results from the years 2005 and 2008 (red circles). Bottom: The data over FONLL ratio [7] [8].

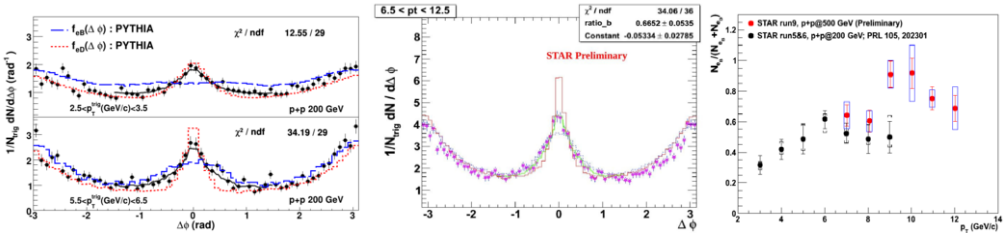

Figure 3: Left/Central: NPE-hadron correlations from data in p+p collisions at $\sqrt{s}$=200 GeV and $\sqrt{s}$=500 GeV (black/magenta dots) compared with PYTHIA simulations of electron(from B/D mesons decays)-hadron correlations (blue dashed and red dotted/solid red lines respectively). The black/green lines are combined fits to the data. Right: The relative bottom contribution to NPE electrons in p+p collisions at $\sqrt{s}$=200 GeV (black dots), and at $\sqrt{s}$=500 GeV (red dots)[9].

4. Non-photonic electrons in Au+Au collisions

The preliminary result of non-photonic spectrum in Au+Au collisions at $\sqrt{s_{NN}}$=200 GeV from the year 2010 is plotted in Figure 4 (left). In the right plot there is the non-photonic electrons over photonic electrons ratio as a function of p_T. For these results, just a part of data collected in Au+Au collisions in the year 2010 was used.

Non-photonic-hadron correlations in 0-10% and 10-40% of the most central Au+Au collisions are plotted in Figure 5. Correlations in 10-40% central collisions are plotted with associated tracks with different p_T^{asso}. Both the near side and the away side correlations are observed. Due to the fact that the NPE elliptic flow v_2 is still under the study, the v_2 background is not subtracted yet. In each plot there are two red dotted curves representing the minimum and the maximum of the supposed NPE v_2. The minimum possible v_2 is estimated to be zero, the maximum is assumed to be the same as hadron v_2 [10]. The NPE elliptic flow v_2 was calculated from the electron-event plane correlations. The preliminary result for 10-40% central Au+Au collisions shows finite v_2 [11].

5. Summary and Outlook

In this proceedings, results of non-photonic electrons measurements in p+p collisions at $\sqrt{s}$=200 GeV and $\sqrt{s_{NN}}$=500 GeV and preliminary results of the NPE analysis in Au+Au collisions at $\sqrt{s_{NN}}$=200 GeV from STAR

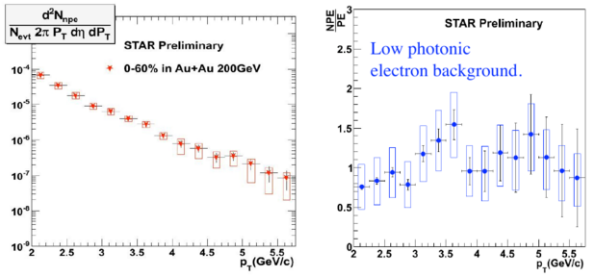

Figure 4: Left: The preliminary result of the non-photonic electron spectrum, for 0-60% of the most central Au+Au collisions at $\sqrt{s_{NN}}$=200 GeV. Right: The NPE over PHE ratio as a function of p_T.

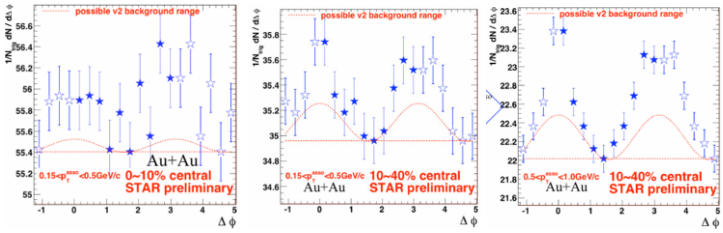

Figure 5: Non-photonic-hadron azimuthal corelations in Au+Au collisions at $\sqrt{s_{NN}}$=200 GeV for 0-10% central collisions (left), 10-40% central collisions with associated track 0.15< p_T^{asso} <0.5 GeV/c (central), and 10-40% central collisions with associated track 0.5< p_T^{asso} <1 GeV/c (right). Red dotted lines represent upper and lower limits of the estimated NPE elliptic flow v_2 background.

are presented. The preliminary result for p+p collisions at $\sqrt{s}$=500 GeV shows that the B contribution is above 60% and seems to be larger than in 200 GeV. Two STAR detector upgrades planned for the years 2013 and 2014 will significantly improve the open heavy flavor measurements. Muon Telescope Detector [12] will allow muon measurements at mid-rapidity, and Heavy flavor tracker [13] will allow measurements of displaced vertices of charm and bottom decays.

This work was supported by grant INGO LA09013 of the Ministry of Education, Youth and Sports of the Czech Republic, and by the Grant Agency of the Czech Technical University in Prague, grant No. SGS10/292/OHK4/3T/14.

References

[1] A. D. Frawley, T. Ullrich and R. Vogt, Phys. Rept. 462, 125 (2008).
[2] B. I. Abelev et al. [STAR Collaboration], Phys.Rev.Lett. 98, 192301 (2007); Erratum-ibid. 106, 159902 (2011).
[3] M. Djordjevic, M. Gyulassy, S. Wicks, Phys. Rev. Lett. 94, 112301 (2005).
[4] N. Armesto et al., Phys. Rev. D71, 054027 (2005).
[5] Y. L. Dokshitzer, D. E. Kharzeev, Phys. Lett. B519, 199 (2001).
[6] J. Adams et al. [STAR Collaboration], Phys. Rev. Lett. 105, 202301 (2010).
[7] H. Agakishiev et al. [STAR Collaboration], Phys. Rev. D83, 052006,(2011).
[8] M. Cacciari, P. Nason and R. Vogt, Phys. Rev. Lett. 95, 122001 (2005).
[9] M. M. Aggarwal et al. [STAR Collaboration], Phys. Rev. Lett. 105, 202301 (2010).
[10] J. Adams et al. [STAR Collaboration], Phys. Rev. C 72, 014904 (2005).
[11] Wenqin Xu [STAR Collaboration], arXiv:1106.6020v1 (2011).
[12] L. Ruan, G. Lin (Yale U.), Z. Xu, K. Asselta, H.F. Chen, W. Christie, H. J. Crawford, J. Engelage, G. Eppley, C. Li et al. [STAR Collaboration], J. Phys. G G36, 095001, (2009).
[13] Spiros Margetis [STAR Collaboration], Nucl. Phys. Proc. Suppl. 210-211 (2011).

Measurements of non-photonic electrons with the STAR experiment

Olga Rusňáková for the STAR Collaboration

Czech Technical University in Prague
Faculty of Nuclear Sciences and Physical Engineering
Břehová 7, 11519, Prague 1, Czech Republic

E-mail: olga.hajkova@fjfi.cvut.cz

Abstract. Non-photonic electrons (NPE), produced by semileptonic decays of D and B mesons, are good probes to study the properties of hot and dense medium created in relativistic heavy ion collisions at RHIC. Studies of heavy quark production in p+p collisions can test the validity of perturbative QCD. They also provide a baseline to study the effects of nuclear matter on the production of heavy quarks in heavy ion collisions. In this paper, we present recent results of NPE spectra measured in p+p collisions at $\sqrt{s} = 200$ GeV in mid-rapidity. We also report NPE nuclear modification factor R_{AA} and elliptic flow v_2 in Au+Au collisions at $\sqrt{s_{NN}} = 200$ GeV.

1. Introduction

Heavy quarks are good probes to study the properties of strongly interacting matter, Quark-Gluon Plasma (QGP). Due to their large masses, they are produced mainly during initial hard parton scatterings at RHIC, before the QGP phase. They are expected to interact with the medium differently from the light quarks. Hot nuclear matter effects, such as heavy quark inteactions with the QGP, change the heavy quark kinematic distribution but do not change the total heavy quark yield. Due to energy loss of heavy quarks in the QGP, their transverse momentum p_T distributions in heavy ion collisions may fall steeper than those in p+p collisions. At small p_T, heavy quarks may thermalize with the medium and exhibit collective flow effects [1].

At RHIC, heavy quarks could be studied by measuring NPE which are produced from semileptonic decays of D and B mesons. Measurements of NPE provide information on heavy quarks energy loss and elliptic flow in the hot and dense nuclear matter created in relativistic heavy ion collisions.

Hot nuclear matter effects could be quantified by the nuclear modification factor (R_{AA}). R_{AA} is defined as the ratio of the number of particles produced in nucleus-nucleus collisions to that in proton-proton collisions, scaled by the average number of binary collisions for a given centrality. $R_{AA} < 1$ may indicate heavy quark energy loss. In the case there are no medium effects the nuclear modification factor will be equal to unity.

2. Analysis

Data reported in this proceedings were collected in p+p collisions at $\sqrt{s} = 200$ GeV in 2009, and in Au+Au collisions at $\sqrt{s_{NN}} = 200$ GeV in 2010 with Minimum Bias (MB) and High Tower (HT) triggers, where MB triggered data are used for $p_T < 2$ GeV/c results and High Tower triggered data for $p_T > 2$ GeV/c results.

The Time Projection Chamber (TPC) is the primary tracking device for charged particle momentum determination at STAR. Information from the TPC was used for particle identification together with information from the Barrel Electromagnetic Calorimeter (BEMC), and the Time Of Flight (TOF) detector. The BEMC was used for high p_T electron energy measurement and online trigger. The TOF detector was used to reduce hadron contamination at low p_T.

Electron candidates are identified via ionization energy loss measured by the TPC combined with TOF velocity information, which together provide good PID capability at low-p_T region. Electrons at high-p_T are selected using the ratio of the track momentum and the energy deposited in the BEMC, the BSMD shower profile, and the distance between TPC track projected position at BEMC and reconstructed BEMC cluster position. The raw NPE yield is calculated as: $N_{NPE} = N_{Inc} * \epsilon_{pur} - N_{PHE}/\epsilon_{PHE}$, where N_{NPE} is NPE yield, N_{Inc} represents inclusive electron candidate yield, ϵ_{pur} is the purity of inclusive electron sample, N_{PHE} is the yield of reconstructed photonic electron background, which mainly originates from photon conversion in the detector material and from Dalitz decay of π^0 or η mesons, and ϵ_{PHE} represents the photonic electron reconstruction efficiency. ϵ_{PHE} is estimated by full GEANT simulation. Finally, NPE yield is corrected by detector acceptance and efficiencies.

3. NPE results in p+p collisions at $\sqrt{s} = 200$ GeV

The recent results of STAR NPE measurement in p+p colisions at $\sqrt{s} = 200$ GeV are shown in Fig. 1. Left panel presents the measured NPE yield as a function of p_T, where black marks show results obtained in the 2009 analysis and blue points show former analysis results [3]. The new data extends to lower p_T region compared to the previous STAR measurement. Green points represent data from PHENIX (pseudorapidity range $|\eta| < 0.35$) [4]. STAR and PHENIX results are consistent in the overlappping p_T range. STAR results are also compared with pQCD FONLL calculation (Fixed Order plus Next-to-Leading Logarithms [2]), where the FONLL central result is presented by the blue solid line and its upper and lower uncertainties by black lines. Experimental results are in good agreement with FONLL calculation and lie between its central value and the upper limit.

Data and FONLL calculation are also compared in Fig. 1 (right panel) where a ratio to FONLL central values is plotted.

4. NPE results in Au+Au collisions at $\sqrt{s_{NN}} = 200$ GeV

In this section the recent results of NPE measurements in Au+Au collisions at $\sqrt{s_{NN}}$=200 GeV will be discussed. The NPE invariant yields were compared with FONLL calculations scaled by the average number of binary collisions in five centrality bins. In central and semicentral Au+Au collisions we observed a suppresion of NPE production compared to the FONLL calculation [2]. Figure 2 (left) shows NPE R_{AA} for the 0-10% most central collisions compared to several theoretical models of heavy quark energy loss [5]-[9]. Gluon radiation scenario alone [5] (dashed green line) fails to explain the large NPE suppression at high p_T. When the collisional energy loss is added model calculations describe the data better. The collisional dissociation model [8] (red line) and the AdS/CFT calculation [9] (blue line) also describe the data well. Note that the baseline for nuclear modification factor calculation is produced from a combination of NPE spectra measured in the years 2005 and 2008 [3]. By including the aforementioned new p+p results from 2009 data, the R_{AA} uncertainties will be reduced.

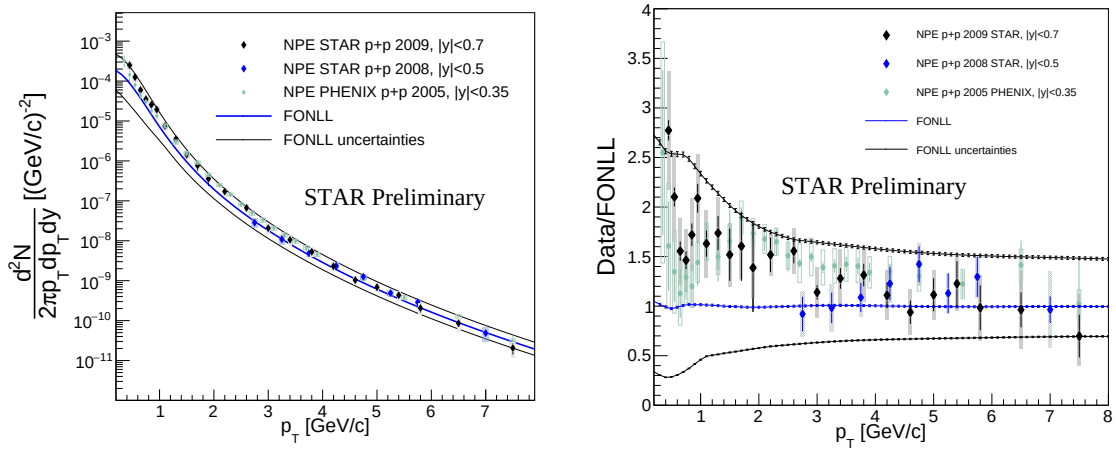

Figure 1. Non-photonic electron yield (left) and ratio of data over FONLL calculation (right) [2], STAR results from p+p collisions at $\sqrt{s}$=200 GeV from the year 2009 (black) compared with STAR data from the year 2008 (blue) [3] and PHENIX p+p results [4].

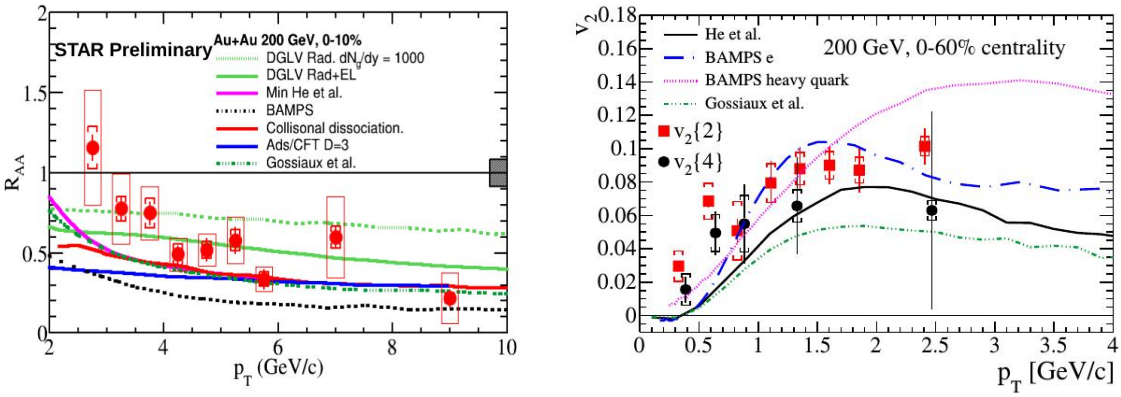

Figure 2. Non-photonic electron results from Au+Au collisions at $\sqrt{s}$=200 GeV from 2010. On the left plot is the NPE nuclear modification factor and on the right plot is the NPE elliptic flow. Both results are compared with theoretical models [5]-[14].

The right panel of Fig. 2 shows a measurements of NPE v_2 in Au+Au collisions at $\sqrt{s_{NN}}$=200 GeV. These results are obtained using 2-particle ($v_2\{2\}$) and 4-particle ($v_2\{4\}$) correlations [10]. These results are compared with theoretical models [11]-[14]. We observe finite v_2 at low p_T and at high p_T we observe increasing of v_2 which can arise from non-flow effects such as jet-like correlations.

5. Summary

The NPE invariant yield in p+p collisions at $\sqrt{s}$ = 200 GeV has been measured by the STAR experiment using high statistics data. The result can be described by FONLL calculations. Compared to the previously published STAR results, the new measurement using 2009 data extends the NPE spectrum to lower p_T region. Results of NPE measurements in Au+Au collisions at $\sqrt{s_{NN}}$=200 GeV from STAR show large suppression of NPE production in central

Au+Au collisions which cannnot be explained by gluon radiation energy loss alone. Finite NPE v_2 is observed at low p_T which together with strong NPE suppresion in central collisions indicates strong charm-medium interaction.

6. Outlook

The new STAR detector, Heavy Flavor Tracker (HFT), which started its operation in 2014, extends the STAR particle identification capability to heavy flavor particles (i.e. particles containing heavy quarks). The HFT is able to topologically reconstruct charm mesons and baryons. This is made possible by reconstruction of secondary vertices with high precision. For NPE measurements it will be possible to distinguish between electrons from D and B mesons. Such studies will improve our understanding of heavy quarks interaction with QGP. Projected R_{CP} results for electrons from these two sources are shown in Fig. 3, where R_{CP} is a central to peripheral nuclear modification factor, define as a ratio of yield in central collisions to yield in peripheral collisions scaled by number of binary collisions.

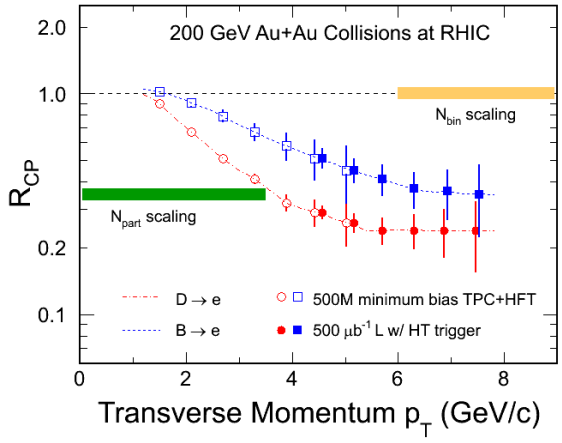

Figure 3. Projection of R_{CP} of non-photonic electrons from D (red) and B (blue) mesons separately [15]. Open symbols are for 500M Au+Au simulated minimum-bias events, and filled symbols are for HT data with 500 μb^{-1} sampled luminosity.

Acknowledgments

This work was supported by Grant Agency of the Czech Technical University in Prague, grant No. SGS13/215/OHK4/3T/14 and by Grant Agency of the Czech Republic, grant No.13-20841S.

References

[1] A. D. Frawley, T. Ullrich, and R. Vogt, Phys. Rept. 462, 125 (2008).
[2] M. Cacciari, P. Nason and R. Vogt, Phys. Rev. Lett. 95, 122001 (2005).
[3] H. Agakishiev et al. [STAR Collaboration], Phys. Rev. D83, 052006,(2011).
[4] A.Adare et al. [PHENIX Collaboration, http://dx.doi.org/10.1103/PhysRevC.84.044905
[5] M. Djordjevic, M. Gyulassy, R. Vogt, and S. Wicks, Phys. Lett. B 632, 81 (2006).
[6] A. Buzzatti, M. Gyulassi, arXiv:1207.6020.
[7] H. Van Hees, M. Mannarelli, V. Greco, and R. Rapp, Phys. Rev. Lett. 100, 192301 (2008).
[8] R. Sharma, I. Vitev, B. Zhang, Phys. Rev. C 80, 054902 (2009).
[9] W. A. Horowitz, J.Phys. G35 044025 (2008).
[10] L.Adamczyk et al. [STAR Collaboration], arXiv:1405.6348 (2014).
[11] J. Uphoff, O. Fochler, Z. Xu, C. Greiner, Phys.Rev. C84 024908 (2011).
[12] J. Uphoff, O. Fochler, Z. Xu, C. Greiner, Phys.Lett. B717 430435 (2012).
[13] M. He, R. J. Fries, and R. Rapp, Phys.Rev. C86 014903 (2012).
[14] Gossiaux, J. Aichelin, T. Gousset, and V. Guiho, J.Phys. G37 094019 (2010).
[15] The STAR Heavy Flavor Tracker, Technical Design Report, (2011).

QUARKONIUM MEASUREMENTS AT STAR

O. Hajkova for STAR Collaboration, olga.hajkova@fjfi.cvut.cz, Faculty of Nuclear Sciences and Physical Engineering, Czech Technical University in Prague, Brehova 7, Praha 1

ABSTRACT. During the last decade STAR experiment has studied the hot and dense nuclear matter produced in heavy ion collisions at RHIC. The study of quarkonium production provides the information about the properties of this nuclear matter. However the production mechanism of quarkonia is not yet satisfactorily understood and cold nuclear effects have to be quantified. Due to the Debye color screening of the quark-antiquark potential the quarkonium production is expected to be suppressed when QGP is formed. Recent J/ψ measurements at mid-rapidity in p+p, and Au+Au at $\sqrt{s_{NN}}$= 200 GeV at STAR, and Υ measurements in p+p, and Au+Au collisions are reported. In Au+Au the suppression was observed in central and semi-central collisions, while at high p_T only in central collisions. Production of Υ(1S+2S+3S) in central Au+Au collisions is observed to be suppressed. Centrality dependence of the nuclear modification factor is reported.

INTRODUCTION

The strongly interacting nuclear matter at sufficiently high density undergoes a phase transition from the hadronic matter to a new state, so-called quark gluon plasma (QGP), in which quarks are no longer confined into color neutral bound states. QGP is believed to exist in the early universe, shortly after the Big Bang. Current experiments as Relativistic Heavy Ion Collider (RHIC), located at the Brookhaven National Laboratory in Upton, New York or at Large Hadron Collider in CERN provide a possibility to produce QGP in a laboratory in nucleus-nucleus collisions and the experimental detection of QGP represents one of the greatest challenges of present high energy physics. The cardinal question is what observable signatures can the predicted new form of the matter provide. One of the probes, proposed by Matsui and Satz [1], for searching for QGP and for investigating its properties is a study of the quarkonium production. It is predicted that due to the color screening the quarkonium production is suppressed when QGP is present at sufficiently high temperature. Before resolving whether QGP was formed or not, it is necessary to study the production of J/ψ in hadron-hadron, hadron-ion and ion-ion collisions separately to distinguish cold nuclear matter effects from the suppression due to the formation of QGP. The STAR allows to study J/ψ meson in e^+e^- channel. The summary of the measurements in p+p, d+Au, Cu+Cu, and Au+Au collisions at $\sqrt{s_{NN}}$=200 GeV is presented in this contribution. Due to the low production cross section of $b\bar{b}$ pairs it is expected that color screening is the major effect playing role in bottomonium suppression. Recombination and comovers effects are negligible. Υ production results in p+p, and Au+Au collisions obtained via e^+e^- channel are presented.

STAR EXPERIMENT

The RHIC is an intersection storage ring particle accelerator designed to collide light nuclei like polarized proton and heavy nuclei such as Cu, Au and U. Also d+Au collisions can be measured. The maximum available energy is in p+p collisions 500 GeV and in heavy ion systems 200 GeV per nucleon-nucleon pair in center of mass system.

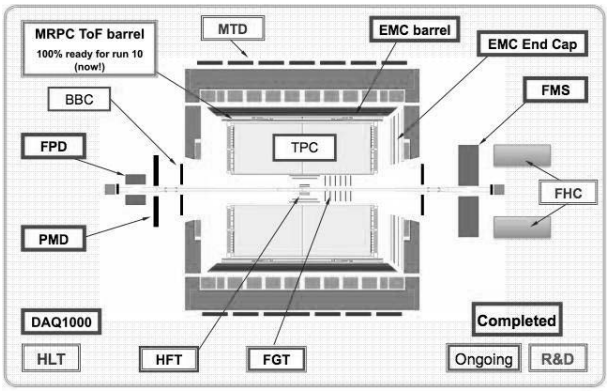

Fig. 1. The experimental setup of the STAR detector.

The Solenoidal Tracker at the RHIC (STAR) is a massive detector that was designed especially for identified particle and search for signatures of the quark gluon plasma formation and its properties. Most detectors of the STAR experiment are inside a large solenoidal magnet with an approximately uniform magnetic field, B=0.5 T maximally, parallel to the beam pipe. The major parts related to results presented here are the Time Projection Chamber (TPC) [2], Barrel Electromagnetic Calorimeter (BEMC) [3]. The general STAR detector schema is shown in Fig. 1.

STAR RESULTS

Let us first discuss the production at high transverse momentum in p+p collisions at$\sqrt{s_{NN}}$=200 GeV (years 2005 and 2006 [4]), and production in p+p collisions at$\sqrt{s_{NN}}$=200 GeV (year 2009) [5]. J/ψ were reconstructed via dielectron decay channel with branching ratio 5.9%. Using TPC and BEMC the electrons and positrons were identified and the J/ψ yield was extracted by subtracting the invariant mass spectrum of like-sign pairs from that of unlike-sign pairs. In Fig. 2 is shown the J/ψ p_T distributions in p+p collisions from years 2005, 2006 (violet triangle), and 2009 (red boxes) compared with PHENIX data (white boxes). The gray band, the dashed line, and the dashed-dotted line denote theoretical calculations, NNLO$\star$ CS (Color Singlet Model), CS+CO (Color Octet Model), and CEM (Color Evaporation Model) models respectively. The CEM calculation describes data well [5].

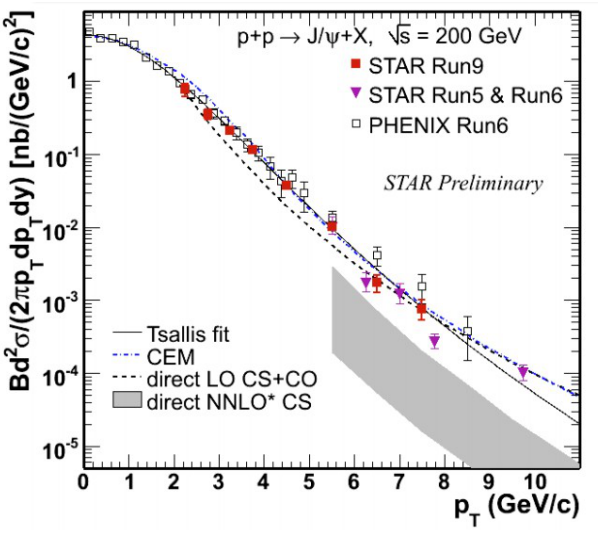

Fig. 2. The J/ψ p_T distributions in p+p collisions at $\sqrt{s_{NN}}$=200 GeV [5].

The nuclear modification factor R_{AA} is the ratio of the yield in nuclear collisions to that in p+p collisions scaled by the number of binary collisions. This factor is used to quantify medium-induced effects on particle production such as Debye screening, nuclear absorption, gluon shadowing, recombination etc. In Fig. 3 is shown the R_{AA} as a function of J/ψ p_T in Au+Au collisions (years 2009 and 2010). The suppression was observed in central and semi-central collisions. At high p_T the suppression was observed only in central collisions [6].

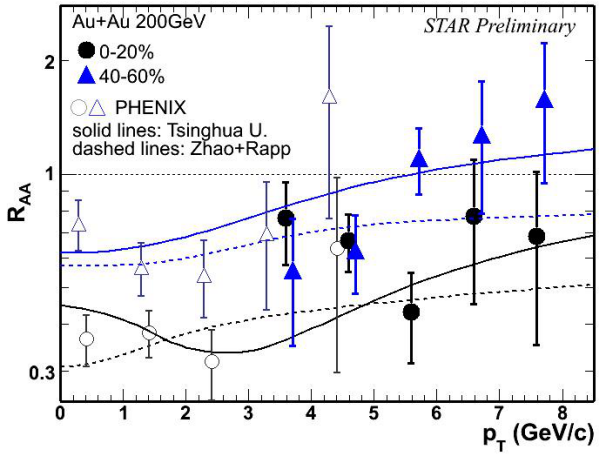

Fig. 3. The J/ψ R_{AA} factor in Au+Au collisions at$\sqrt{s_{NN}}$=200 GeV as a function of J/ψ p_T [6].

The azimuthal correlation between high-p_T J/ψ and charged hadrons with $p_T > 0.5$ GeV/c provides an estimation of B-meson decays to the inclusive J/ψ production. Contribution of B-meson feeddown to the J/ψ production in p+p collisions at 200 GeV is 13±5% [4].

Furthermore we would like present Υ(1S+2S+3S) results in p+p and Au+Au collisions at $\sqrt{s_{NN}}$=200 GeV. Upsilon were reconstructed from electron-positron pairs using information from TPC and BEMC. After like-sign background subtraction the significance of Upsilon signal in Au+Au collisions is 5.5 sigma. From these results was calculated nuclear modification factor R_{AA} as a function of the centrality (Fig. 4). Black points denote Υ result compared with J/ψ result (red points), and the solid blue box is the systematic uncertainty from the p+p cross-section [8].

On Fig. 4 is seen that R_{AA} slopes down with increasing centrality. The R_{AA} for 0-60% most central collisions was calculated to be 0.56±0.11(stat)+0.02/-0.14(sys) [7].

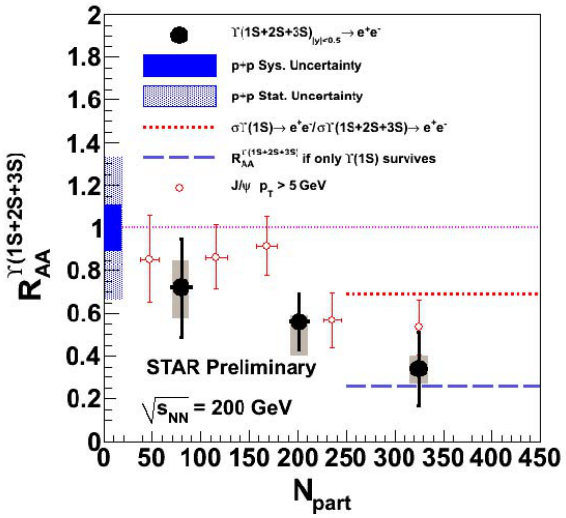

Fig. 4. The Υ R_{AA} factor in Au+Au collisions at$\sqrt{s_{NN}}$=200 GeV as a function of the centrality [7].

SUMMARY

The STAR collaboration reported measurements of J/ψ production in $\sqrt{s_{NN}}$=200 GeV in p+p and Au+Au collisions. The J/ψ nuclear modification factor R_{AA} in Au+Au was calculated. The suppression was observed in central and semi-central collisions. Production of Υ(1S+2S+3S) in central Au+Au collisions is observed to be suppressed. This work was supported by grant INGO LA09013 of the Ministry of Education, Youth and Sports of the Czech Republic.

REFERENCES

1. T. Matsui, H. Satz, Phys. Lett. B, 178 4 (1986).
2. M. Anderson et al. (STAR Collaboration), Nucl.Instrum.Meth.A499 659-678 (2003).
3. M. Beddo et al. (STAR Collaboration), Nucl.Instrum.Meth. A483 734-746 (2002).
4. B. I. Abelev et al. (STAR Collaboration), Phys. Rev. C 80, 041902 (2009).
5. C. Powell (STAR Collaboration), EPS HEP (2011).
6. Zebo Tang (STAR Collaboration), Quark Matter (2011).
7. R. Reed (STAR Collaboration), Quark Matter (2011).
8. B. I. Abelev et al. (STAR Collaboration), Phys. Rev. D 82, 012004 (2010).

J/Ψ MEASUREMENTS AT STAR

Olga Hájková for STAR Collaboration

Faculty of Nuclear Sciences and Physical Engineering, Czech Technical University in Prague, Břehová 7, Praha 1, 224 358 355, olga.hajkova@t-email.cz

Abstract

The study of J/ψ production provides the information about character and properties of the matter originated in high energy collisions. It is supposed that due to the color screening the production is suppressed when QGP is formed. Recent J/ψ measurements at mid-rapidity in p+p, Cu+Cu and d+Au collisions at $\sqrt{s_{NN}} = 200$ GeV at STAR are reported. At high-p_T measurement in Cu+Cu no suppression was observed. The J/ψ – hadron azimuthal correlations allow to extract the fraction of J/ψ that originates from B-meson. This contribution has been established as 13±5%. The J/ψ production in d+Au collisions at $\sqrt{s_{NN}} = 200$ GeV was analyzed and the nuclear modification factor was computed.

Key words: *high energy physics; STAR; quark gluon plasma; quarkonia; J/ψ*

Introduction

The strongly interacting matter at sufficiently high density undergoes a phase transition from the hadronic matter to a new state, so-called quark gluon plasma (QGP), in which quarks are no longer confined into color neutral bound states. QGP is believed to exist in the early universe, shortly after the Big Bang. Current experiments as RHIC or at LHC provide a possibility to produce QGP in a laboratory in nucleus-nucleus collisions and the experimental detection of QGP represents one of the greatest challenges of present high energy physics. The cardinal question is what observable signatures can the predicted new form of the matter provide. One of the probes, proposed by Matsui and Satz [1], for searching for QGP and for investigating its properties is a study of the quarkonia production. It is predicted that due to the color screening the quarkonia production is suppressed when QGP is present at sufficiently high temperature. Before resolving whether QGP was formed or not, it is necessary to study the production of *J/ψ* in hadron-hadron, hadron-ion and ion-ion collisions separately to distinguish cold nuclear matter effects from the suppression due to the formation of QGP. The STAR allows to study J/ψ meson in e^+e^- channel. The summary of the measurements in p+p, d+Au, Cu+Cu collisions at $\sqrt{s_{NN}} = 200$ GeV are presented in this contribution.

STAR experiment

The Relativistic Heavy Ion Collider (RHIC) is located at the Brookhaven National Laboratory in Upton, New York. The RHIC is an intersection storage ring particle accelerator composed of two independent rings in the same tunnel. It is designed to collide light nuclei like proton and heavy nuclei such as Cu, Au as U. Also d+Au collisions can be measured. The maximum available energy is in p+p collisions 500 GeV and in heavy ion systems 200 GeV per nucleon-nucleon pair in center of mass system.

The Solenoidal Tracker at the RHIC (STAR) is a massive detector that was designed especially for a study of the hadron production and search for signatures of the quark gluon plasma formation and its properties. Most detectors of the STAR experiment are inside a large solenoidal magnet with an approximately uniform magnetic field, B=0.5 T maximally, parallel to the beam pipe. The major parts are the Time Projection Chamber (TPC) [7], Barrel Electromagnetic Calorimeter (BEMC) [8]. The general STAR detector schema is shown in Fig.1.

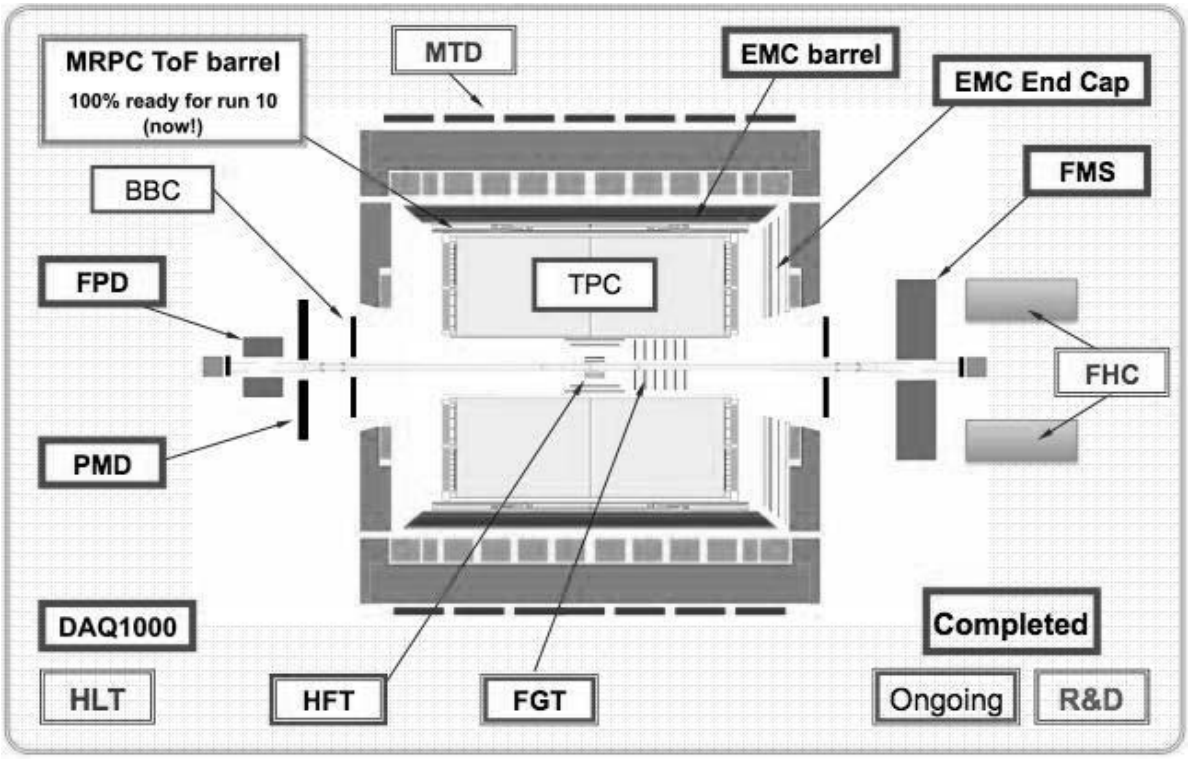

Figure 1: The experimental setup of the STAR detector.

STAR results

Let us first discuss the J/ψ production at high transverse momentum in p+p and Cu+Cu collisions at $\sqrt{s_{NN}} = 200$. The Cu+Cu data are from year 2005 measurements and the p+p data are from years 2005 and 2006. The Cu+Cu data were analyzed in two centrality classes, 0-20% and 0-60% most central collisions. J/ψ were reconstructed via dielectron decay channel with branching ratio 5.9%. Using TPC and BEMC the electrons and positrons were identified and the J/ψ yield was extracted by subtracting like-sign pairs invariant mass spectrum from unlike-sign pairs. J/ψ mass spectrum is shown in Fig.2 [9]. After that the J/ψ reconstruction efficiency was calculated by embedding simulated J/ψ into the real events [9].

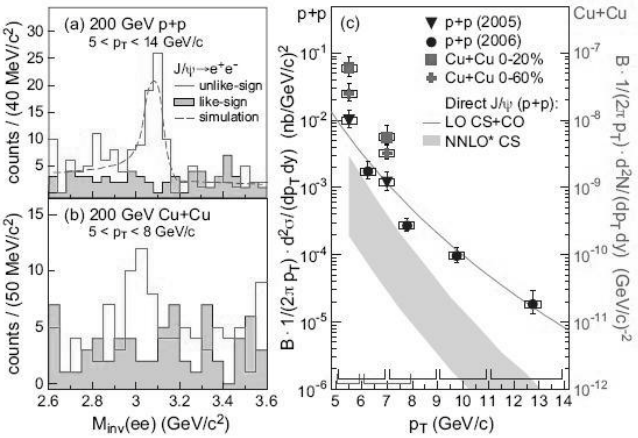

Figure 2: The dielectron mass spectrum in p+p (up) and Cu+Cu (down) collisions, the solid line denotes the unlike sign signal and the gray zone is the like-sign background on the left and the J/ψ p_T distributions in p+p and Cu+Cu collisions at $\sqrt{s_{NN}} = 200$ GeV on the right [9].

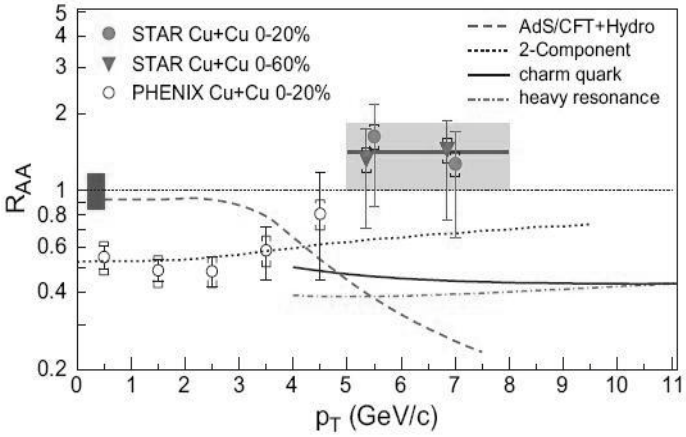

Figure 3: The J/ψ R_{AA} factor in Cu+Cu collisions at $\sqrt{s_{NN}} = 200$ GeV as a function of J/ψ p_T [9].

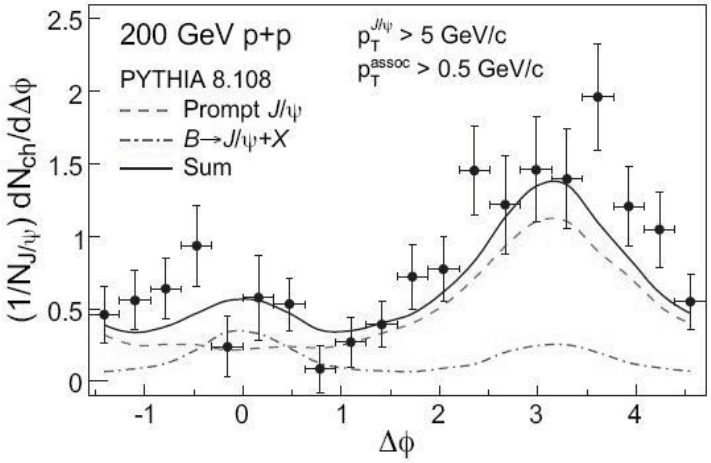

Figure 4: J/ψ - hadron azimuthal correlations. Dashed line and dash-dotted line denote prompt and B-meson feeddown contributions (PYTHIA) and solid line shows theirs sum [9].

The nuclear modification factor R_{AA} is the ratio of the yield in nuclear collisions to that in p+p collisions scaled to the one nucleon-nucleon collision. This factor is used to quantify medium-induced effects on particle production. The R_{AA} factor for J/ψ at higt-pT is shown in Fig.3. The dashed line, solid line, dash-dotted and the dotted one represent different theoretical predictions. The average R_{AA} measured at STAR in Cu+Cu collision is 1.4±0.4(stat.)±0.2(syst.). This suggests that there is no significant suppression observed at high p_T. This can be related to the fact that initial state effects such as anti-shadowing play appreciable role and may lead to the increasing J/ψ production with increasing p_T [9].

In Fig.4 is shown the azimuthal correlation between high-p_T J/ψ and charged hadrons with $p_T > 0.5$ GeV/c in p+p collisions at 200 GeV. Lines denote simulations from PYTHIA of prompt J/ψ, feed down from B-meson and their sum. This gives the contribution of B-mesons decays to the inclusive J/ψ production of 13±5% [9].

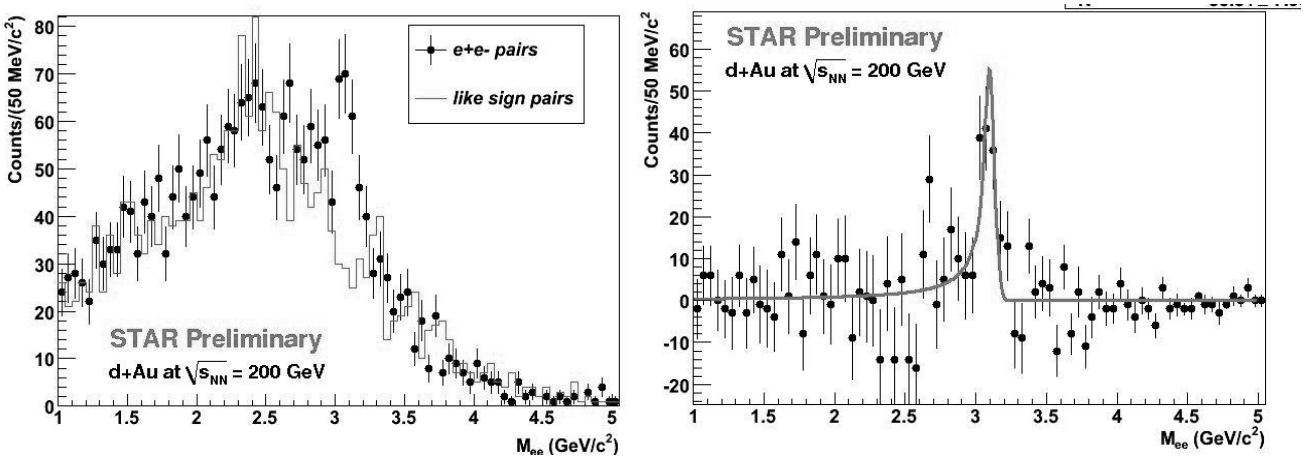

Figure 5: The J/ψ mass spectrum in d+Au collisions at $\sqrt{s_{NN}} = 200$ GeV before background subtraction on the left and after on the right. The peak is fitted by the Crystal Ball function [10].

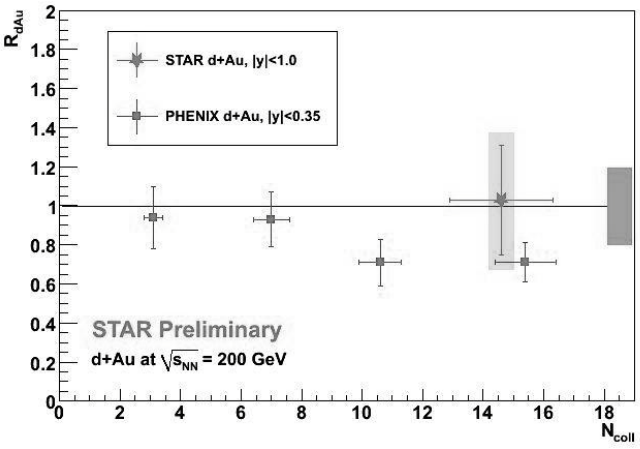

Figure 6: The R_{dA} factor in d+Au collisions at $\sqrt{s_{NN}} = 200$ GeV [10].

Further we would like report on J/ψ production in d+Au collisions at $\sqrt{s_{NN}} = 200$ GeV (year 2008) shown in Fig.5 before (left) and after (right) background subtraction. Finally, Fig.6 shows the R_{dA} factor for 0-20% most central collisions compared to other RHIC measurements. They are consistent with each other.

Summary

The STAR collaboration reported measurements of J/ψ production in $\sqrt{s}$ =200 GeV in p+p and Cu+Cu collisions at high pT. The J/ψ nuclear modification factor R_{AA} in Cu+Cu is consistent with no suppression.. The yield from d+Au collisions was also extracted. The results are consistent with other RHIC measurements.

Bibliography:

[1] T. Matsui, H. Satz, *J/ψ* Suppression by Quark Gluon Plasma, Phys. Lett. B, 178 4 (1986)
[2] S. Digal, P. Petreczky and H. Satz, Phys. Rev. D 64, 094015 (2001)
[3] G. Ropke, D. Blaschke and H. Schulz, Phys. Rev. D 38 3589 (1988)
[4] F. Karsch, M. T. Mehr and H. Satz, Z. Phys. C 37 617(1988)
[5] T. Hashimoto, K. Hirose, T. Kanki and O. Miyamura, Z. Phys. C 38 251 (1988)
[6] M. Harisson et al., Nucl. Instr. and Meth. A 499 235 (2003)
[7] M. Anderson et al. (STAR Collaboration), The STAR Time Projection Chamber: A Unique Tool for Studying High Multiplicity Events at RHIC, Nucl.Instrum.Meth.A499:659-678 (2003)
[8] M. Beddo et al. (STAR Collaboration), The STAR Barrel Electromagnetic Calorimeter, Nucl.Instrum.Meth. A483 734-746 (2002)
[9] B. I. Abelev et al. (STAR Collaboration), J/ψ production at high transverse momenta in p+p and Cu+Cu collisions at $\sqrt{s_{NN}}$ =200 GeV, Phys. Rev. C 80, 041902 (2009)
[10] Ch. Powell (STAR Collaboration), Low pT J/Ψ production in *d*+Au collisions at $\sqrt{s_{NN}}$ =200 GeV in STAR, DNP (2009)